GEOLOGICAL SURVEY OF FINLAND

Special Paper 58

2015

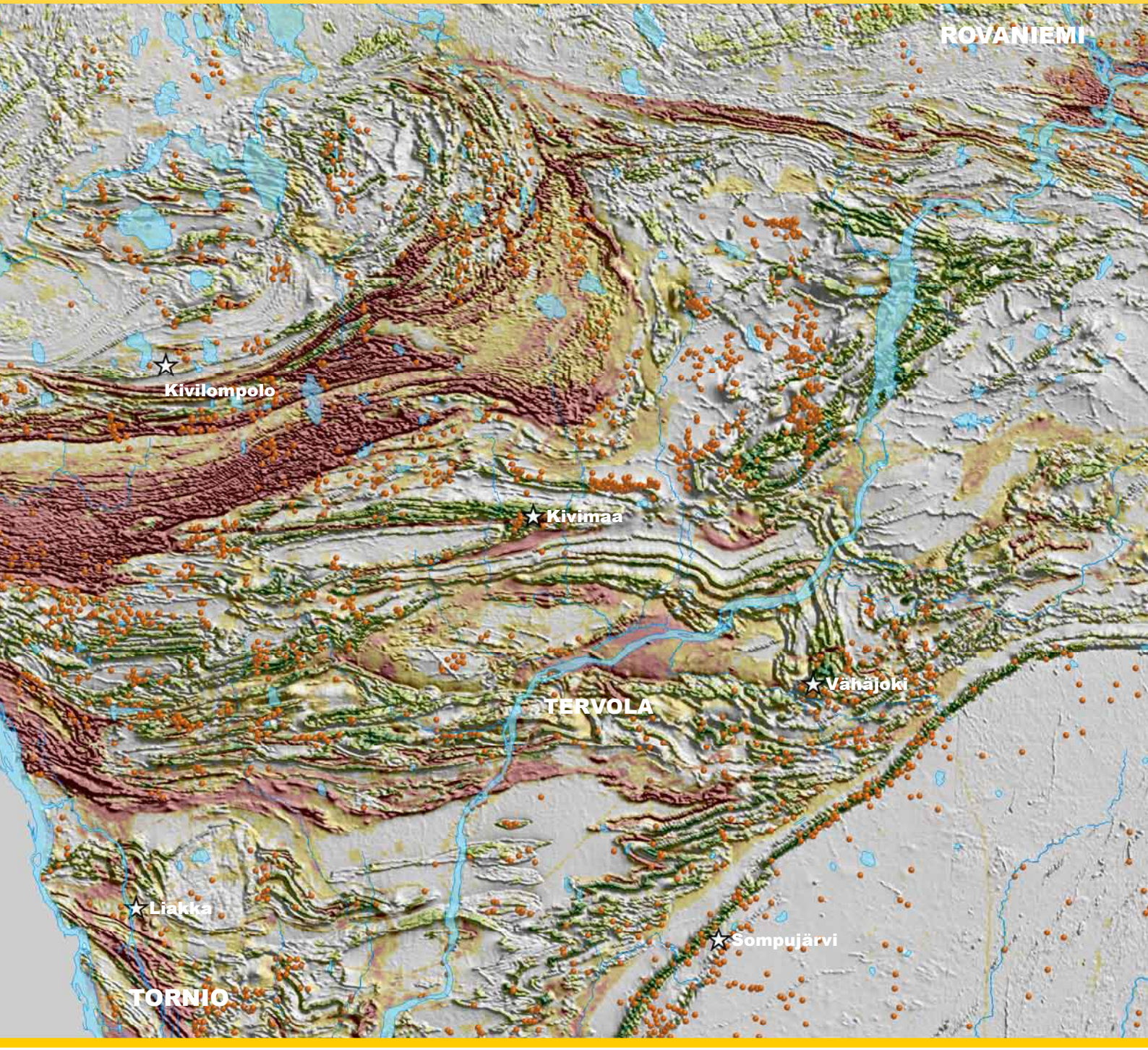

Geophysical signatures of mineral deposit types in Finland

GTK

Edited by Meri-Liisa Airo

Geological Survey of Finland, Special Paper 58

Geophysical signatures of mineral deposit types in Finland

Edited by
Meri-Liisa Airo

Geological Survey of Finland
Espoo 2015

Unless otherwise indicated, the figures have been prepared and photos taken by the authors.

Front cover: A combination of GTK's airborne geophysical datasets from the Peräpohja schist belt, northern Finland. Structural enhancement of magnetic field data (in grey), overlain by the classification of electromagnetic data: red indicates good electrical conductivity, green shows magnetite-bearing rock units (method explained in the text). Circles denote petrophysical sampling sites (Petrophysical database 05/2015). Topographic data © National Land Survey of Finland Topographic Database 03/2013.

ISBN 978-952-217-336-2 (paperback)
ISBN 978-952-217-337-9 (PDF)
ISSN 0782-8535

Layout: Elvi Turtiainen Oy
Printing house: Juvenes Print – Tampereen Yliopistopaino Oy

Airo, M.-L. (ed.) 2015. Geophysical signatures of mineral deposit types in Finland. *Geological Survey of Finland, Special Paper 58*, 144 pages, 13 inserts, 61 figures and 17 tables.

This review provides an overview of geophysical signatures associated with the major mineral deposit types known in Finland. Key geophysical characteristics are portrayed on the basis of petrophysical properties and airborne geophysical patterns related to different mineralization styles. The geophysical response of an ore deposit depends on the contrast between its physical properties and those of its host rock, which in turn depend on the content of minerals having anomalous physical properties. Some types of deposits may be directly detectable by geophysical techniques, in particular those with extra high magnetic properties or density, but many ore deposits in Finland show only weak geophysical responses, at least at the regional scale. However, favourable structures for mineral deposits can easily be mapped using country-wide airborne geophysical data, and even a target-scale structural framework can be outlined. As the direct location of new ore deposits will become less likely, the trend of geophysical surveying is to provide mappable parameters and criteria that can be applied in mineral system research and mineral potential mapping.

Keywords (GeoRef Thesaurus, AGI): geophysics, geophysical surveys, airborne methods, petrophysics, metal ores, mineral exploration, Proterozoic, Archean, Finland

Meri-Liisa Airo
Geological Survey of Finland
P.O. Box 96
FI-02151 Espoo
Finland

E-mail: meri-liisa.airo@gtk.fi

CONTENTS

Preface....7
Meri-Liisa Airo

Geophysical signatures of mineral deposit types – SYNOPSIS....9
Meri-Liisa Airo

Practical 3D electromagnetic modelling and magnetic susceptibility effects
– the case of Kellojärvi, eastern Finland....71
Ilkka Suppala

Petrophysical and rock magnetic studies to aid Au exploration
– case studies from the Häme belt, southern Finland....89
Satu Mertanen and Fredrik Karell

Airborne radiometric data as a uranium exploration tool – case studies from southern Lapland....107
Laura S. Lauri and Pertti Turunen

Hyperspectral close-range LWIR Imaging spectrometry – 3 case studies....117
Viljo Kuosmanen, Hilkka Arkimaa, Markku Tiainen and Rainer Bärs

PREFACE

The power of geophysical methods is to see undercover, below thick overburden. Because finding new mineral deposits at the surface will become less likely, locating targets at greater depths is gaining increasing importance. Furthermore, the role of geophysical prospecting is changing from the direct detection of new targets to incorporating mappable parameters that can be applied in mineral system research.

The purpose of this review is to collect and summarize available geophysical information about the main mineral deposit types in Finland. The overall geophysical characteristics of different ore deposit types or mineralization styles are for the most part well-known and their exploration methods have been routinely used. However, in reality, ore deposits may geologically and geophysically be much more complex than expected. Understanding of geophysical signatures associated with various mineral deposit types can be improved by knowledge of the physical properties, i.e. density, magnetic properties, radiometric signatures and electrical properties, of the principal ore minerals and common associated minerals and host rocks. The interpretation will be promoted by recognizing the geophysical signatures of expected alteration patterns instead of only mapping the distribution of the actual ore mineralization. The problem is to find detectable and characteristic geophysical parameters from the huge amount of multivariate geophysical data that are nowadays available.

The key geophysical responses of mineral deposit types emphasized in this review are based on regional geophysical data sets. These include systematically conducted airborne geophysical survey data that cover the whole of Finland: magnetic, multi-frequency electromagnetic and radiometric data. The whole of Finland is also covered by regional gravity data, complemented by more detailed data from many parts of the country. In addition to the airborne geophysical manifestations, this report summarizes the existing petrophysical information in the databases of the Geological Survey of Finland (GTK). New petrophysical measurements were also conducted for this study on various types of ore samples. Petrophysical properties of mineralized and barren source rocks link geophysics and geology and they have an essential role in the integrated interpretation. They are necessary for more reliable 3D inversion and modelling of mineral systems.

The first part of this Special Paper volume presents published general physical properties of mineral deposit types. This review follows the genetic classification of mineralization styles in Finland and points out geophysically relevant minerals that are the reasons for different geophysical expressions. Only a brief description of each type is given, because detailed information on many of them is provided in the literature. The description of each type is supplemented by selected examples and case histories. Technically, the synopsis part contains Inserts and Fact Sheets. The inserts include figures and tables related to specific issues in text. The fact sheets, when highlighted by a blue background, provide an illustrative summary of the geophysical manifestations for

various mineral systems. The yellow background of the text means that a general description of the mineral system is provided.

The second part of this Special Paper includes four case histories by various authors. The case histories focus on special geophysical methods applied in various mineral system studies.

Article 1 by Suppala describes and evaluates 3D modelling of GTK's airborne frequency domain electromagnetic data. This article presents new thinking on the use of magnetic properties as inversion parameters. The example deposit type is a strongly remanently magnetized ultramafic Ni-Cu-bearing formation at Kellojärvi at the southern end of the Archaean Kuhmo-Suomussalmi greenstone belt (~2.8 Ga).

Article 2 by Mertanen & Karell is a review of petrophysical laboratory studies of gold deposits in the Palaeoproterozoic Häme belt (~1.88 Ga) in southern Finland. The referenced Au occurrences are the porphyry copper type Cu-Au deposit at Kedonojankulma, the orogenic Au deposit of Uunimäki and the exploration target at Mäyrä. Basic petrophysical properties (density, magnetic susceptibility and remanence) were completed by rock magnetic tests to identify the magnetic minerals and their grain sizes. Palaeomagnetic studies were conducted to delineate the timing for alteration processes and AMS (anisotropy of magnetic susceptibility) studies to characterize the magnetic fabrics. As the known ore bodies are related to alteration zones, detailed petrophysical outcrop-scale investigations can delineate differences between the mineralized and barren rocks. Hence, the studied petrophysical properties have importance in prospectivity mapping.

Article 3 by Lauri & Turunen is a compact evaluation of airborne and ground radiometric measurements for the identification of three uranium prospects in southern Lapland: the Asentolamminoja uranium target and the gold-uranium prospects in the Rumavuoma and Rompas-Rajapalot areas. High-resolution airborne radiometric data helps in delineating areas for ground follow-up exploration. Ternary images of K, Th and U channels are especially important, as they reveal the source of the radiometric anomaly and point out regions of chemical alteration.

Article 4 by Kuosmanen et al. describes tests of a mineral mapping method using hyperspectral near-distance LWIR imaging spectrometry. The investigated samples represent three diverse targets: the Kemi Cr mine, the Pyhäsalmi Cu-Zn-S deposit and the Kedonojankulma Cu-Au prospect. This rapid method is capable of measuring millions of spectra per minute. The technique can quantify the main minerals, including the alteration minerals, with accuracy and can be expected to gain more importance in future exploration studies. Because of the nature of article 4 in describing a rarely used method, it is presented in this volume in more detail and at greater length than articles 1–3, which more closely resemble reviews or brief communications.

A number of referees are acknowledged for their valuable comments on the articles included in this volume of the Special Paper. I want to warmly thank Pasi Eilu and Risto Pietilä for their advice to improve the content of the synopsis part. Special thanks go to Maija Kurimo for patiently discussing the content and numerous details in the course of preparing this volume. Eija Hyvönen and Heikki Säävuori are highly appreciated for their help in preparing the figures and tables. I also thank Roy Siddall for checking the English and Pirkko Surakka for technical revision.

August 17, 2015
Meri-Liisa Airo

Geophysical signatures of mineral deposit types in Finland
Edited by Meri-Liisa Airo
Geological Survey of Finland, Special Paper 58, 9–70, 2015

GEOPHYSICAL SIGNATURES OF MINERAL DEPOSIT TYPES – SYNOPSIS

by

Meri-Liisa Airo

GENERAL ISSUES

A mineral deposit, as an anomalous unit of metalliferous minerals, contains minerals with quite different physical properties to those of country rocks. Pyrite, pyrrhotite or magnetite are common minerals in ore deposits, all of which have distinctive physical properties and may greatly affect the geophysical response. In addition to petrophysically relevant ore minerals, other geological or geometrical factors or environmental conditions influence the geophysical expressions of ore deposits or mineralized systems. The main factors are gathered below. This list is inspired by a summary of the geochemical expressions of ore deposit types presented by McQueen (2005):

1. Composition of the ore deposit and the contained elements.
   - Density depends on the elementary composition of minerals; many metals have high specific densities.
   - Magnetically, the most distinctive are the ferrimagnetic minerals magnetite and the monoclinic form of pyrrhotite.
   - All metals are electrically conductive in a broad sense, but the conductivity of an ore deposit primarily lies with sulphides or graphite.
   - The radioactivity of rocks is based on radioactive elements, mainly potassium (K), uranium (U) and thorium (Th).
2. Form of an ore deposit (e.g., size, shape, orientation, depth; ore mineral distribution and texture).
   - The size, orientation and depth extent of a mineral deposit are the main factors with regard to geophysical expressions.
   - A great depth suppresses geophysical signatures.
   - Gravity and magnetic methods only detect lateral contrasts in density or magnetization, but in contrast, electrical and seismic methods can detect vertical, as well as lateral, contrasts of resistivity and velocity or reflectivity.
   - In the case of sulphide mineralization, the shape of the deposit may affect the magnetic signature by strengthening the remanent magnetization in the direction of the long axis of the deposit.
   - The electrical conductivity of a rock is a function of many factors, among which the mineral texture (galvanic structure) and porosity (with contained water) have a significant role.
3. Associated geological structures.
   - Most of the mineral deposits are structurally controlled; mineral occurrences are often restricted to structural elements such as faults, shear zones and lithological unconformities; some deposits form stratiform bodies, while

others are formed in a specific stratigraphic interval as a stratabound formation.
- Knowledge of the structure interrelationship and stratigraphic units is essential for mineral exploration. Seismic methods are able to produce high-resolution images of the geological structure.

4. Associated host rocks.
   - The association of particular ore types with particular host rock assemblages broadly reflects the geological environment and processes that have formed the ore, e.g. metamorphosed graphitic shales (black schists) in Finland are distributed along all major crustal boundaries. As sensitive and highly reactive, reducing rocks, they may host or be associated with mineralization, and their geophysical properties related to chemical composition can be used as indicators of the geological settings in which they formed (Airo & Loukola-Ruskeeniemi 2004).
   - Mineralization tends to accumulate along plate boundaries. The composition of sedimentary rocks along these boundaries may reveal information on the crustal conditions and processes at the time of mineralization.
5. Non-ore element component.
   - Sometimes, chemical alteration of host rocks produces detectable geophysical signatures if it produces minerals having anomalous physical properties. Although the petrophysical properties of different host rocks or ore deposits may be well studied, there is a lack of information on how the physical properties are related, for instance, to proportional alteration of various kinds.
   - Extensive fluid-related alteration of the host rocks may have a significant effect on geophysical signatures: sulphidization or pyritization (electrical properties), sericitization (potassium radiation), chloritization, carbonate alteration or tourmalinization (e.g. magnetic properties).
   - Mineralogical changes associated with the formation or emplacement of mineralization (such as hydrothermal alteration haloes). In regional geophysics, the expressions of alteration haloes may be minor, but the detailed study of radiometric or hyperspectral analyses permits the mapping of key minerals. If highlighted by more detailed investigations, these haloes may also be recognized by high-resolution airborne surveys.

Regional geophysical data sets

Airborne geophysical data sets provide full coverage of Finland and form the basic material for regional investigations, particularly greenfield exploration. The use of regional data sets in an automated approach to characterizing areas containing known deposits and seeking similar areas elsewhere, or similarity analysis of certain geophysical key signatures, benefits from high-resolution, multivariate geophysical datasets. Concerning more detailed investigations, airborne geophysical data also can motivate applications that require improved spatial resolution and accurate positioning. The integration of different geophysical data sets is a current theme in geophysical and geological interpretation, and there are now more software tools available to facilitate this. However, as stated by Thomson et al. (2007), although image analysis may often seem intuitive, simple image-based assessments of data are not a substitute for proper geologically supported interpretation.

Specifications and general uses of geophysical methods are outlined in the following. The airborne geophysical concept of GTK has been described in detail by Hautaniemi et al. (2005).

Airborne magnetics

The magnetic method utilizes small variations in magnetic mineralogy among rocks (magnetic iron and iron-titanium oxide minerals, including magnetite, titanomagnetite, titanomaghemite and titanohematite, and some iron sulphide minerals, including pyrrhotite and greigite). Magnetic rocks contain various combinations of induced and remanent magnetization, depending on the Earth's primary field. The magnitudes of both induced and remanent magnetization depend on the quantity, composition and size of magnetic-mineral grains. The magnetic method gives a coherent picture of the distribution of magnetization of the crust and is not disturbed by lakes, waterways or soils that may cover the bedrock. In Finland, exposed bedrock hardly makes up more than 3% of the surface. The aim of the magnetic method is to detect

magnetically anomalous source bodies, but also to determine structural trends. Detailed magnetic investigations on magnetic mineralogy complement the regional picture of magnetic anomaly source rocks. Studies on remanent magnetization and the anisotropy of magnetic susceptibility (AMS) are gaining increasing interest as a mineral exploration tool (Willliams 2009). Palaeomagnetic studies may be important for the timing of the mineralizing fluids or the alteration. Discussion of the magnetic mineralogy responsible for magnetization effects is presented in this Special Paper volume in the chapter on Au deposits in southern Finland by Mertanen & Karell (*p. 89*).

Airborne radiometrics

Gamma-ray methods identify the presence of the natural radioelements potassium (K), uranium (U), and thorium (Th) in rocks. Gamma ray penetration is only of the order of half a metre, so that in regions with poor exposure due to glacial, largely transported overburden, the measurement of natural radioactivity due to K, U and Th may not be very useful. In Finland, the use of radiometrics is frequently limited by the wide coverage of glacial soil, with a thickness varying from 0 to 100 m and an average of <10 m. In southern Finland, cultivated land dominates the variation in radiation observed on radiometric maps. Locally, however, gamma-ray spectrometry can be effective in geological mapping and targeting mineralization. The results depend on several factors, including whether (1) there are measurable differences in the radioactive element distributions that can be related to differences in host rock lithologies, (2) the K content of the rock has been modified by alteration processes, and (3) mineralization and alteration have affected surface rocks. Mobilization of individual radioelements in response to specific geochemical conditions makes radioelement ratios sensitive in locating areas of mineralization (Thomas et al. 2000, cited in Morgan 2012). An example of this is the elevated potassium radiation associated with ultramafic rocks in Finnish Lapland (in *Insert 12*). In uranium exploration, gamma-ray methods may provide a means of direct detection. Good results from the use of airborne radiometric data for targeting promising areas for U-Au and U occurrences are reviewed in this volume by Lauri & Turunen (*p. 107*), who discuss the use of airborne radiometric data as a uranium exploration tool in southern Lapland.

Airborne electromagnetics

Airborne electromagnetic (EM) methods are used to screen large areas and provide information for targeting ground surveys. They are capable of directly detecting conductive base-metal deposits. The traditional application of EM methods in mineral exploration has been in the search for low-resistivity (high-conductivity) massive sulphide deposits. The wide whole-country coverage of frequency-domain EM data in Finland is unique in the world and allows mapping of the regional distribution of bedrock conductivity, also supporting structural interpretation. GTK used a fixed-wing multi-frequency survey system that is better suited to relatively near surface applications than deeper investigations (down to 100 m). Electromagnetic survey data are vulnerable to non-geological noise, but also to conductivity anomalies due to soil properties and moisture. The noise is worth filtering out in the case of mineral exploration. The interpretation of electromagnetic data may be demanding, and 3D interpretation methods would greatly strengthen the use of the airborne electromagnetic method. An example of 3D EM modelling by Suppala (*p. 71*) utilizes the effectiveness of frequency-domain electromagnetic data to discriminate magnetite-bearing source rocks and to evaluate the type of magnetism associated with an ultramafic intrusion (Kellojärvi in eastern Finland).

Regional ground gravity data

A high density is the most anomalous physical property of almost every ore mineral. Regional gravity data reveal the density contrasts and can be used to outline geological structures controlling mineralization. Qualitative interpretation of structural features from gravity data is benefitted by the same types of processing methods as used for magnetic data, e.g. horizontal gradients, vertical or tilt derivatives, filtering or upward continuation. Exploration has for long been the primary target of regional gravity measurements in Finland. Gravity surveys have been focused on the most important mineral provinces, such as the Central Finnish Lapland gold province, the Raahe-Ladoga zone and parts of the Häme belt in southern Finland.

Major tectonic provinces, crustal weakness zones and province boundaries have been described using these data (Elo 1997, Elo 2003). A country-wide Bouguer anomaly map has been prepared based on gravity data, provided by the Finnish Geodetic Institute (Kääriäinen & Mäkinen 1997).

Airborne gravity gradiometry

Airborne gravity surveys for GTK have been conducted in three areas: Hammaslahti and Pori (in 2009) and Savukoski (in 2011). In principle, gravity gradiometer systems are more sensitive to shorter spatial wavelengths than sensors that attempt to measure the total gravitational acceleration. For comparable sensitivities to that of an airborne gravity system, this system on a fixed wing aircraft can be used to map features typified by half-wave distances of 200 m. This corresponds to an order of magnitude better spatial resolution than achieved from total field systems at short wavelengths.

Remote / close-range sensing

Remote sensing based on visible to thermal wavelengths (0.3–14000 microns) of reflected and emitted electromagnetic radiation is widely used to scan targets of mineral exploration and mining to obtain information on the mineral composition, vegetation, environment, and the geological structure. The detailed wavelength samples, bands, and spatial resolutions are selected according to their ability to detect specific minerals or vegetation/environmental anomalies due to mineralization. The number of bands roughly divides the method into multispectral (typically 5–20 bands) or hyperspectral (from 20 to several hundred bands) remote sensing. The distance (D) between the sensor and the exploration target roughly divides the method into regional (satellite borne, D = hundreds of kilometers), local (airborne, D = some kms) or close-range (D = some dms) sensing. The ground resolution is typically from tens to hundreds of meters for regional data, from centimeters to meters for local data, and millimeters for close-range data.

In Finland, the following multispectral and hyperspectral remote/close-range sensing data have been used for mineral exploration, environmental research, or mineral species assessment:

- Landsat and Aster satellite regional multispectral data (VIS, NIR, SWIR, LWIR)
- EO-1 satellite regional hyperspectral Hyperion data (VIS, NIR, SWIR)
- HyMap and AISA airborne local hyperspectral data (VIS, NIR, SWIR)
- SisuROCK hyperspectral close-range imaging workstation data (VIS, NIR, SWIR, LWIR)
- Portable FieldSpecFR for close-range spectral single measurements (VIS, NIR, SWIR)

(Abbreviations: VIS = visual, NIR = near infrared, SWIR = short-wave infrared, LWIR = long-wave infrared)

Several published or archived spectral reflectance and emittance libraries are available for training the interpretation of these remote sensing data sets in mineral exploration and mining. LWIR close-range reflectance spectrometry, used in the characterization of selected mineral deposits, is reviewed in this volume by Kuosmanen et al. (p. 117).

Petrophysical database and detailed studies

Information on rock density and magnetic properties especially facilitates the interpretation of aeromagnetic and gravity surveys. Petrophysical sampling covers the whole of Finland and offers background information for the interpretation of the country-wide geophysical surveys. The petrophysical register currently includes measurement results of more than 130 000 bedrock samples: density, magnetic susceptibility and the intensity of remanent magnetization for different rock types, including information on the sampling site and rock type. Petrophysical properties of rocks mainly depend on the dominant rock-forming minerals and their relative concentrations, so that they can be used in characterizing different rock types in Finland (Airo & Säävuori 2013). The amount of petrophysical data at GTK is continually increasing as new measurements are conducted. The collection of data has also included some 200 samples from different ore deposit types. Although the number of different specific types is limited, their petrophysical properties nevertheless give background data for reference. The values of magnetic susceptibility for ore samples are an order of magnitude higher than those of common rock types, even that of ultramafic rocks. To complement the ore deposit data set, new measurements of ore samples were carried out for the current study and are also summarized here (see *Insert 6)*. In addition to surface petrophysics, GTK provides density and

Table 1. Applicability of different geophysical methods in the exploration of various mineral systems (modified from Ford et al. 2007).

● Highly effective ● Moderately effective ● Generally ineffective

Geo-physical method	Air or ground	Appli-cation	Ni-Cu-PGE	Fe-Ti BIF	Gold	VMS	Olympic Dam-type	SEDEX	Por-phyry Cu	Pb-Zn	Dia-monds
Magnetic	Air	Geological framework	●	●	●	●	●	●	●	●	●
		Direct targeting	●	●	●	●	●	●	●	●	●
	Ground	Geological framework	●	●	●	●	●	●	●	●	●
		Direct targeting	●	●	●	●	●	●	●	●	●
Electro-magnetic	Air	Geological framework	●	●	●	●	●	●	●	●	●
		Direct targeting	●	●	●	●	●	●	●	●	●
	Ground	Geological framework	●	●	●	●	●	●	●	●	●
		Direct targeting	●	●	●	●	●	●	●	●	●
Electric	Ground	Geological framework	●	●	●	●	●	●	●	●	●
		Direct targeting	●	●	●	●	●	●	●	●	●
Gravity	Air	Geological framework	●	●	●	●	●	●	●	●	●
		Direct targeting	●	●	●	●	●	●	●	●	●
	Ground	Geological framework	●	●	●	●	●	●	●	●	●
		Direct targeting	●	●	●	●	●	●	●	●	●
Radio-metric	Air	Geological framework	●	●	●	●	●	●	●	●	●
		Direct targeting	●	●	●	●	●	●	●	●	●
	Ground	Geological framework	●	●	●	●	●	●	●	●	●
		Direct targeting	●	●	●	●	●	●	●	●	●
Seismic	Ground	Geological framework	●	●	●	●	●	●	●	●	●
		Direct targeting	●	●	●	●	●	●	●	●	●

magnetic property information on thousands of samples from exploration drill cores. One example of utilizing petrophysical data in characterizing propitious rock units for mineralization is the Lomalampi case by Salmirinne (2010) (Fig. 5).

Table 1 summarizes the application and suitability of different geophysical methods for the exploration of various mineral systems in Canada (based on Ford et al. 2007), and also gives an idea of their overall suitability in Finland. In general, the magnetic method is highly effective both for the impression of the geological framework and for direct targeting of most of the mineralization types. In general, electromagnetic, electric and gravity methods are effective for magmatic Ni-Cu-PGE and VMS deposits, and radiometrics and the magnetic method for porphyry Cu deposits.

Geophysical responses

Geophysical anomalies are primarily affected by the source mineralogy and secondly by source geometry and various factors determined by the geological conditions of the source body. The petrophysical properties of ore minerals and common associated host rocks provide information that makes it easier to understand the geophysical signatures of a certain deposit type (King 2007).

The likelihood of locating an ore deposit or its host rock by means of a geophysical anomaly depends on many factors, including the petrophysics of the ore minerals and their host rock, and the thickness and physical properties of the overburden cover. The size of the ore occurrence and its outcrop and the distance of its top from the ground surface are geometrical factors. The geology in the area and the anomalies caused by the country rocks, and the mode of occurrence of the ore deposit in relation to the anomalous rocks are geological factors (Ketola 1982).

Geophysical anomalies are described by their amplitude and form. The main factors influencing the amplitude and shape of geophysical anomalies include:

- *Source mineralogy and dimensions*: geophysically anomalous minerals contained in the source, their physical properties and texture (fabrics); size, geometry, depth of mineralization and its orientation relative to magnetic north, and the inclination of the Earth's magnetic field at its location.
- *Depth* of investigation of the method in question: depends on many factors, including system characteristics (*Table 2*).
- *Survey resolution*: the terrain clearance and flight line separation will affect the resolution of the detected geophysical anomalies.
- *Method footprint* – depends on the sampling density and the speed of aircraft.
- *Measurement techniques*: for example, the measurement frequency in frequency-domain electromagnetic measurements affects the response.
- *Wavelength* of the observed potential field. Geophysical responses for deeply buried sources decrease in amplitude and increase in spatial wavelength until they disappear into geological noise.
  - Effect of the observation level on the magnetic and gravity anomaly of a small and a large source body.
  - Short wavelength anomalies: shallow sources.

Modelling examples of gravity and magnetic anomalies at increasing depths for source bodies of different sizes and varying petrophysical parameters are collected in *Insert 1*. Magnetic or gravity methods are sensitive to completely different physical rock properties and they have very different roles in geological interpretation. The gravity method reveals information on the distribution of density and is routinely used for the identification of lithologies, structures and ore bodies themselves. The magnetic method is sensitive to the distribution of magnetic minerals and it is the main method for the interpretation of bedrock lithology and structure. Magnetic anomalies sometimes coincide with gravity anomalies, and rock alteration can cause a change in bulk density as well as magnetization. If the distributions of density or magnetization reflect geologically significant features, the interpretation of gravity and magnetic data can give 3D information on the distribution and structure of these features. The sources of gravity anomalies can be modelled from >1 km depth if the density difference between the source formation and the surroundings is great enough.

Table 2. Depth of investigation (general) for different geophysical methods.

Method	Typical source of anomaly	Depth of investigation
Magnetic	Magnetic susceptibility and/or remanent magnetization contrasts	From surface down to Curie isotherm
Gravity	Rock density contrasts	All below
Gamma-ray spectrometry	K, U and Th contrasts	Upper 50 cm
Electromagnetic (EM)	Lateral or vertical changes in Earth conductivity	GTK airborne EM system down to 70-100 m

Insert 1.
Modelling examples of gravity and magnetic anomalies for source bodies of different sizes and petrophysical parameters at increasing depths (in Kukkonen & Airo 2012, presentation at the GTK Academy, Espoo, Finland 12.12. 2011).

Case 1: 1Mton (small sized)

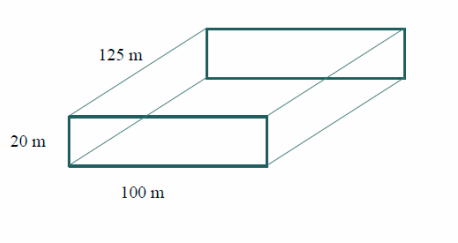

Modelling parameters:

Density of ore body 4000 kg/m^3 and country rock 2750 kg/m^3

susceptibility of ore body 30000 x 10^{-6} (Q=3), and of country rock 1000 x 10^{-6} (Q=0).

Outcropping source:

Magnetic anomaly 400 nT and 200 m wide, gravimetric anomaly 0.9 mGal.

At the depth of z = 500 m:

Magnetic anomaly 1.3 nT and 1 km wide, gravimetric anomaly 0.008 mGal.

Not detectable among other anomalies.

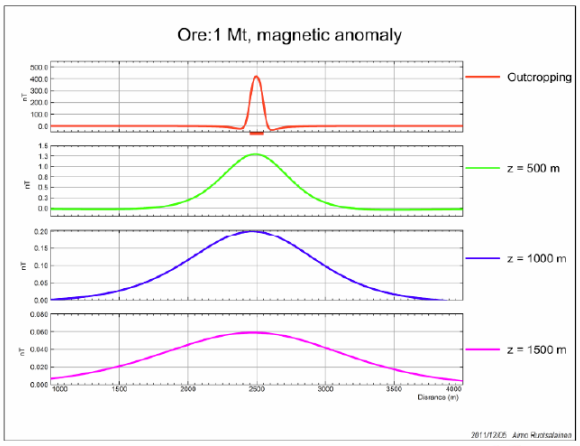

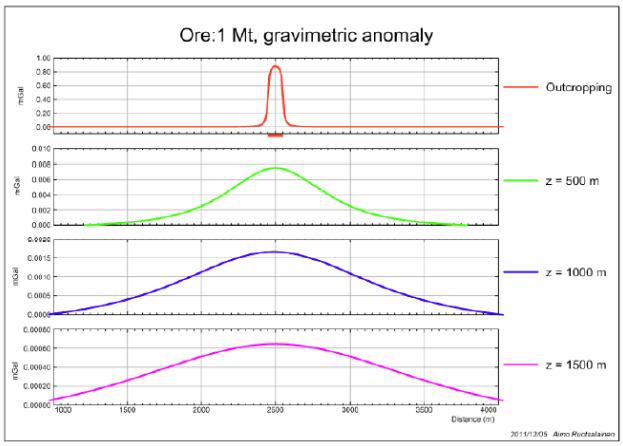

Case 2: 27Mton (“Outokumpu-size”)

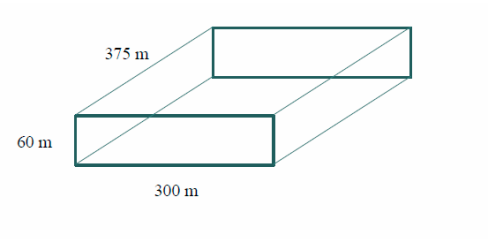

Modelling parameters:

Density of ore body 4000 kg/m^3 and country rock 2750 kg/m^3

susceptibility of ore body 30000 x 10^{-6} (Q=3), and of country rock 1000 x 10^{-6} (Q=0).

Outcropping source:
Magnetic anomaly 200 nT and 500 m wide, gravimetric anomaly 2.5 mGal.

At the depth of z = 500 m:
Magnetic anomaly 7 nT and 1 km wide, gravimetric anomaly 0.16 mGal and 600 m wide.
Not easily detectable among other anomalies.

Insert 1. (cont)

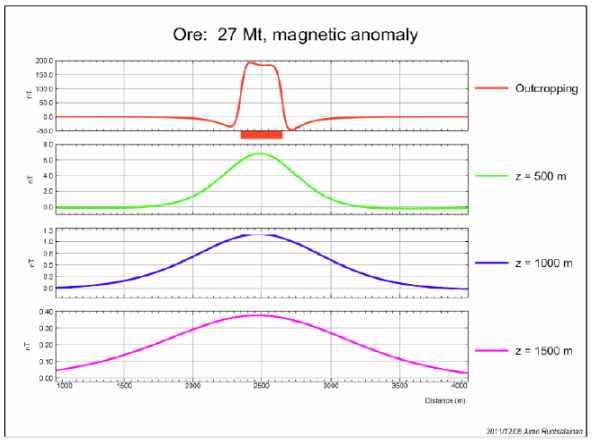

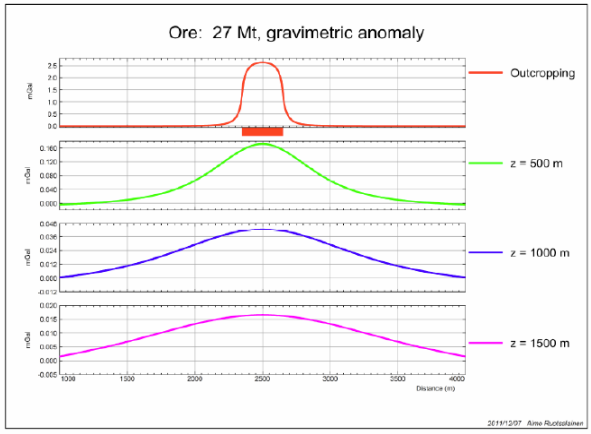

Case 3: 135 Mton ("world class")

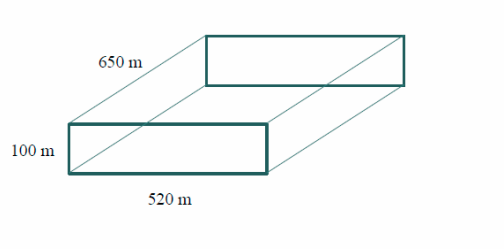

Modelling parameters:

Density of ore body 4000 kg/m^3 and country rock 2750 kg/m^3

susceptibility of ore body 30000 x 10^{-6} (Q=3), and of country rock 1000 x 10^{-6} (Q=0).

Outcropping source:

Magnetic anomaly 250 nT and 600 m wide, gravimetric anomaly 4 mGal, 600 m wide.

At the depth of z = 500 m:

Magnetic anomaly 25 nT and 1.5 km wide, gravimetric anomaly 0.8 mGal.

Not detectable among other anomalies.

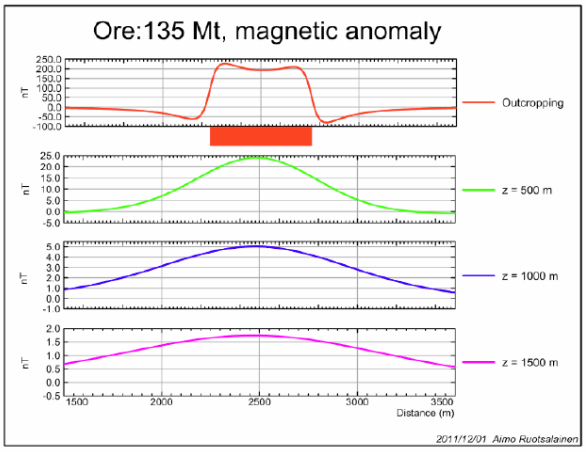

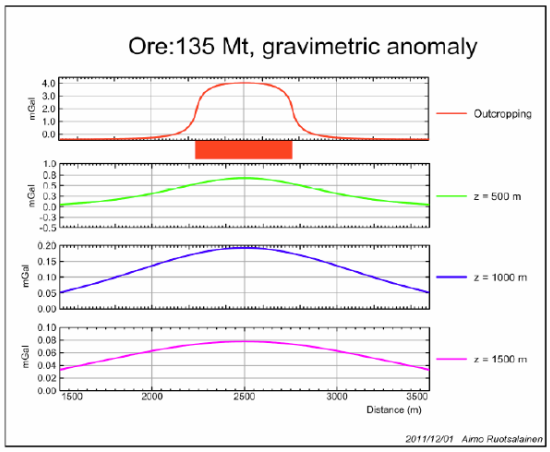

Geophysically relevant minerals

The physical properties of minerals that are relevant for the physical properties of rocks and ores are reviewed in the following. These properties include density, magnetic properties, electrical properties, radioactivity and seismic velocity.

Different rock types often have distinctive and characteristic physical properties, as illustrated for density and magnetic susceptibility in Figure 1 (from Airo & Säävuori 2013). This reflects the iron content, bound either in rock-forming minerals or in ore minerals. Density depends on the proportional content of Fe and Mg-bearing minerals in the rock's main mineral composition, so that in each rock class the mean densities increase due

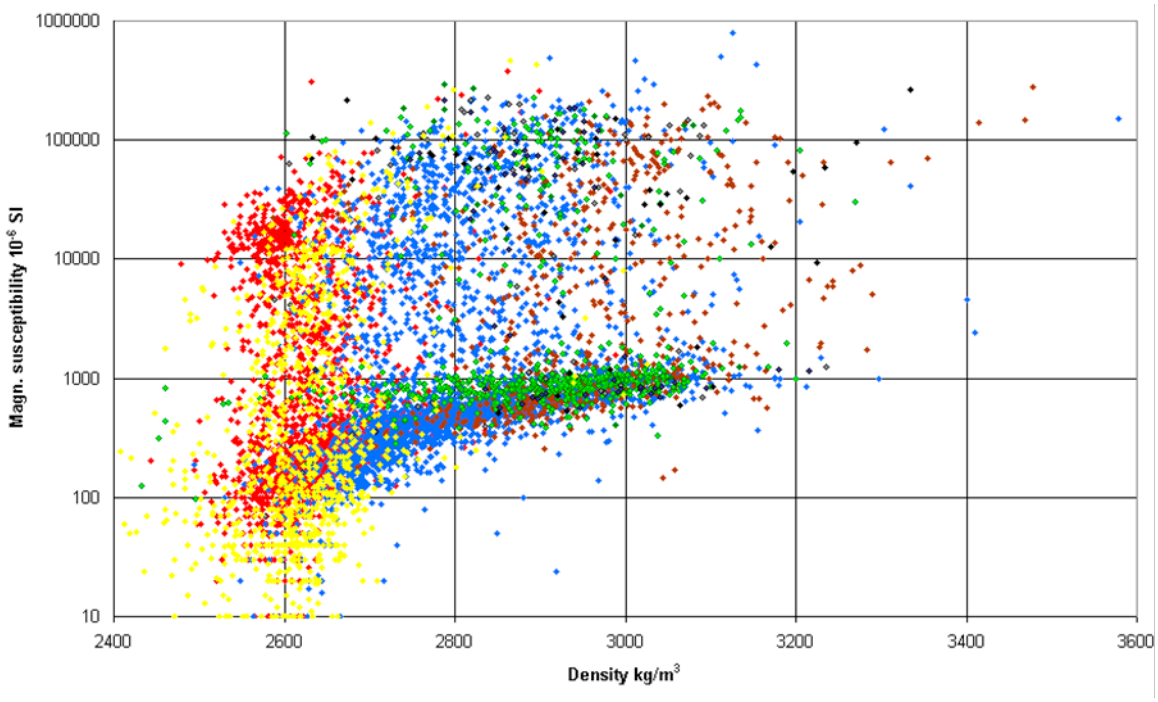

Fig. 1. Ranges of density and magnetic susceptibility of rock classes from GTK's petrophysical database. The densities of quartzites (yellow) and granites (red) are mainly below 2700 kg/m^3 and the densities above 2800 kg/m^3 characterize mica schists (blue), metavolcanic rocks (green), gabbros (brown) and ultramafic rocks (black). The susceptibility distribution is bimodal, with a lower susceptibility mode caused by the paramagnetism of rock-forming silicates, and a higher mode that is due to ferrimagnetic minerals.

Table 3. Ore mineral and host rock densities (g/cm^3) and magnetic susceptibilities (10^{-6} SI) (after King 2007 and Morgan 2012). Typical susceptibility and density values for country rocks in Finland from Airo & Säävuori 2013.

Mineral	**Density g/cm^3**		**Susceptibility 10^{-6}**	
Sulfides / Oxides	Range	Average	Range	Average
Chalcopyrite	4.1-4.3	4.2	300 - 400	
Pentlandite		4.8		< 1000
Pyrite	5.02		-6 - 100	
Pyrrhotite	4.5-4.8	4.65	up to 6 000 000	
Pyrrhotite (mono)				700 000
Pyrrhotite (hex)				2000
Sphalerite		4	-15 - 2000	
Magnetite		5.18	1 000 000 - 15 000 000	3 000 000
Hematite		5.26	1300 - 7000	
Maghemite				up to 3 000 000
Ilmenite			1000 - 8000	
Host rocks				
Felsic igneous	2.3-3.11	2.61	500 - 80 000	
Mafic igneous	2.09-3.17	2.79	1000 - 100 000	
Ultramafic rocks(peridotite)	2.78-3.37	3.15	10 000 - 100 000	

to an increase in the proportion of mafic minerals. Similarly, magnetic susceptibility depends on the proportional content of mafic / felsic rock-forming minerals, but in addition on the iron bound in magnetic minerals. Iron sulphides and iron oxides (mainly magnetite) are the principal ore minerals, and have distinctive physical properties. Of the other geophysically distinctive minerals that may be related to ore mineralization, graphite in metamorphosed graphitic shales (black schists) might, for example, also have a strong impression for geophysics. The clustering of rocks into specific ranges of density and magnetic susceptibility is typical for Precambrian, metamorphic and highly deformed terrains (also Reeves 2005).

Density of ore minerals

The densities of common ore minerals are all above 4.0 g/cm^3, so that their presence increases the bulk density of rock. Of the common ore minerals, magnetite, pyrrhotite and pyrite all have densities ~5 g/cm^3, and cannot be separated by the gravimetric method, but their magnetic properties deviate characteristically. The density and susceptibility ranges for common ore minerals and some typical host rocks are shown in *Table 3*.

Magnetic minerals

Minerals that can cause a significant magnetic response are magnetite, pyrrhotite, hematite, ilmenite/titanohematite and maghemite. Pyrite is non-magnetic, but can be metamorphosed to pyrrhotite at upper greenschist-lower amphibolites grades. Pyrrhotite can be metamorphosed to magnetite (Clark 1997, Gunn & Dentith 1997). Table 4 compares the magnetization type and susceptibility of various magnetic or rock-forming minerals. Fe,Mg-bearing silicates are generally paramagnetic and only reach a maximum susceptibility level of 0.001–0.002 x 10^{-6} . The same level is, however, reached by a magnetite concentration as low as 0.01% (Hrouda et al. 2009). Thus, even a minor concentration of ferrimagnetic minerals has a dominant effect on the magnetic susceptibility of rock.

Of the two types of magnetization that exist, induced magnetization is proportional to the susceptibility of the material being magnetized and can be in the same direction as the Earth's field. Remanent (permanent) magnetization can have any direction and it is carried by ferrimagnetic minerals. In certain cases, remanent magnetization can be orders of magnitude greater that the induced.

The ferrimagnetic susceptibility of rocks depends on:

- the magnetic mineral type and content (seldom >10%)
- the measuring field and temperature
- the grain size of ferrimagnetic minerals
- the content of iron in rock (principally, but in a complex way).

The amplitude and shape of a magnetic anomaly can be strongly affected by remanent magnetization, which may be useful to take into account in magnetic modelling. The ratio of remanent to induced magnetization (Königsberger ratio, Q-value) can be used to predict the magnetic mineralogy in the anomaly source simply by using the information based on petrophysical laboratory

Table 4. Magnetization type and susceptibility (from Reeves 2005, Clark 1997 and Schön 2004).

Minerals	Magnetic susceptibility (SI)		Magnetization type
Magnetite Magnetite ore	15 (pure) 0.07-14	Positive, very high, complex function of the magnetizing field	Ferrimagnetic
Pyrrhotite (monoclinic)	0.001- 1	Positive, may be high	Ferrimagnetic
Hematite Hematite ore	0.013-0.07 0.0004 - 0.01	Positive relatively low	Antiferromagnetic
Ilmenite Ilmenite ore	0.01- 0.08 0.3 - 4	Positive relatively low	Antiferromagnetic
Rock-forming Fe,Mg-silicates	< 0.001	Positive, relatively low, independent of the magnetizing field	Paramagnetic
Quartz, calcite, graphite, tremolite		Negative and independent of the magnetizing field	Diamagnetic

Table 5. Magnetic susceptibilities for selected diamagnetic and paramagnetic minerals (modified from Clark 1997 and Schön 2004). The susceptibilities are in 10^{-6} SI-units.

Diamagnetic	Susceptibility average	Paramagnetic	Susceptibility range
Quartz	-15	Garnet	500-6000
Orthoclase	-10	Muscovite	30-700
Calcite	-13	Biotite	800-3000
Forsterite	-13	Pyroxenes	500-5000
Galena	-33 (to 9)	Olivine	100-4000
Sphalerite	-13	Amfiboles	600-5000
Graphite	-70 (to -180)	Pyrite	-10-60
		Chalcopyrite	300-400

measurements. Ferrimagnetic minerals (magnetite, monoclinic form of pyrrhotite) are typically associated with significant remanence, and metamorphic and alteration processes often affect the remanent magnetization by modifying the concentration of grain sizes of these minerals. A high metamorphic grade produces fine-grained magnetite (magnetite content grows + the amount of fine-grained magnetite increases). Ferrimagnetic minerals also are a typical constituent in common rock types. For example, Q-ratios are between 1 and 10 for plutonic and dyke rocks, and for volcanic and metasedimentary rocks (Airo & Säävuori 2013). For metamorphic and altered rocks (schists with monoclinic pyrrhotite and skarns), as well as rocks bearing ore minerals, Q-values sometimes reach into the hundreds. In a broad sense, particularly strong remanence in rocks is either due to monoclinic pyrrhotite or fine-grained magnetite. A decreased remanence is typical for shear zones or any zones of hydrothermal alteration. As deformation may have an influence on the magnetic mineralogy of rocks, knowledge of rock properties and their variation helps to focus more detailed investigations.

Very weak rock susceptibilities most probably contain a component due to the diamagnetic behaviour of some minerals. In diamagnetism, the magnetic moment vector tends to be in the opposite direction to the magnetizing field (*Table 5*). Quartz, which is present in many rocks, is a typical diamagnetic mineral, and graphite is a common diamagnetic mineral in metamorphosed shales. Of the ore minerals, galena and sphalerite are diamagnetic. Pyrite has a very low susceptibility and tends to lower the rock susceptibility.

Electrical conductivity of metallic minerals

Electrical and electromagnetic methods observe the distribution of the electrical conductivity in the ground. In normal rocks, the electric current flows by ionic conduction in the electrolyte in the pores of the rock. However, certain minerals have a measure of electronic conduction (almost all the metallic sulphides (except sphalerite) such as pyrite, graphite, some coals, magnetite, pyrolusite, native metals, some arsenides, and other minerals with a metallic lustre). Even small quantities of metallic ore minerals can significantly affect the bulk resistivity of geological materials. Of all the geophysical properties of rocks, electrical resistivity is by far the most variable and it depends on many factors, including the rock type, porosity, the connectivity of pores, the nature of the fluid, and the metallic content of the solid matrix. Values ranging by as much as 10 orders of magnitude may be encountered, and even individual rock types can vary by several orders of magnitude (Fig. 2). The measurement procedure also affects these parameters, so that the reported values of these parameters may show some variation in different studies.

Most metallic ore minerals are electronic semiconductors. Their resistivities are lower than those of metals and highly variable, because the inclusion of impurity ions into a particular metallic mineral has a significant effect on the resistivity (Palacky 1987). Information on the conductivity properties of important ore minerals is summarized in the following fact sheet (based on Oldenburg & Jones 2007 and Palacky 1987). The range of resistivity and conductivity of typical ore minerals is shown in Table 6 and the range of IP chargeability in Table 7. IP measures the chargeability of the ground, i.e. how well materials tend to retain electrical charges. Measurements are made either

in the time domain or the frequency domain; their units are respectively milliseconds (msec) and the percentage frequency effect. In general, disseminated sulphides have very good induced polarization responses.

Although metallic minerals (particularly sulphides) may be conductive, there are at least two reasons why ore-grade deposits of these minerals may not be as conductive as expected (Palacky 1987). In theory, massive sulphides should have lower responses, but in practice they may have very good responses. This is due to the mineralization halo generally surrounding massive sulphides (Ford et al. 2007). Sulphide deposits can be either disseminated or massive. In disseminated sulphides, the mineral occurs as fine particles dispersed throughout the matrix, and they may be resistive or conductive. In massive sulphides, the mineral occurs in a more homogeneous form, and they are likely to be conductive. Chemical and/or thermal alteration can convert metallic minerals into oxides or other forms that are not as conductive as the original minerals. The selection of the electromagnetic method may have a crucial effect on the success of the operation, depending on the target.

Electrical properties of important ore minerals

- Pyrrhotite (FeS) is a consistently highly conductive mineral.
- Graphite (C) is a true conductor, like a metal (i.e. not a semiconductor like ore minerals), and it is very conductive, even at very low concentrations. It is also chargeable, and it is notoriously difficult to distinguish from metallic ore minerals. Graphite is a metallic conductor with a resistivity of 10^{-4} to 5 x 10^{-3} Ωm and is found in many crustal rocks. Graphite occurs in metamorphic rocks and is difficult to distinguish from metallic ore minerals. The substitution of impurity ions into the lattice of a particular metallic mineral may have a significant effect on the resistivity.
- Pyrite (FeS_2) is the most common metallic sulphide and has the most variable conductivity. Its conductivity is generally higher than that of porous rocks. Pure pyrite has a resistivity of about 3 x 10^{-5} Ωm, but mixing in minor amounts of copper can increase the resistivity by six orders of magnitude to 10 Ωm.
- Galena (PbS) and magnetite (Fe_3O_4) are conductive as minerals, but much less conductive as ore because of their loose crystal structures.
- Other conductive minerals include bornite ($CuFeS_4$), chalcocite (Cu_2S), covellite (CuS), ilmenite ($FeTiO_3$), molybdenite (MoS_2), and the manganese minerals holandite and pyrolusite.
- Hematite and zincblende (sphalerite) are usually nearly insulators.
- Gold (Au) has among the most anomalous physical properties: its density is 19 300 kg/m^3 and electrical conductivity 5 x 10^7 S/m. The conductivity of an iron formation may reach very high values: min 0.05 to max 3300 mS/m.

(based on Oldenburg & Jones 2007 and Palacky 1987)

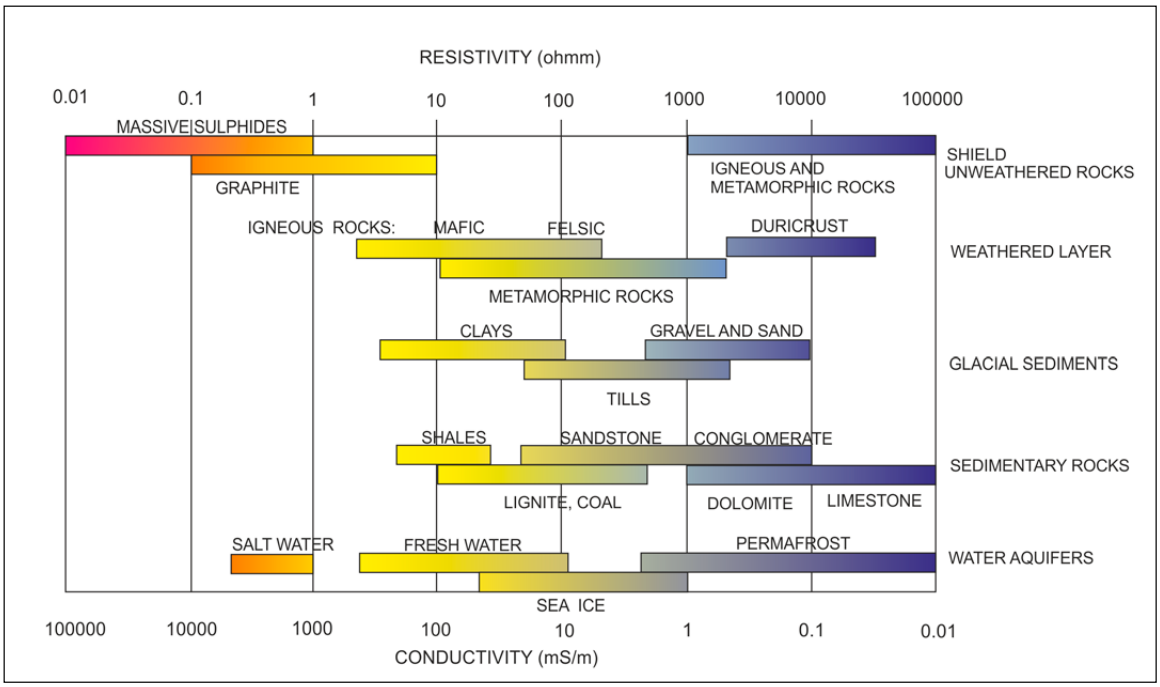

Fig. 2. Resistivities (conductivities) of rocks and earth materials (after Oldenburg & Jones 2007).

Table 6. Resistivities and conductivities of selected metals and minerals (modified from King 2007 and Peltoniemi 1988).

Resistivity of selected ore minerals (King 2007)		**Electrical conductivity of selected metals and minerals (Peltoniemi 1988)**	
Minerals	**Resistivity (Ohm-m)**	**Material**	**Typical conductivity, S/m**
		Gold	$50 \cdot 10^{6}$
		Copper	$3 – 80 \cdot 10^{6}$
		Graphite	10^{2} - 10^{6}
Chalcopyrite, CuFeS2	$1.2 \times 10^{-5} – 0.3$	Chalcopyrite	10 - 10^{4}
Pyrite, FeS2	$3.0 \times 10^{-5} – 1.5$	Pyrite	1 - 10^{5}
Magnetite, Fe3O4	$5.0 \times 10^{-4} – 5.0 \times 10^{4}$	Magnetite	10^{-4} - 10^{5}
		Mica	$10^{-3} – 10^{-14}$
		Quartz	$10^{-10} – 10^{-14}$
Hematite, Fe2O3	3.5×10^{-3} - 10^{7}		
Galena, PbS	$3.0 \times 10^{-5} – 3.0 \times 10^{2}$		

Table 7. Relative IP chargeability for common ore minerals and rocks (after King 2007 and Oldenburg & Jones 2007).

Material type	**Chargeability (msec)**	**Material type**	**Chargeability (msec)**
Chargeability of minerals at 1% concentration in the samples		*Charging and discharging times about one minute each (much longer than field survey systems), therefore values are larger than field measurements*	
Pyrrhotite	~10	20% Sulphides	2000 - 3000
Pentlandite	~10	8-20% Sulphides	1000 - 2000
Pyrite	13.4	2-8% Sulphides	500 - 1000
Copper	12.3	Volcanic tuffs	300 - 800
Graphite	11.2	Sandstone, Siltstone	100 - 500
Chalcopyrite	9.4	Dense volcanic rocks	100 - 500
Magnetite	2.2	Shale	50 - 100
Galena	3.7	Granite, Granodiorite	10 - 50
Hematite	0.0	Limestone, Dolomite	10 - 20

Radioactive minerals

Gamma-ray spectrometry can provide direct quantitative measures of the natural radioelements potassium (K), thorium (Th) and uranium (U). In general, felsic (acid) and intermediate rocks commonly show higher mean radioelement concentrations than mafic (basic) or ultramafic rocks and can be outlined on the basis of their radiometric patterns (Dickson & Scott 1997). Examples of both depletion and enrichment of the three radioelements have been reported. Hydrothermal alteration and mineralizing processes can affect the radioelement content, with K being the most easily affected. For instance, the potassium content increases in altered rocks surrounding both base metal and Au deposits. Thorium may be mobilized during mineralization processes, being partly depleted in areas of K-alteration or intense silicification, but concentrated in Th-rich materials such as laterite (Gunn & Dentith 1997). Where sulphide minerals are present, their oxidation accelerates uranium mobilization (Killeen 1979). Uranium and (or) potassium are commonly enriched in or adjacent to some ore deposits, and their presence may often be used in indirect targeting. Geological processes leading to various styles of mineral deposits may result in variations in radioelement contents. In particular, radioelement signatures are modified by weathering processes. The search for U and Th deposits involves the direct use of airborne gamma-ray surveys in mineral exploration, where elevated concentrations of these elements or element ratios (e.g. Th/U or K/U) are searched for. The radioactivity of minerals is further reviewed in Lauri & Turunen in this volume (*p. 107*).

Seismic velocity of rocks and ore minerals

The application of seismic methods for mineral exploration has good potential, as these methods are capable of imaging mineral deposits at various depths. The average velocities of acoustic waves in igneous and metamorphic rocks typically increase with density. For example, velocities for ultramafic rocks, with densities ranging from 3.0 to 3.5 kg/m^3, are in the category of 8 km/s, and for serpentinites (with densities below 3 kg/m^3), the velocities are in the range of 5–6 km/s (Milkereit et al. 2000). Most economically significant sulphides and pyrrhotite are all uniformly of very low velocity. This makes them ideal targets for crosshole transmission seismic tomography, which measures only velocity. Because they are also anomalous in density, they produce acoustic reflectivity anomalies. However, as stated by King (2007), since acoustic reflectivity is proportional to the acoustic impedance (product of velocity x density), their high densities and lower velocities can result in reduced reflectivity. Sulphide ores and the concentration of certain Fe oxides, because of their high density, have higher acoustic impedance with respect to surrounding rocks. Massive ore mineralization with a relevant size and geometry should produce a strong seismic response in many geological situations (Milkereit et al. 2000, Salisbury et al. 2000). The contrast of acoustic impedance between felsic and mafic rocks is also significant; this allows an opportunity to detect mafic intrusions: dykes or sills. The high acoustic impedance of massive mineral deposits, which has been disclosed by laboratory measurements, should also be confirmed by *in situ* measurements from borehole logging.

Magnetite or pyrrhotite as anomaly sources

The magnetic properties of rocks yield abundant information on the source minerals, their grain size and texture, and the age of magnetization. When the petrophysical properties of rocks bearing magnetite or pyrrhotite as their main magnetic minerals are compared, a general clustering of pyrrhotite- or magnetite-bearing rocks can be observed. Their remanent magnetization is an effective discriminator. The ferrimagnetic type of pyrrhotite may be associated with intensive remanence, and hence with extremely high Königsberger ratios, even up to thousands. In contrast, the intensity of remanent magnetization of magnetite, particularly if coarse grained, may be much lower. This fact can be used in predicting magnetic mineralogy from petrophysical plots. In Figure 3, Q-ratios of 1 to 2 denote an equal contribution of remanent and induced magnetization to the intensity of the magnetic anomaly. Samples with coarse-grained magnetite typically have Q-ratios below 1, but the Q-ratios increase as a function of decreasing magnetite grain size. Samples that contain monoclinic pyrrhotite typically have Q-ratios close to ten or above. Fine-grained magnetite may also be associated with a strong remanent component. This means that if magnetite and monoclinic pyrrhotite are present together in the same anomaly source body, it may be difficult to sepa-

rate them only on the basis of magnetic properties. Thermomagnetic tests to identify the monoclinic /hexagonal type of pyrrhotite have been carried out for mineralized black schists from several locations in eastern Finland, and the monoclinic type of pyrrhotite appears to be more prevalent (Airo & Loukola-Ruskeeniemi 2004).

Säävuori et al. (1991) correlated magnetic and electrical conductivity anomalies and petrophysical properties of sulphide-bearing rocks from 7 targets in Finland. The samples could be divided into two main categories on the basis of their susceptibilities and Q-ratios: 1) a magnetite population and 2) a pyrrhotite population (with pyrrhotite-dominant and pyrite-dominant subcategories). The anomalies selected for sampling and analysis consisted of plutonic, metasedimentary and metavolcanic rocks, of which about one-third comprised mica gneisses and one sample was composed of graphitic black schist. In almost 100 sulphide-bearing samples, the relative proportions of different iron-bearing sulphides and magnetite were distinguished. The results demonstrate that sulphides may be a considerable source of conductivity anomalies, and that magnetite, when present with pyrite, may also be related to conductivity anomalies.

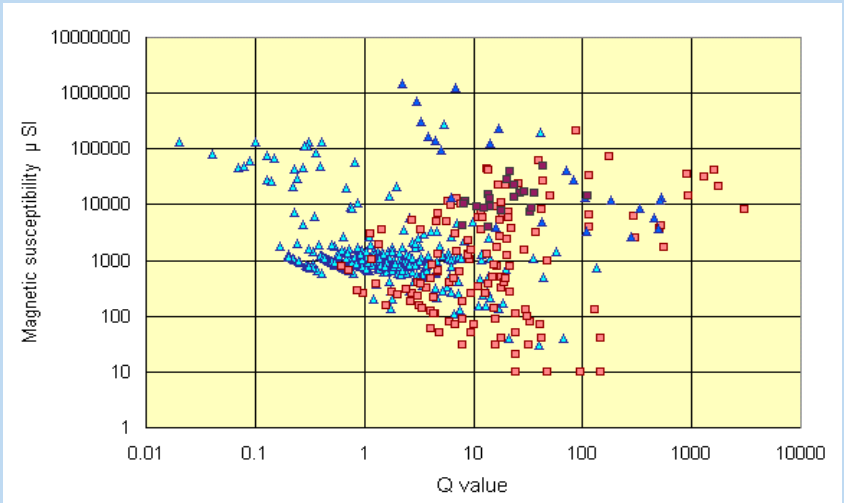

Blue samples:
Magnetite-bearing dolerites and iron ore samples

Red samples:
Pyrrhotite-bearing black schists and VMS samples

Q = Jr/Ji
Ji = Induced magnetization
Jr = Remanent magnetization

Q ~1-2	Equal contribution of remanent and induced magnetization on magnetic anomaly intensity
Q <1	Coarse-grained magnetite, remanence has irrelevant effect on magnetic anomaly
Q >>1	Fine-grained magnetite or monoclinic pyrrhotite (Q ~10 and susc. > 10 000 µSI); remanence has strong effect on magnetic anomaly intensity and shape

Fig. 3. Comparison of susceptibilities and Königsberger ratios of typical magnetite- or pyrrhotite-bearing rocks and their importance to the magnetic anomaly intensity and shape. Sampled from the Finnish National Petrophysical Database.

Tools for visualization and anomaly enhancing

For the purpose of introducing geophysical signatures related to different mineral systems, the magnetic total intensity image may in itself be very expressive, particularly so as a grey-scale presentation. These images are sensitive to delicate magnetic patterns and signatures that may be related to mineralization. However, additional information may be obtained by using some mathematical tools to enhance certain geophysical signatures or suppressed geological features. These common tools include potential field derivatives, frequency filters, upward continuation or spatial derivatives. To analyse shallow geological structures, short frequencies are enhanced, and to extract deep features, the regional, long-wavelength structures are enhanced. The following inserts illustrate ways of processing data sets and their combinations, and these are applied throughout this report in outlining the geophysical footprints of mineralization styles.

Insert 2 is an example of the integrated use of airborne magnetic and electromagnetic data sets in the visualization of an ultramafic intrusion in northern Finland (Airo & Kurimo 1999). The ability of GTK's electromagnetic data to be used in calculating the apparent susceptibility is useful when *in situ* petrophysical measurements are lacking. The remanent magnetization was suspected to affect the magnetic anomaly related to the intrusion. Field checking verified that the magnetite-bearing part of the anomaly could be outlined by using the magnetite effect. The effect of remanence was excluded by calculation of the apparent susceptibility on the basis of the electromagnetic data.

Insert 3 shows a collection of composite maps with mineral deposits, in which techniques for enhancing surface features in airborne geophysical data have been applied. This collection displays various thematic and integrated maps produced from GTK's airborne magnetic, electromagnetic and radiometric datasets. These may be useful in analysing geophysical surface anomalies and comparing geophysical information with observed geology. Classified electrical conductivity anomalies are also widely used in this report (e.g., Fig. 4b).

Insert 4 describes how the electromagnetic response can be used in distinguishing rocks with magnetite or pyrrhotite as their main magnetic mineral. Remanence affects the style of magnetic anomalies (magnetic anomaly intensity and shape). In the lower part of the aeromagnetic map "A", magnetic anomalies are due to magnetite, whereas in the upper part they are due to monoclinic pyrrhotite. This is verified by conductivity categories in map "B", in which pyrrhotite-caused anomalies are associated with electromagnetic anomalies indicating conductivity. In the case of coarse-grained magnetite, with Q-values below unity, the magnetic anomaly depends almost entirely on the induced magnetization, and in this case the anomaly signatures are smooth. Along with decreasing magnetic grain sizes, the remanent magnetization becomes more dominant. This brings sharp gradients and variation in anomaly intensities due to alternating directions of remanence. This is why the magnetic anomalies due to pyrrhotite or due to fine-grained magnetite are very similar.

The GTK frequency-domain airborne electromagnetic system provides a possibility for classifying electromagnetic anomalies as conductive or non-conductive. Map "C" shows the classification of anomalies on the basis of the ratio of the real (Re) to the imaginary (Im) component of electromagnetic data (Re/Im). The phenomenon is based on the negative response in the real component at low conductivity and with high magnetic permeability (the so-called magnetite effect, diagram "D") (Suppala et al. 2005, Leväniemi et al. 2009). Although magnetite has intrinsically high conductivity, magnetite grains are rarely well electrically connected in unaltered intrusive rock. Even nearly massive magnetite can be relatively resistive, despite its high intrinsic conductivity.

Insert 5 displays techniques for the detection of magnetic anomalies of a certain type: extremely high amplitudes + expected remanent magnetization (Airo et al. 2014). This type of classification is constantly used in this report (*Insert 9* for the whole of Finland and, for example, Fig. 4a). The highly magnetic anomaly source rocks may be, for instance, serpentinite bodies, ultramafic intrusions with abundant magnetite, or iron-bearing formations (iron ore, BIF, magnetite type IOCG).

Insert 2.
Palaeoproterozoic mafic-ultramafic intrusion Suukisjoki, Finnish Lapland (from Airo & Kurimo 1999).

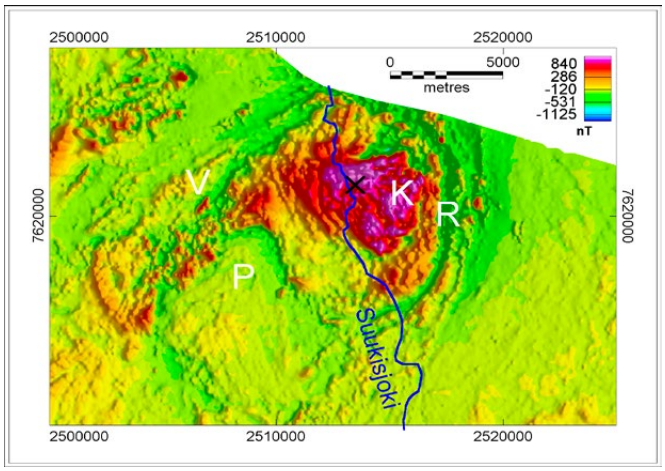

Aeromagnetic anomaly map showing the mafic-ultramafic intrusion.
K: magnetic anomaly influenced by both induced and remanent magnetizations
R: electrical conductivity + weak magnetization
V: weak magnetization
P: weakly magnetic country rocks

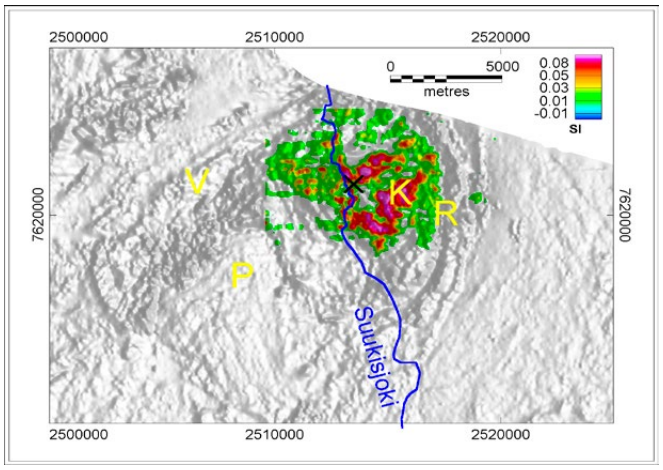

EFFECT OF REMANENCE EXCLUDED:
Apparent susceptibility was calculated from negative airborne electromagnetic in-phase component. The highest susceptibility (K) is shown in the colour overlay on the magnetic derivative map. Overall susceptibility was calculated from the negative AEM in-phase data as 0.05 SI (formulas by Keller & Frischknecht 1966)

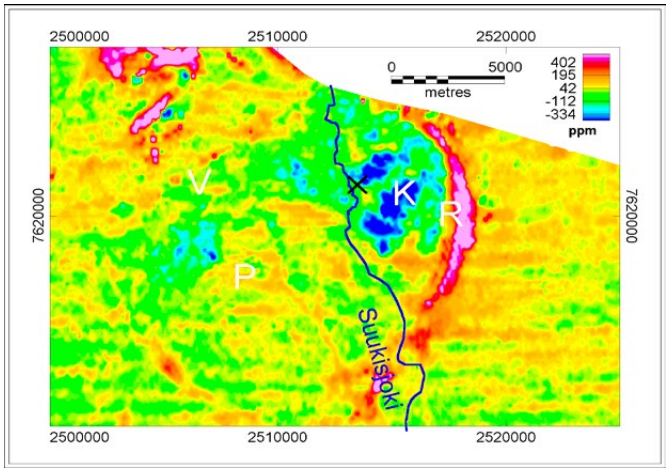

Airborne electromagnetic in-phase (real) component shows negative response over the magnetite-bearing ultramafic intrusion (K). It corresponds to the high susceptibility parts of the intrusion. The conductivity anomaly (R) is based on pyrrhotite in country rocks.

Location of the example anomaly in northern Finland.

Insert 3.
Detailed airborne geophysical signatures denote close-to-surface features of ground. Special techniques may be used for enhancing subtle signatures. The map layers for whole of Finland have been prepared by E. Hyvönen, GTK. Map area is 25 km x 30 km.

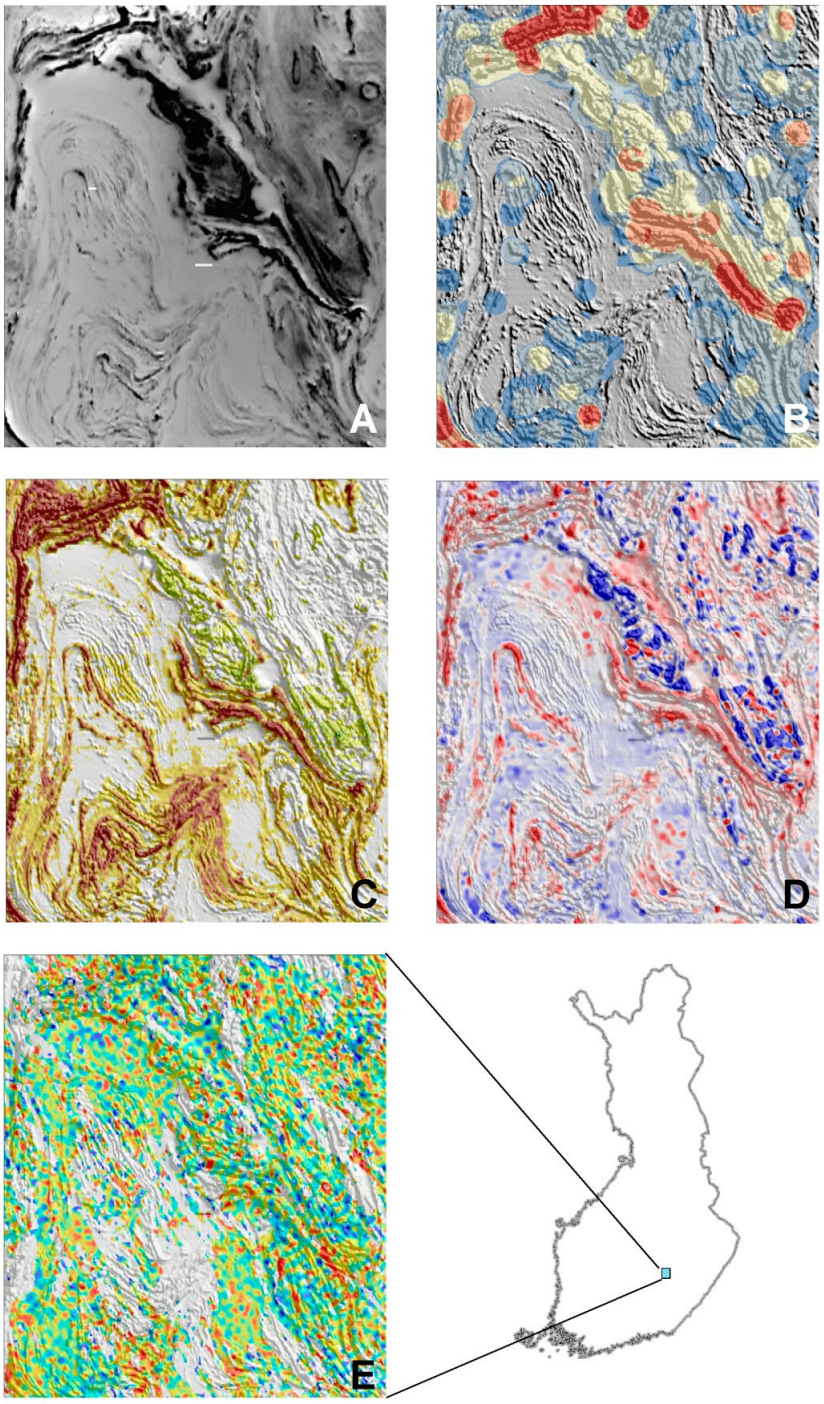

A. Aeromagnetic grey-scale image (dark = high intensity anomaly). Notice the ring-like magnetic anomaly in the right upper corner; it will be discussed in more detail in Insert 13.
B. Classification of magnetic anomalies. Red = high amplitude (techniques and colour categories are explained in Insert 5).
C. Electromagnetic classified real component (red/brown = good conductivity: green = low conductivity). Low-amplitude noise has been removed.
D. Electromagnetic ratio map (Real/Imaginary components). Red = good conductivity; blue = low (no) conductivity.
E. Aeroradiometric image: uranium (cut-off).

Insert 4.
Magnetite or pyrrhotite? How to use the electromagnetic response to distinguish rocks with magnetite or pyrrhotite content.

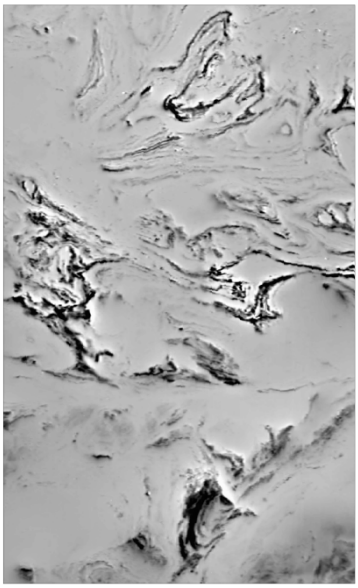

A. Aeromagnetic grey-shaded image. Dark shades denote high anomaly intensity.

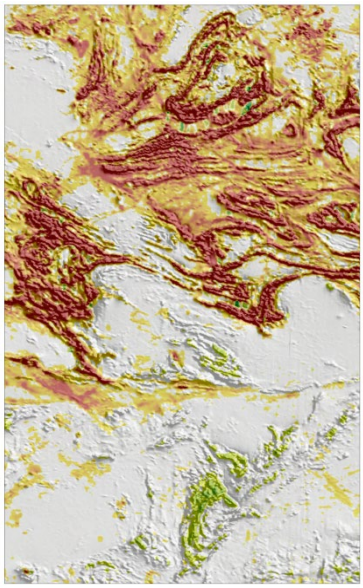

B. Electromagnetic classification image (real component).
Electrically conductive zones (pyrrhotite and graphite bearing rocks) in red/brown; low conductivity (magnetite bearing rocks) in green.

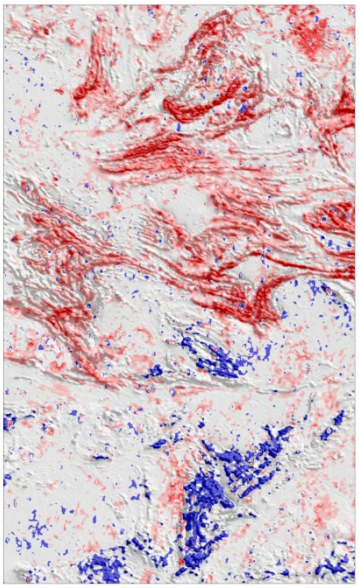

C. Electromagnetic Re/Im ratio (ratio of the Real to the Imaginary component). Red = good conductivity; blue = no conductivity.

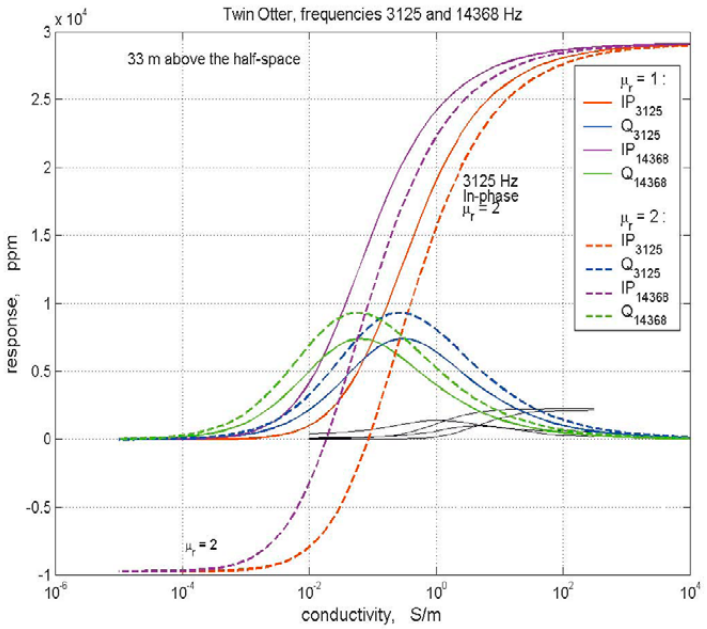

D. At low conductivities the electromagnetic low frequency response is negative. IP = In phase (real) component; Q = Quadrature (imaginary) component. μ_r = magnetic permeability. From: Leväniemi et al. 2009.

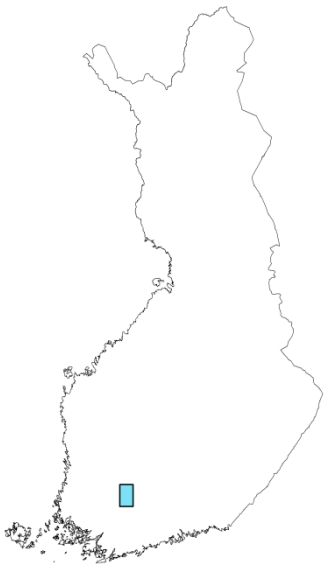

The example area is 30 km wide.

Insert 5.
Method for magnetic anomaly detection by classifying magnetic anomalies (H. Leväniemi, GTK in Airo et al. 2014). Upper right: schist belts surrounding the Central Lapland granitoid area. Three more detailed example maps: Hannukainen (upper left), Vähäjoki (lower left) and Misi (lower right).

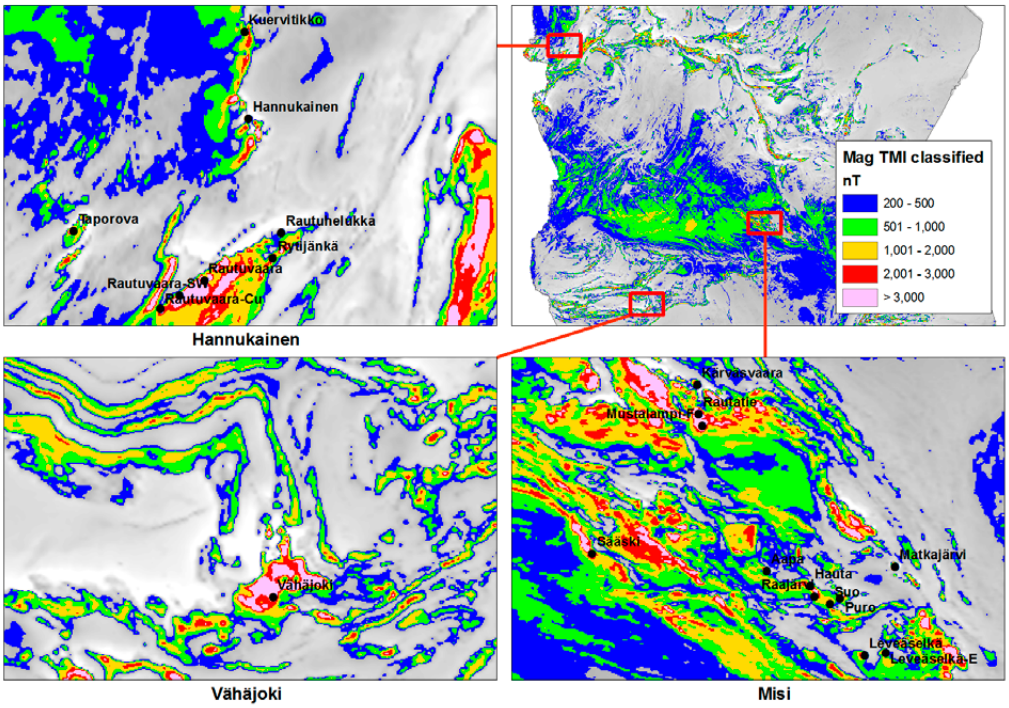

Thematic classification of magnetic total field intensity. TMI = Total Magnetic Intensity in 5 categories. Red and pink indicate the highest magnetic anomaly intensity.

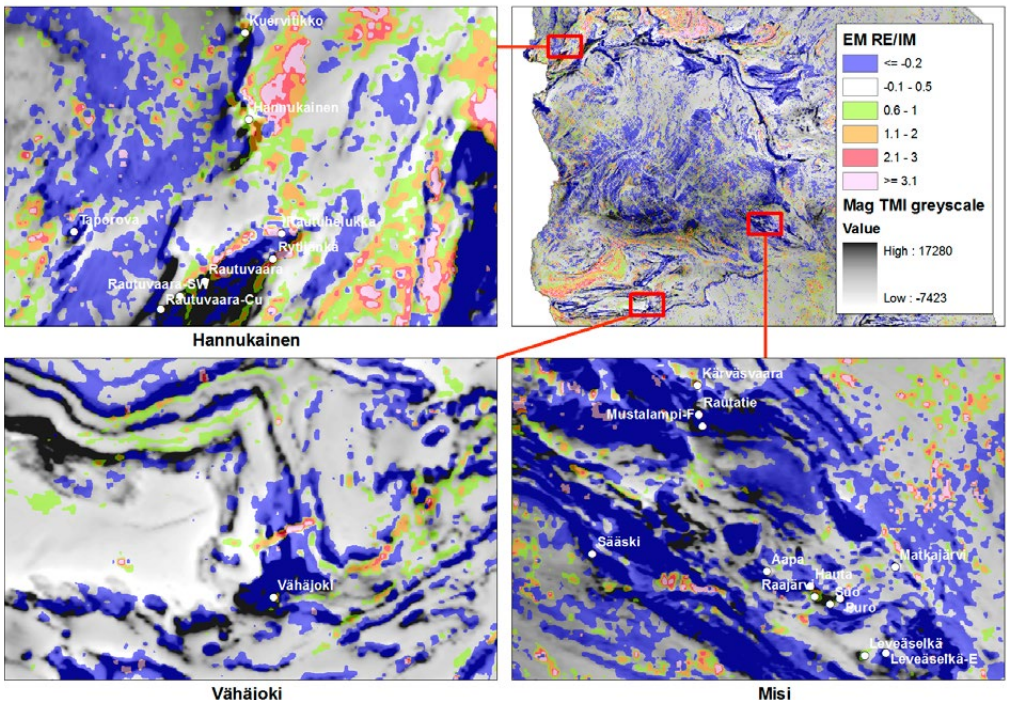

Classification of electromagnetic data: the ratios of Real to Imaginary components (Re/Im).
The upper limit of magnetically susceptive range was set Re/Im = -0.2. Blue indicates low Re/Im ratios (negative values of the real component) and express the so-called magnetite-effect. Red and pink indicate good electrical conductivity. Before classification the data were smoothly filtered (3-point median filter) in order to remove point-distortion due to low original measurement values.

Insert 5 (cont)

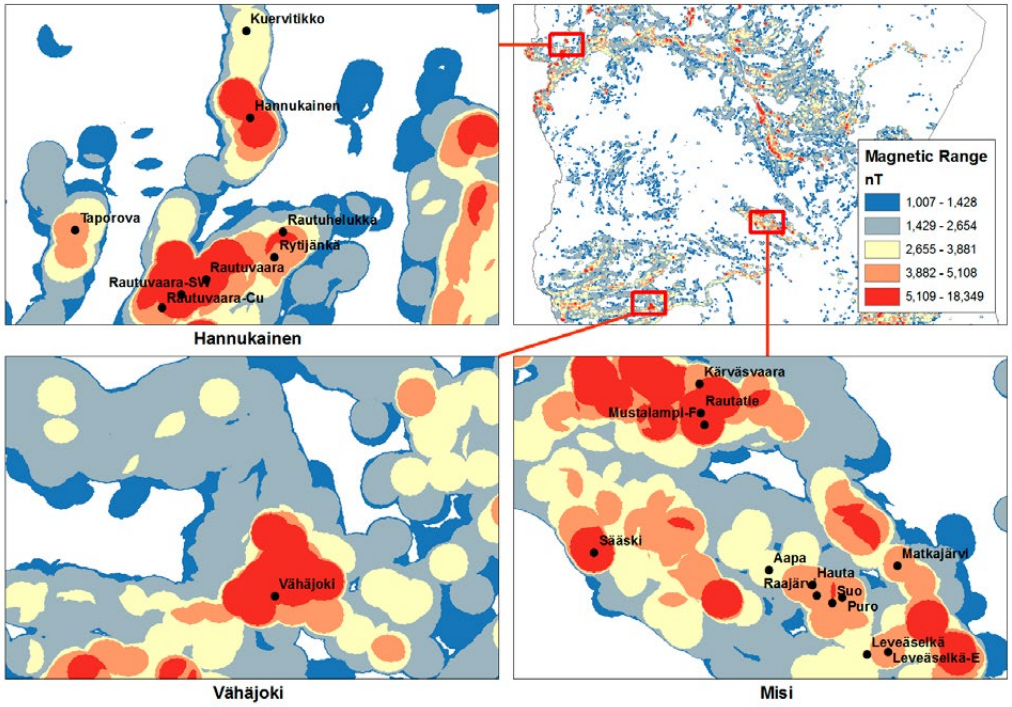

Magnetic anomaly detection.
The method is based on the variation of the magnetic anomaly amplitude (minimum → maximum value) in a circular region at each data cell. The analysed data set comprised aeromagnetic data of 50 m grid cell size. The radius of the moving window was as large as 750 m to ensure an adequate spatial extent of the anomalies.

MINERAL DEPOSIT TYPES

Ore deposit types addressed in this review

Ore deposits can be classified on the basis of the metals they contain, the form of the deposit (i.e. mineral distribution), ore associations (associated host rocks or geological structures), or the genesis of the deposit (processes or controls) (McQueen 2005). For the overview of the geophysical signatures of mineral deposit types, the genetic classification works better than classification based only on metals, because most metals have quite comparable physical properties and are not therefore always distinguishable. The genetic classification of ore deposits presented in Eilu & Lahtinen (2013) is applied in this review for the geophysical characterization (*Table 8).*

More than 30 different genetic types of metal deposits have been encountered in Finland (Eilu et al. 2012, FODD 2013). The most significant types of these, on the basis of past production and present resources, are classified into five main groups. In the following, the discussion of geophysical properties is focused on these five main groups, with critical minerals discussed in the sixth group:

1. Magmatic Ni-Cu, PGE
2. Intrusion-hosted V-Fe-Ti, Cr
3. Orogenic gold
4. Volcanogenic Massive Sulphides (VMS) (Cu, Zn, Pb, Au, Ag)
5. Banded iron formations and IOCG-style Fe±Cu, Au
6. Porphyry Cu-Au
7. High-tech metals and uranium

Genetic classification schemes incorporate elements of composition, forms and association. From these, it is possible to construct predictive models that can be used to search geological environments in which appropriate ore-forming processes have probably operated (McQueen 2005).

The major metallogenic epochs can be related to global geodynamic processes, including major periods of crustal break-up and convergence. Accordingly, in Fennoscandia, the metallogenic events and diagnostic mineralization systems can be related to specific plate tectonic settings (Lahtinen et al. 2012, Eilu & Lahtinen 2013, Weihed et al. 2008). Concerning geophysics, the recognition and outlining of tectonic plates and major structural zones controlling mineralization requires analysis of regional geophysical data suites covering vast areas.

In this Special Paper volume, the review of physical properties of ore deposit types or mineralization styles is mainly based on published information, in particular on the key note speeches and presentations that were given at two geosciences conferences: Exploration07 held in Toronto in 2007 (proceedings by Milkereit (ed.) 2007), and the SGA meeting held in Uppsala in 2013 (proceedings by Johnsson et al. (eds.) 2013).

General petrophysical properties

The physical properties of different mineral systems basically depend on the concentration, texture and properties of petrophysically anomalous minerals and properties of the host rock. The most important anomalous minerals are iron sulphides and iron oxides. In some cases, the ore minerals

Table 8. Genetic classification of the main ore deposit types (mineralization styles) in Finland and selected example deposits. The classification is inspired by metallogenic areas by Eilu et al. (2012) (see indices in the first column). The examples include both metallogenic belts and individual deposits.

METALLOGENIC AREA	MINERALISATION STYLE	EXAMPLES
	ARCHEAN	
F032, F047	Komatiitic Ni(-Cu-PGE)	Kuhmo-Suomussalmi Ni, Ruossakero (Ni,Co)
F032	Epithermal or VMS Ag-Zn	Taivaljärvi Ag-Zn
F030	BIF	Ilomantsi Fe (Huhus)
F023	Orogenic gold	Ilomantsi Au (Pampalo)
F034	Epithermal gold	Oijärvi (Au,Ag)
PALEOPROTEROZOIC RIFTING STAGES OF THE ARCHEAN CONTINENTS		
F035, F045	Layered intrusion Cr	Kemi Cr, Koitelainen Cr, Akanvaara Cr
F036	Mafic intrusion-hosted V-Ti-Fe	Mustavaara V
F035	Layered intrusion PGE ± Ni-Cu	Suhanko PGE, Siika-Kämä PGE
F048	Ultramafic-mafic intrusion Cr, Ni-Cu ± PGE	Sattasvaara Ni, Kevitsa Ni, Sakatti Ni
F031	Alkaline intrusion V-Ti-Fe	Otanmäki V
F029	Black shale –hosted Ni-Zn-Cu- Co	Talvivaara Ni
F038	SEDEX	Haukipudas (Zn,Cu)
F037	Volcanic red-bed Cu	Peräpohja Cu
F021, F020	VMS (Cu-Zn±Co)	Hammaslahti (Cu-Zn), Outokumpu (Keretti)
F039	Skarn Fe	Misi
PALEOPROTEROZOIC SUBDUCTION-RELATED		
F028, F004, F009	VMS (Zn-Cu, Au-Cu)	Vihanti-Pyhäsalmi, Häme (Zn,Cu), Haveri (Tampere Au,Cu)
F004	Porphyry Cu ± Au	Kopsa, Kedonojankulma (Au, Cu)
F009	Epithermal Cu ± Au	Kutemajärvi (Tampere Au,Cu)
PALEOPROTEROZOIC COLLISIONAL		
S034, F037	IOCG (Au, Cu-Au, Fe)	Pajala-Kolari, Vähäjoki
F020	Outokumpu-type Ni	Vuonos
F043, F040	Orogenic gold (Au±Cu,Co,Ni)	Kittilä (Au,Cu), Kuusamo (Co-Au ±Cu ±U± LREE)
F004, F007	Orogenic gold (Au±Cu)	Satulinmäki (Au), Jokisivu (Au)
F016, F027, F006	Mafic-ultramafic intrusion Ni-Cu	Kotalahti (Ni,Co), Hitura (Ni,Co), Vammala (Ni,Co,Cu)
F005, F024, F002	Rare metal pegmatite Sn, Nb-Ta, Li-Be	Somero Li, Emmes Li, Kemiö (Ta,Be)
PHANEROZOIC		
R013	Peralkaline intrusion, Carbonatite	Sokli Apatite-Nb-REE

themselves do not possess properties that are detectable, or their concentration may be too low to have a geophysical influence, but there may be some properties of altered host rock that may indirectly be used in targeting mineralization.

Magnetite and pyrrhotite, or other ferrimagnetic minerals, tend to accumulate in ore deposits (including the non-iron ones) or in their environments. Because these minerals often accompany economic mineralization in various ways, their magnetic properties can be important in the search for ore deposits, even though they do not often represent the economic minerals (Hrouda et al. 2009).

Sulphide deposits occur in rock complexes that were metamorphosed from zeolite to granulite facies and underwent regional metamorphism together with surrounding rocks. During the process of metamorphism, the ores may have recrystallized and partially mobilized together with quartz, carbonates and barite (Hrouda et al. 2009). New minerals may have formed, for example, pyrite, pyrrhotite, magnetite, and Mg- and Fe-carbonates. The most commonly documented ore mineral-related reaction in metamorphosed deposits is an increase in the pyrrhotite/pyrite ratio with increasing metamorphic grade. The transformation can often also be reversed, mostly in the terminal phase of regional metamorphism when new pyrite is created. The reaction of pyrite to produce pyrrhotite in metamorphosed massive sulphide deposits is considered unlikely, and much of the data indicate that the pyrite-pyrrhotite conversion is equivocal. Pyrrhotite can also occur in the form of a hexagonal phase, which is antiferromagnetic and displays only relatively low susceptibility. This pyrrhotite can occur in the deeper parts of massive sulphide ores, whereas a mixture of hexagonal and monoclinic pyrrhotite is typical of the near-surface parts.

Petrophyscial properties determine which geophysical techniques can best be used to investigate a mineral system. A comprehensive collection of geophysical properties for different mineralization styles is available in literature and has been presented by several authors in the proceedings of Exploration 07 (Milkereit (ed.) 2007). They are summarized below to act as background for the following sections:

- **Densities** are largely controlled by the iron content in most rocks and minerals. Iron oxides and sulphides may be identified as gravity anomalies, but so also may dense host rocks such as mafic/ultramafic rocks.
- **Magnetism** readily distinguishes deposits bearing magnetite (Fe-Ti-V ores, iron oxides) or ferrimagnetic pyrrhotite (massive sulphide deposits). Remanent magnetization may have a prevalent role.
- **Remanent magnetism** can cause great difficulties in modelling, especially with automated methods. Disseminated pyrrhotite with relatively low susceptibilities can have Q-values (Q = the ratio of remanent to induced magnetism) over 10, producing significant local anomalies.
- **Electrical conductivity** can usually be used to discriminate between base metal sulphides and Fe oxides. Some ore-related minerals may also have high conductivities. In general, iron oxides or certain rock types such as mafic or ultramafic rocks are not highly conductive.
- **Radioactivity** may have some role in limited cases. Generally, felsic or intermediate rocks may have high radioactivity, whereas mafic and ultramafic rocks and Fe and base-metal sulphides have little or no natural radioactivity. Thorium (Th) tends to enrich in alkaline rocks. It forms complex ions with, for example, sulphides, carbonates and phosphates. Chemical alteration may produce some identifiable change. Uranium (U) is generally highly mobile, leaving thorium behind. Carbonatization may result in enrichment of U and Th, together with Au. Potassic alteration produces increased potassium radiation values, even for mafic and ultramafic rocks.
- **Seismicity** has an important role in structural and lithological mapping. Seismic methods are able to produce high-resolution images of the geological structure and to define sharp boundaries in the subsurface. Seismic imaging techniques require the input of information regarding propagation velocities of the media. This information is usually recovered from seismic data by interactive velocity analysis, or such information can be obtained from borehole acoustic logs. The interpreted boundaries can be used as constraints in the inversion of other methods such as magnetics and gravity, which can be used to fill volumes with physical property values but have poor resolution at depth.
- **Anomalous in most physical properties** are sulphide deposits. These typically include

pyrrhotite, pentlandite and chalcopyrite, which may be the reason for electrical conductivity, chargeability, density, magnetic susceptibility, natural radioactivity and acoustic velocity. This combination of physical properties makes the detection of significant concentrations of sulphides fairly straightforward. Sulphides easily deform plastically so that their hosting structures may be easily identified by geophysical methods.

The petrophysical database of GTK contains laboratory measurement results for various ore deposit types. These are summarized in *Table 9*. The number of samples is annually increasing as new measurements are performed to serve the needs of different GTK projects. The naming of the old database samples is quite generalized and sketchy, but nevertheless the measurement values give an idea of the properties. To complement the ore sample database, new measurements were carried out for this study. The new samples were selected from GTK's rock museum archives to cover different types of ore deposit, and they represent selected ore types from old Finnish mining areas. The new measurements are compiled in *Table 10*, and in addition to density and magnetic properties, they also include electrical properties.

Insert 6 compares the petrophysical properties of various ore deposit types in GTK's petrophysical database and the new measurements for this study (H. Säävuori, GTK), and they display great variation in properties, of course depending on the ore mineral content and type. The overall impression is that remanence is important, as indicated by Q-ratios of >1 for most of the samples.

Spatial distribution of ore deposits

Structural and metamorphic aspects, in addition to geophysical properties, have an important role in affecting the assessment and the type of mineralization. The metamorphic and alteration history of the host rock and the age and timing of mineralization are important, but of ultimate importance is the structural control – at a large or small scale, or both. Mineralization may be related to craton margins or crustal block boundaries, the mineralization may need contrasting redox conditions that may be found at lithological contacts, the fluid propagation needs fault systems or weakness zones formed by regional folding, or the mineralization may favour a certain type of pressure release such as in fold hinges.

Insert 7 summarizes structural lineaments in Finland and adjacent areas, as inferred from Bouguer and magnetic anomaly data. Most mineral deposits are spatially related to these structural unconformities. The lineaments were interpreted at more detailed scale on the basis of processed magnetic and gravity gradient data sets. Major structural zones are indicated in potential field data as parallel or aligned gradient zones following a certain orientation and referring to great unconformity. Frequently, they are associated with a linear change in the overall regional anomaly amplitude. Regional gravity data reveal more prominent and crustal-scale structural features, whereas magnetic anomalies for the most part describe the surface. The major lines traverse from Sweden to Russia and crosscut the whole of Finland. Their main orientations are linked to the main periods of crustal break down in the history of the Fennoscandian shield. *Insert 8* displays the Bouguer anomaly map with the interpreted major structural lines. The map shows regions of regional high gravity that can be related to granulite facies metamorphism, e.g. the Archaean eastern Finland and the granulite belt in Lapland. Granulite facies metamorphic units close to the surface tend to be associated with regional gravity highs, because prograde metamorphic processes increase the content of higher-density mafic silicates in rocks. Block boundaries and major unconformities are outlined by regional gravity lows. One of them is the Raahe-Laatokka zone, with local gravity highs following both sides of the zone. Of the areas with known Ni deposits, Kotalahti (also *Insert 10*) and the Vihanti-Pyhäsalmi area are related to gravity highs.

Insert 9 displays the magnetic anomaly map of Finland with the classification of magnetic anomalies (techniques and colour categories are explained in Insert 5). Magnetic anomaly classification distinguishes the high magnetic anomaly amplitudes, either due to magnetite or monoclinic pyrrhotite. In addition to high magnetic susceptibilities, these anomalies are affected by high remanent magnetization. These techniques are a useful way of detecting iron formations, e.g. BIF, Fe-bearing cherts or

the Fe deposits associated with IOCGs. Some distinctive magnetic anomalies in Finland that stand out are outlined: the Sulkavanniemi-Kitee anomalies in southeastern Finland (A), the Vittinki zones on the west coast (B), Kuusamo schist belt (C) and the Kellojärvi ultramafic body in the southern part of the Kuhmo greenstone belt.

Insert 6.
Comparison of various ore deposit types in the petrophysical database and the new measurements of rock museum archives made for this study (H. Säävuori, GTK). Sampling sites are shown the aeromagneticmap.

Samples from database
Individual information of petrophysical parameters in Table 9. The group "Ores (not specified)" is petrophysically quite homogeneous and probably is composed of the same type having distinctive magnetic properties.
Petrophysical diagrams:
1. Susceptibility versus density; sulphide ores have here generally lower densities than e.g., banded iron ores.
2. Susceptibility versus Q-ratio; line Q = 1 is shown. Q >1 denotes the overall fine magnetic grain size for all except banded iron ores.
3. Remanent versus induced magnetization; line Q = 1 is shown. Remanent magnetization predominates over the induced (Q >1) for all other samples except banded iron ores.

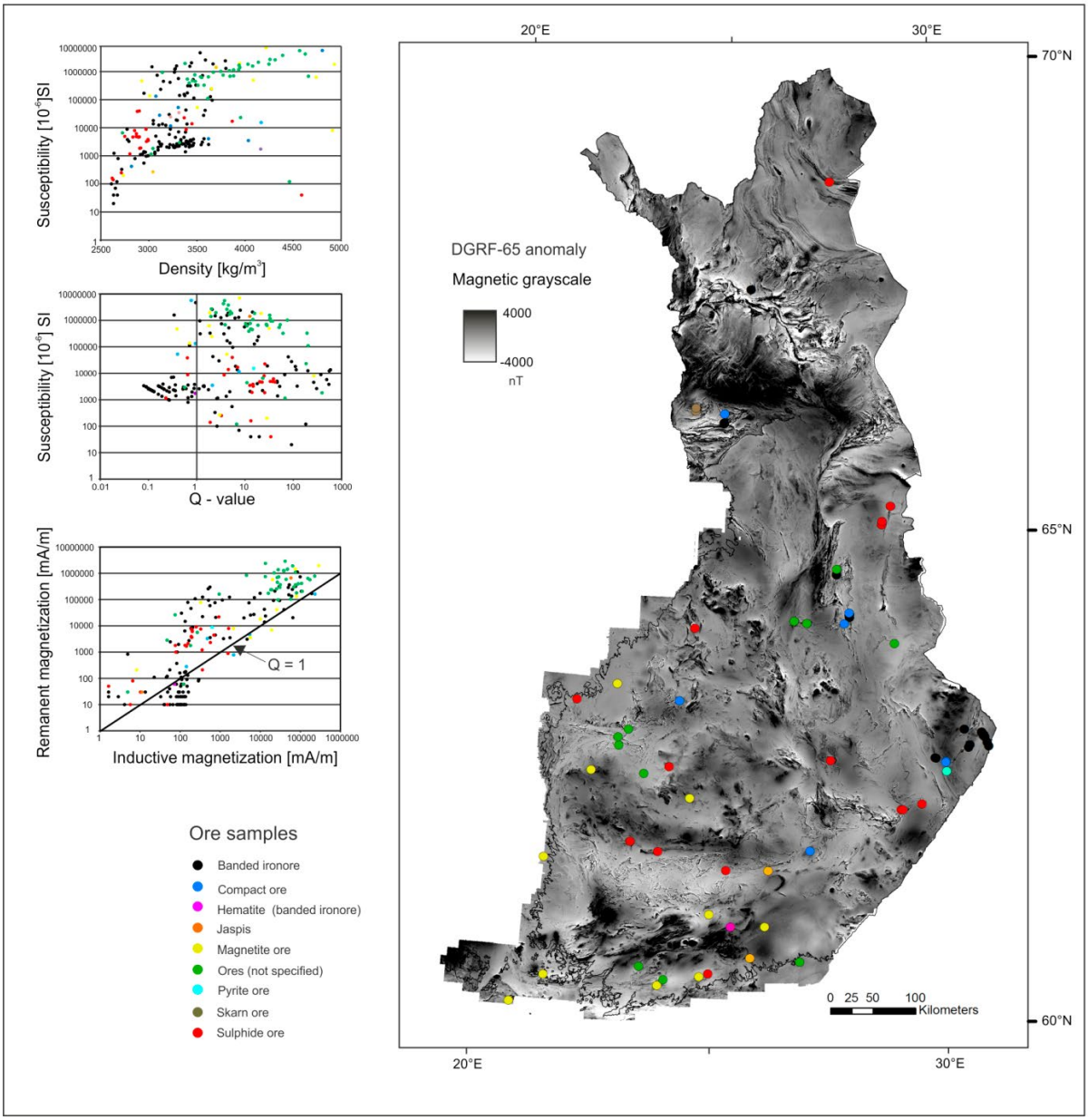

Insert 6 (cont)

Samples from rock museum
Individual information of petrophysical parameters in Table 10. The metallogenic areas by Eilu et al. (2012) are indicated for comparison.
Petrophysical diagrams:
1. Susceptibility versus density quite scattered.
2. Remanent versus induced magnetization; on both sides of line Q =1.
3. Susceptibility versus resistivity: quite scattered and 6 samples have resistivity out of the measurement range.

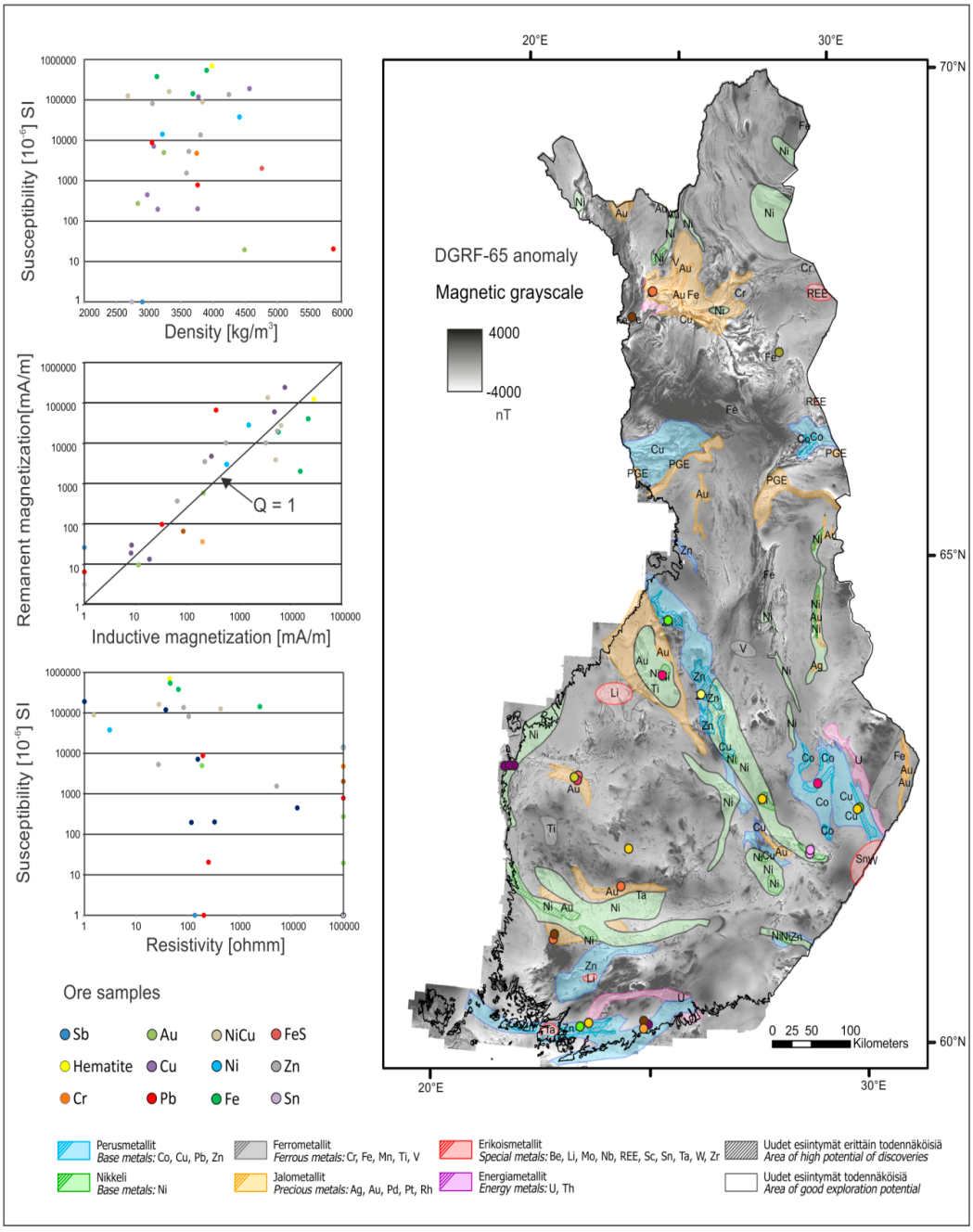

Table 9. Petrophysical data from ore samples measured at GTK. Averages of petrophysical properties. Density g/cm^3, susceptibility ·10^{-6}, remanent magnetization Am·10^{-3}, Q-value (Königsberger ratio), magnetite content calculated.

Ore deposit type	Density	Magnetic susc.	Remanent magn.	Q-value	Magnetite content	N
BANDED IRONORE	3244	238668	56153	41	8	125
COMPACT ORE	3499	735880	34212	2	2	8
HEMATITE (BANDED IRONORE)	4163	1740	60	1	0	1
JASPIS	3371	710350	332375	8	29	2
MAGNETITE ORE	3877	1166924	391160	33	21	11
ORES (not specified)	3860	1145132	647151	43	34	40
PYRITE ORE	4168	15360	8810	15	1	1
SKARN ORE	3269	29440			1	2
SULPHIDE ORE	3032	8300	3816	17	0	25
Total	3386	448774	187277	36	12	215

Table 10. Petrophysical data for ore samples from rock museum archives of GTK. Averages of petrophysical properties. D = density g/cm^3, K = magnetic susceptibility ·10^{-6}, J = the intensity of remanent magnetization Am·10^{-3}, Q-value (Königsberger ratio), R = resistivity Ohms, and б = conductivity (S/m).

Ore type	Metal	Sampling site	D(kg/m^3)	K(10^{-6}SI)	J(mA/m)	R(ohmm)	σ (S/m)	Q-ratio
ANTIMONY ORE	Sb	KALLIOSALO	2903	-5	25	136	0,007	
HEMATITE	Fe	TAPOROVA	3984	698953	119279	44	0,023	4,16
CHROME ORE	Cr	AKANVAARA	3747	4781	35			0,18
GOLD ORE	Au	SAATTOPORA	3236	4972	558	186	0,005	2,74
GOLD ORE	Au	ORIVESI	4489	19	17			21,14
GOLD ORE	Au	JOKISIVU	2833	274	9			0,83
COPPER ORE	Cu	ORIJÄRVI	3774	119185	57592	37	0,027	11,79
COPPER ORE	Cu	ORIJÄRVI	3079	7147	4583	155	0,006	15,65
COPPER ORE	Cu	KERETTI	3761	202	29	326	0,003	3,45
COPPER ORE	Cu	TYNYSNIEMI	3142	197	18	116	0,009	2,25
COPPER ORE	Cu	HAMMAS-LAHTI	2978	449	13	12909	0,000	0,70
COPPER ORE	Cu	OUTOKUMPU	4566	190384	232736	1	1,471	29,83
LEAD ORE	Pb	PAKILA	3052	8792	63578	194	0,005	176,44
LEAD ORE	Pb	METSÄ-MONTTU	3761	784	93			2,90
LEAD ORE	Pb	KORSNÄS	6118	1	6	202	0,005	255,58
LEAD ORE	Pb	KORSNÄS	5869	20	13	249	0,004	15,85
Ni-Cu-ORE	Ni-Cu	KOTALAHTI	3836	88891	129846	2	0,658	35,64
Ni-Cu-ORE	Ni-Cu	PETOLAHTI	3319	161175	26507	27	0,03651	4,01
Ni-Cu-ORE	Ni-Cu	HITURA	2677	125950	3697	426	0,00235	0,72
NICKEL ORE	Ni	LAUKUN-KANGAS	4411	37944	27116	3	0,32680	17,44
NICKEL ORE	Ni	HÄLVÄLÄ	3213	14162	2873			4,95
IRON ORE	Fe	BÖLE	3128	379479	1932	65	0,01530	0,12
IRON ORE	Fe	SUSIMÄKI	3901	540796	38739	45	0,02208	1,75
IRON ORE	Fe	SUUOJA	3687	142900	18198	2445	0,00041	3,11
PYRITE ORE	FeS	PYHÄSALMI	4758	2027	63			0,76
ZINK ORE	Zn	HAMMAS-LAHTI	3625	5307	3357	27	0,03729	15,44
ZINK ORE	Zn	PAKILA	3588	1553	353	5153	0,00019	5,54
ZINK ORE	Zn	VIHANTI	4247	135891	19110	82	0,01216	3,43
ZINK ORE	Zn	VIHANTI	3059	81476	9835	103	0,00968	2,95
ZINK ORE	Zn	ORIJÄRVI	3805	13619	9828			17,61
TIN ORE	Sn	PERÄLÄ DIKE	2739	0	3			1836,10

Insert 7.
Structural lineaments inferred from potential field data (Airo, M.-L., GTK 2013). Three main orientations are indicated by green, blue and purple lines. Ore deposits (FODD 2013) are spatially related to the structural zones.

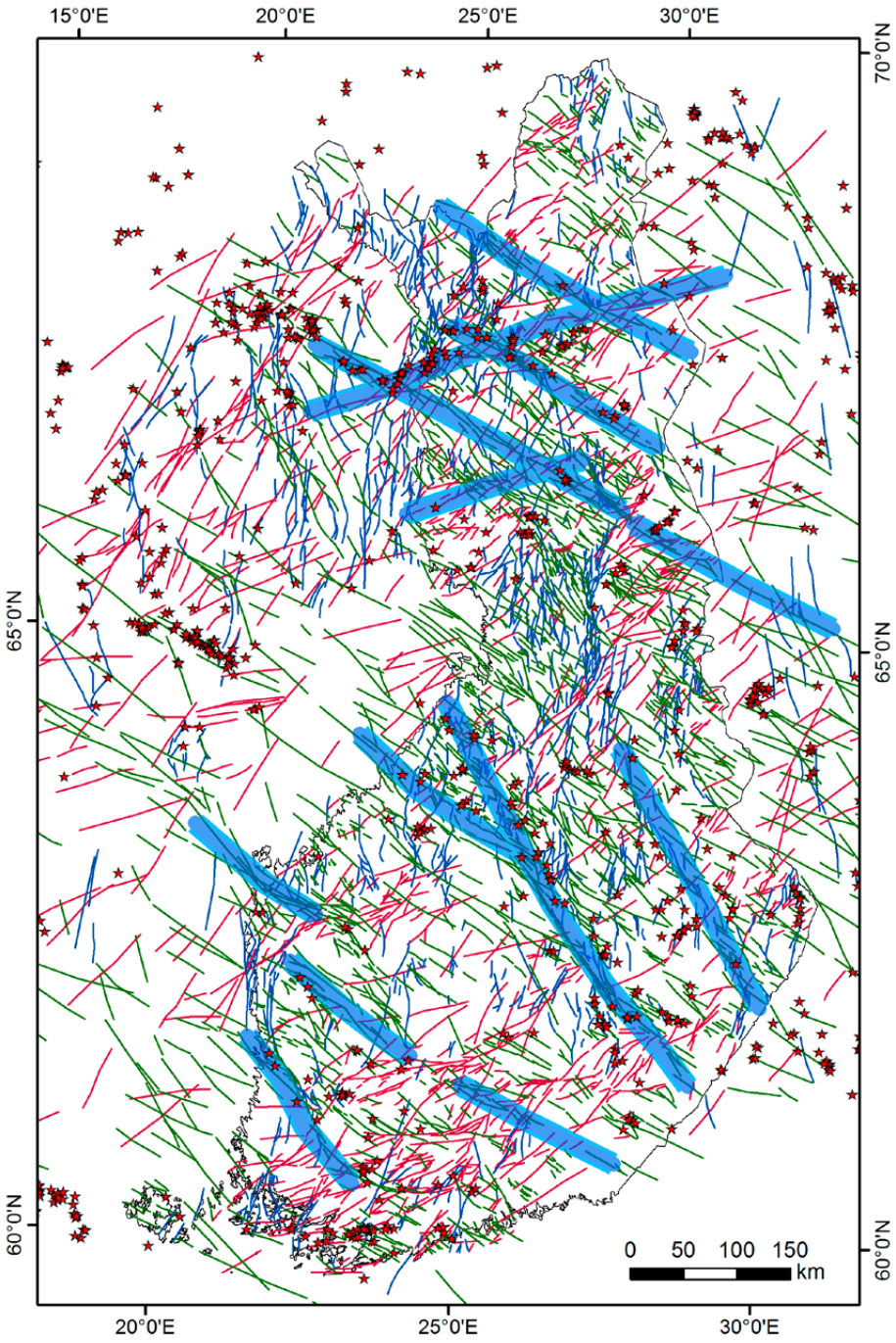

Insert 8.
Bouguer anomaly map of Finland and adjacent areas. The main interpreted structural zones (as in Insert 7) follow crustal scale lineaments in gravity data. Mineral deposits (FODD 2013) are spatially related to the structural zones.Bouguer anomaly map of Fennoscandia based on Korhonen et al. 2002.

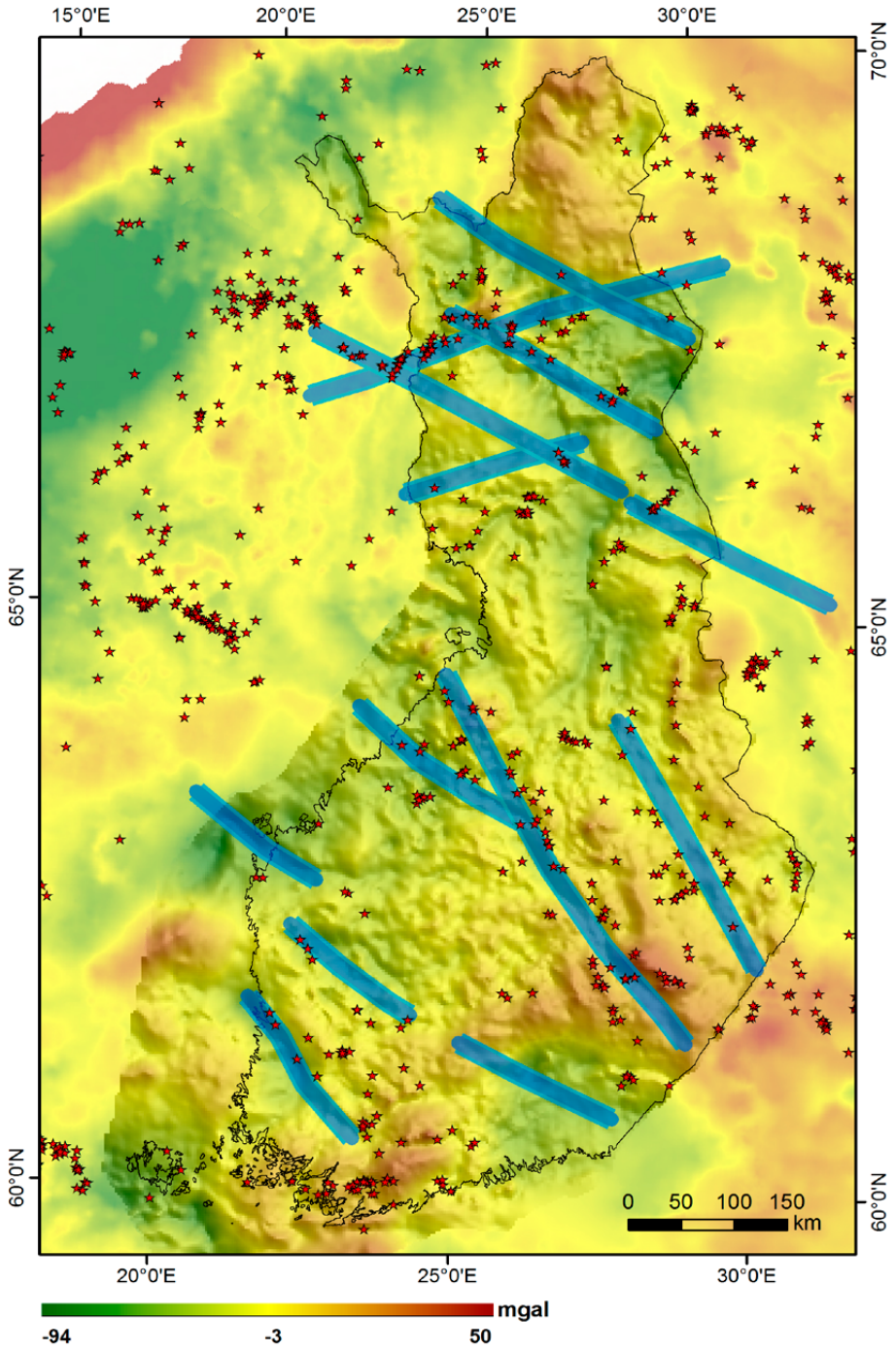

Insert 9.
Aeromagnetic anomaly map with classified magnetic anomalies. The techniques and colour categories are explained in Insert 5.The outlined regions with prominent magnetic anomaly intensities are discussed in the text. Magnetic anomaly map of the Fennoscandian Shield based on Korhonen et al. 2002.

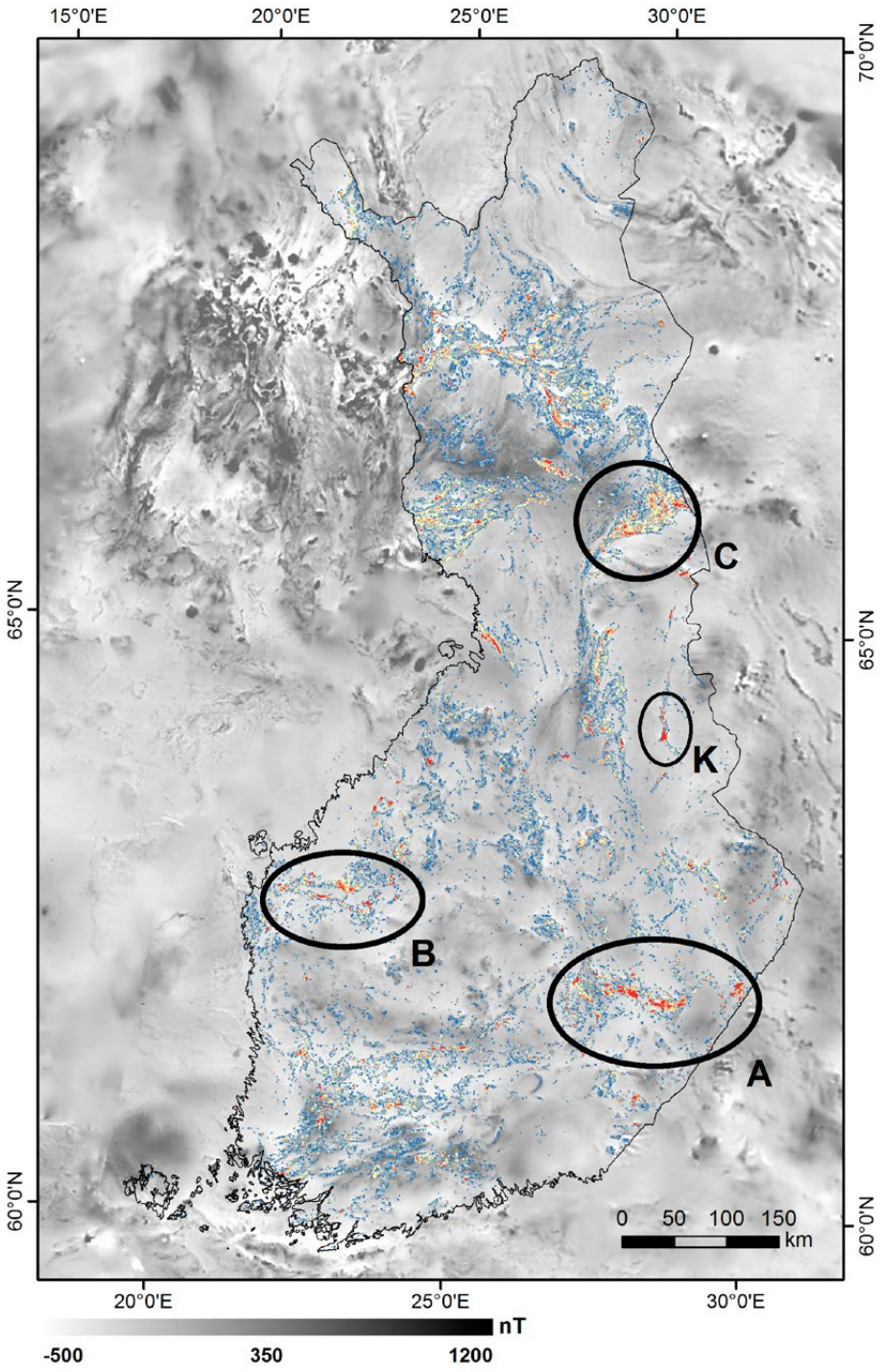

MINERAL SYSTEMS: GEOPHYSICAL MANIFESTATIONS

Magmatic Ni-Cu, PGE

Ni-Cu sulphides are frequently magnetic but not always, and they may produce a wide variety of geophysical signatures. Despite the association of magnetic anomalies with many nickel sulphide ore bodies, magnetic data alone are unreliable for locating ore bodies, and the use of other geophysical methods, particularly electromagnetic, is essential for target selection (Gunn & Dentith 1997). The physical properties of PGE (platinum group element) minerals are not usually apparent because of their low concentrations. Common characteristics of Ni-Cu sulphides, including magmatic or sulphidic mineralization, can include magnetic high signatures, density and gravity highs, and/or either electrical conductivity (due to the presence of massive sulphides) or chargeability (due to disseminated sulphides), magnetic susceptibility, natural radioactivity, and acoustic velocity (Lightfoot 2007, King 2007).

Geophysically, the most relevant mineral among Ni-Cu sulphides is pyrrhotite. It is dense, highly magnetic in its monoclinic form, and electrically conductive. The hexagonal form of pyrrhotite is antiferromagnetic and may display only relatively low susceptibility. Pyrrhotite and magnetite are present in the Co, Ni and PGE deposits, and the measurement of magnetic susceptibility from drill cores is a good addition to susceptibility well logging. The susceptibility measurement of cores also helps in searching for the relationship between ferrimagnetic minerals and economic ore minerals and/or footwall rocks. The magnetic susceptibility can also be used in the selection of samples for more detailed laboratory study.

The known Finnish magmatic nickel deposits have been classified into three types (Rasilainen et al. 2012):

1) Ni-Cu deposits associated with synorogenic Palaeoproterozoic (~1.89–1.87 Ga) mafic-ultramafic intrusions in central and southern Finland,
2) Ni-Cu deposits associated with Archaean (~2.8 Ga) komatiitic rocks in eastern and northern Finland and Palaeoproterozoic (~2.05 Ga) komatiitic rocks in northern Finland, and
3) Ni-Cu-PGE deposits associated with Palaeoproterozoic (~2.45 Ga) mafic-ultramafic layered intrusions in northern Finland.

The two large nickel deposits, Kevitsa Ni-Cu-PGE deposit and Talvivaara Ni-Zn-Cu-Co deposit, represent rare Ni deposit types, and are not included into the classes above.

Most of the important nickel deposits worldwide are located along craton margins, which are commonly associated with prominent gravity and also magnetic signatures. Good examples are Kotalahti-Sulkavanniemi occurrences located on the eastern side of the regional gravity low indicating the Raahe-Laatokka zone (*Insert 10*). Magmatic Ni-Cu and Ni-Cu-PGM deposits are associated with mafic-ultramafic rocks, which themselves produce strong magnetic and gravity anomalies. However, deposits of *type 1* are hosted by weakly magnetic mafic-ultramafic intrusives. The komatiitic host rocks (*type 2*) in general are highly magnetic on the basis of their magnetite content, as are the mafic-ultramafic layered intrusions (*type 3*). On closer inspection, *type 3* intrusions are associated with variable magnetic signatures, depending on the alteration of magnetite-bearing units. The PGE deposits in the Suhanko-Siikakämä and Koillismaa areas are related to the weakly magnetic parts of layered intrusions. Zientek (2012) reviews the geophysical characteristics of contact-type Cu-Ni-PGE and Reef-type PGE deposits. The main issue is that geophysical methods do not map PGE minerals directly, but they indicate physical property contrasts of primarily sulphide minerals and magnetite that may be associated with mineralization.

- Detailed aeromagnetic surveys may be used to establish a geologic framework of an area, but do not generally give a direct indication of mineralized rock. High-resolution surveys can be used to map igneous layering and tectonic structures, particularly if the data are enhanced to distinguish subtle features.
- Gravity studies may be used to determine the subsurface extent of rocks with variable density, and they are particularly well suited to mapping and modelling the extent and volume of

Insert 10.
The Sulkavanniemi-Savonlinna belt in southeastern Finland is associated with intensive magnetic anomalies.

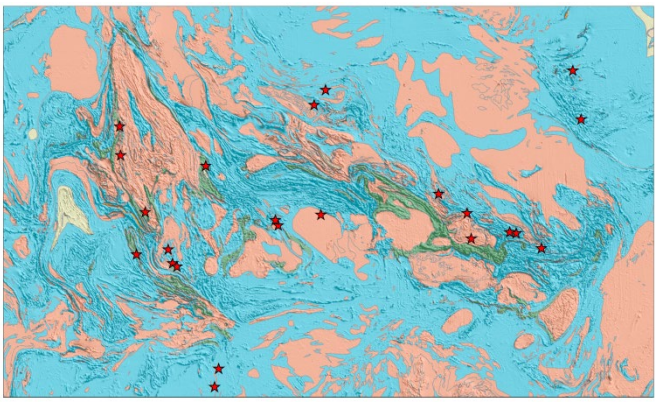

Mineral deposits are from FODD (2013).

The geological map is based on the GTK in-house digital bedrock database (Geological Survey of Finland 2010).

The map area is 130 km wide.

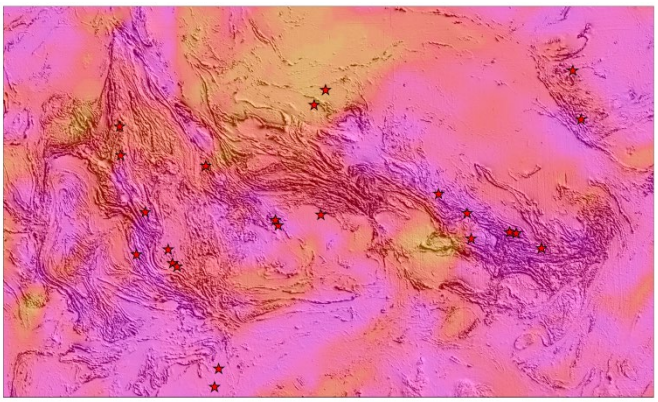

High intensity short wave-length magnetic anomalies along the block boundary that is indicated by gravity data.

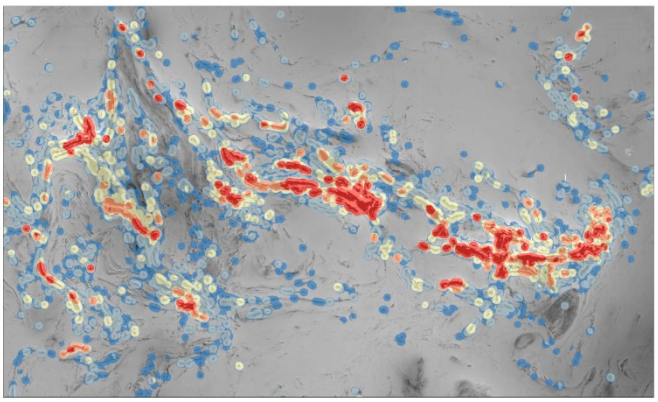

Highest magnetic anomaly amplitudes are related to the schists (not volcanic rocks).

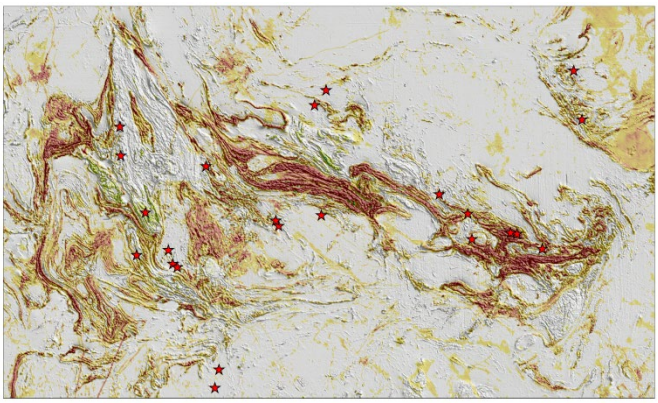

High intensity magnetic anomalies are associated with coincident conductivity, so the magnetism is carried by abundant monoclinic pyrrhotite.

Red = good conductivity
Green = magnetite

mafic and ultramafic igneous rocks. However, gravity measurements are not used to directly locate mineralized rocks.

- Electrical methods work best on rocks that are conductive. For contact-type deposits, airborne and ground electromagnetics and induced polarization surveys can be used to identify and delineate rocks that contain conductive and interconnected net-textured or massive sulphide ores. For reef-type ores, with low sulphide mineral contents, electrical responses are subtle.
- Once a rock layer that contains reef-type mineralization has been identified, seismic studies can be used to map the subsurface extent of the rocks. Three-dimensional seismic surveys have been used to identify structural features such as faults, depressions and cavities.

Three examples, in Figures 4–5 and Insert 10, show how magnetite-bearing komatiitic rocks can be distinguished by the classification of airborne magnetic and electromagnetic (frequency-domain) data.

A negative AEM response meaning non-conductivity characterizes the host rocks of Lomalampi, Kevitsa and Sakatti Cu-Ni-PGE occurrences in northern Finland (Fig. 4). However, on closer inspection, in Kevitsa the major part of the intrusion is recognized as conductive due to pyrrhotite as the main magnetic mineral. The magnetic anomaly classification enhances magnetic signatures associated with relevant remanence. The Sakatti anomaly stands out locally in the detailed image.

Petrophysical properties for the komatiite-hosted Lomalampi PGE-Ni-Cu-Au deposit in northern

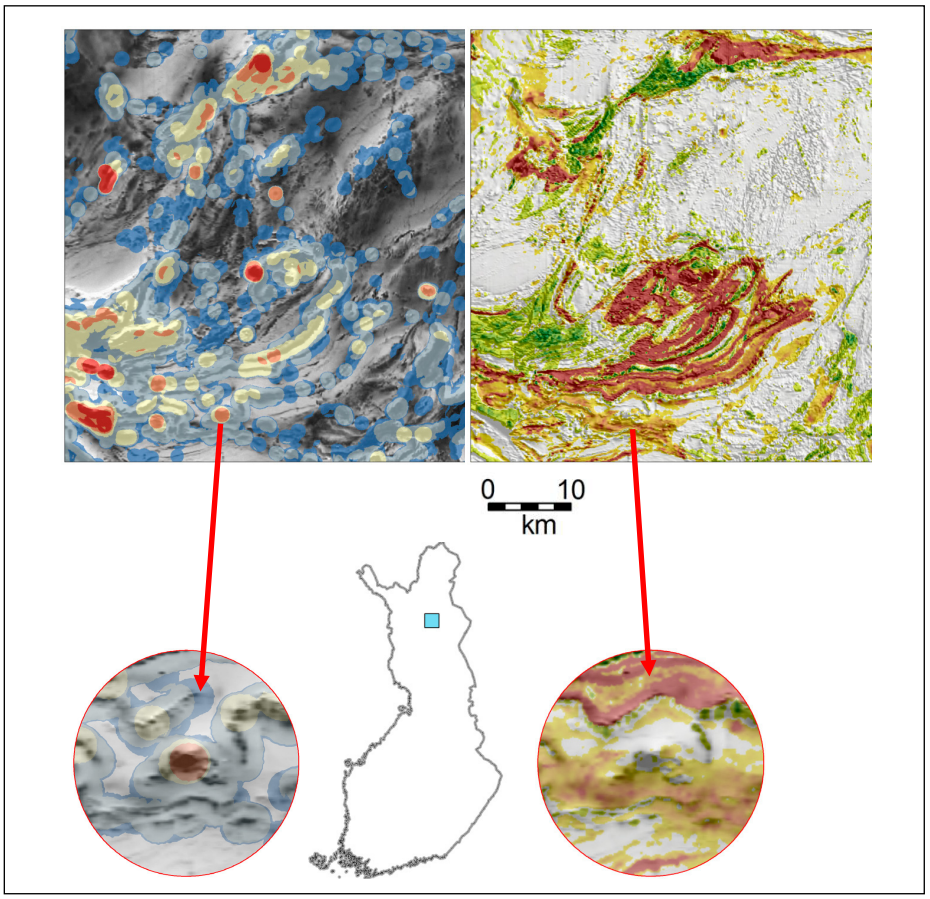

Fig. 4. Airborne geophysical integrated maps from northern Finland covering the Koitelainen gabbro and adjacent areas. The upper images are 50 km wide. Rounded circles below show detail of the Sakatti occurrence.
Upper left: Aeromagnetic anomaly classification map. This classification points out magnetic anomalies of very high intensity and short wavelength (red circles; see more detailed explanation and colour categories in Insert 5). Sakatti and some other similar targets can be noticed.
Upper right: Airborne electromagnetic (AEM) classification; background magnetic derivative map. AEM categories are explained in Insert 4; good conductivity is indicated in red and poor/no conductivity in green. The magnetite-bearing komatiitic rocks stand out as resistive. The electrical conductors are related to greenstones with a graphite-bearing interlayer or the sheeted dyke complex.
Circles below: The Sakatti formation is associated with a magnetic anomaly (left), but not with electrical resistivity or conductivity (right).

Finland have been summarized by Salmirinne (2010), in Figure 5. Various rock groups can easily be classified in the density/susceptibility plot. Peridotites hosting the mineralization have the highest susceptibilities, whereas sulphide schists have lower susceptibilities but higher densities.

The Sulkavanniemi-Savonlinna belt in south-eastern Finland is associated with highly intensive magnetic anomalies (Insert 10). These are related to volcanic rocks and black schists, and the magnetic zone continues to Kitee, close to the Russian boarder.

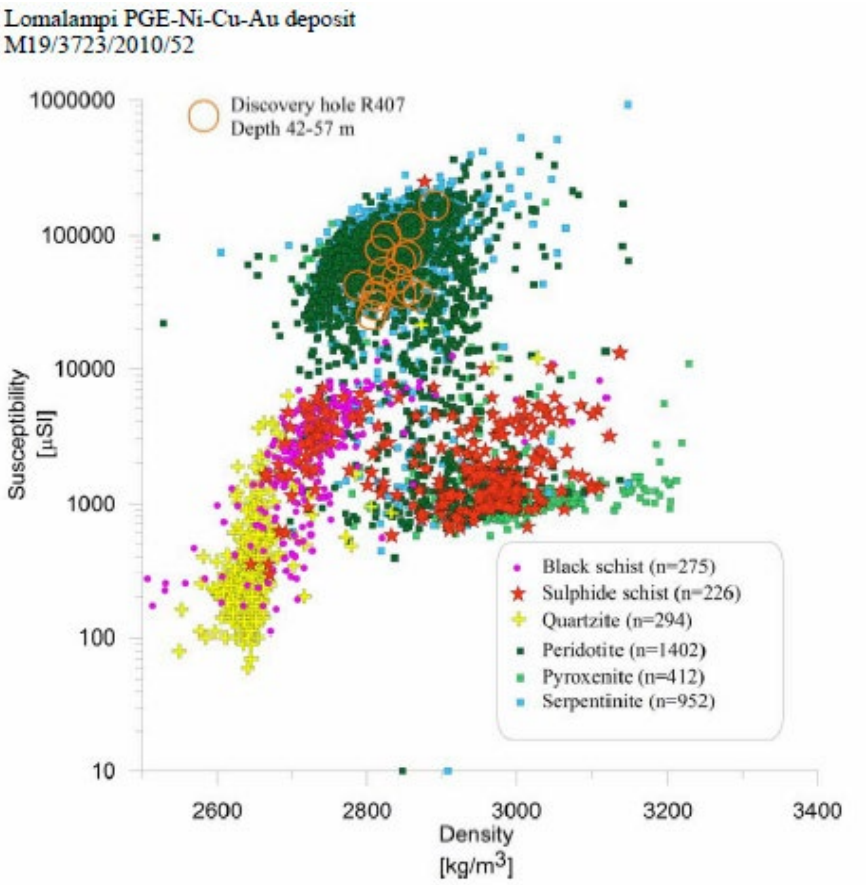

Fig. 5. Petrophysical properties from Lomalampi (Salmirinne 2010). Diverse rock types are clustered into typical density/susceptibility ranges. Serpentinites and peridotites have the highest susceptibilities. The mineralized peridotites (orange circles) cannot be distinguished from other peridotites by their density/ susceptibility distributions. Black schists and sulphide schists are clustered into one group with pyrrhotite susceptibility and density < 2800 kg/m^3, but sulphide schists also form another cluster with a higher density range.

Table representing petrophysical properties: Median values of petrophysical in-situ loggings for the main rock types reported from drill holes in the Lomalampi area (8 drill holes, 2004). Note the low level of radioactivity of ultramafic rocks.

Rocktype	Count	Density [kg/m3]	Susceptibility [µSI]	Chargeability [%]	App. Resistivity [Ωm]	Tot. Radiation [µR/h]
Graywacke	631	2588	293	2.85	4686	3.23
Felsic tuffite	165	2742	732	5.69	69	7.39
Graphite schist	92	2796	855	1.24	371	0.50
Graphite-sulphide schist	605	2707	2790	7.65	21	18.54
Gabbro	102	3082	1801	1.79	2019	6.21
Peridotite	1320	2810	60861	3.19	6153	0.57
Pyroxenite	589	2993	5346	1.47	5022	0.87
Ultramafic hyalotuffite	914	2920	934	0.88	835	1.06
Ultramafic lava	387	3027	1170	1.32	2784	3.72

Geophysical key factors for Ni-Cu-PGEs

Density
The density of sulphide minerals is generally anomalously high, generally >4 g/cm^3. Mafic and ultramafic rocks hosting Ni-Cu-PGE deposits also have high densities because of the elevated abundance of mafic minerals such as olivine and pyroxene. Thus, density may be used for the direct detection and quantitative measurement of many sulphide ores.

Gravity
Regional airborne gravity (or regional ground gravity with fair resolution) and gravity gradiometer coverage would be one of the best ways to promote nickel sulphide (and other) exploration. Gravity is an effective technique for defining the geometry and structure of the deposits and their host rocks at a regional scale.

Magnetic susceptibility
Ni-Cu sulphides may be magnetic, but not always. The economic sulphides pentlandite and chalcopyrite are non-magnetic, whereas the magnetic properties of many sulphide ores are dominated by pyrrhotite. The latter is moderately magnetic in its monoclinic form but non-magnetic in its hexagonal form. The mafic and ultramafic host rocks may be highly magnetic, depending on the concentration of magnetite, which is a common primary mineral or a hydrothermal alteration product. However, depending on the degree of serpentinization, their magnetization may be very variable.

Electrical properties: conductivity/resistivity
Electrical conductivity is the most effective single tool in the identification of semi-massive to massive Ni-Cu sulphides. There is a very large contrast (about 8–9 orders of magnitude) between the electrical properties of Ni-Cu sulphides and their host rocks. Pyrrhotite has one of the highest conductivities: only graphite is of the same order or higher, but graphite rarely occurs in a truly massive crystalline form over large thicknesses, i.e. tens of metres thick. This makes massive to semi-massive pyrrhotite-dominated bodies, with or without nickel sulphides, fairly unique in conductance (conductivity x thickness).

Electrical chargeability
Since the Ni-Cu-S minerals all have high metallic conductivity, they have high electrical chargeability. The good contrast with most host rocks makes them good induced polarization (IP) targets. Chargeability may be a good indicator of vein-type deposits or unconnected disseminated sulphides which are rarely conductive. If country rocks have too similar properties to the exploration target, the application may be complicated. Both barren and nickelferous sulphides are conductive and chargeable – as are carbonaceous shales and graphite (i.e. black shales in Finland). In the case of low levels of sulphides, disseminated magnetite in mafic to ultramafic rocks can cause chargeability anomalies.

Natural radioactivity
Radiometric data have been acquired on a regional basis comparable in scale to magnetics in many countries and in Finland as well. The anomalously low radioactivity of mafic and ultramafic rocks makes radiometrics a very valuable tool in areas where surface soils have weathered in place. The almost non-existence of U, K and Th in massive Ni-Cu-S also makes natural radiometrics a potentially useful passive radioactive method for identifying massive sulphides (through the absence of a response).

Seismics
Density plays an equal part with acoustic velocity in the acoustic reflectivity coefficient. This is an important factor in hard rock seismics, where velocity variations can be small and density values dominate the reflectivity. Seismic reflection is the only method in which spatial resolution does not decline rapidly with depth and has the capability to directly detect deposits at depths that are many multiples of their size. However, due to non-uniqueness in simple reflection images, these signatures may not be definitive.

Ketola (1982) evaluated the applicability of exploration methods in the search for Ni-Cu ores in Finland, the emphasis being on those methods that contributed to the discovery of known ore deposits. The report describes the geology, geophysics and petrophysics of most of the Ni-Cu ore deposits found at that time in Finland. Geophysical surveys play a key role in the search for Ni-Cu ores associated with mafic and ultramafic rocks. The large number of magnetic and electromagnetic anomalies in areas with pyrrhotite-bearing black schists has made it increasingly necessary to use geochemical surveys for classifying geophysical anomalies. The detectability of an ore-potential mafic intrusion depends not only on its dimensions and attitude, but also on its grade of serpentinization, which is reflected in the variation of the petrophysical properties. The main point is how well an anomaly produced by a certain method can be distinguished from the environment.

The summary of geophysical key properties in the following fact sheet is mainly after King (2007) and Lightfoot (2007).

Intrusion hosted Fe-Ti-V, Cr

Magmatic rocks containing economic concentrations of iron, titanium, vanadium and phosphorous are commonly associated with massif-type anorthosites and related rocks. Aeromagnetic surveying is an essential geophysical tool for the exploration of Fe–Ti–V–P ore bodies, because these deposits contain ferrimagnetic Fe-Ti oxides. The gravity method is also utilized, because of the high density minerals. The magnetic properties of Fe–Ti ore deposits present contrasting signatures, depending whether the natural remanent magnetization is dominated by hemo-ilmenite or multi-domain magnetite (Charlier et al. 2015). Characterization of the rock magnetic properties in the Rogaland Anorthosite Province led McEnroe et al. (2001) to distinguish between two groups of Fe–Ti mineralization types that produce large and contrasting anomalies on aeromagnetic maps, a classification that can be extended to Fe–Ti oxide deposits worldwide. Bolle et al. (2014) also suggested anisotropy of magnetic susceptibility (AMS) analysis for studying the structural details of folding and stretching of a layered intrusion.

Magnetic properties of Fe-Ti deposits

The first group of Fe–Ti occurrences encompasses noritic rocks with relatively abundant coarse (multi-domain) magnetite and homogeneous (near-end-member) ilmenite. Ores from this group have high values of natural remanent magnetization (NRM) and magnetic susceptibility (K), coupled with low values of coercivity and Koenigsberger ratios (Q, the ratio of NRM to induced magnetization, i.e. K multiplied by the ambient magnetic field). They produce an induced-current magnetic response parallel to the Earth's present-day magnetic field, giving rise to positive anomalies on aeromagnetic maps. The magnetic properties of these rocks are dominated by magnetite; in particular, the viscous NRM behaviour is "more or less as predicted from the common behavior of multi-domain magnetite".

The second group of Fe–Ti deposits, with a magnetic signature drastically different from the former group, includes hemo-ilmenite rich noritic rocks and massive hemo-ilmenite ores, containing no or minor multi-domain magnetite. Rocks from this group have high NRM and Q values, and moderate to high coercivities and susceptibilities. They produce remanence-influenced to remanence-dominated anomalies, and are thus strongly dependent on the orientation of the Earth's magnetic field at the time of emplacement and cooling. The strong and stable NRM of this group primarily results from hemo-ilmenite; however, oxide exsolutions in silicates, chiefly exsolved blades and rods of hemo-ilmenite and/or magnetite with ilmenite oxy-exsolution in pyroxenes, may contribute significantly to NRM in some cases.

from *McEnroe et al. 2001*

Intrusion-hosted Fe mineralization types in Finland include mafic intrusion-hosted (Mustavaara) and alkaline intrusion-hosted (Otanmäki) V-Fe-Ti ore deposits. These are associated with strong magnetic responses. The Koivusaarenneva metallogenic zone contains ilmenite-rich gabbro intrusions and magnetite-bearing gabbros: magnetic and gravity anomalies have been used in their definition. The Koitelainen Cr, V, PGE deposits, associated with a mafic to ultramafic weakly magnetic layered intrusion, include two sulphide-free, PGE-enriched chromite reefs and a V-rich gabbro (Mutanen 1997).

The Misi Fe-deposits contain martitizied magnetite (Saltikoff et al. 2006, Niiranen et al. 2003). When magnetite is gradually replaced with martite (hematite), the effective magnetic grain size of magnetite decreases, resulting in an increased intensity of remanent magnetization, and this in turn is reflected in the magnetic anomaly signature. The magnetite destruction associated with magnetite oxidation and deep weathering to hematite is directly measurable as decreased magnetic susceptibility, and finally it may be that the iron ore deposits form clear magnetic lows.

The example Otanmäki V-Fe-Ti area (metallogenic zone F031 in Eilu et al. 2012) is characterized as follows (Fig. 6):

- magmatic vanadium-rich magnetite-ilmenite deposits in deformed and metamorphosed gabbros;

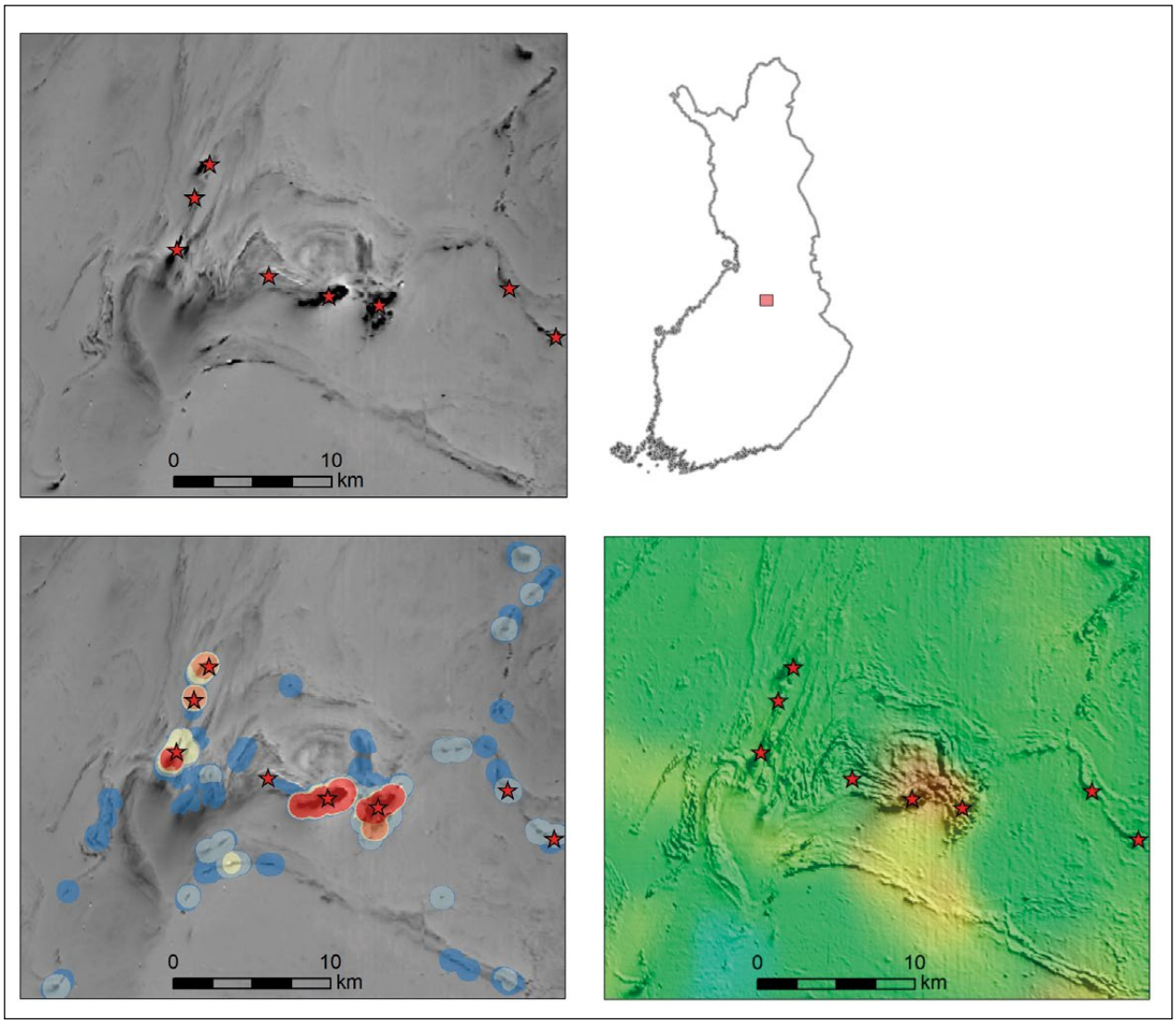

Fig. 6. The Otanmäki V-Fe-Ti area comprises local magnetic anomalies located along a regional gravity gradient zone (lower right). The outline of detailed maps is 40 km wide. Upper left: aeromagnetic map; lower left: magnetic anomaly classification with the magnetic derivative map as background. Mineral deposits from FODD (2013).

- in addition to ferrous metals, a potential source of REE, Zr and Nb in gneissic alkaline granitoids;
- Proterozoic rocks inside Archaean gneisses;
- introduce a local gravity anomaly north of the regional gravity gradient zone;
- magnetite-bearing units are distinguished by electromagnetic data.

Orogenic gold

Most of the gold in Fennoscandia is produced from orogenic gold deposits with gold as the main product. Orogenic gold deposits occur throughout the Palaeoproterozoic of southern and central Finland. However, a number of gold deposits may alternatively be classified as volcanogenic massive sulphides (VMS) or iron oxide-copper-gold (IOCG) or porphyry copper deposits, where gold is the by-product. These categories will be discussed separately later in this article. The undiscovered resources in orogenic gold deposits in Finland have recently been assessed by Eilu et al. (2015).

The physical properties of gold (Au), with a density of 19 300 kg/m3 and an electrical conductivity of 5·107 S/m, are one of the most anomalous of all elements. However, gold occurs in such low concentrations that it does not give any direct geophysical response, although the influences of geological processes that result in gold deposition may be detectable. A key element is to understand and detect the different types of gold deposits and their favourable geologic settings and controls at regional to local scales, especially in covered terrains (Robert et al. 2007, Hoover et al. 1995).

Orogenic gold deposits

These have occasionally formed from the Mesoarchaean to younger Precambrian and during the whole Phanerozoic eon. Orogenic gold occurrences are associated with processes involving the flow of sulphur-bearing hydrothermal fluids transferring a considerable amount of the leachable gold through major fault networks and along migration paths. Eventually, gold precipitates in secondary and tertiary fault zones in shallow areas of uplifting orogens (Goldfarb et al. 2001, Groves et al. 1998). Three main types of orogenic deposits are distinguished based on their host-rock environment: greenstone-hosted, turbidite-hosted, and BIF-hosted types. The dominant sulphide mineral is pyrite at greenschist grade and pyrrhotite at amphibolite grade. Ore bodies are surrounded by zoned carbonate-sericite-pyrite alteration haloes that are variably developed depending on the host rock composition. The ore bodies are associated with quartz veins, brittle faults, brittle–ductile shear zones and some strongly ductile shear zones. In greenstone belts, the significant vein deposits are typically distributed along specific regional compressional to transpressional structures (Robert et al. 2007).

Geophysically relevant minerals in gold deposits are pyrite, pyrrhotite and magnetite. The dominant sulphide mineral in metamorphic rocks is commonly pyrite at greenschist grade and pyrrhotite at amphibolite grade. At a regional scale, the majority of deposits are spatially associated with regional shear zones and commonly occur in greenschist to lower-amphibolite grade rocks, consistent with the overall brittle-ductile nature of their host structures. Alteration characteristics for orogenic gold deposits include Fe-Mg-carbonate alteration associated with magnetite destruction. The structural control of mineralization is characterized by fault or shear zones, especially with bends and intersections or culminations of anticlines, high-angle reverse faults or cross-structures. EM methods can also be used to map alteration, lithological contacts and faults. Regional potassium highs in radiometric data may indicate felsic magmatism, and local potassium highs with low Th/K may be associated with potassic alteration. For Au-quartz vein deposits, IP methods and gamma-ray spectrometry may be applied to map massive quartz veins (resistivity highs) and potassic alteration (potassium highs, respectively). Regional gravity lows over thick volcanic sequences or local gravity highs associated with felsic intrusions may indicate alteration.

Geophysical key factors or methods for gold deposits

Petrophysical data
These may be collected via borehole logging or hand sample analysis. Density, magnetic susceptibility, resistivity, chargeability and gamma radiation may be good indicators, depending on the contrast in physical properties of the mineralized and the unaltered country rocks. Petrophysical data have also been used at the regional scale, for example, to look at the effects of metamorphism on the geometry and geophysical response of greenstone belts.

Gravity methods
These are used at all scales from the identification of prospective gold districts to that of gold-related hydrothermal alteration at a local scale (from airborne gravity gradient systems to deposit-scale ground gravity). At a regional scale, gravity is an effective technique for defining the geometry and structure of greenstones belts. The structure and alteration can also be mapped.

Magnetic method
This provides information on geological units, faults, and shear and alteration zones that may control the mineralization. Magnetite destruction due to chemical alteration can be outlined from magnetic lows.

Radiometric data
These work well in defining chemically altered rock units if the alteration has introduced significant amounts of potassium, as is typical for orogenic gold systems. Uranium is generally mobile, leaving thorium behind.

Electric or electromagnetic methods
These are effective if sulphides are included. The conductive and chargeable sulphides are commonly associated with orogenic gold. Airborne electromagnetic methods reveal the geological framework or delineate zones of high conductivity within resistive mafic to ultramafic host rocks. The methods most successfully applied for gold exploration have been DC resistivity and induced polarization (IP). Other important electromagnetic methods used are VLF-R, SP and HLEM. Electromagnetic anomalies are caused by graphite, sulphides and fractures containing water. IP may detect disseminated sulphides and SP is used to map and classify conductive sulphide and graphite occurrences.

Seismic surveys
These are not widely applied in gold exploration. This is largely due to the complicated 3D geometry of lithological contacts and their often steeply dipping nature. In recent years, seismic surveys have nevertheless been used at local and regional scales to map the stratigraphy and structure in the appropriate geological settings.

Remote sensing
Very significant technological advances have been made in the last ten years in the field of infrared spectroscopy for alteration mapping. Satellite multispectral systems such as ASTER and airborne hyperspectral sensors such as Hymap have improved spatial and spectral resolution, higher signal-to-noise ratios, and wider spectral range coverage. Field portable hyperspectral instruments such as Pima have become standard tools for alteration mapping since they were first introduced to the mineral industry in the mid-1990s (Robert et al. 2007).

Archaean greenstone belts hosting orogenic gold in Finland are Tuntsa, Oijärvi, Suomussalmi, Kuhmo, Tipasjärvi and Hattu belt (Eilu et al. 2015, Airo 2007, Airo & Mertanen 2008). The magnetic anomalies of greenstones are generally of low intensity because of the deficiency of magnetite in greenstone grade mafic rocks. The effect of hydrothermal alteration on the petrophysical properties of ultramafic units in the Kittilä greenstone belt are described in *Insert 11*.

The Palaeoproterozoic Kittilä greenstones host several orogenic gold deposits (Eilu et al. 2015). The Kittilä and Salla greenstone belts, and Kuusamo and Peräpohja schist belts are all characterized by weakly magnetic host rocks. Petrophysical properties have been widely used in selecting the best methods for ground surveys in gold prospects of the Kittilä greenstone belt. For example, Salmirinne and Turunen (2006) reported detailed petrophysical investigations from Kaaresselkä and Loukinen. Results based on 24 drill hole sections below the ground water table displayed the difference between gold-bearing mylonites and other rocks. In the apparent resistivity and gamma radiation results, there were satisfactory differences between the two classes, but in the density, susceptibility and chargeability measurements, the distributions of the parameter values overlap too much for practical use in field exploration. The use of gamma radiation is insignificant in field mapping, as the radiation attenuates to zero within 30 cm of the source. However, in drill hole logging, the gamma radiation can be used to detect the potassic alteration zones that are commonly related to gold mineralization. Electrical and electromagnetic methods were best suited to gold exploration in the Kaaresselkä area. Results from Loukinen were based on 15 drillhole sections and showed a significant difference in chargeability between gold-bearing and other rocks. Another clear difference was in gamma radiation. Although the logged chargeability appears to be a very good parameter, the presence of black schists makes its use difficult in practice. There is incompatibility between the histograms of apparent resistivity and chargeability. It is not clear how the gold mineralization is related to black schists and sulphides, which can be detected with electrical methods regardless of the gold content. The chargeability works in much the same way, but is affected by polarization effects. For some reason, possibly mineralogical or structural, mineralized rocks polarize more than barren rocks. The overall result is that the induced polarization may be effective as a ground survey method, and gamma radiation in the logging environment.

The Palaeoproterozoic Svecofennian Häme and Pirkkala belts in southern Finland are highly prospective for gold (metallogenic zones F004, F007, F009 by Eilu et al. 2012). Insert 12 provides a regional overview of the geophysical data for this area, which is characterized by magnetic anomalies coinciding with conductivity anomalies. The magnetic and electrical signature is due to monoclinic pyrrhotite, which is the main ferrimagnetic mineral in this area. It also carries high remanent magnetization, which is why these anomalies are distinguishable. A regional gravity high is associated with migmatites, indicating a high metamorphic degree (also noted by Hölttä, unpublished information on metamorphic zones in Finland). Petrophysical properties produce mappable criteria for separating mineralized source rocks and barren intrusions (Mertanen & Karell, *p. 89*). Different rock types are clearly distinguished by their petrophysical properties.

Volcanogenic Massive Sulphides (VMS) (Cu, Zn, Pb, Au, Ag)

Volcanogenic massive sulphide (VMS) deposits are significant sources of Zn, Cu and Ag, Au and other metals. The most common sulphide mineral in VMS deposits is pyrite, which is often associated with other sulphides such as pyrrhotite, chalcopyrite, sphalerite and galena (Morgan 2012). Magnetite and hematite may also be associated. This combination of geophysically relevant minerals indicates that the VMS deposits are anomalous in most physical properties, including electrical conductivity, chargeability, density, magnetic susceptibility, natural radioactivity and acoustic velocity.

Insert 11.
Effect of hydrothermal alteration on gold-potential ultramafic rocks at Kettukuusikko site in northern Finland (Airo 2007).

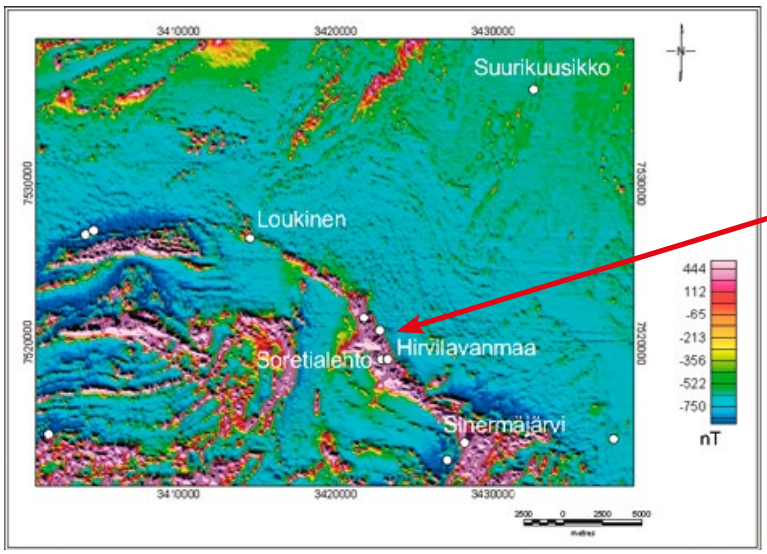

Aeromagnetic map showing highly magnetic ultramafic rocks at the southern boundary of Kittilä greenstones. Known gold occurrences are indicated.

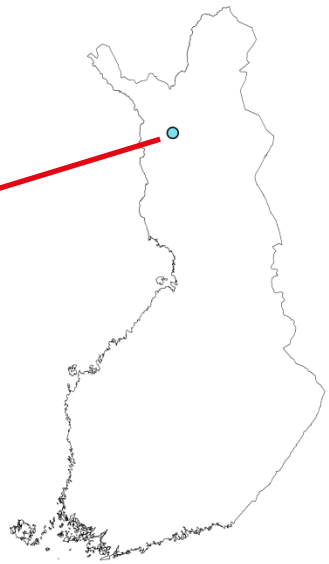

Kettukuusikko site.

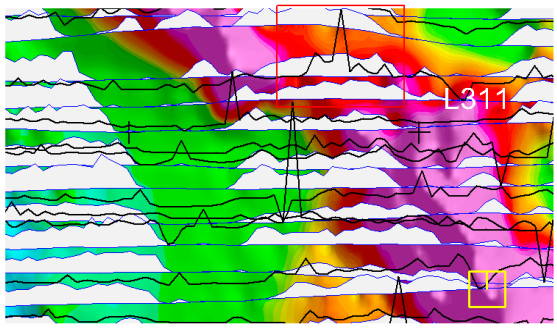

Detail of the Kettukuusikko site. Aeromagnetic grid + Potassium radiation profiles along survey lines. Line 311 is displayed as detailed panel on the right side.

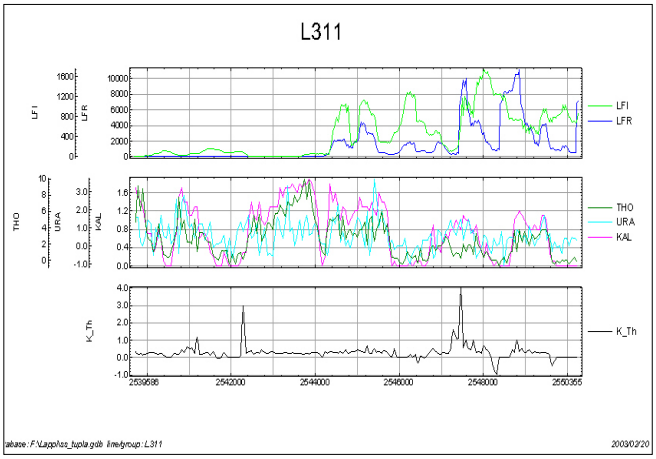

Electromagnetic (upper profiles) and radiometric (in the middle) data along flight line 311. K/Th (below) peaks at the contact of altered ultramafic unit and graphite-bearing volcanogenic schists.

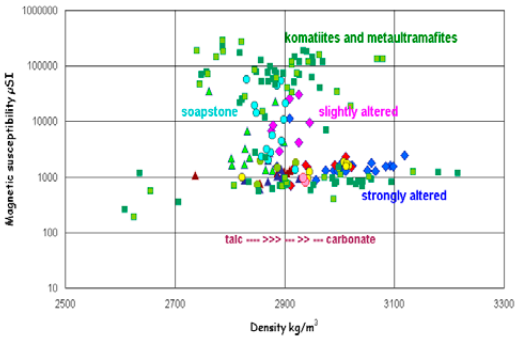

Talc-Carbonate alteration in the ultramafic unit: Decrease in magnetic susceptibility because of the destruction of magnetite. Densities grow because the released iron is incorporated with silicates and iron-bearing carbonates.

Characteristics of orogenic gold mineralisation in ultramafic rocks :

- **increased K/Th**
- **reduced magnetization**
- **electrical conductor in contact**

Insert 12.
Southern Finland, Svecofennian volcanic and schist belts prospective for orogenic gold, VMS and porphyry copper deposits. The geological map is based on the GTK in-house digital bedrock database (Geological Survey of Finland 2010).

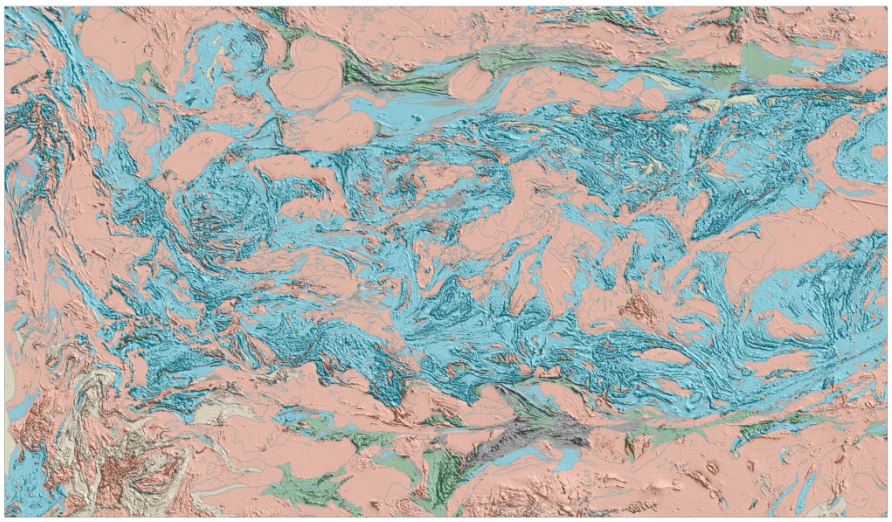

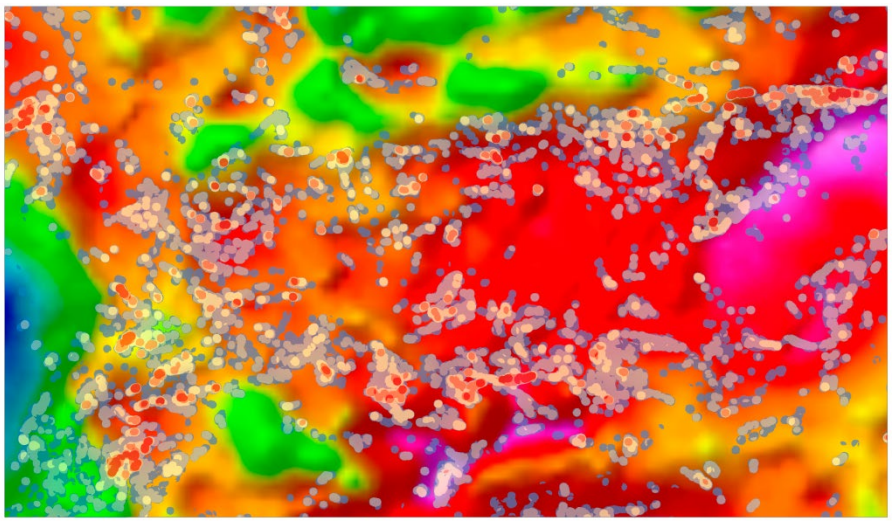

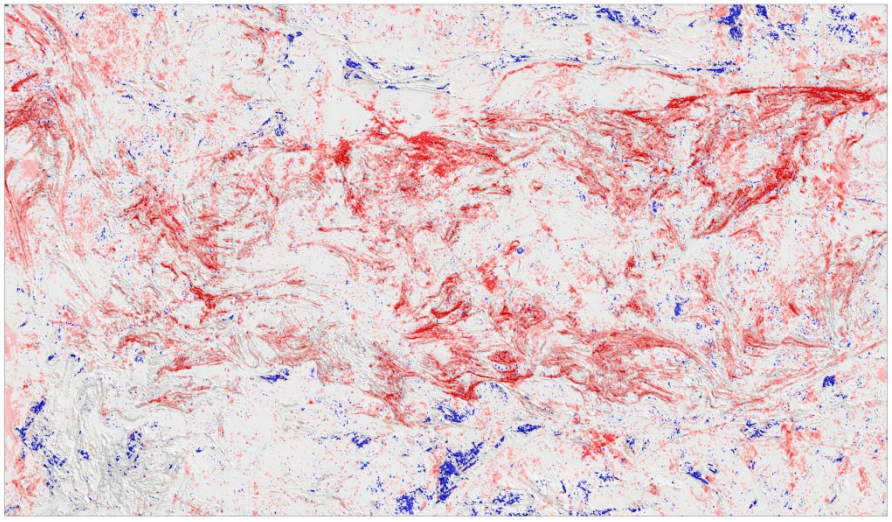

Map area is 170 x 100 km^2.

Bedrock (Digikp 2015)
- light blue = mica gneiss
- pink = granitegneiss
- green = volcanic rocks

Detailed magnetic anomalies are due to pyrrhotite in mica gneiss.
The positive regional gravity anomaly (in red) implies a high metamorphic degree of the migmatitic basin.

High amplitude magnetic anomalies outline the gravity high, and refer to more intense growth of monoclinic pyrrhotite along the margins of the basin, or thickening of magnetic rock units by tectonic processes.

Electrical conductivity aligns with magnetic anomalies of mica gneiss. Volcanic rocks are non-conductive.

Classification of electromagnetic real-component.
- red = conductivity
- blue = magnetite effect

VMS deposits

These occur in volcanic, volcaniclastic and sedimentary rocks and are typically lenticular in shape, and broadly stratiform. They form on and immediately below the seafloor, where discharging high temperature hydrothermal fluids are cooled through mixing with seawater or porewater in near-seafloor lithologies. This process occurs in association with synchronous volcanism and/or plutonism. The primary horizontal extent of VMS deposits varies from tens of thousands of square metres to giant dimensions of several square kilometres. The form of VMS deposits depends on the original hydrothermal geometry and on different post-deformations such as folding, faulting, and shearing. In areas with minimal deformation, deposits can correspond to sheets, layers, lenses, mounds, pipes, and stockwork forms. In deformed areas, the sulphide bodies can be complexly folded and dismembered. The diverse range of deposit morphologies, sizes and also compositions reflects the nature and duration of hydrothermal activity, the topography of the sea floor, footwall and host-rock lithology, temperature gradients, shearing, folding, and faulting, and the degree of erosional preservation. The VMS deposits are commonly developed in extensional tectonic environments, including both oceanic spreading zones and arc terranes. The age range is from the Archaean to modern actively forming deposits. (Galley et al. 2007)

The marked contrasts between the physical properties of minerals associated with VMS mineralization and their host rocks make VMS deposits ideally suited to geophysical exploration (Gibson et al. 2007, Gunn & Dentith 1997). Because all ore minerals in VMS mineralization have high density values, ground gravity surveys have been successful in several cases for first detecting and then delineating the shape and size of unexposed sulphide mineralization. Gravity surveys generally accompany other geophysical (magnetic, electrical, or electromagnetic) and geochemical surveys. They also help to delineate structural alignments or faults and identify structures that potentially provide structural control on the localization of sulphide-bearing ore bodies.

The electromagnetic method has been in a key role in VMS discoveries for decades. Electromagnetic techniques can directly detect conductive base metal deposits. Significant contrasts in conductivity values commonly occur between the ore bodies and their resistive host rocks. Both airborne and ground electromagnetic techniques are effective in detecting massive sulphide mineralization, but only if the sulphide grains in the deposit are electrically connected. When there is a lack of electrical connection, induced polarization can be successfully employed to detect the disseminated sulphides. High-resolution magnetic data can be an excellent tool in identifying the broad geological framework of an area and often show contrasting patterns that reflect differences in lithological compositions, crustal structures, and the type and degree of alteration. There is evidence that sufficiently massive sulphide ores might also be detectable as reflectors revealed in large-scale reflection seismics due to their high acoustic impedance, although the majority of reflectors are due to lithological contacts. Thus, seismic profiles may yet prove useful in direct exploration.

Volcanogenic massive sulphides were the original reason for the development of airborne electromagnetic exploration in Finland. Highly conductive sulphides in massive lenses and combined with base metals (copper, lead, and zinc) may be detectable at great depths with airborne EM. In Finland, the known sulphide deposits are related to steeply dipping or nearly vertical structures, close to the surface. GTK decided to develop its own frequency-domain electromagnetic system with the idea of conducting similar surveys systematically throughout the whole country. The history of this development work is reviewed by Peltoniemi (2005). VMS deposits in Finland have been the most important source for zinc and the second most important source for copper, after the Outokumpu-type deposits. These two deposit types have produced over 90% of the total cumulative production of zinc and copper in Finland (Rasilainen et al. 2014).

In Sweden, the Skellefte mining district includes over 85 VMS deposits that contain the commodities Zn, Cu, Au, Ag, and Pb, and whose geophysical characteristics have been thoroughly investigated.

The deposits are generally characterized by higher magnetic susceptibility, density, chargeability and conductivity than many other rocks (Tavakoli 2012, Carranza & Sadeghi 2010). The VMS deposits are mainly hosted within a volcanic sequence consisting of felsic to intermediate juvenile volcaniclastic rocks, lavas and subvolcanic intrusions. To create a 3D geological model extending to a depth of 10 km, Tavakoli (2012) utilized known geology, petrophysics, seismic reflection data, magnetotelluric (MT) and gravity and magnetic data. Seismic interpretations supported potential field methods for investigating the structure of the key geological contacts and lithological units. Shallow and deeper 3D resistivity and IP investigations (down to ~2.2 km depth) were used for locating previously unknown VMS deposits.

Geophysical key factors for VMS systems

Gravity signature
In general, the VMS-related minerals and ores have high density contrasts with their host rocks. The most common sulphide mineral in VMS deposits is pyrite, which is often associated with other sulphides such as pyrrhotite, chalcopyrite, sphalerite, and galena. Other possible non-sulphide minerals associated in VMS deposits include magnetite, hematite and barite, with densities comparable with most sulphides, and graphite with a typically much lower density (~2.5 g/cm^3).

Magnetic signature
Sulphides with high values of magnetic susceptibility (monoclinic pyrrhotite) are associated with VMS ore bodies. Additionally, non-sulphide metallic minerals with high susceptibility values, such as magnetite (55 000 × 10^{-6} SI) and hematite (40 000 × 10^{-6} SI), may also be common in some massive sulphide deposits and contribute to the strong positive magnetic anomalies. The susceptibility of pyrrhotite is approximately one-tenth of the susceptibility of magnetite. Both of these minerals have high induced magnetization, but pyrrhotite may frequently also have significant remanent magnetization. Magnetite in VMS deposits typically occurs in the core of the stockwork and central basal part of the overlying sulphide lens. Furthermore, magnetite and hematite are common minerals in iron-formation deposits that can be temporally and spatially associated with VMS deposits. Other common sulphide minerals in VMS deposits, such as chalcopyrite, sphalerite and galena, have lower values of magnetic susceptibility that are similar to those found for their sedimentary and volcanic host rocks and thus do not contribute to any magnetic anomaly associated with the VMS ore body. Sphalerite, the most commonly mined Zn-bearing mineral, is not magnetic, is very resistive, and has a relatively low specific gravity.

Electrical signature
Electrical and electromagnetic methods are highly effective in VMS exploration, and various EM techniques are currently used in surveying for VMS deposits. IP methods are also widely used: both massive and disseminated sulphide ores commonly have a high chargeability. Most sulphide minerals, with the exception of sphalerite, are good to excellent conductors, and thus in theory would be easily distinguished from the host rocks by EM methods. Compared to igneous and metamorphic rocks with typical conductivities of <1 mS/m and sedimentary rocks with conductivities from 1 to 500 mS/m, the contrast between VMS deposits and their host rock may be significant (Morgan 2012). Some types of VMS deposits are typically associated with reducing sediments. Noneconomic pyrite-rich or pyrrhotite-rich deposits are not distinguishable from potentially economic deposits, so conductivity and other electromagnetic techniques are not fully definitive exploration tools in VMS exploration.

Graphite has conductivity values similar to sulphide minerals. Anoxic sedimentary rocks that contain graphite or sulphide (metamorphosed black shales in Finland) are also highly conductive, and distinguishing them from massive sulphide deposits may be demanding. The bulk conductivity of deposits may vary

greatly depending on many factors (e.g. deposit geometry, connectivity of electrical conductors – partly dependant on ductility of the material, metamorphic history and tectonic events), so that unlike density, for instance, the conductivity of the ore is not directly proportional to relative mineral concentrations. Under some conditions, massive ores that should be conductive may become resistive and vice versa, some deposits with low sulphide content can be quite conductive. Cu-bearing VMS ores are likely to be more conductive than sphalerite-rich Zn ores. For non-conductive Zn-rich sphalerite deposits in general, IP has been the most successful exploration technique, although EM might perform better, as other sulphides may actually still produce an anomaly. The water content greatly influences the conductivity of a unit. Saturated overburden may produce conductivity values that effectively mask the EM of the VMS mineralization (Thomas et al. 2000).

Radiometric signature

Although no direct indication of VMS ore can be predicted in the natural gamma-ray radiation elements potassium (K), thorium (Th) and uranium (U), some evidence of hydrothermal alteration related to mineralization process (VMS or any other) may be present in the case of shallow deposits (the gamma-ray radiation emits from the upper 0.5 to 1 m of the surface). The processes related to hydrothermal alteration can result in changes in the respective ratios of radiometric elements; K is most often affected by the processes, whereas Th is less often affected and U only rarely. In the case of no weathering or very active mineralizing fluid (causing K depletion), the amount of K is usually increased in the processes (Dickson and Scott 1997). Thus, a ratio of K/Th (or Th/K) could be used in exploration to detect the alteration halos related to mineralization. The origin of such anomalies can be ambiguous and needs to be cross-referenced with topographic and lithological data.

Seismic techniques

Velocities of the most common sulphide minerals are quite variable and range from 8.04 km/s (kilometres per second) for pyrite to 4.68 km/s for pyrrhotite. In comparison, the measured densities are 5.02 g/cm^3 for pyrite to 4.63 g/cm^3 for pyrrhotite. Ore minerals associated with pyrite-dominated ores increase in velocity with increasing density, whereas sphalerite-, chalcopyrite-, and pyrrhotite-dominated ores typically have velocity values that decrease with increasing density. Host rocks have a much narrower and lower range of density values and have a wide range of velocities. Seismic reflectivity is controlled by several factors, but one dominant factor is the difference in impedance between lithologies (Salisbury et al. 1996). Impedance is defined as the product of density and compressional wave velocity in a given material. Measurements of the specific gravities and velocities of common silicate rocks and ore minerals indicate that ore minerals have significantly higher density values and a broad range of velocities, and therefore tend to have higher impedances than their host rocks. The difference in the impedance value between the ore body and its host rock can be significant enough to result in high amplitude reflections and identification of the ore body.

In Finland, zinc deposits of possibly VMS category occur in three main geological settings: in Palaeoproterozoic Svecofennian arcs, in Palaeoproterozoic rifts and in Archaean greenstone belts. Vihanti, Pyhäsalmi and Rauhala belong to the group of Svecofennian VMS deposits in central Finland and resemble the Skellefte ore field in northern Sweden. Another group of this kind is located in southwestern Finland, where Orijärvi, Aijala and Metsämonttu have many similarities with the Bergslagen region in Sweden. If VMS deposits are classified into mafic, bimodal-mafic and felsic types (Rasilainen et al. 2014), Pyhäsalmi represents the felsic type. VMS deposits do not necessarily produce any significant airborne geophysical expression, as can be seen, for example, for the Rauhala deposit in Figure 7.

Hammaslahti is an example of rift-related zinc deposits in southeastern Finland. This sediment-hosted massive sulphide Cu-Zn-Au deposit has

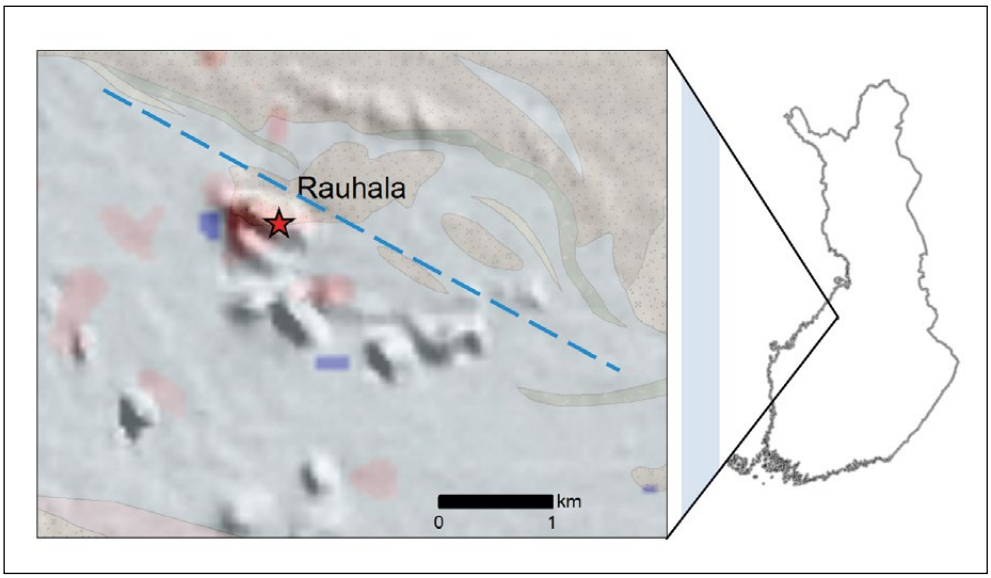

Fig. 7. The Rauhala VMS deposit is situated along a regional NW–SE-oriented fault (blue dashed line) and has weak magnetic and conductivity signatures. Magnetic derivative with a background geological map, based on the GTK in-house digital bedrock database (Geological Survey of Finland 2010) and the electromagnetic ratio as an overlay (conductivity anomalies in red).

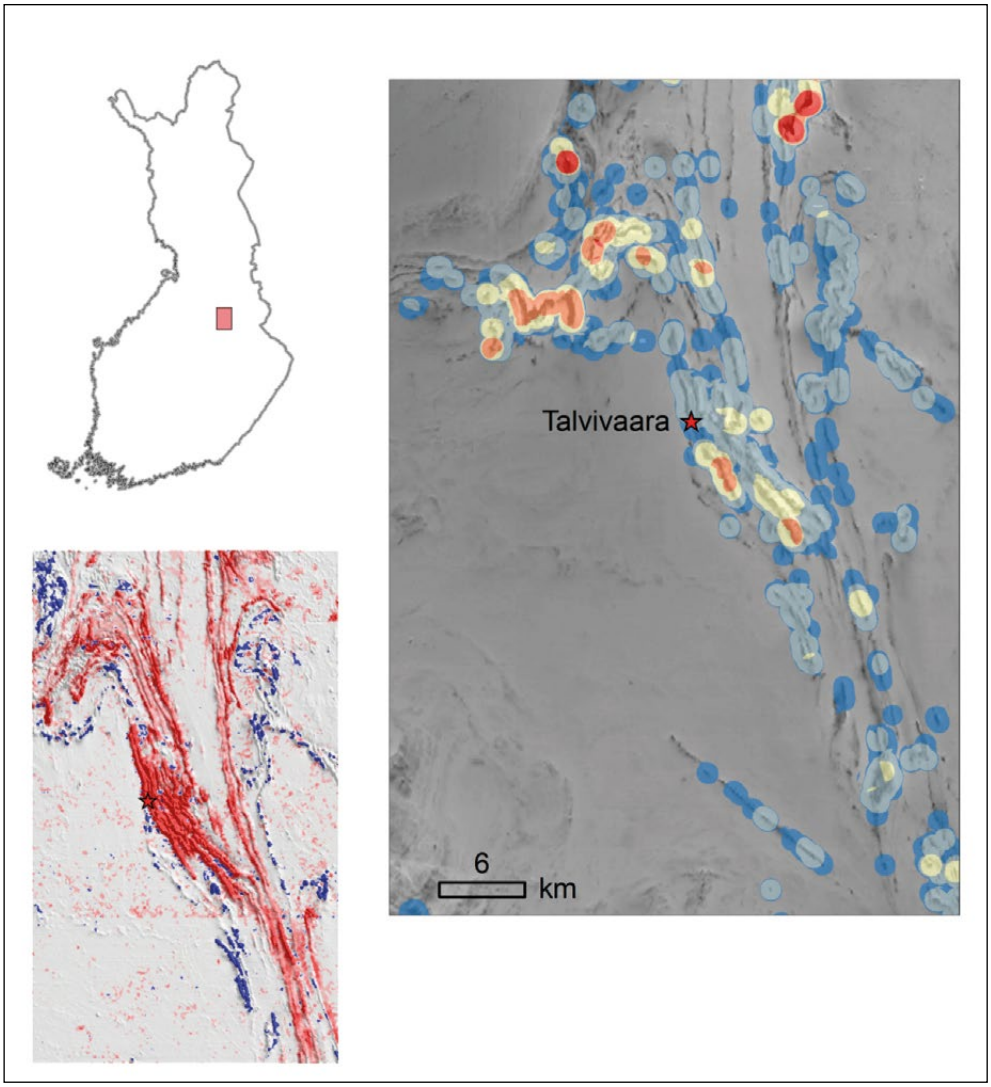

Fig. 8. The black schist-hosted Talvivaara Ni-Zn-Cu-Co sulphide deposit in eastern Finland.
Left: Conductivity anomalies (in red) are enhanced on the basis of AEM classification.
Right: Magnetic anomaly classification (see colour scale in Insert 5).

been regarded as either of the SEDEX or mafic VMS style. Two-phase pyrrhotite, a hexagonal form together with the monoclinic type, has been reported by Airo & Karell (2001).

The Häme belt in southern Finland is considered to be highly prospective for VMS deposits. Leväniemi & Karell (2013) describe geophysical indications of possible VMS targets in the Häme belt and give an appraisal of how regional datasets work in VMS exploration. They describe geophysical characteristics for several deposits and present new petrophysical data measured from drill cores. *Insert 12* presents a regional overview of the magnetic, gravity and electromagnetic data from the Häme-Pirkkala area. The folded, small-scale magnetic anomalies in migmatitic rocks are due to pyrrhotite, probably of metamorphic origin. Electrical conductivity anomalies coincide with magnetic anomalies. The migmatitic rocks form a basin that is associated with a positive regional gravity anomaly (in red), also implying the high metamorphic degree of the area. High amplitude magnetic anomalies are found surrounding the gravity high, referring to more intense growth of monoclinic pyrrhotite due to tectonic processes along the margins of the basin.

The graphitic shale-hosted Talvivaara Ni-Zn-Cu-Co deposit in eastern Finland is one important resource of copper and zinc. It is hosted by Palaeoproterozoic (2.1–1.90 Ga) carbonaceous metasedimentary rocks of the Kainuu schist belt (Loukola-Ruskeeniemi & Heino 1996, Loukola-Ruskeeniemi 1999). More than 20 occurrences and one operating mine of Talvivaara-type metal-enriched black schists (metamorphosed carbonaceous muds) occur in 2.0 ± 0.1 Ga sequences of metasedimentary

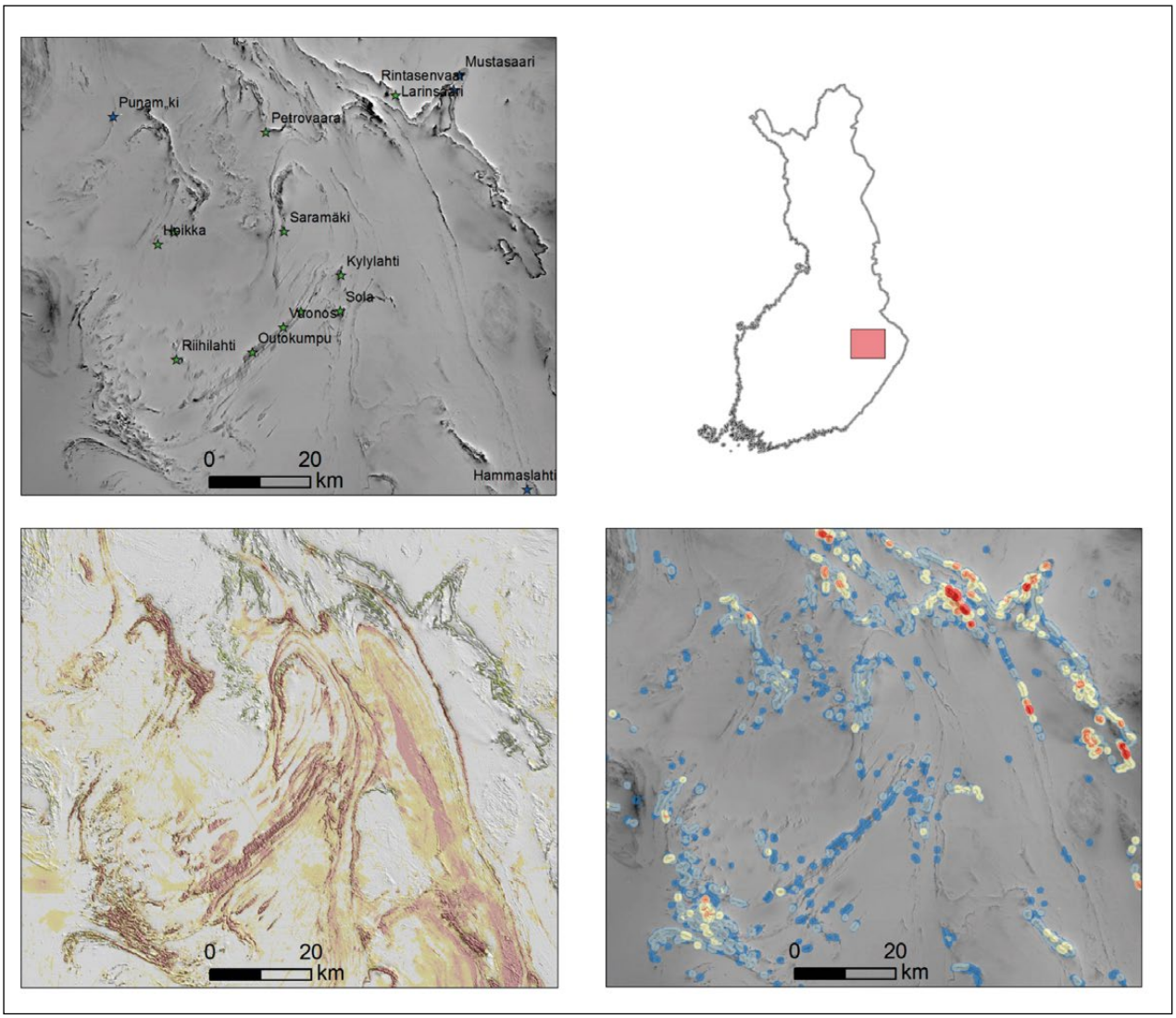

Fig. 9. Outokumpu-type Cu-Zn-Co deposits (green = Cu, blue = Zn). Upper left: Aeromagnetic map (Mineral deposits FODD 2013); lower left: conductivity anomalies (in red), enhanced on the basis of AEM classification; lower right: magnetic anomaly classification (see colour scale in Insert 5).

rocks in the Kainuu and North Karelia schist belts (brief description in Rasilainen et al. 2012). The highest and the most uniform concentrations of base metals in the Talvivaara-type deposits occur in pyrrhotite-dominated parts. Geophysical signatures of Talvivaara include moderate magnetic anomalies due to monoclinic pyrrhotite, high-intensity conductivity anomalies and U radiation revealed by airborne radiometric data (Fig. 8). U-radiation values are typically high along the regional crosscutting faults, referring to enrichment of uranium. Organic materials, clay minerals, Fe^{3+}, Mn and Ti also have a role in the enrichment of U (Airo & Hyvönen 2008).

The Cu-Zn deposit types in Finland where copper, zinc or both occur as main commodities are VMS deposits, porphyry copper deposits and Outokumpu-type Cu-Zn-Co deposits (Fig. 9). All the known Finnish Outokumpu-type deposits occur in a rather restricted area in eastern Finland. Petrophysical properties of the Outokumpu Deep Drill Core have been reported by Airo et al. (2011).

Banded iron formations and IOCG-style FeCu, Au

The magnetic signature of iron deposits depends on whether the mineralization is in the form of magnetite or hematite. The presence of strong remanent magnetization, demagnetization, and the markedly anisotropic nature of the magnetic properties of banded iron formations (BIF) may complicate the interpretation of magnetic surveys (Hagemann et al. 2007).

Banded iron formations
are usually associated with Precambrian (Archaean to earliest Palaeoproterozoic successions) sedimentary sequences, which typically contain shales, dolomites and volcanic mafic rocks. The presence of a large supply of iron in ocean water from hydrothermal sources was one reason for the global accumulation of BIFs in the Precambrian period. Favourable structures for BIF-hosted gold deposits are fold hinge zones or faults, or shear zones intersecting an iron formation, and their alteration style is chlorite-carbonate or amphibole alteration and sulphidation of iron formation. Geophysical tools are used in structure mapping, identification of stratigraphy and faults controlling fluid movement, and finally in direct detection.

Geophysical characteristics of BIF

Magnetic method
- traditionally, the magnetic method is used to map the magnetite rich rocks that host the deposits
- iron oxides may be strongly magnetic (remanent magnetization)
- magnetite destruction associated with magnetite oxidation and deep weathering to hematite and resulting in low magnetic anomaly intensity
- destruction of magnetic anisotropy or magnetic fabrics
- obligatory for structural and stratigraphy mapping

Gravity method
- airborne gravity gradiometry systems, but ambiguity in the density contrast
- density of magnetite and hematite >5 g/cm^3

Radiometric method
- at a local level, the down-hole radiometric method is most useful: lithological information
- airborne radiometric measurement to assist in structural and stratigraphy mapping

DC resistivity, induced polarization, electromagnetic and seismic methods
- mainly as problem-specific solutions; stratigraphic and structural mapping with magnetics
- conductivity of iron formation: min 0.05 – max 3300 mS/m (Morgan 2012)
- frequency domain EM: the ability to differentiate magnetite
- deeper looking: airborne transient electromagnetic method (TEM)

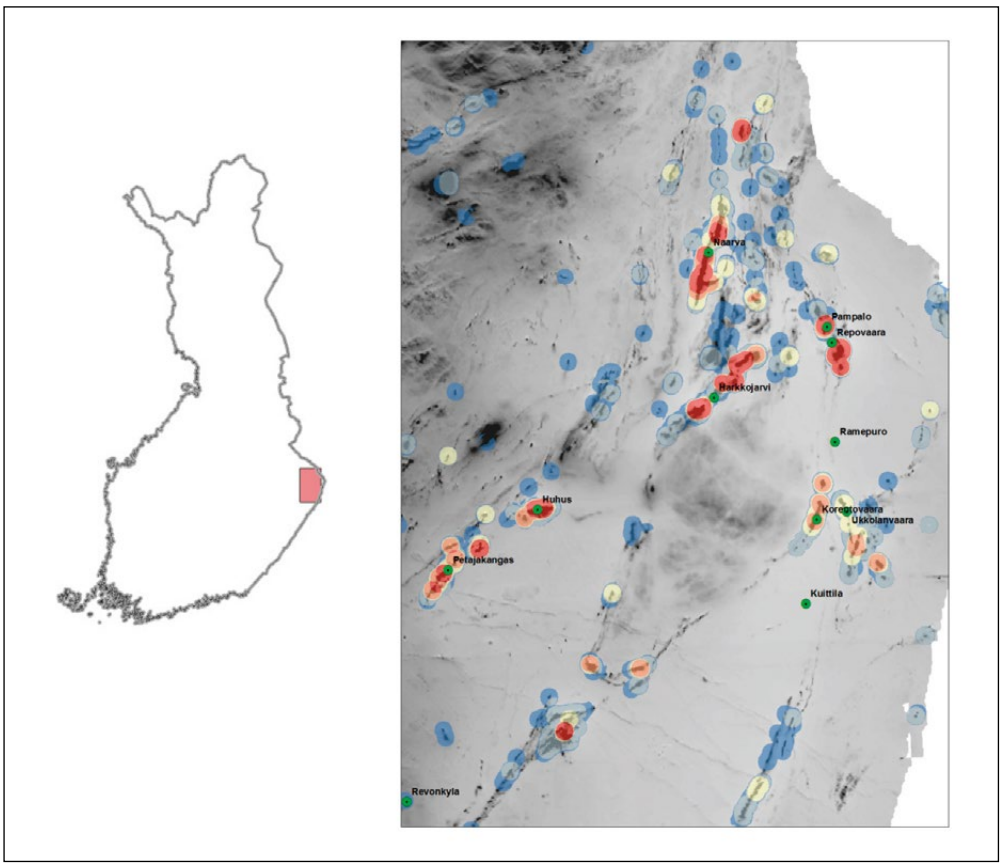

Fig. 10. Magnetic anomaly classification of the Hattu belt. The map area is 50 km wide. Colour categories are explained in Insert 5.

In Finland, the Huhus Fe area as part of the Hattu belt contains banded iron formations (BIF) of Archaean age (Sorjonen-Ward & Luukkonen 2005), where the Fe deposits have been delineated by their geophysical indications. Magnetic anomaly classification (Fig. 10) shows the distribution of the BIFs as high-amplitude anomalies. High-amplitude magnetic anomalies also characterize the Misi area in Figure 11 (F039 by Eilu et al. 2012, Niiranen et al. 2003). In southern Finland, Fe mineralizations of skarn and banded iron formation types occur as part of the Orijärvi Zn-Cu-Pb+Fe zone (Saltikoff et al. 2006). They belong to the same type as the Zn-Cu-Pb and Fe deposits of the Bergslagen province in Central Sweden.

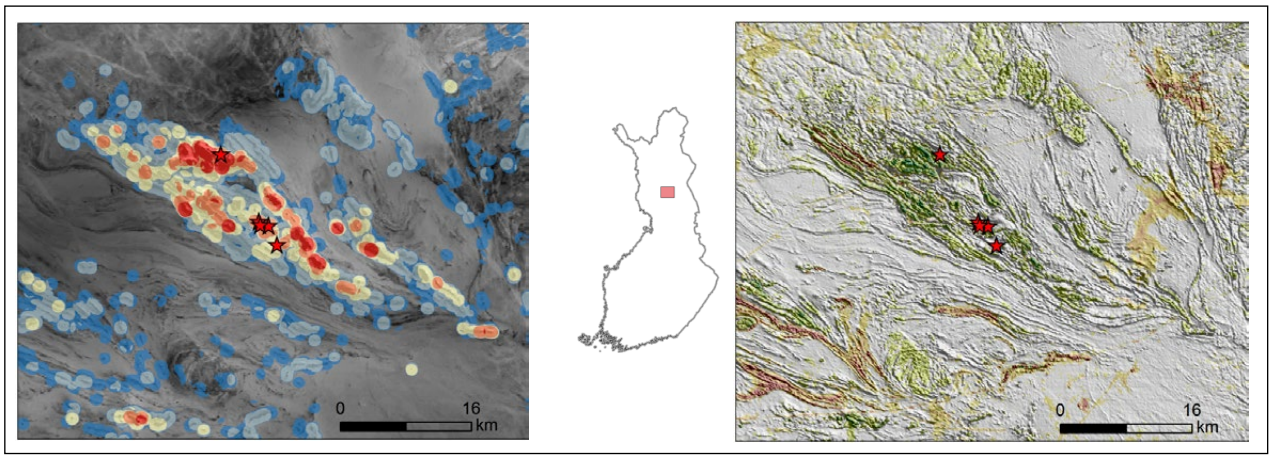

Fig. 11. Misi area: magnetic anomaly classification (left), colour categories are explained in Insert 5; electromagnetic classification (right), red = conductive, green = magnetite.

IOCG deposits
have been successfully explored by magnetic, gravimetric, electrical and radiometric methods. However, the complex structure and diverse materials complicate geophysical interpretation. The IOCG districts are well controlled by structural and/or stratigraphic factors with ore occurrences typically confined to fault bends, shear zones, rock contacts, breccia bodies, or as lithology-controlled replacements, and they are associated with extensive prograde and retrograde alteration (Groves et al. 2010). IOCG-related hydrothermal systems share certain distinguishing features, notably including (1) extensive alkali-rich alteration, (2) voluminous low-Ti magnetite and/or hematite, (3) a distinctive suite of minor elements (REE, Co, Ag, ± U, P), and (4) prominent structural control.

Exploration methods presently utilized include regional geology, detailed geological and alteration studies, airborne and ground geophysics (gravity, magnetic, radiometrics, induced polarization and electromagnetic) and geochemistry (Smith 2002, Barton & Johnson 2004). A Titan-24 array magnetotelluric survey has been successfully used to locate conductive bodies at greater depth. However, even in ideal cases, geophysical interpretation can be complicated by the varied and complex origins and fates of Fe oxides, Cu-Fe sulphides and alteration minerals.

Geophysical footprints of iron-oxide Cu-Au (IOCG) deposits

- Fe-rich host rocks; the abundance of iron oxides (magnetite or hematite) produces very strong magnetic anomalies
- Typical ore minerals: magnetite, pyrite, pyrrhotite, Cu sulphide
- A deficiency or irregular presence of sulphides, but generally highly conductive
- Widely developed hydrothermal alteration (commonly U and Th)
- Regional albititisation; potassic and sericitic alteration may be detectable with a gamma-ray spectrometry survey;
- Local alteration: Fe-, Na-Ca- and K-metasomatism
- Crosscuts the primary bedding and is associated with shear zones; are associated with coincident magnetic and gravity highs
- In Finland, close to the Archaean/Proterozoic boundary (±100 km).

after Barton & Johnson (2004)

In Finland, well-known deposits include Hannukainen and Rautuvaara in western Lapland, and Vähäjoki in southwestern Lapland (Billström et al. 2010). Magnetic anomaly classification in *Insert 5* indicates many of the known IOCG prospects that are located around the granitoid massif in central Lapland. In northern Sweden, apatite-Fe ores, porphyry-Cu and Fe oxide Cu-Au deposits have been proposed to be related (Sandrin et al. 2007). The famous Kirunavaara and Malmberget mines belong to the apatite-Fe subclass, and have been producing around 31 Mt of ore per year during the last 100 years.

Petrophysical properties of rock samples representing various mineral deposit types, including magnetite-type IOCG mineralization, were investigated for comparison of their associated airborne geophysical signatures (Airo & Säävuori 2013). A dominant remanent magnetization component was verified for magnetite-type IOCG test samples as having high Q-ratio values. This knowledge was used in the method for magnetic anomaly detection by classifying magnetic anomalies (Airo et al. 2014).

Porphyry Cu-Au

Porphyry deposits are igneous in nature, and may have a cylindrical or torus shape, thus in an ideal case producing a near-circular geophysical response. The porphyry deposits are the largest source of copper and molybdenum in the world and a significant storage of gold and silver. The porphyric systems have been formed from the Archaean to the Quaternary in age. Large economic deposits of Cu and Mo are associated with these intrusives in South America, Asia and North America, and the geophysical properties of this type are well documented. In a general sense, magnetic field data delineate the geological structure relatively well, and are best suited for this purpose. While the main economic mineralization may only be moderately conductive, the pyrite halo and secondary mineralization may be very conductive, and could be an excellent EM target. The large size of the intrusives could make them excellent targets for regional mapping. Radiometric and hyperspectral surveys can be useful in arid climates to aid in identifying the lithology and search for characteristic alteration minerals. Interpretation may require a solid understanding of the expected alteration patterns rather than the actual ore mineralization distribution.

Porphyry deposits
are generally related to shallow located intrusive complexes and underlying plutons and batholiths, where volcanic rocks typically have dioritic to granitic compositions. Porphyry systems are surrounded by different rock types such as igneous, sedimentary and metamorphic rocks. The deposit grade can be raised by the presence of a particular lithology of the hosted rocks. For instance, the concentration of high-grade ore can be formed in carbonate successions (especially like marble) or other fine-grained and low-permeable rocks that may seal a porphyry deposit all around. Lithological clusters, which are rich in ferrous iron, can also assist in high-grade porphyry mineral accumulation. Porphyry districts are associated with the subduction of submarine ridges and seamount chains, and oceanic plateaus beneath continental arcs. (Sillitoe 2010)

Summary of general geophysical properties:

- to some extent magnetic: contrast positive or negative, depending on host rock magnetization;
- potassic intrusions, hydrothermal (potassic) alteration zones, are in an ideal case detectable by the radiometric, and even the aeroradiometric method;
- disseminated sulphide mineralization: IP method;
- circular shape (if no tectonic deformation) possible to distinguish by pattern recognition.
- Oasis montaj offers software system (CET porphyry analysis, 2012) to analyse the shape of gridded geophysical anomalies to detect near-circular, symmetrical features of a given range.

These intrusion-related gold-copper occurrences are associated with syntectonic granitoids in and close to the Archaean-Proterozoic margin, for example Kopsa in central Finland. A suspected occurrence is Kedonojankulma in the Häme belt (Mertanen & Karell, p. 89, Kuosmanen et al., p. 117). Neither of these possesses any clear or detectable signature in airborne geophysics. The open pit mine of Aitik (Gällivare, Sweden) is a major Cu-Au producer and the only sizable porphyry-Cu deposit presently mined in Sweden.

Insert 13 shows an example of a circular magnetic anomaly ring (visual inspection) surrounded by magnetic and radiometric haloes (potassium and uranium radiation data). This type of combination would be a typical geophysical signature for porphyry systems; so far, no deposit has been identified at this site.

Geophysical key factors for Cu-Au porphyry deposits

Magnetics
Many of the intrusive complexes driving porphyry mineralization will to some extent be magnetic and will contrast either positively with volcanic and sedimentary country rocks, or negatively with highly magnetic volcanic country rocks. Hydrothermal alteration in porphyry systems can provide distinct signatures, for instance, magnetite in K silicate alteration zones in the core of the system, intense magnetite replacement in peripheral skarns, and magnetite alteration or destruction in volcanic rocks adjacent to intrusions.

Radiometrics
Radiometric data, usually collected in conjunction with magnetic data during airborne surveys, are an excellent aid to geological mapping. In porphyry settings, a radiometric survey can quickly identify both potassic intrusions and potassic alteration zones if they are at the surface. Generally, however, in areas of good outcrop, these indicators have already been detected by geological work, so surface radiometric methods have rarely had a major role in porphyry exploration.

Gravity
The porphyry model can be used to predict that there may be significant, sharp density contrasts between intrusive and country rocks, but that recognizable contrasts related directly to alteration and mineralization are much less likely because these features usually have a disseminated character and diffusive boundaries.

Induced polarization (IP)
IP is particularly suited to detecting large bodies of disseminated sulphide mineralization and, if used extensively, to producing a three-dimensional sulphide distribution map of a prospect area. It is an excellent method for detecting subsurface phyllic zones within porphyry systems, because these zones usually have the highest sulphide content, mainly pyrite.

Electromagnetic (EM) methods
EM methods have not been extensively used in porphyry exploration. Conductivity contrasts tend to be moderate and diffusive in the porphyry environment, and resistivity has always been an accessory measurement during IP surveys for porphyry exploration, but it has not been a significant discovery tool. A recent development is the co-acquisition, during distributed acquisition IP surveys, of DC resistivity and magnetotelluric (MT) resistivity data. Combined TDEM and magnetic surveys and inversion of electromagnetic data have been used to locate conductive bodies >400 m below the surface. 3D inversion of time-domain airborne EM data, combined to ZTEM airborne audio-frequency magnetics, has recovered conductors coincident with alteration (Pare et al. 2012).

Seismics
The use of seismic methods is rare in porphyry exploration. It is possible that the use of seismic methods will increase in covered areas where strata generally dip less than 45°, with the aim of determining the cover thickness, volcanic architecture beneath the cover and overall structural architecture.

Spectral scanning methods
Airborne multi-spectral scanning methods have also not had a major role in porphyry exploration, although this technique can discriminate complex phyllosilicate alteration assemblages efficiently, something which can be very important in porphyry lithocap settings. The more standard approach in these settings is to use hand-held devices on rock samples and drill cores. A significant development in this direction is the HyLogger™, a semi-automated core-logging device that combines rapid hyperspectral mapping of mineralogy and very high resolution imaging of cores (Huntington et al. 2006). The device can identify phyllosilicates, amphiboles, carbonates, sulphates and iron oxides, and with the recent addition of scanning in the thermal infra-red spectral range will recognize quartz, feldspars, garnets, olivines and pyroxenes. The ability to rapidly (~100 core trays per day) and objectively collect such data and

then interpret these data in terms of alteration zones utilizing the porphyry model would be a significant advance for exploration targeting in an advanced porphyry exploration project, and may be of particular benefit for targeting mineralized zones within or beneath lithocaps.

after Holliday & Cooke (2007)

Insert 13.
Example of a circular magnetic anomaly surrounded by magnetic and radiometric haloes (potassium and uranium radiation data). This type of combination would be a typical geophysical signature for porphyry systems or an impact crater.

Magnetic field derivative enhances shallow structural features. Radiometric data sets were improved by masking out the low – value noise that may be due to wet areas. Electromagnetic ratio map (the ratio of the real to the imaginary component) reveals magnetite bearing units in blue. The geological map is based on the GTK in-house digital bedrock database (Geological Survey of Finland 2010).

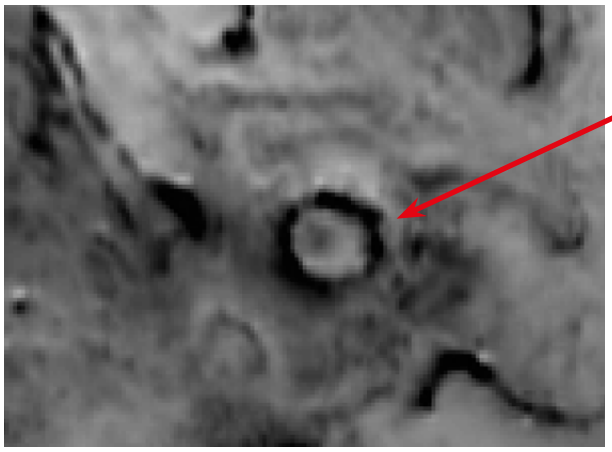

Magnetic field (total intensity). Positive anomalies are dark. The map area is 8 km wide.

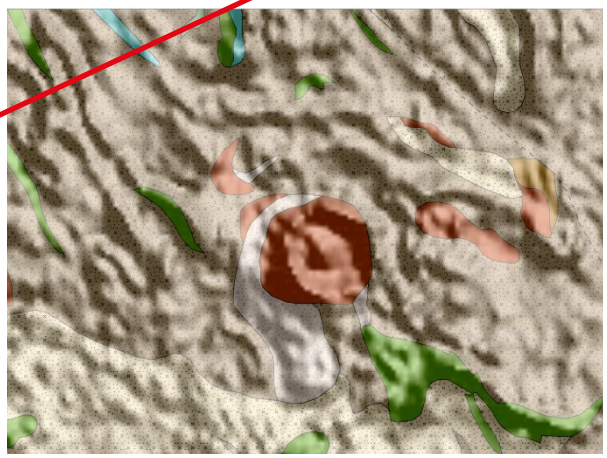

Bedrock (Digikp2015) + Magnetic field derivative. Brown = gabbro, green = volcanic rock.

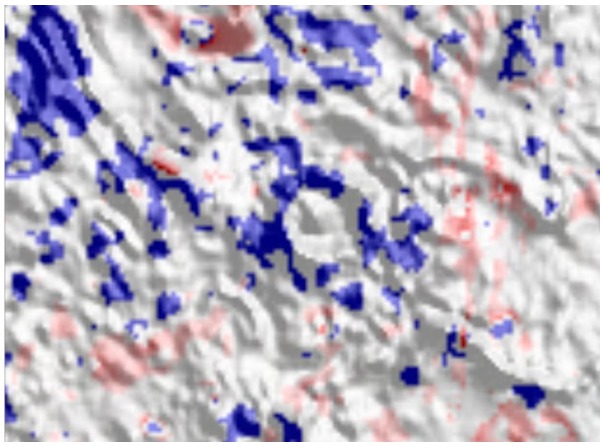

Electromagnetic ratio Re/Im + Magnetic field derivative. The magnetic ring is caused by magnetite.

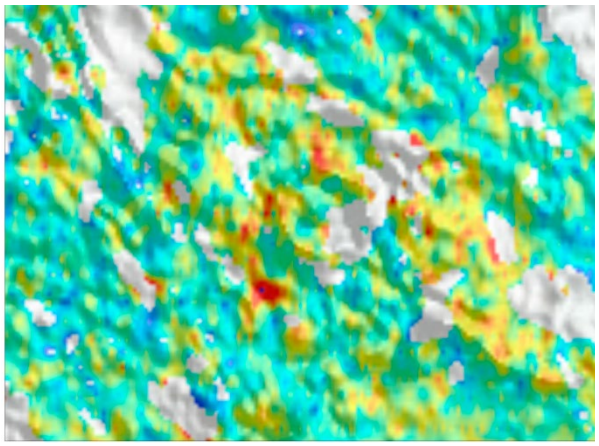

K (potassium) + Magnetic field derivative. High K radiation (in red) around the magnetic ring.

High-tech minerals and uranium

The discussion here includes so-called high-tech metals (Nb, Ta, In, REE), rare-element pegmatites (Li) and uranium (U). Rare earth metals are characteristically associated with carbonatitic and alkaline intrusions, pegmatites and intrusive dykes. The discovery of intrusion-related rare earth metals has been based on a variety of exploration techniques and occasionally by chance. Geophysical methods are successful only if there is a sufficiently large contrast in the rock properties of the investigated geological units. For example, indium (In) may occur with base metal sulphides so that conductivity might be observed. Intrusive carbonatites typically show concentric zoning of carbonate and alkalic rocks. Variable concentrations of magnetite in these zones produce strong magnetic anomalies dominated by remanence, such as Nb and REE-bearing Sokli carbonatite in northern Finland. Uranium prospects in northern Finland are discussed by Lauri & Turunen *(p. 107)*.

Geophysical methods for REE minerals

Gravity method
Many of the REE minerals have a higher density in comparison with country rocks. Ground gravity data yield sufficiently high resolution, but these surveys can only be focused on small areas. Modern airborne gravity methods may be promisingly effective for the detection of intrusions hosting rare earth metals. Density values for the alkaline and carbonatitic rocks may be in the range of 2.8–3.1 g/cm^3, compared to country rock vales of 2.7–2.75 g/cm^3. Aligned with the gravity anomaly, the magnetic gradient anomaly and the radiometric expression may help in discovering promising targets for more detailed evaluation.

Magnetic method
REE minerals themselves are commonly weakly magnetic, but their host rocks may produce significant magnetic anomalies. Carbonatitic-alkalic complexes potential for rare earths may produce circular magnetic anomalies with amplitudes attaining several thousands of nT and which coincide with a radiometric response. Recently automated methods in locating circular magnetic anomalies have become popular. The carbonatite cores may coincide with magnetic lows, whereas the surrounding ring-like anomaly may be associated with magnetite-bearing carbonatite or a ring of alkali rocks. In Finland, the Sokli and Iivaara carbonatite complexes produce strong magnetic anomalies.

Radiometric method
The airborne radiometric method has proved to be efficient in detecting equivalent thorium or uranium anomalies, even in glaciated terrains. For example, the radiometric method has been successful in outlining different parts of the intrusion of Sokli carbonatite (e.g., Airo et al. 2014). The equivalent thorium signature also outlines the glacial dispersal train.

Thomas et al. (2011) reviewed the rock properties of 28 minerals that may contain rare earth elements, and showed high densities of almost all of these minerals, with a general range of 3.26–5.90 g/cm^3. Many of these minerals are radioactive, and practically all are non-magnetic. The direct detection of these minerals, however, depends on their concentration and the size of the deposit. Therefore, their detection is generally based on the detection of promising host rocks.

Kihlman et al. (2014) presented a list of 14 metals and minerals that are considered as critical by the EU; these include antimony, beryllium, cobalt, fluorite, gallium, germanium, graphite, indium, magnesium, niobium, platinum group metals (PGM), rare earth elements (REE), tantalum and tungsten. They reviewed the mine production (2013) of critical commodities (including silver) and the most important known platinum group element deposits in Finland, and predicted the mineral potential.

Rare element pegmatites can only be described as geophysical non-responders. They are non-magnetic, they contain insufficient metallic minerals to be conductive and do not have a sufficient den-

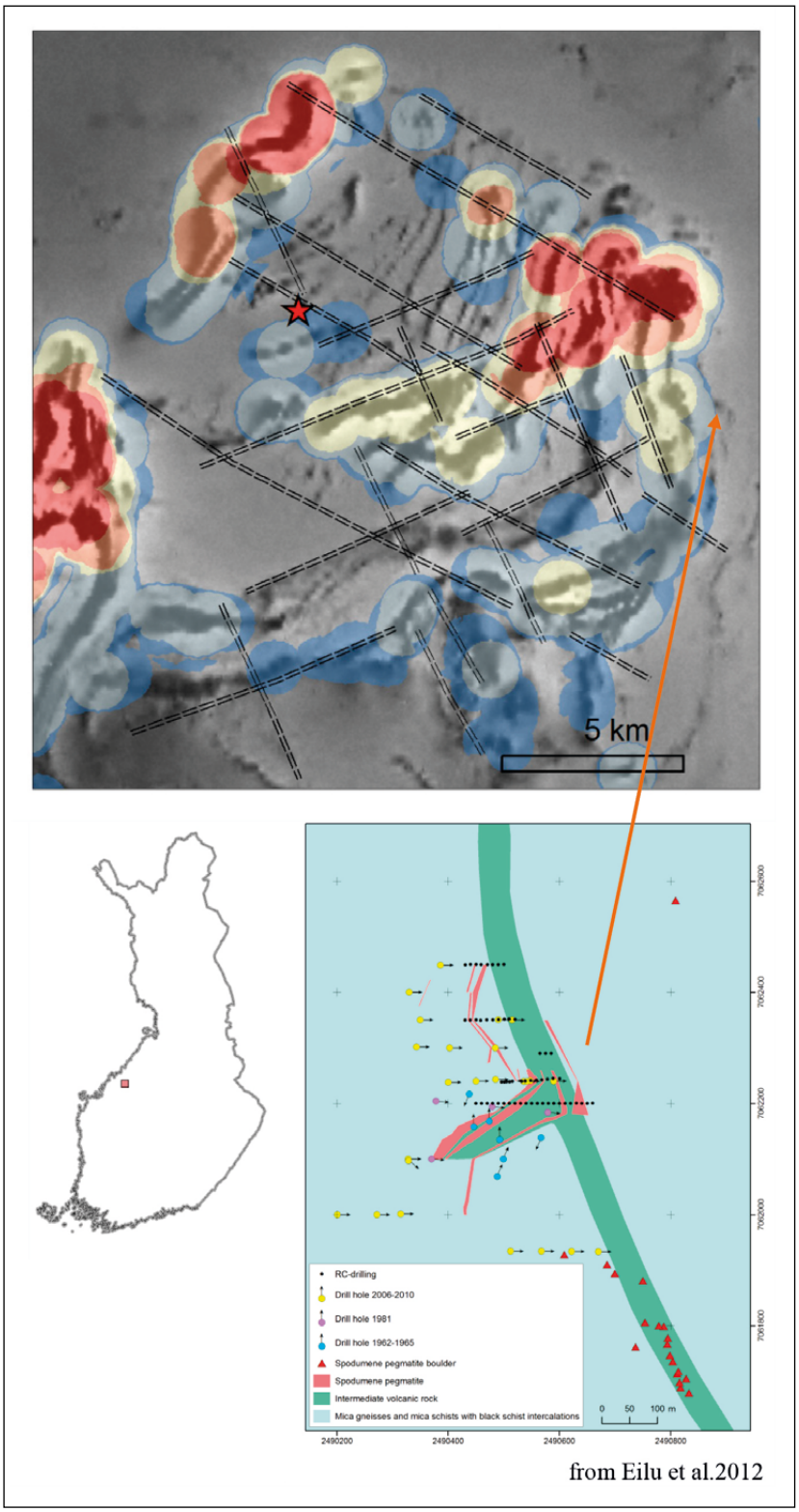

Fig. 12. The LCT (Li, Cs, Ta) pegmatites at Kaustinen (metallogenic zone F024, Eilu et al. 2012) include several occurrences from Emmes (red star) in the west to Länttä in the east. The pegmatitic dykes are 200–400 m long and 10–25 m wide and show no geophysical expression. A regional structural overview of fracture network indicates that all the occurrences are located along fracture zones of two certain directions. These directions also are related to the weakness structures of volcanic rocks in the area and their brittle nature gives the idea that they were formed after the peak regional metamorphism. In particular, in the Syväjärvi spodumene pegmatite area (local geology to the right, from Eilu et al. 2012), the geometry of the pegmatitic dykes appears to be controlled by the structural details of the intermediate volcanic rock along the strike of bedding and along the crosscutting axial weakness zone of regional folding.

sity/mass to be differentiated from their host rock by gravity methods. Structural interpretation of high-resolution geophysical data might, however, be a non-direct way of locating favourable sites for rare element pegmatites. The following general structural characteristics are from Galeschuk & Vanstone (2007):

- dyke-like geometries,
- propagation in horizontal and vertical directions,
- association with deep-seated structures and fractures,
- host rock competency and metamorphic grade may have some importance.

In the case of lithium occurrences at Kaustinen, western Finland, structurally favourable locations for pegmatitic dykes were investigated by using high-resolution aeromagnetic data (Fig. 12).

CONCLUDING REMARKS

The direct use of geophysical surveys in mineral exploration aims to locate and identify potential targets having anomalous physical properties. Further uses are the delineating of the larger-scale structures in the deposit they may be related to, or the investigation of finer scale detail within the deposit. However, direct targeting of new shallow-level mineral deposits is becoming increasingly rare. A key element for exploration is to understand and detect different types of mineral systems, and their favourable geological settings and controls at regional to local scales (Oldenburg & Pratt 2007). In Finland, as early as in the 1980s, Ketola (1982) summarized that since exploration is becoming more and more difficult, geological knowledge must be increasingly supplemented by the application of geophysics to indirect exploration. If ores are to be found, the most effective use must be made of the simultaneous application of geology, geophysics, geochemistry and drilling.

An understanding of the physical properties of rocks and minerals provides a link between geophysical interpretation and geology. The importance of reliable physical property information is enhanced as 3D interpretation, modelling and inversion of geophysical data are becoming common practice. Available geological knowledge must be translated into physical property constraints to derive models that are consistent with measured geophysical responses and the observed geology (Williams 2009). The non-uniqueness of geophysical modelling solutions is both a mathematical problem and one related to the multiplicity of sources that can cause geophysical anomalies.

Looking back

In the last decade, significant advances have been made in proven geophysical methods and in techniques to interpret and visualize geophysical data. The data models have been visually integrated, but not necessarily constrained. Such advances reach their full impact through appropriate consideration of the physical properties of rocks in relation to the key manifestations of the different deposit types and the key features of their host environments.

Exploration 07, Paine 2007:

> *Inversion of all types of geophysical data has doubled its importance and use in the past decade. There has been a general improvement in the quality, density and variety of geophysical data collected. Airborne surveys now usually use GPS navigation and improved positional accuracy. Improvements in data acquisition devices also mean that the data measurements are more accurate and more closely spaced. Developments of sensor types such as gravity gradiometer, squid-based B-field sensors for collecting magnetic and EM data have been reported. Increased data density has been accompanied by improved processing techniques for improving data quality. Processor speed, available memory and storage space have all increased significantly in the last ten years.*

Exploration 07, Oldenburg & Pratt 2007:

> *Developments in instrumentation, data collection, computer performance, and visualization have been catalysts for significant advances in modelling and inversion of geophysical data. Forward modelling has progressed from simple 3D models to whole earth models using voxels and discrete surfaces. Potential field, IP and electromagnetic inversion methods have become an essential part of most mineral exploration programs. The last decade has produced*

significant research advances in 3D modelling and inversion for gravity, magnetic, DC resistivity, induced polarization, audio magnetotelluric, frequency-domain EM and time domain EM methods.

Challenges

- ***Simultaneous analysis of multiple datasets,*** which contain information about different physical properties. To maximize the efficiency of exploration programmes, it is essential that multidisciplinary methods include all geological, geochemical and geophysical data and knowledge in integrated models. The trend towards multi-sensor systems using multiple low-cost sensors and receivers has been ongoing. Increasing computer power will make detailed 3D imaging of most surveys possible, as well as joint and cooperative inversions. The challenge is to use physical properties more quantitatively to link geological and geophysical models.
- ***Joint and cooperative inversions*** will offer a greater opportunity to integrate different types of data into the interpretation procedure. Applications include the inversion of full tensor magnetic and gravity data, cross-gradient total field surveys, DC resistivity and EM data, and many others (Oldenburg & Pratt 2007). The use of optimized geophysical data, e.g. derivative data that have been converted into forms, can facilitate the inversion process. A vast increase in the size of problems that can be handled includes the introduction of practical voxel-based 3D magnetic, gravity and IP inversion programs and the ability to include topography in 2D and 3D inversion, as well as the capacity to include drilling and geological information to constrain the inversion. Progress has also been made in including remanence and demagnetization effects into magnetic inversions (Paine 2007).
- ***Geophysical techniques reaching greater depth*** are gaining interest with the depletion of metallic mineral sources in surface or near-surface settings. Exploration must focus at much greater depths, which requires sophisticated techniques. Whereas potential field geophysical techniques or combined airborne electromagnetic and magnetic surveys have been highly successful to depths of up to 300 m, high-resolution seismic reflection profiling can target much greater depths. The seismic methods have good potential for mineral exploration, and these methods are capable of imaging mineral deposits at various depths (Tertyshnikov 2014). Recent interest in finding deeper sources has led to the development of deeper penetrating electromagnetic systems: high-resolution and deep-penetrating surveys, e.g., ZTEM, Megatem™, magnetotellurics and the Titan array (Boivin 2007).
- ***Geologically realistic outputs:*** Petrophysical data can, if available in sufficient quantity, constitute a basis for statistically characterizing and constraining the property distribution in the sub-surface. Although textbook physical property values are commonly used, ancient rocks have complex histories and standard values may not be representative. The ability to simultaneously model and interpret geophysical, geological, geochemical and geotechnical data will reduce geological uncertainty. The characterization of a mineralized target depends as much on data accuracy and coverage as it does on a good representation of the subsurface. In this sense, inversion approaches that fit the source geometry and properties are constantly improving. After inversion of pure property models, geology can be inferred from the rock properties (Fullagar & Pears 2007, Jessel 2001, McGaughey 2007). Obtaining reliable images of subsurface geological structures is a great support for successful mineral exploration, and there are a number of further developments and improvements in seismic imaging that will allow their advanced applications in the mining industry.

Looking forward

The enormous quantity of multiple geophysical sets that are nowadays available may require automated methods of analysing and evaluating the data. Sophisticated inversion techniques are needed, incorporating adaptive learning procedures to determine complex 3D geometries of source bodies. Greater volumes of petrophysical data will allow more complete spatial characterization of rock properties, thereby expanding the role of geostatistical techniques in property modelling. Mappable criteria to be applied in mineral system research are provided by wider knowledge of the petrophysical properties of mineralized or barren source rocks responsible for geophysical responses.

REFERENCES

Airo, M.-L. 2007. Application of Aerogeophysical Data for Gold Exploration: Implications for Central Lapland Greenstone Belt. In: Ojala, J. V. (ed.) Gold in the Central Lapland Greenstone Belt, Finland. Geological Survey of Finland, Special Paper 44, 171–192.

Airo, M. L. (ed.) 2015. Geophysical signatures of mineral deposit types in Finland. Geological Survey of Finland, Special Paper 58, 144 p.

Airo, M.-L. & Hyvönen, E. 2008. Petrophysical data coupled with airborne magnetic, conductive and radiometric signatures identifying bedrock conductors. Proceedings of the 5th International Conference on Airborne Electromagnetics, Porvoo, Haikko, Finland, 28–30 May 2008, keynote paper. 4 p.

Airo, M.-L. & Karell, F. 2001. Interpretation of airborne magnetic and gamma-ray spectrometric data related to Hammaslahti Cu-Zn-Au deposit in eastern Finland. In: Autio, S. (ed.), Geological Survey of Finland, Special Paper 31, 97–103.

Airo, M.-L. & Kurimo, M. 1999. Paleoproterozoic Suukisjoki mafic-ultramafic intrusion in northern Finland: combined aerogeophysical, geological and tectonic studies. In: Autio, S. (ed.) Geological Survey of Finland, Special Paper 27, 141–149.

Airo, M.-L. & Loukola-Ruskeeniemi, K. 2004. Characterization of sulfide deposits by airborne magnetic and gamma-ray responses in eastern Finland. Ore Geology Reviews 24 (2004), 67–84.

Airo, M.-L. & Mertanen, S. 2008. Magnetic signatures related to orogenic gold mineralization, Central Lapland Greenstone Belt, Finland. Journal of Applied Geophysics 64, 14–24.

Airo, M.-L. & Säävuori, H. 2013. Petrophysical characteristics of Finnish bedrock – Concise handbook on the physical parameters of bedrock. Geological Survey of Finland, Report of Investigation 205. 33 p.

Airo, M.-L., Hyvönen, E., Lerssi, J., Leväniemi, H. & Ruotsalainen, A. 2014. Tips and tools for the application of GTK's airborne geophysical data. Geological Survey of Finland, Report of Investigation 215. 33 p.

Airo, M.-L., Säävuori, H. & Vuoriainen, S. 2011. Petrophysical properties of the Outokumpu Deep Drill Core and the surrounding bedrock. In: Kukkonen, I. (ed.) Outokumpu Deep Drilling Project 2003–2010. Geological Survey of Finland, Special Paper 51, 63–82.

Barton, M. D. & Johnson, D. A. 2004. Footprints of Fe-oxide (-Cu-Au) systems. SEG 2004: Predictive Mineral Discovery Under Cover. Centre for Global Metallogeny, Spec. Pub. 33, University of Western Australia, 112–116.

Billström, K., Eilu, P., Martinsson, O., Niiranen, T., Broman, C., Weihed, P., Wanhainen, C. & Ojala, J. 2010. IOCG and Related Mineral Deposits of the Northern Fennoscandian Shield. In: Porter, T. (ed.) Hydrothermal Iron Oxide-Copper-Gold & Related Deposits: A Global Perspective, vol. 4. Advances in the Understanding of IOCG deposits. PGC Publishing, Adelaide, 367–400.

Boivin, M. 2007. Advances in Geophysical Technology for VMS Exploration. In: Milkereit, B. (ed.) "Proceedings of Exploration 07: Fifth Decennial International Conference on Mineral Exploration", 731–739.

Bolle, O., Charlier, B., Bascou, J., Diot, H., McEnroe, S. A. 2014. Anisotropy of magnetic susceptibility versus lattice- and shape-preferred orientation in the Lac Tio hemoilmenite ore body (Grenville province, Quebec). Tectonophysics 629, 87–108.

Carranza, E. J. M. & Sadeghi, M. 2010. Predictive mapping of prospectivity and quantitative estimation of undiscovered VMS deposits in Skellefte district (Sweden). Ore Geology Reviews 38 (2010), 219–241.

Charlier, B., Namur, O., Bolle, O., Latypov, R., & Duchesne, J. 2015. Fe–Ti–V–P ore deposits associated with Proterozoic massif-type anorthosites and related rocks. Earth-Science Reviews 141 (2015), 56–81.

Clark, D. A. 1997. Magnetic petrophysics and magnetic petrology: Aids to geological interpretation of magnetic surveys. AGSO Journal of Australian Geology and Geophysics 17(2), 83–103.

Dickson, B. L. & Scott, K. M. 1997. Interpretation of aerial gamma-ray surveys -adding the geochemical factors. AGSO Journal of Australian Geology & Geophysics, Vol. 17, No 2, 187–200.

Eilu, P. & Lahtinen, R. 2013. Fennoscandian metallogeny and supercontinent cycles. Mineral deposit research for a high-tech world • 12th SGA Biennial Meeting 2013. Proceedings, Vol. 4, 1632–1634.

Eilu, P., Ahtola, T., Äikäs, O., Halkoaho, T., Heikura, P., Hulkki, H., Iljina, M., Juopperi, H., Karinen, T., Kärkkäinen, N., Konnunaho, J., Kontinen, A., Kontoniemi, O., Korkiakoski, E., Korsakova, M., Kuivasaari, T., Kyläkoski, M., Makkonen, H., Niiranen, T., Nikander, J., Nykänen, V., Perdahl, J.-A., Pohjolainen, E., Räsänen, J., Sorjonen-Ward, P., Tiainen, M., Tontti, M., Torppa, A. & Västi, K. 2012. Metallogenic areas in Finland. Geological Survey of Finland, Special Paper 53, 207–342.

Eilu, P., Rasilainen, K., Halkoaho, T., Huovinen, I., Kärkkäinen, N., Kontoniemi, O., Lepisto, K., Niiranen, T. & Sorjonen-Ward, P. 2015. Quantitative assessment of undiscovered resources in orogenic gold deposits in Finland. Geological Survey of Finland, Report of Investigation 216. 318 p.

Elo, S. 1997. Interpretations of the gravity anomaly map of Finland. In: The lithosphere in Finland - a geophysical perspective. Geophysica 33 (1), 51-80.

Elo, S. 2003. Gravity operations of the Geological Survey of Finland. In: Poutanen, M., Jokela, J. & Ollikainen, M. (eds) Geodetic operations in Finland 2000–2003. Kirkkonummi: Finnish Geodetic Institute, 31–33.

FODD 2013. Fennoscandian Ore Deposit Database. Geological Survey of Finland (GTK), Geological Survey of Norway (NGU), Geological Survey of Russia (VSEGEI), Geological Survey of Sweden (SGU), SC Mineral. Online database. [Electronic resource]. Available at: http://en.gtk.fi/informationservices/databases/fodd/index.html. Last accessed 15 May 2015.

Ford, K., Keating, P. & Thomas M. D. 2007. Mineral Deposits of Canada - Overview of geophysical signatures associated with Canadian ore deposits. In: "Mineral Resources of Canada: A Synthesis of Major Deposit-types, District Metallogeny, the Evolution of Geological Provinces, and Exploration Methods". Geological Survey of Canada (GSC) and the Mineral Deposits Division (MDD) of the Geological Association of Canada.

Fullagar, P. K. & Pears, G. A. 2007. Towards Geologically Realistic Inversion. In: Milkereit, B. (ed.) "Proceedings of Exploration 07: Fifth Decennial International Conference on Mineral Exploration", 444–460.

Galeschuk, C. & Vanstone, P. 2007. Exploration Techniques for Rare-Element Pegmatite in the Bird River Greenstone Belt, Southeastern Manitoba. In: Milkereit, B. (ed) "Proceedings of Exploration 07: Fifth Decennial International Conference on Mineral Exploration", 823–839.

Galley, A. G., Hannington, M. & Jonasson, I. 2007. Volcanogenic massive sulphide deposits, in: Goodfellow (ed.), Mineral deposits of Canada—A synthesis of major deposit-types, district metallogeny, the evolution of geological provinces, and exploration methods: Geological Association of Canada, Mineral Deposits Division, Special Publication 5, 141–161.

Gibson, H. L., Allen, R. L., Riverin, G., Lane, T. E. 2007. The VMS Model: Advances and Application to Exploration. In: Milkereit B. (ed.) "Proceedings of Exploration 07: Fifth Decennial International Conference on Mineral Exploration", 713–730.

Geological Survey of Finland 2010. Bedrock map database DigiKP Finland. In-house GIS map database.

Goldfarb, R., Groves, D. & Gardoll, S. 2001. Orogenic gold and geologic time: a global synthesis. Ore geology reviews, 18(1), 1–75.

Groves, D. I., Bierlein, F. P., Meinert, L. D. & Hitzman, M. W. 2010. Iron oxide copper-gold (IOCG) deposits through earth history: implications for origin, lithospheric setting, and distinction from other epigenetic iron oxide deposits. Economic Geology, 105(3), 641–654.

Groves, D. I., Goldfarb, R. J., Gebre-Mariam, M., Hagemann, S. & Robert, F. 1998. Orogenic gold deposits: a proposed classification in the context of their crustal distribution and relationship to other gold deposit types. Ore geology reviews, 13(1), 7–27.

Gunn, P. J. & Dentith, M. C. 1997. Magnetic responses associated with mineral deposits. AGSO Journal of Australian Geology and Geophysics 17(2), 145–158.

Hagemann, S., Dalstra, H. I., Hodkiewicz, P., Flis, M., Thorne, W. & McCuaig, C. 2007. Recent Advances in BIF-related Iron Ore Models and Exploration Strategies. In: Milkereit, B. (ed.) "Proceedings of Exploration 07: Fifth Decennial International Conference on Mineral Exploration", 811–821.

Hautaniemi, H., Kurimo, M., Multala, J., Leväniemi, H. & Vironmäki, J. 2005. The 'three in one' aerogeophysical concept of GTK in 2004. In: Airo, M.-L. (ed.). Aerogeophysics in Finland 1972-2004: Methods, System Characteristics and Applications, Geological Survey of Finland, Special Paper 39, 21–74.

Holliday, J. R. & Cooke, D. R. 2007. Advances in Geological Models and Exploration Methods. In: Milkereit B. (ed.) "Proceedings of Exploration 07: Fifth Decennial International Conference on Mineral Exploration", 791-809.

Hoover, D. B., Klein, D. P. & Campbell, D. C. 1995. Geophysical methods in exploration and mineral environmental investigations. In: Edward, A. du Bray (ed.): Preliminary compilation of descriptive geoenvironmental mineral deposit models. USGS Open-File Report 95–831.

Hrouda, F., Chlupácová, M. & Chadima, M. 2009. The Use of Magnetic Susceptibility of Rocks in Geological Exploration. Terraplus, Brno 2009. 25p.

Huntington, J., Quigley, M., Yang, K., Roache, T., Young, C., Roberts, I., Whitbourn, L. & Mason, P. 2006. A geological overview of Hylogging 18000 m of core from the eastern goldfields of Western Australia: 6th Australasian Institute of Mining and Metallurgy International Mining Geology Conference, 1–8.

Jessel, M. 2001. Three-dimensional geological modelling of potential-field data. Computers & Geosciences 27 (2001) 455–46.

Johnsson et al. (eds) 2013. Mineral deposit research for a high-tech world. Proceedings of the 12th Biennial SGA Meeting, 12–15 August 2013, Uppsala, Sweden, ISBN 978-91-7403-207-9. 1882 p.

Kääriäinen, J. & Mäkinen, J. 1997. The 1979-1996 Gravity Survey and Results of the Gravity Survey of Finland 1945–1996. Publications of the Finnish Geodetic Institute 125. 24 p.

Keller, G. V. & Frischknecht, F. C. 1966. Electrical methods in geophysical prospecting, Pergamon, London.

Ketola, M. 1982. On the application of geophysics and geology to exploration for nickel-copper ore deposits in Finland. Geological Survey of Finland, Report of Investigation 53. 103 p.

Kihlman, S., Lauri. L. S. & Kivinen, M. 2014. Kriittisten metallien ja mineraalien maailmanlaajuinen tuotanto ja malmipotentiaali Suomessa seka Suomen metallikaivosteollisuuden mahdolliset kehityspolut matalahiilisessä yhteiskunnassa. Summary: Critical metals and minerals: their global production and exploration potential in Finland and the possible evolution paths of the Finnish metal mining industry in a low-carbon society. Geological Survey of Finland, Report of Investigation 213. 117 p.

Killeen, P. G. 1979. Gamma-ray spectrometric methods in uranium exploration - application and interpretation. In: Hood, P. J. (ed.) Geophysics and Geochemistry in Search for Metallic Ores: Geological Survey of Canada, Economic Geology Report 31, 163–230.

King, A. 2007. Review of Geophysical Technology for Ni-Cu-PGE deposits. In: Milkereit B. (ed.) "Proceedings of Exploration 07: Fifth Decennial International Conference on Mineral Exploration", 647–665.

Korhonen, J. V., Aaro, S., All, T., Elo, S., Haller, L. Å., Kääriäinen, J., Kulinich, A., Skilbrei, J. R., Solheim, D., Säävuori, H., Vaher, R., Zhdanova, L. (eds). 2002. Bouguer anomaly map of the Fennoscandian Shield : IGSN 71 gravity system, GRS80 normal gravity formula. Bouguer density 2670 kg/m^3, terrain correction applied. Anomaly continued upwards to 500 m above ground: scale 1 : 2 000 000. Erikoiskartat - Special Maps, Vol. 53, ISBN:951-690-818-7.

Korhonen, J. V., Aaro, S., All, T., Nevanlinna, H., Skilbrei, J. R., Säävuori, H., Vaher, R., Zhdanova, L., Koistinen, T. (eds). 2002. Magnetic anomaly map of the Fennoscandian Shield: DGRF-65 anomaly of total field. Anomaly continued upwards to 500 m above ground: scale 1: 2 000 000. Erikoiskartat - Special Maps, Vol. 54, ISBN: 951-690-817-9.

Kuosmanen, V., Arkimaa, H., Tiainen, M. & Bärs, R. 2015. Hyperspectral close-range LWIR Imaging spectrometry - 3 case studies. In: Airo, M. L. (ed.) 2015. Geophysical signatures of mineral deposit types in Finland. Geological Survey of Finland, Special Paper 58, 117–144.

Lahtinen, R., Hallberg, A., Korsakova, M., Sandstad, J. S. & Eilu, P. 2012. Main metallogenic events in Fennoscandia: summary. Geological Survey of Finland, Special Paper 53, 397–401.

Lauri, L. S. & Turunen, P. 2015. Airborne radiometric data as a uranium exploration tool - case studies from southern Lapland. In: Geophysical signatures of mineral deposit types in Finland. Geological Survey of Finland, Special Paper 58, 107–116.

Leväniemi, H. & Karell, F. 2013. Geophysical Indications of VMS Deposits in the Häme Volcanic Belt. Geological Survey of Finland, archive report. 64 p.

Leväniemi, H., Beamish, D., Hautaniemi, H., Kurimo, M. Suppala, I., Vironmäki, J., Cuss, R. J., Lahti, M. & Tartaras, E. 2009. The JAC airborne EM system AEM-05. Journal of Applied Geophysics 67, 219–233.

Lightfoot, P. C. 2007. Advances in Ni-Cu-PGE Sulphide Deposit Models. In: Milkereit, B. (ed.) "Proceedings of Exploration 07: Fifth Decennial International Conference on Mineral Exploration", 629–646.

Loukola-Ruskeeniemi, K. 1999. Origin of black shales and the serpentinite-associated Cu-Zn-Co ores at Outokumpu, Finland. Economic Geology 94, 1007–1028.

Loukola-Ruskeeniemi, K. & Heino, T. 1996. Geochemistry and genesis of the black shale-hosted Ni-Cu-Zn deposit at Talvivaara, Finland. Economic Geology 91, 80–110.

McEnroe, S. A., Robinson, P. & Panish, P. T. 2001. Aeromagnetic anomalies, magnetic petrology, and rock magnetism of hemo-ilmenite- and magnetite-rich cumulate rocks from the Sokndal Region, South Rogaland, Norway. Am. Mineral. 86, 1447–1468.

McGaughey, J. 2007. Geological Models, Rock Properties and the 3D Inversion of Geophysical Data. In: Milkereit, B. (ed.) "Proceedings of Exploration 07: Fifth Decennial International Conference on Mineral Exploration", 473–483.

McQueen, K. G. 2005. Ore Deposit Types and their Primary Expressions. Regolith Expression of Australian Ore Systems in: Butt, C. R. M, Robertson, I. D. M, Scott, K, M. & Cornelius., M. (eds) CRC LEME.

McQueen, K. G. 2005. The key primary geochemical expressions of the main metalliferous ore deposit types in Australia). [Electronic resource]. Available at: crcleme.org.au/RegExpOre/1-oredeposits.pdf. Last accessed 10 June 2015.

Mertanen, S. & Karell, F. 2015. Petrophysical and rock magnetic studies to aid Au exploration – case studies from the Häme belt, southern Finland. In: Airo, M. L. (ed.) 2015. Geophysical signatures of mineral deposit types in Finland. Geological Survey of Finland, Special Paper 58, 89–106.

Milkereit, B. (ed.) 2007. Proceedings of the Fifth Decennial International Conference on Mineral Exploration. Decennial Mineral Exploration Conferences, Toronto, Canada. ISBN -9784320.

Milkereit, B., Berrer, E. K., King, A. R., Watts, A.H ., Roberts, B., Adam, E., Eaton, D. W., Wu, J. & Salisbury, M. 2000. Development of 3-D seismic exploration technology for deep nickel-copper deposits – a case history from the Sudbury basin, Canada, Geophysics, 65, 1890–1899.

Morgan, L. A. 2012. Geophysical characteristics of volcanogenic massive sulfide deposits in volcanogenic massive sulfide occurrence model: U.S. Geological Survey Scientific Investigations Report 2010–5070 –C, chap. 7. 16 p.

Mutanen, T. 1997. Geology and ore petrology of the Akanvaara and Koitelainen mafic layered intrusions and the Keivitsa-Satovaara layered complex, northern Finland. Geological Survey of Finland, Bulletin 395. 233 p.

Niiranen, T., Hanski, E. & Eilu, P. 2003. General geology, alteration, and iron deposits in the Palaeoproterozoic Misi region, northern Finland. Bulletin of the Geological Society of Finland 75, 69–92.

Oasis montaj 2012. How-To Guide. CET Porphyry Analysis – Detect Porphyry Features. [Electronic resource]. Available at: http://www.geosoft.com/ . Last accessed 10 June 2015.

Oldenburg, D. W. & Jones, F. H. M. 2007. Inversion for Applied Geophysics. *Version 1.0 (2007/06/28)* University of British Columbia, Geophysical Inversion Facility, 2000 - 2007. [Electronic resource]. Available at: http://www.eos.ubc.ca/ubcgif/iag/foundations/properties/2physpropiag.htm. Last accessed 10 June 2015.

Oldenburg, D. W. & Pratt, D. A. 2007. Geophysical Inversion for Mineral Exploration: a Decade of Progress in Theory and Practice. In: Milkerei,t B. (ed.) "Proceedings of Exploration 07: Fifth Decennial International Conference on Mineral Exploration", 61–95.

Paine, J. 2007. Developments in Geophysical Inversion in the Last Decade. In: Milkereit, B. (ed.) "Proceedings of Exploration 07: Fifth Decennial International Conference on Mineral Exploration", 485-488.

Palacky, G. V. 1987. Resistivity characteristics of geologic targets, in Electromagnetic Methods in Applied Geophysics, Vol 1, Theory, 1351. http://www.eos.ubc.ca/ubcgif/iag/foundations/properties/resistivity.htm

Pare, P., Gribenko, A. V., Cox, L. H., Cuma, M., Wilson, G. A., Zhdanov, M. S., Legault, J., Smit, J. & Polome, L. 2012. 3D inversion of SPECTREM and ZTEM airborne electromagnetic data from the Pebble Cu-Au-Mo porphyry deposit, Alaska. Exploration Geophysics 43(2012), 104–115.

Peltoniemi, M. 1988. Maa- ja kallioperän geofysikaaliset tutkimusmenetelmät. Otakustantamo, 411 p.

Peltoniemi, M. 2005. Airborne geophysics in Finland in perspective. In: Airo, M.-L. (ed.) Aerogeophysics in Finland 1972–2004: Methods, System Characteristics and Applications, Geological Survey of Finland, Special Paper 39, 7–20.

Rasilainen, K., Eilu, P., Äikäs, O., Halkoaho, T., Heino, T., Iljina, M., Juopperi, H., Kontinen, A., Kärkkäinen, N., Makkonen, H., Manninen, T., Pietikäinen, K., Räsänen, J., Tiainen, M., Tontti, M. & Törmänen, T. 2012. Quantitative mineral resource assessment of nickel, copper and cobalt in undiscovered Ni-Cu deposits in Finland. Geologian tutkimuskeskus, Tutkimusraportti 194 – Geological Survey of Finland, Report of Investigation 194. 514 p.

Rasilainen, K., Eilu, P., Halkoaho, T., Karvinen, A., Kontinen, A., Kousa, J., Lauri, L., Luukas, J., Niiranen, T., Nikander, J., Sipilä, P., Sorjonen-Ward, P., Tiainen, M., Törmänen, T. & Västi, K. 2014. Quantitative assessment of undiscovered resources in volcanogenic massive sulphide deposits, porphyry copper deposits and Outokumpu-type deposits in Finland. Geological Survey of Finland, Report of Investigation 208. 60 p.

Reeves, C. 2005. Aeromagnetic Surveys: Principles, Practice & Interpretation. e-Published by GEOSOFT. [Electronic resource]. Available at: http://www.geosoft.com/knowledge, 155 p. Last accessed 10 June 2015

Robert, F., Brommecker, R., Bourne, B. T., Dobak, P. J., McEwan, C. J., Rowe, R. R. & Zhou, X. 2007. Models and Exploration methods for Major Gold Deposit Types. In: Milkerei,t B. (ed.) "Proceedings of Exploration 07: Fifth Decennial International Conference on Mineral Exploration", 691–711.

Säävuori, H., Korhonen, J. V. & Pennanen, M. 1991. Petrophysical properties of Finnish sulfide-bearing rocks and their expression as geophysical anomalies in the central part of the Fennoscandian Shield. In: Autio, S. (ed.) Geological Survey of Finland, Current Research 1989– 1990.

Geological Survey of Finland. Special Paper 12, 201–208.

Salisbury, M., Milkereit, B. & Bleeker, W. 1996. Seismic imaging of massive sulfide deposits—Part I. Rock properties: Economic Geology 91, 821–828.

Salisbury, M. H., Milkereit, B., Ascough, G., Adair, R., Matthews, L., Schmitt, D. R., Mwenifumbo, J., Eaton, D. W. & Wu, J. 2000. Physical properties and seismic imaging of massive sulfides. Geophysics 65(6), 1882–1889.

Salmirinne, H. 2010. In: Törmänen, T., Heikura, P. & Salmirinne, H. 2010.The komatiite-hosted Lomalampi PGE-Ni-Cu-Au deposit, Northern Finland, archive report. [Electronic resource]. Available at: http://tupa.gtk.fi/raportti/arkisto/m19_3723_2010_52.pdf.

Salmirinne, H. & Turunen, P. 2006. Ground Geophysical Characteristics of Gold Targets in the Central Lapland Greenstone Belt. Geological Survey of Finland, Special Paper 44, 193–207.

Saltikoff, B., Puustinen, K. & Tontti, M. 2006. Metallogenic zones and metallic mineral deposits in Finland: explanation to the Metallogenic map of Finland. Geological Survey of Finland, Special Paper 35. 66 p.

Sandrin, A., Bergren, R. & Elming, S. Å. 2007. Geophysical targeting of Fe-oxide Cu-(Au) deposits west of Kiruna, Sweden. Journal of Applied Geophysics 61, 91–101.

Schön, J. 2004. Physical Properties of Rocks. Pergamon Press, 583 p.

Sillitoe, R. H. 2010. Porphyry copper systems. Economic Geology, 105(1), 3–41.

Smith, R. J. 2002. Geophysics of iron-oxide copper-gold systems, in: Porter, T. M. (ed.) Hydrothermal Iron Oxide Copper-Gold & Related Deposits: A Global Perspective, 2: Adelaide, Australia, PGC Publishing, 357–367.

Sorjonen-Ward, P. & Luukkonen, E. J. 2005. Archean rocks. In: Lehtinen, M., Nurmi, P. A. & Rämö, O. T. (eds) Precambrian Geology of Finland – Key to the Evolution of the Fennoscandian Shield. Amsterdam: Elsevier 19–99.

Suppala, I. 2015. Practical 3D electromagnetic modelling and magnetic susceptibility effects - the case of Kellojärvi, eastern Finland. In: Airo, M. L. (ed.) 2015. Geophysical signatures of mineral deposit types in Finland. Geological Survey of Finland, Special Paper 58, 71-88.

Suppala, I., Oksama, M. & Hongisto, H. 2005. GTK airborne EM system: characteristics and interpretation guide lines. Geological Survey of Finland, Special Paper 39, 103–118.

Tavakoli, S. 2012. Geophysical Investigations for 3D Geological Modelling and Ore Exploration in the Skellefte Mining District. Doctoral Thesis, Luleå University of Technology. 33 p.

Tertyshnikov, K. 2014. Seismic imaging in hard rock environments. Ph.D. Curtin University, Western Australia School of Mines, Department of Exploration Geophysics. 170 p.

Thomas, M. D., Walker, J. A., Keating, P., Shives, R., Kiss, F., & Goodfellow, W. D. 2000. Geophysical atlas of massive sulphide signatures, Bathurst mining camp, New Brunswick: Geological Survey of Canada Open File 3887. 105 p.

Thomas, M. D., Ford, K. L. & Keating, P. 2011. Exploration geophysics for intrusion-hosted rare earth metals. Geological Survey of Canada, Open File 6828, 2011.

Thomson, S., Fountain, D. & Watts, T. 2007. Airborne Geophysics - Evolution and Revolution. In: Milkereit, B. (ed.) Proceedings of Exploration 07: Fifth Decennial International Conference on Mineral Exploration, 19–37.

Weihed, P., Eilu, P., Larsen, R. B., Stendal, H. & Tontti, M. 2008. Metallic mineral deposits in the Nordic countries. Episodes 31, 125–132.

Williams, N. C. 2009. Mass and magnetic properties for 3D geological and geophysical modelling of the southern Agnew–Wiluna Greenstone Belt and Leinster nickel deposits, Western Australia. Australian Journal of Earth Sciences 56, 1111–1142.

Zientek, M. L. 2012. Magmatic Ore Deposits in Layered Intrusions—Descriptive Model for Reef-Type PGE and Contact-Type Cu-Ni-PGE Deposits. USGS Open-File Report 2012–1010. 48 p.

Geophysical signatures of mineral deposit types in Finland
Edited by Meri-Liisa Airo
Geological Survey of Finland, Special Paper 58, 71–88, 2015

PRACTICAL 3D ELECTROMAGNETIC MODELLING AND MAGNETIC SUSCEPTIBILITY EFFECTS - THE CASE OF KELLOJÄRVI, EASTERN FINLAND

by

Ilkka Suppala[1]

Suppala, I. 2015. Practical 3D electromagnetic modelling and magnetic susceptibility effects – the case of Kellojärvi, eastern Finland. *Geological Survey of Finland, Special Paper 58,* 71–88, 10 figures.

This paper discusses the effect of anomalous magnetic susceptibility in frequency-domain airborne electromagnetic (AEM) and ground Slingram measurements of the Geological Survey of Finland (GTK). Numerical modelling using tabular bodies having anomalous electric conductivity and/or magnetic susceptibility demonstrated differences in the response behaviour. A magnetized vertical plate causes a maximum anomaly when the magnetizing field is along the plate. Conductivity causes a maximum anomaly when the transmitted magnetic flux is perpendicular to the plate. The footprints of the EM systems are different in shape and volume for conductivity and susceptibility. Measured total magnetic intensity (TMI) depicts the anomalous magnetic field caused by induced and natural remanent magnetization, whereas the static remanent component has no effect on the susceptibility model inverted from EM data. The combined interpretation of TMI and EM data provides a way to differentiate the contributions of induced and remanent parts in the TMI anomaly field.

Three-dimensional (3D) geophysical modelling is needed to construct realistic 3D earth models that are consistent with the available geological and geophysical data. However, large-scale and accurate numerical 3D EM modelling is a demanding computational problem. Here, the computational efficiency was improved by separating local 3D computational meshes from the 3D earth model. The 3D interpretation model was composed of layers and tabular bodies. The 3D earth model was mapped to a local mesh to obtain an effectively equivalent local simulation mesh where the complex response was calculated for each source point and each frequency. The diffuse EM equations were solved using the finite-volume method, in which the mesh is composed of rectangular cells. The objective was to make the calculations possible on an ordinary PC, but computations could be made significantly faster in a parallel computing environment.

The 3D model-based interpretation process was tested on the Kellojärvi serpentinitic formation, which is known for its high magnetite content. Both conductivity and susceptibility were taken into account in the interpretation of Twin Otter AEM and ground Slingram data. A parametric 3D interpretation model gave an (approximate) outline of the true conductivity and susceptibility structure. The modelled susceptibilities and conductivities were in agreement with petrophysical measurements from drill core samples. In the ultramafic formation, the ratio of

the remanent to the induced magnetization has been estimated to be two or more, which agrees with petrophysical information on the serpentinites in the study area.

Keywords (GeoRef Thesaurus, AGI): geophysical methods, airborne methods, electromagnetic methods, electrical conductivity, magnetic susceptibility, three-dimensional models, ultramafics, serpentinite, Kellojärvi, Finland

[1]*Geological Survey of Finland, P.O. Box 96, 02151 Espoo, Finland*

E-mail: Ilkka.suppala@gtk.fi

INTRODUCTION

Electromagnetic (EM) methods are used for mapping electromagnetic properties of the ground, for locating conductors, and for mapping overburden and the geology and structure of bedrock. The principal task of airborne or ground EM surveys is to delineate the subsurface electrical conductivity (σ), but frequency domain EM methods are also sensitive to anomalous magnetic susceptibility (χ). The effect of dielectric permittivity (ε) is negligible at low frequencies, but a dielectric response may be observable in high-frequency EM data (e.g. using a helicopter-borne EM system; Huang & Fraser 2001). The low altitude airborne EM (AEM) data in Finland measured by the Geological Survey of Finland (GTK) (e.g. Leväniemi et al. 2009) using one, two or four frequencies have primarily been interpreted visually, e.g. using original or transformed EM data, other geophysics, geological information and known the topography.

In many geological studies, the goal is to build a three-dimensional (3D) geological model of the study area. These 3D earth models should be consistent with available geophysical and other information, which means that geophysics should be modelled and inverted as 3D models. To extract geological information from AEM and ground EM surveys on a local scale, it should be possible to simulate the responses with 3D numerical models.

In this paper, I discuss the numerical calculation of the frequency-domain EM responses of GTK's Twin Otter AEM system with vertical coplanar coils (Suppala et al. 2005), and a ground Slingram system with horizontal coils. The 3D ground is assumed to be composed of layers and tabular bodies of varying electromagnetic properties. Accurate numerical 3D EM modelling can be a challenging computational problem. Therefore, in practice a compromise has to be made between accuracy and computational speed in the modelling process. To limit the computer memory requirements and to speed up the computation, Plessix et al. (2007) separated the modelling mesh representing the whole 3D earth from the computational local meshes used in the finite-integration (finite-volume) method. The computational local meshes are composed of rectangular cells that are made to adapt to the source and receiver location and to the frequency. Commer and Newman (2008) used a similar local mesh approach in 3D EM inversion, but they used the finite-difference method for calculations. In this study, the simulations were carried out using the finite-volume method (Haber & Ascher 2001).

The objective of this study was to simulate the effect of anomalous magnetic permeability ($\mu = 1+\chi$) and to interpret magnetic permeability/susceptibility together with electrical conductivity from AEM and Slingram measurements. The Kellojärvi ultramafic unit has been widely investigated in the context of Ni exploration, and there are excellent geophysical datasets for this type of comparison. Huang and Fraser (2001) simultaneously recovered resistivity ($1/\sigma$), magnetic permeability (μ) and dielectric permittivity (ε) from multifrequency AEM data using half-space models. Simultaneous 1D inversion of conductivity and susceptibility has also been demonstrated to work (e.g. Farquharson et al. 2003, Pirttijärvi et al. 2013). Sasaki et al. (2010) presented an inversion algorithm to simultaneously recover multidimensional distributions of resistivity and magnetic susceptibility from various types of loop–loop frequency-domain EM data (e.g. AEM and Slingram). The calculations were carried out in 3D to invert 2D (elongated 3D) models.

GTK's low altitude (nominal survey altitude of 35 m) AEM measurements have been simultaneously performed with total magnetic intensity (TMI) measurements. Likewise, ground Slingram measurements are accompanied by ground TMI measurements. TMI depicts the anomalous magnetic field caused by induced and remanent magnetization. The induced part is caused by the susceptibility of the ground. The effect of remanent magnetization is often unknown due to the lack of petrophysical measurements. Usually, only the effective susceptibility, assuming no remanence exists, has been inverted from the magnetic data.

By comparing the modelled TMI using susceptibility inverted from AEM data and the observed TMI, we were able reveal near-surface formations with remanent magnetization. For example, Tschirhart et al. (2013) have carried out this type of comparison between modelled and measured TMI data. In magnetic modelling, they used the apparent susceptibility (of a half-space) inverted from AEM data. The purpose of their work was to carry out regional–residual separation for magnetic data utilizing regional apparent susceptibility. As the EM primary field is caused by a magnetic

dipole (rather than by the geomagnetic field), the footprint, i.e. the volume from which the measured information comes, is local, and for susceptibility it is smaller for EM measurements than TMI data. Evidently, frequency-domain AEM and TMI measurements complement each other.

Herein, I present some theoretical 3D modelling results to elucidate the effect of magnetization in AEM and Slingram responses. The measured secondary magnetic field was generated by EM induction and induced magnetization caused by the conducting and magnetically permeable ground. Finally, I present results from a simple case study of Kellojärvi near Kuhmo. A model composed of parametrized bodies and layers makes the computations easier and enables a simple model-based interpretation process.

Numerical modelling on the local meshes

In this study, the theoretical effects of anomalous conductivity and magnetic permeability/susceptibility were calculated using EH3D software, which calculates EM fields in the 3D domain (Haber & Ascher 2001). In EH3D, the system of partial differential equations is discretized using a finite-volume scheme on a staggered grid. The sparse linear system of equations for scattered potentials is solved using an iterative solver (a preconditioned Krylov subspace method BiCGStab). The linear system of equations needs to be solved separately for each source point and each frequency. Therefore, an efficient solution strategy is needed (e.g. Um et al. 2013, Yang et al. 2014).

Plessix et al. (2007) presented a practical approach for multisource, multifrequency controlled-source EM modelling which is well adopted in large-scale EM modelling and inversion (e.g. Cox & Zhdanov 2007). They separated the 3D computational meshes used in the calculations for each source point and each frequency from the modelling mesh, which presents the 3D earth model. An optimal local simulation mesh could be constructed taking into account the resolution capability and the volume of influence (the footprint) of the EM system at the used frequency *f*. The local mesh uses fine cells near the transmitter and the receiver, and coarse cells further away. The volume of the mesh should be larger than the footprint. The grid spacing could be determined from skin depths δ [m] using, for instance, 3–5 mesh nodes per skin depth, where skin depth $\delta = \sqrt{(1/(\mu\sigma\pi f))}$ (Plessix et al. 2007, Commer & Newman 2008).

One way to visualize the volume in which the resolution is higher or lower is to view the EM system's 3D sensitivity distributions. The 3D sensitivity to conductivity for the Twin Otter AEM system has been shown by Suppala et al. (2005), who also used it to delineate the size of the footprint of the EM system. Rahmani et al. (2014) showed 3D sensitivities to both conductivity and magnetic permeability/susceptibility for a crosswell EM configuration. Their theoretical results for the "Slingram in whole space" demonstrated that the sensitivity patterns are different for conductivity and magnetic permeability. The relative sensitivity to magnetic permeability is higher close the EM transmitter and receiver and drops off more quickly than the relative sensitivity to conductivity. These results are congruent with calculations performed in this study.

The geological structure, the model of the survey area, is presented as a set of layers and tabular bodies, where the electromagnetic properties σ, χ and ε are constant. The local meshes are slid along the profile and along the model. For each measurement point and frequency, the electromagnetic properties are mapped to the mesh, and the complex response with sensitivities is calculated. The model is presented as 2D polygons on the vertical plane along the horizontal measurement profile. The polygons are extended along the strike direction perpendicularly to that polygon plane. If only one data line is used in the interpretation, the tabular bodies are extended to effectively 2D models. If multiple data profiles are used, the polygons extend to the middle position between adjacent profiles.

The electromagnetic properties of the tabular bodies formed by 2D polygons are mapped to rectangular cells. When the boundary between different materials cuts the cell, the material averaging/mixing rule determines (approximately) the effectively equivalent properties of the cell. The material averaging formula used here is similar to that of Commer and Newman (2008). A simple method to calculate these averaged (upscaled) values is presented by Abubakar et al. (2009) and is outlined in Figure 1. The resulting mixed material

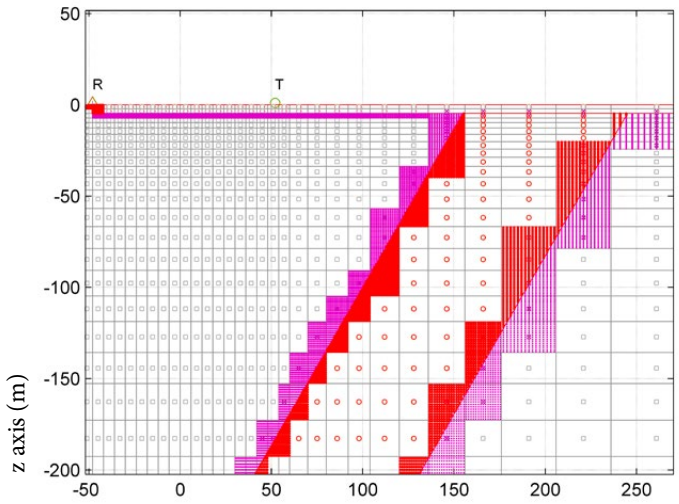

$$\sigma_x(i,j,k) = \left[\sum_{x'}\left(\sum_{z'}\sigma_{x'z'}\right)^{-1}\right]^{-1}$$

The property σ_x of slices perpendicular to the x axis is first calculated as parallel resistors, then the property σ_x of the serial slices.

$$\sigma_z(i,j,k) = \left[\sum_{z'}\left(\sum_{x'}\sigma_{x'z'}\right)^{-1}\right]^{-1}$$

The property σ_z of slices perpendicular to the z axis is first calculated as parallel resistors, then the property σ_z of the serial slices.

Fig. 1. Material averaging of equivalent effective properties for intersected cells with composite materials (Abubakar et al. 2009). The resulting mixed properties σ, χ and ε are anisotropic. The subcells used in the calculation are plotted in small red dots when they are inside the polygons representing a dipping prism and a layer, and in purple when they are outside. The local mesh is used for the Slingram system with a transmitter (T) and receiver (R) coil separation of 100 m and a frequency of 14080 Hz.

properties σ, χ and ε are effectively anisotropic in the scale of the cells. In the EH3D program, σ and ε in these cells are anisotropic and χ is made isotropic, taking the geometric mean of the anisotropic value.

The aim of material averaging is to compute effective material properties on a coarser scale to be used in solving "equivalent" coarse-scale equations. In this study, the used frequencies were relatively low (max 14 kHz), so the diffusive forms of Maxwell's equations were solved. EM systems have a limited resolution (depending on the frequency), which in a sense justifies the approximations explained above. The procedure enables the use of a finite-volume program together with a simple 3D model-based interpretation process.

The matrix of partial derivatives of the system responses with respect to model parameters, i.e., the Jacobian matrix, is calculated as presented by Abubakar et al. (2009). The matrix is computed using the partial derivatives of responses with respect to conductivities of the cells and the partial derivatives of the cell conductivities with respect to the model parameters. The first set of derivatives is calculated by EH3D using an adjoint approach and the second set using effective conductivities (mixing formulas in figure 1) in finite-difference approximations. The method works well with moderate conductivity contrasts that were tested in this study by comparison with finite-difference derivatives (based on changes in the modelled responses due to a slight perturbation of a model parameter). This method is efficient in the calculation of the Jacobian matrix and accurate enough for model-based parametric inversion.

The interpretation of anomalous conductive and magnetically permeable 3D models was carried out here by simple trial-and-error interpretation for one ground profile or flight line at a time, starting with 2D models. So far, model-based optimization using Jacobian matrices has only been tested.

Effect of magnetization in AEM and Slingram responses

The measured quantity of the Twin Otter AEM system and the ground Slingram system is the ratio between the secondary and the primary magnetic fields. The primary magnetic field is produced by a small transmitter coil and could be approximated as a magnetic dipole. The secondary magnetic field is generated by EM induction and induced magnetization caused by the conducting and magnetically permeable ground. The effect of dielectric permittivity ε is negligible at the frequencies used in this study, but in modelling permittivity is also taken into account

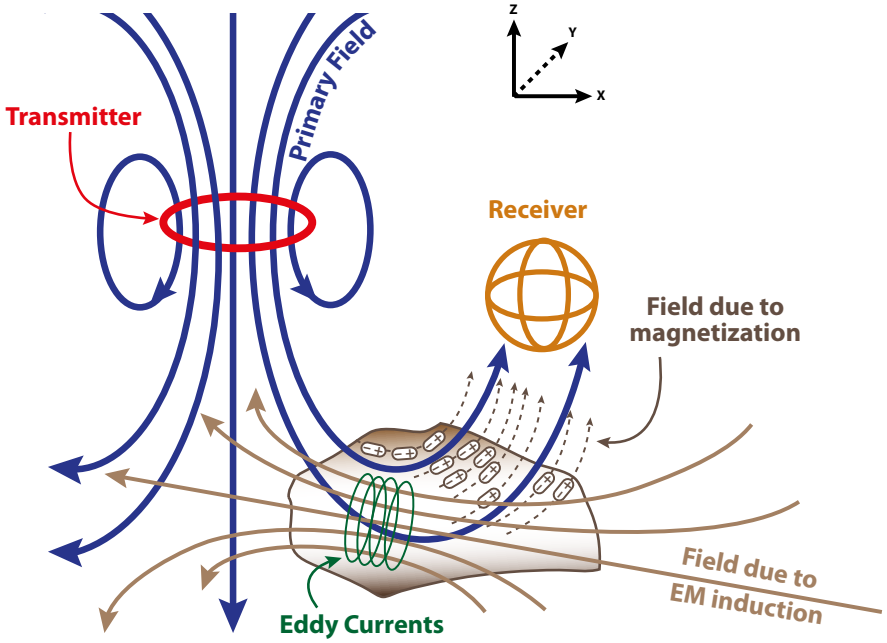

Fig. 2. The principle of EM induction and induced magnetization. The primary field is generated by a transmitter loop or coil. The secondary field is caused by eddy currents and induced magnetization due to the conducting and magnetically permeable subsurface, respectively. (Modified from Grant and West 1965; drawing Harri Kutvonen, GTK).

using some plausible values for water, ice, rock and other media.

The time harmonic primary field induces eddy currents in conductive bodies, which tend to cancel out the changes in the incident primary magnetic field and generate a secondary field. The induced magnetization enhances the internal magnetic field, causing a secondary magnetic field that is in phase with the primary field. This is shown schematically in Figure 2. In the Twin Otter EM system, the conducting ground causes positive in-phase and quadrature responses, while the in-phase component response caused by the magnetically permeable ground has the opposite (negative) sign.

Figure 3 verifies the calculated results by comparing the responses from extensive 3D formations with theoretical 1D solutions. The procedure of local mesh sliding along the profile is used to calculate responses for the Slingram system, where the separation of horizontal loops is 100 m and the frequencies are 3520 and 14080 Hz. Below a 4.7 m thick overburden with a resistivity of 500 Ωm is located a 540 m wide and 800 m long prism in a half-space of 3000 Ωm. The resistivity of the prism is 3000 Ωm or 50 Ωm, and the magnetic susceptibility is 0 or 0.25 [SI]. The height of the prism is 300 m. The 3D model becomes one-dimensional above the centre of the body, when the width of the prism is about 300 m or more. The volumes of the used local meshes were $1100 \times 760 \times 1200$ m^3 and $770 \times 650 \times 920$ m^3 for the frequencies of 3520 and 14080 Hz, respectively. The volumes were discretized into $54 \times 40 \times 42$ and $56 \times 40 \times 38$ cells along x-, y- and z-directions. The minimum cell size was $4.25 \times 4.25 \times 2.2$ m^3 for the frequency of 14080 Hz. The air layer (upper half-space) had a thickness slightly greater than the modelled half-space.

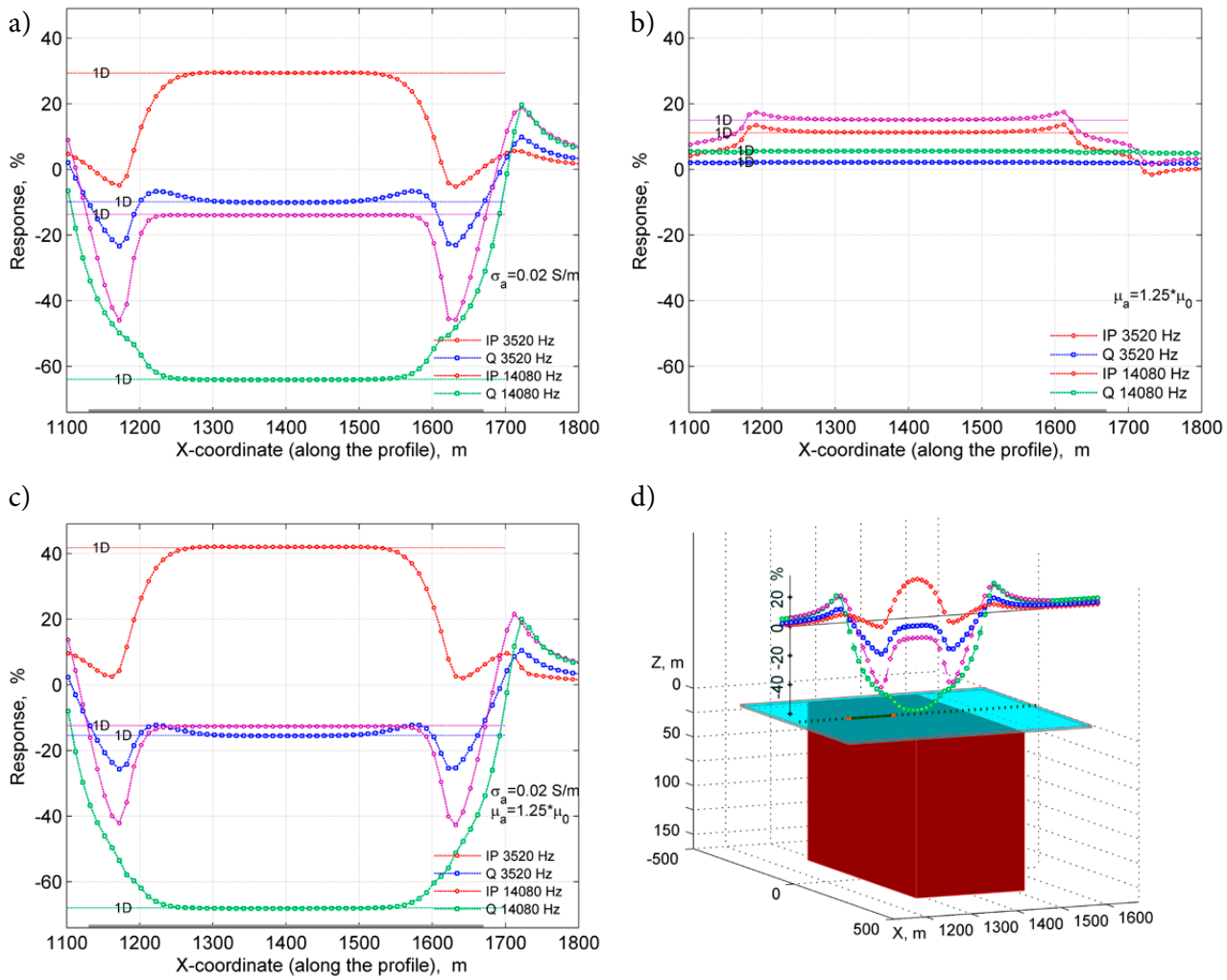

Fig. 3. Slingram profiles (IP = in-phase, Q = quadrature component) over an extensive 3D formation and comparison with 1D results (horizontal lines) at two frequencies (3520 and 14080 Hz). The responses are plotted for a) anomalous conductivity σ, b) anomalous permeability μ and c) anomalous σ and μ. The location of the profile above the 540 m wide prism is indicated in figure 3d.

Figure 4 shows the calculated results for a thinner, 30 m wide, vertical 3D target. Other parameters are the same as those in Figure 3. The magnetized vertical plate causes a maximum anomaly when the receiver or the transmitter is above the plate, i.e. when the magnetizing field is along the plate (Fig. 4b). The conductivity causes a maximum anomaly when the varying transmitted magnetic flux passes through the plate (in Figs 4a and 4c).

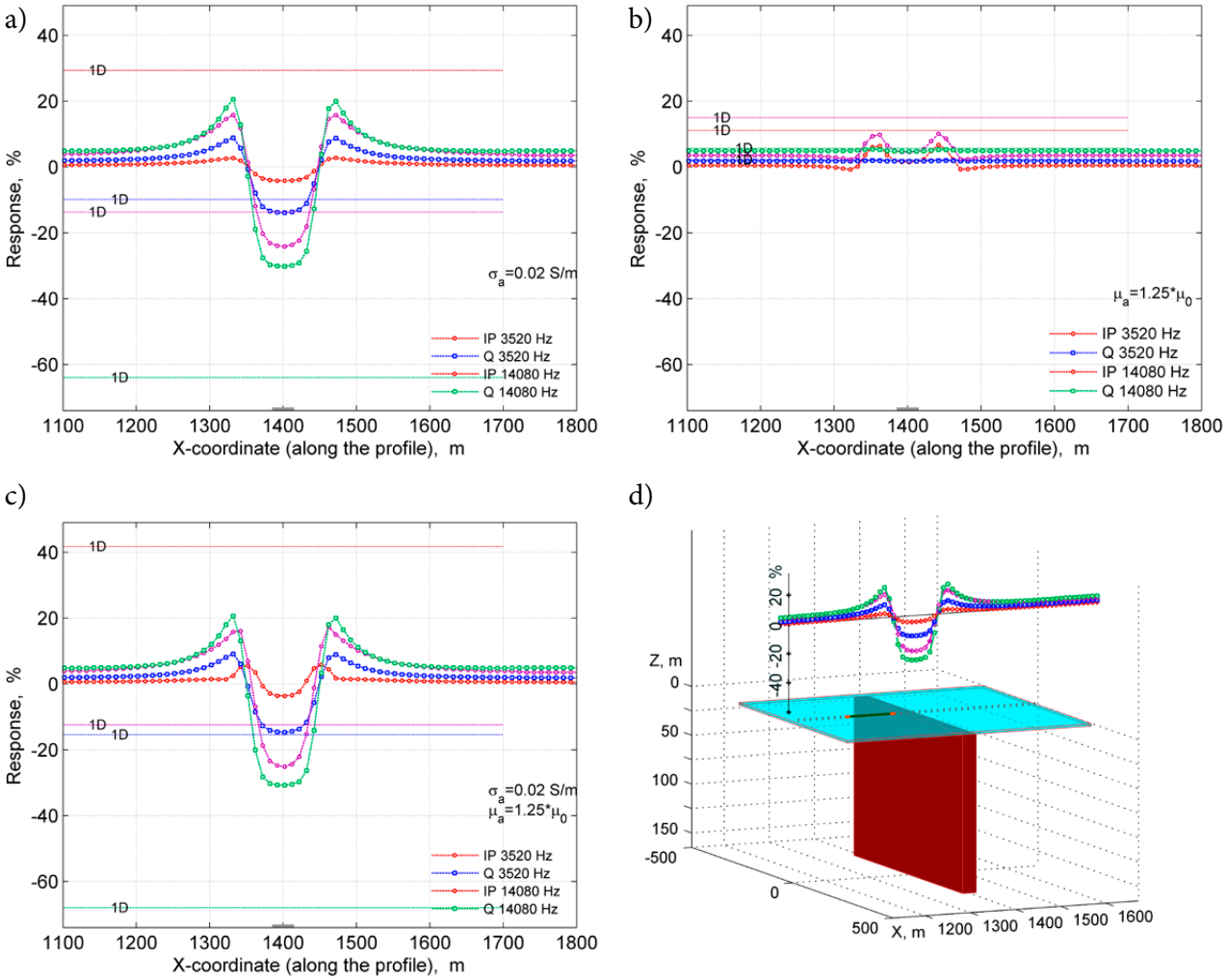

Fig. 4. Slingram profiles (IP = in-phase, Q = quadrature component) over a thin 3D formation and comparison with 1D results (horizontal lines) at two frequencies (3520 and 14080 Hz). The responses are plotted for a) anomalous conductivity σ, b) anomalous permeability μ and c) anomalous σ and μ. The location of the profile above the 30 m wide prism is indicated in Figure 4d.

Figure 5 shows the calculated responses for the GTK Twin Otter AEM system over a thin conductive and/or magnetically permeable vertical prism. The model consists of a vertical rectangular plate with lateral dimensions of 30 m by 270 m, and a vertical height of 254 m. The target is located at a depth of 2.5 m below the overburden within a homogeneous half-space with a resistivity of 3000 Ωm. The resistivity of the overburden is 266 Ωm. The flight lines traverse the centre of the plate, across and along the strike direction. The used frequency was 3113 Hz, and the two flight altitudes were 30 m and 42 m. The volume of the used local mesh was 1190 × 1180 × 1270 m^3. The volume was discretized into 51 × 42 × 45 cells along x-, y- and z-directions. The minimum cell size was 4 × 5.1 × 2.5 m^3. The thickness of the air layer was 730 m.

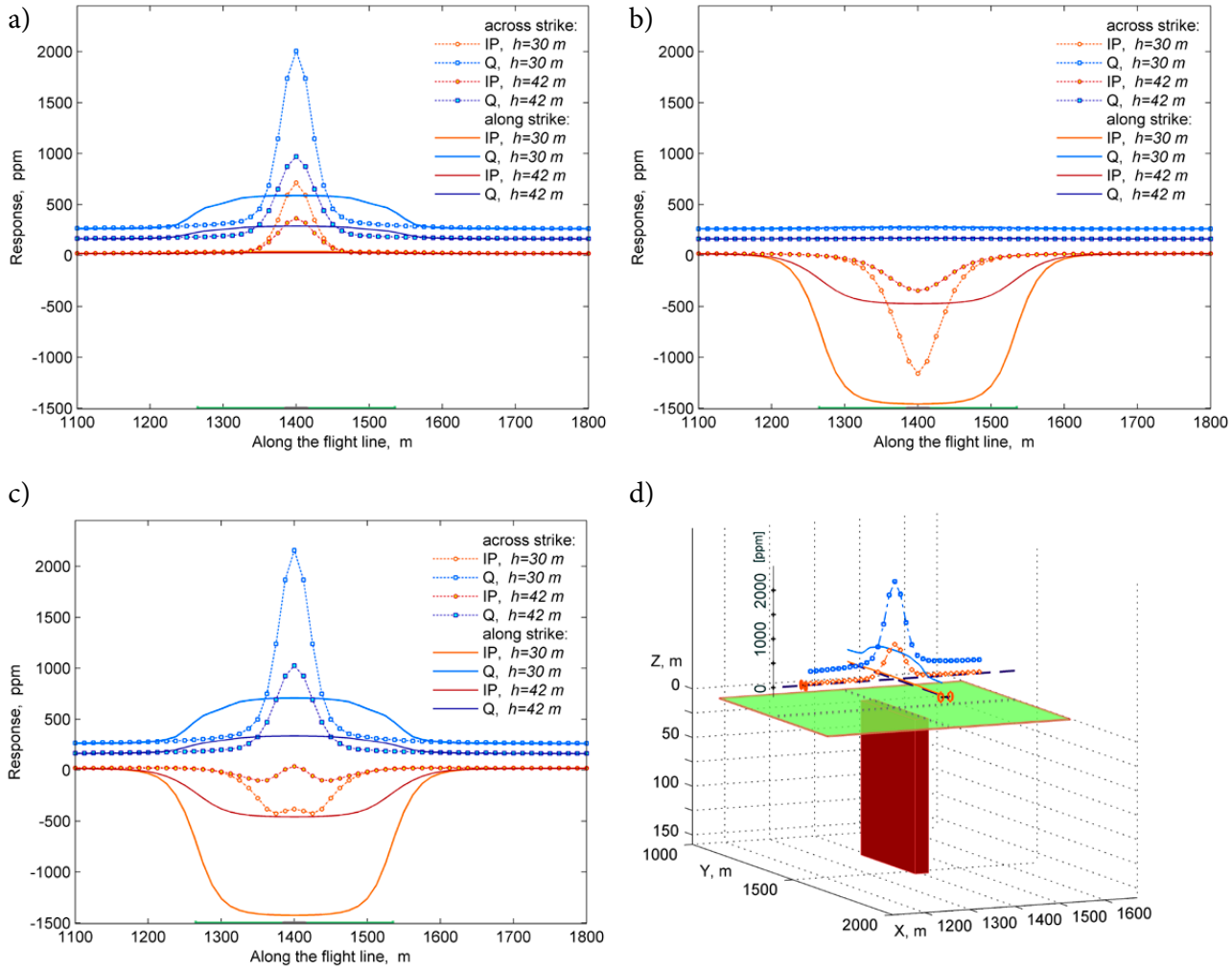

Fig. 5. AEM profiles (IP = in-phase, Q = quadrature component) over the centre of a plate, across and along the strike direction. The responses are plotted for a) anomalous conductivity σ (20 Ωm), b) anomalous permeability μ (1.25*μ_0) and c) for anomalous σ and μ (20 Ωm and 1.25*μ_0). The responses are plotted at two flight altitudes, 30m and 42 m. The locations of the profiles are indicated in Figure 5d.

The results demonstrate the effect of the flight altitude (or the depth of the upper surface of the anomalous body) on the responses. The amplitude of the dipolar primary field as well as the secondary field caused by the anomalous body falls off rapidly ($1/r^3$). All calculated results (see also Rahmani et al. 2014) indicate that the response caused by the magnetization is more sensitive to the distance between the EM system and the target than the response caused by electromagnetic induction by eddy currents.

Calculated synthetic Slingram and AEM responses demonstrate different types of couplings to tabular bodies with anomalous conductivity and/or magnetic susceptibility. The footprints of the Twin Otter EM system are different in shape and volume to conductivity and susceptibility. These theoretical EM results characterize the differences between EM induction and induced magnetization.

On the EM interpretation of conductivity and susceptibility

It is a common situation in geological studies that only incomplete and imprecise geophysical (and geological) data are available. The requirement for the resulting model to be consistent with all available information (as a necessary condition) reduces uncertainty and resolves possible non-uniqueness problems in the interpretation. The ultimate goal should be joint inversion with all

available data and constraining *a priori* information. In this study, the aim was to interpret conductivity and susceptibility from GTK Twin Otter AEM and ground Slingram EM data. Evidently, geophysical magnetic measurements would give mutual and complementary information for the inversion of the susceptibility model.

Magnetic anomalies in TMI measurements are caused by induced magnetization and natural remanent magnetization. The induced magnetization is caused by the susceptibility χ of the ground (multiplied by the inducing magnetic field). The effect of remanent magnetization is caused by permanent static magnetization in ferrimagnetic minerals (e.g. Airo and Säävuori 2013). The static remanent component has no effect on the susceptibility model inverted from AEM data. Calculating TMI values using the inverted susceptibility model and comparing these with the observed TMI values is one method to reveal the near-surface formations with remanent magnetization. Tschirhart et al. (2013) have carried out such work using 1D EM models. This type of cooperative interpretation provides information on the magnitude and direction of remanent magnetization (Clark 2014).

AEM and Slingram surveys use a dipolar inducing field, whereas the geomagnetic field is effectively static and uniform. Therefore, the volume from which the measured information on susceptibility comes is local and smaller in EM surveys than in TMI surveys. In EM surveys, the volume of influence, i.e., the footprint, is clearly shallower. AEM results are more sensitive to the distance from the system to the magnetized target, and are consequently more sensitive to errors in the measured flight altitude. Moreover, the ground magnetic data have better spatial resolution than Slingram in-line measurements made with a wide coil spacing.

Shortening of the transmitter–receiver coil spacing would increase the spatial resolution of Slingram-type EM systems. This would reduce the sensitivity of the EM system to conductivity (operating at a fixed frequency), but not to susceptibility (Won & Huang 2004). Hand-held Slingram-type conductivity meters also operate as susceptibility meters. For example, Wilt et al. (2013) and Rahmani et al. (2014) have examined the possibility to prospect for magnetic targets using a low frequency controlled source in combination with oriented magnetic field receivers. They referred to the method as dipole magnetics or dipole magnetic tomography. Dense measurements with various coil configurations would increase the spatial resolution of susceptibility imaging.

In AEM interpretation, the simplest (and often most practical) model is a 1D layered model of the magnetized and conductive earth. Figure 6 illustrates the sensitivity to the depth to the upper surface of the magnetized basement and the sensitivity to the susceptibility of the basement. The two-layer model has non-magnetized overburden and magnetized basement. The resistivity ρ_1 of the overburden is either 2000 Ωm or 200 Ωm. The thickness of the overburden varies. The resistivity of the basement ρ_2 is 2000 Ωm and its susceptibility χ_2 is 0.1 [SI]. The simulated results are calculated for the two-frequency Twin Otter EM system at the flight altitude of 33 m. Figure 6a shows the change in the AEM response, i.e. the sensitivity, as a function of depth, when the thickness of the overburden increases by one metre. Figure 6b illustrates the change when the susceptibility increases from 0.1 to 0.11 [SI].

In resistive ground, parameters such as the depth to the upper surface of the magnetized body and interpreted susceptibility have a strong (negative) correlation in the in-phase components (e.g. in Fig. 6 when ρ_1 and ρ_2 are 2000 Ωm). The effects of these parameters cannot be interpreted separately (at least by 1D inversion), and one parameter has to be known or predicted to estimate the other. The use of a higher frequency (14 kHz) does not provide any extra information on the magnetized basement (assuming that the possible frequency dependence of the susceptibility is below the noise level), and it does not have a sufficient sensitivity to the thickness of the resistive overburden. When the conductivity of the overburden layer increases to 200 Ωm, the situation is different. Both parameters can be resolved and the information at an additional frequency will benefit in the inversion. This AEM system is also rather insensitive to the thicknesses of the resistive and magnetized formation.

If conventional EM and magnetic survey data are available, the need for joint or combined inversion/interpretation with *in situ* information is emphasized to reduce possible non-uniquenesses in the inversion.

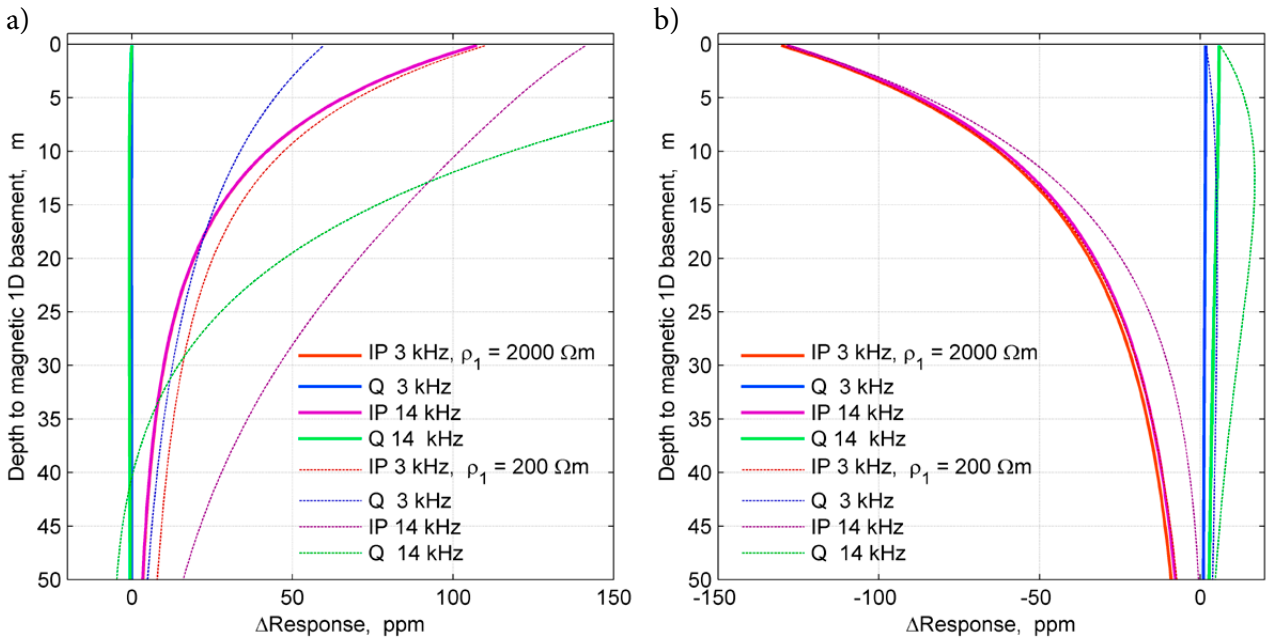

Fig. 6. 1D sensitivities to a magnetic basement below an overburden (ρ_1 = 2000 or 200 Ωm, χ_1 =0.0 [SI], ρ_2 = 2000 Ωm, χ_2 = 0.1 [SI]). Fig. a) illustrates the change in the AEM response as a function of depth if the thickness of the overburden increases by one metre. Fig. b) illustrates the change if the susceptibility increases from 0.1 to 0.11 [SI]. The flight altitude is 33 m.

Kellojärvi interpretation example

2D and 3D model-based interpretation has been tested in the western part of the Kellojärvi ultramafic complex. The area has potential for nickel deposits, and it has been covered by geological and geophysical surveys (e.g. Halkoaho & Niskanen 2012). The area was surveyed in 1994 with 100 m line spacing using a Twin Otter aircraft, simultaneously measuring TMI with two magnetometers, the EM response at 3113 Hz and gamma radiation (Hautaniemi et al. 2005). Large areas have also been covered by ground TMI and Slingram measurements with a line spacing of 50 m. The magnetized ultramafic formation is clearly outlined from aeromagnetic and AEM in-phase data (Fig. 7). The AEM flight profiles and ground profiles are E–W directed. The bedrock is partly outcropping. The topography (Fig. 7a) and bathymetry show rapid topographic variations with clear elongated depressions. The deepest parts of the lake are nearly 20 m deep, while the average depth is less than 10 m.

The bedrock model has been interpreted from the AEM and ground Slingram data using homogeneous 3D σ and χ bodies below Lake Kellojärvi and using estimated overburden resistivity and thickness values. In particular, the lake bathymetry along the measurement profiles has been taken into account. The thickness values for the lake layer are interpolated from the bathymetric elevation model. The 3D models below the profile are extended to the middle position between adjacent profiles, if there is also an interpreted adjacent measurement profile. Otherwise, the model is made infinitely long in that direction. The actual 3D model is comprised of modelled 3D slices, which have a width of about 100 m (AEM) or 50 m (Slingram) and which are wider in the peripheral parts of the modelled area. In principle, all modelled slices are taken into account when the responses along one line are calculated on local meshes, as explained above. In this case study, one "good" local mesh was used per EM system and frequency. Calculated 3D responses caused by wide conductivity and susceptibility formations were tested against 1D results.

The airborne geophysical surveys were conducted in the summer, but the ground geophysics was measured (on the ice) during the winter. The electrical conductivity of the lake water was estimated from AEM results and its dependence on the temperature was taken into account in the Slingram interpretation. The model for the water layer could be more detailed between the flight lines, but this is not a major problem due to the rather high (estimated 240 Ωm) resistivity of the lake water. More

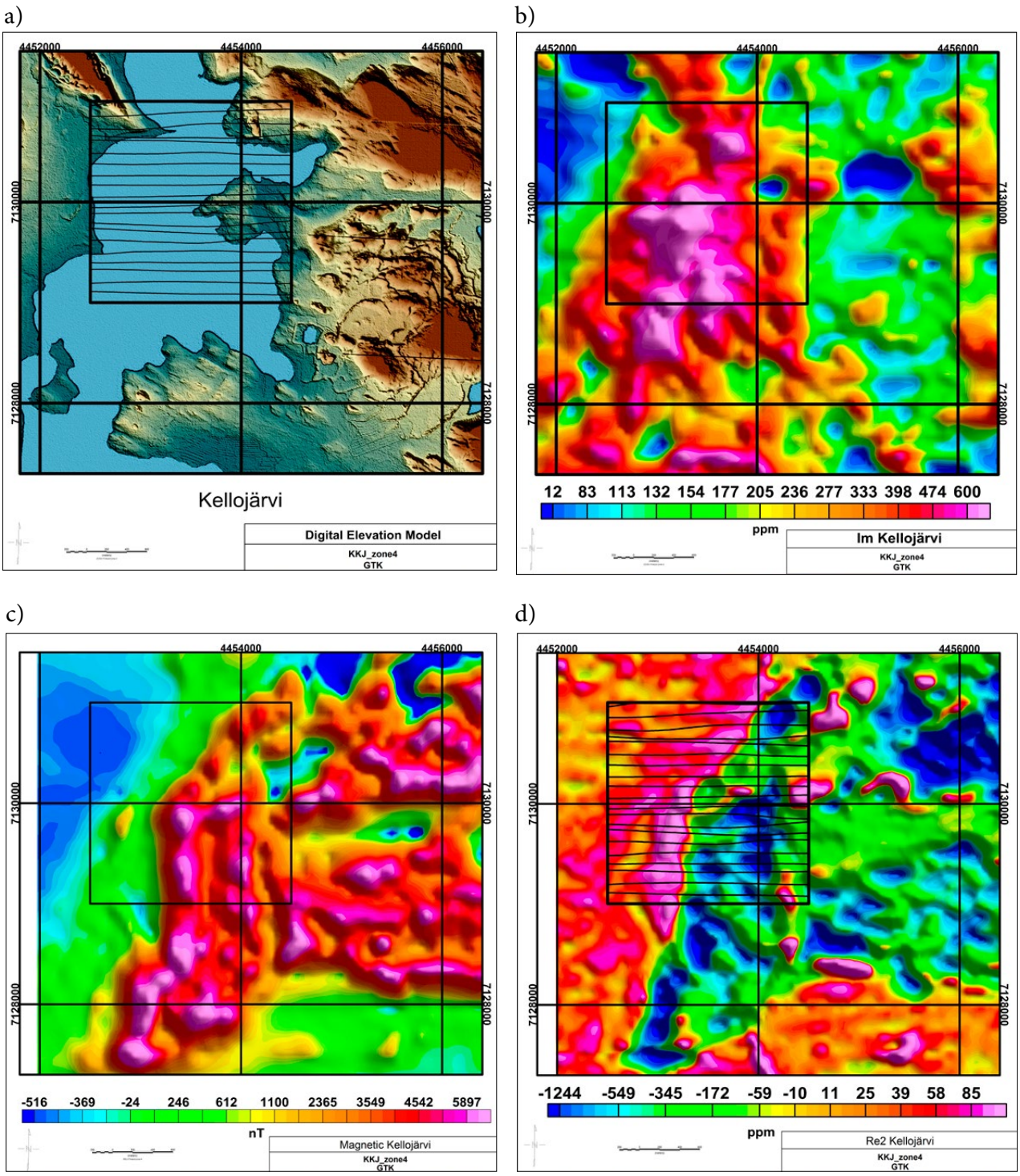

Fig. 7. a) A digital elevation model of the Kellojärvi study area (National Land Survey of Finland) (in the black rectangle, elevation varies from 161 m to 196 m); b) the AEM quadrature component; c) airborne TMI data (IGRF removed); and d) the AEM in-phase component. The black rectangle outlines the study area presented in Figure 10. The AEM flight lines are indicated in Figs a) and d).

care should be taken in estimating the partly outcropping magnetized bedrock formations below abruptly variable topography. Here, the surface topography was assumed to be flat.

In the Twin Otter system, the altitude of the sensors is measured by a radar altimeter. Hautaniemi et al. (2005) estimated that the accuracy of the used radar altimeter is normally better than 0.5 metres. Here, the accuracy of the altitudes was good enough over the lake. Problems arise when the radar altimeter has measured (smoothed) distances to tree tops. Here, the values of the radar

altimeter were (partially) corrected by applying the same type of adaptive (max) filtering as used in Beamish and Leväniemi (2010). The method corrects excessively low altitude values at least to the right direction using measured heights and the digital elevation model. Some more or less erroneous values are nevertheless left, as seen in Figure 8. The high sensitivity of the AEM system to the distance to upper surface of a shallow magnetized body clearly manifests these errors. The (median) filtering of the AEM measurements in the processing step (Hautaniemi et al. 2005) has also caused some minor effects in the AEM responses: the maximum and minimum values have been removed.

Figure 8 displays the AEM interpretation result for flight line 201, which is the nearest to three drill holes shown in Figure 8 c) and d). In this case, a simple visual interpretation of AEM results is also straightforward. In the study area (Fig. 7) there is one evident bedrock conductor; otherwise, the bedrock is resistive. Elongated depressions in topography are related to less resistive bedrock faults/fracture zones cross-cutting the magnetized formation and its surroundings. The westernmost drill hole penetrates into a layer of sulphide-bearing phyllite. The drill core samples give resistivities from few a hundred to 20 Ωm. The easternmost drill hole is in serpentinite, and the middle one penetrates serpentinite at the depth of about 100 m. The measured susceptibilities of the serpentinite are between 0.03–0.22 [SI], and the ratios of the remanent to the induced magnetization, i.e. Q-values, range between 1.2–17, so that there appears to be a positive correlation between susceptibility and remanence.

In this study, the aim was to obtain rough models of conductivity and susceptibility. 3D models give quantitative estimates of model properties. However, these results are still conditional, and the assumptions made should be borne in mind. The usual goodness-of-fit that is attempted to achieve is shown in Figure 8a. As is a common practice in data fitting and inversion, we attempted to find a model for which the modelled and measured data agreed to within noise/error tolerance. In addition, the used parametric tabular 3D bodies may not necessarily explain the measurements more exactly. Thus, the interpretation models give only an outline of the true conductivity and susceptibility models. Twin Otter AEM data are rather insensitive to the dip of the structure. Because the contacts and faults appear to be vertical or subvertical, only vertical tabular bodies were used in interpretation.

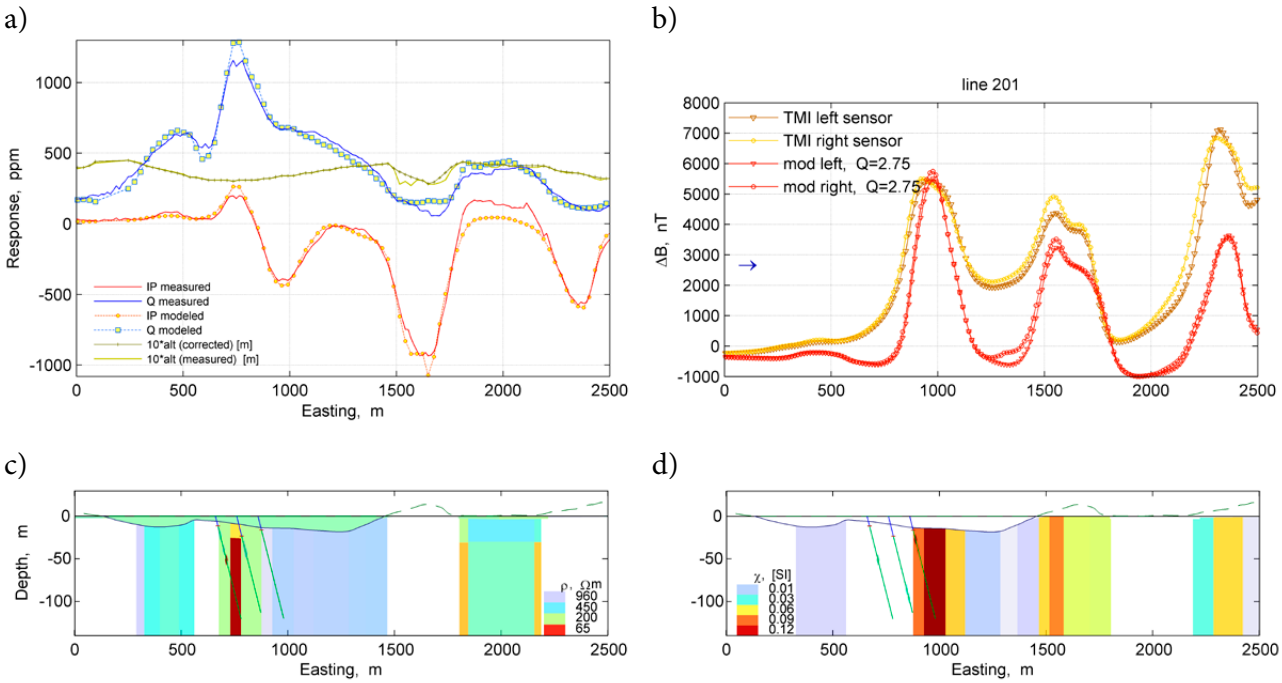

Fig. 8. Interpretation of Kellojärvi AEM data for one profile (201). a) Measured and modelled responses (IP = in-phase, Q = quadrature component) and measured and corrected altitudes; b) measured TMI (IGRF removed) and calculated TMI using the AEM susceptibility model and remanence directed along the geomagnetic field using the Q-value 2.75, with the blue arrow showing the flight direction; c) the resistivity model; d) the susceptibility model. The dashed line in c) and d) indicates the true topography.

The effects of median filtering and errors in the flight altitude can be seen in Figure 8. The variable topography can cause some effects, which were not accounted for in the modelling. The observed in-phase values over a topographic depression (at 2000 m) were not explained well by the model. It is assumedly a fracture zone with increased conductivity, which is more clearly seen in the Slingram results. The values can be explained by a deeper horizontal good conductor. Similar topographic (?) effects can be seen on some other lines.

Comparing the measured TMI values and the modelled TMI response calculated using the interpreted susceptibility model shows a strong effect of the remanent magnetization. In the formation, the ratio of the remanent to the induced magnetization could be 2 or more, which is in agreement with petrophysical measurements from drilled serpentinite in the study area. The modelled susceptibilities are also in agreement, at least qualitatively, with measurements from the drill core samples. Here, the self-demagnetization was not taken into account.

Figure 9 displays the ground Slingram and TMI measurements from profile 7130050, which is closest to the AEM profile line 201. The ground Slingram system is very sensitive to thin vertical conductive structures, which are clearly delineated by the measurements. The dip was also taken into account in the interpretation of the the Slingram data. The (too) fine resolution of the ground TMI is seen over the partly outcropping magnetized formation between Easting 1450 and 1750 m. The small-scale magnetized structures cannot be interpreted from the Slingram data. The topographic variations can cause some error in Slingram measurements.

Figure 10 shows the AEM and Slingram interpretations as maps of vertical cross-sections of conductivity and susceptibility along the measurement profiles. The better resolution of ground Slingram data for vertical conductive structures compared to airborne AEM data is evident. The ground TMI data were partially taken into account in the Slingram susceptibility interpretation. The AEM interpretations were carried out without TMI information to better assess the direction of remanent magnetism. The results in Figure 8c indicate that the remanence could be directed along the geomagnetic field, but there also appears to be another consistent, more westward direction.

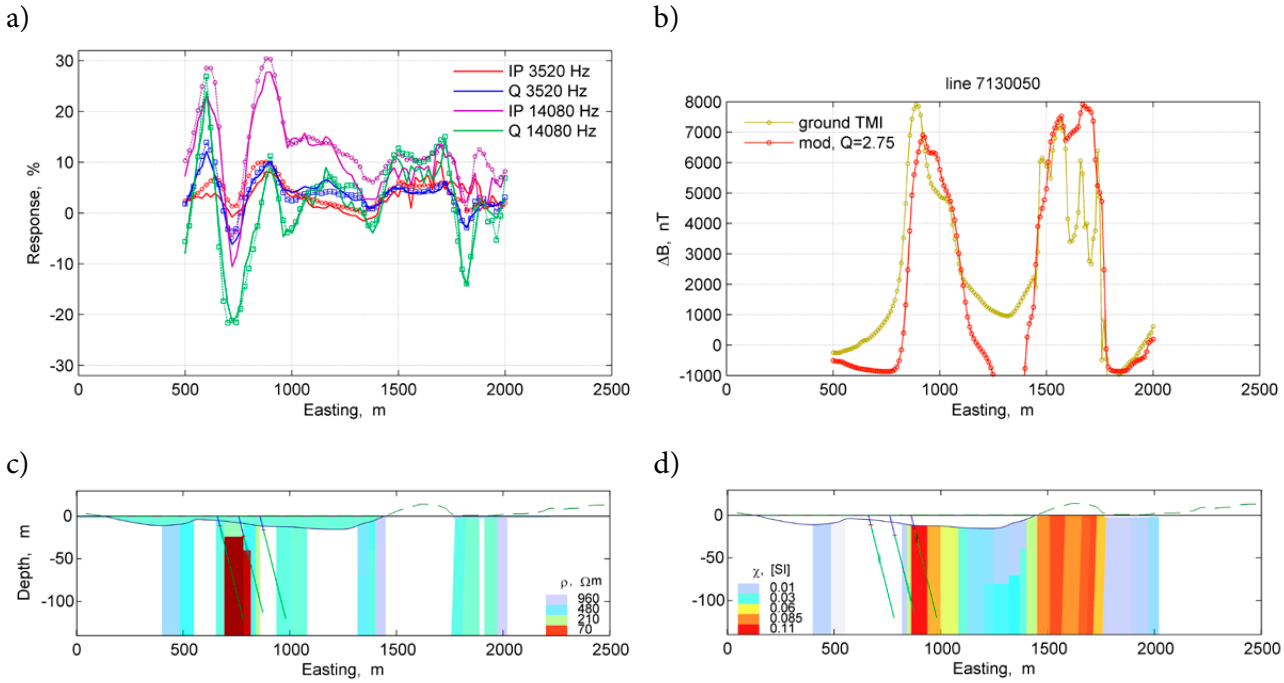

Fig. 9. Interpretation of Kellojärvi Slingram data for one profile (7130050). a) Measured and modelled responses (IP = in-phase, Q = quadrature component); b) measured ground TMI (IGRF removed) and calculated TMI using the EM susceptibility model and remanence directed along the geomagnetic field using the Q-value 2.75; c) the resistivity model; d) the susceptibility model.

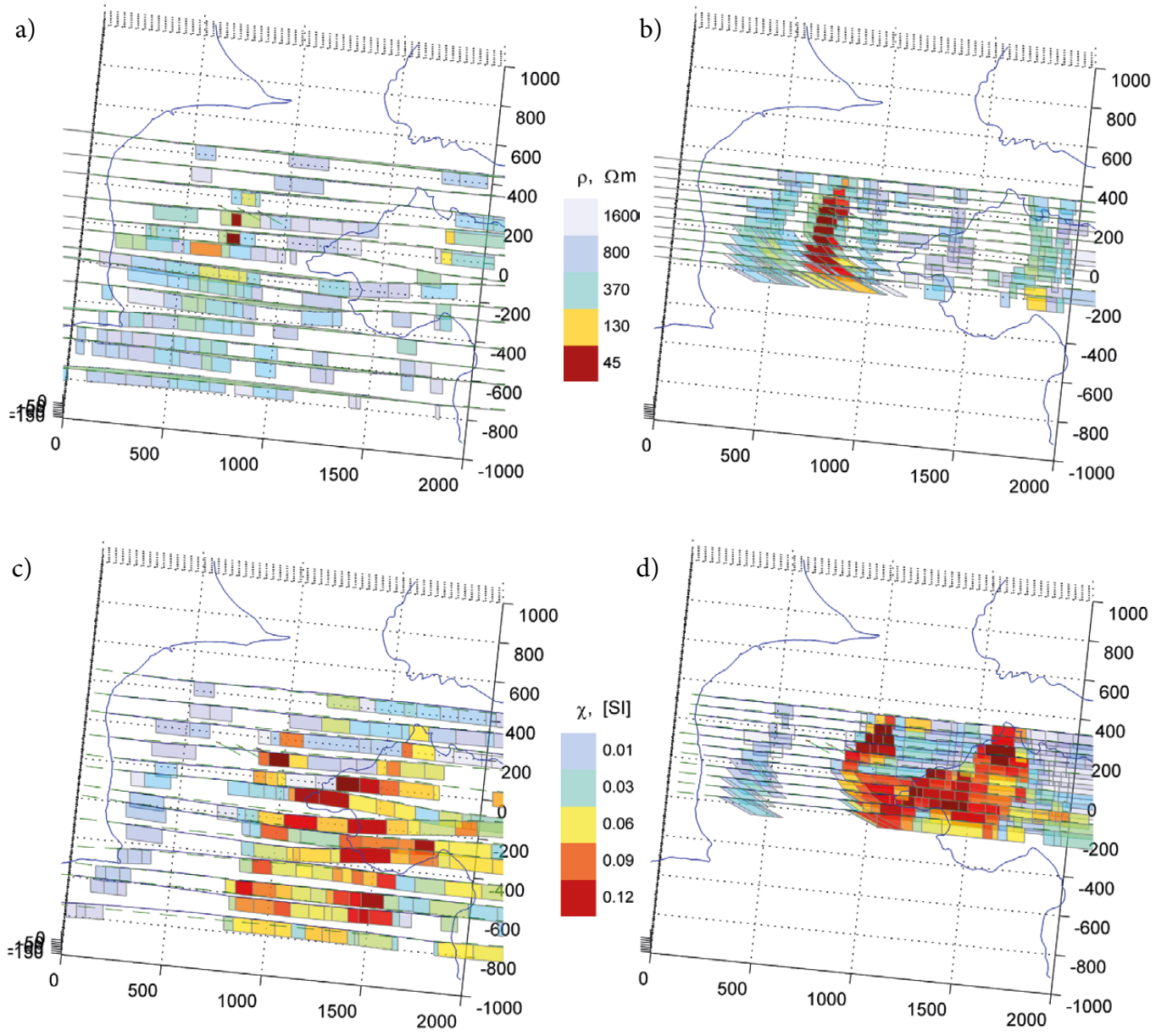

Fig. 10. Interpretation of electrical resistivity (Figs a and b) and susceptibility (Figs c and d) from Kellojärvi AEM (Figs a and c) and Slingram data (Figs b and d). The depth scale in metres of the cross-sections is in the lower-left corner of the maps. The blue lines depict the shoreline of Lake Kellojärvi. Flight line 201 is the nearest to the three drill holes.

CONCLUSIONS

3D geophysical modelling and inversion are needed to construct realistic earth models that are consistent with available geological and geophysical data. Large-scale and accurate numerical 3D EM modelling is a demanding computational problem. A common strategy to improve the computational efficiency is to separate the 3D computational meshes from the 3D earth model and, for instance, from the cell-based inversion mesh. Here, the 3D earth model, i.e. the interpretation model, was composed of layers and tabular bodies with individual electromagnetic properties. A local simulation mesh was used to calculate the complex response for each source point and each frequency. A local simulation mesh was constructed taking into account the resolution capability and the volume of influence (footprint) of the EM system at the used frequency in the local conductivity and magnetic permeability model. The local mesh should use small cells near the transmitter and receiver and coarser cells further away, and the volume of the local mesh should be larger than the volume of influence. The diffuse EM equations were solved using the finite-volume method, in which the local mesh is composed of rectangular cells. This type of approach limits the computer memory requirements. It could also speed up the computations, but above all it makes these calculations possible on an ordinary PC.

In practice, it is required that the 3D model is mapped properly from one presentation to another. Here, the calculated model in the local mesh should be effectively equivalent to the model presented as tabular bodies or as the modelling/inversion mesh. The method to calculate averaged values for a local mesh and to calculate partial derivatives of the system responses with respect to model parameters of tabular bodies is presented by Abubakar et al. (2009). The diffusive nature of the EM fields justifies this scheme for mapping.

Partitioning of the earth by geometric models with individual material properties σ, χ, and ε aids in the use of this finite-volume program and enables a simple 3D model-based interpretation process. The 2D modelling scheme presented by Abubakar et al. (2009) was in this study extended to three dimensions for the EM multiprofile data. The extension is straightforward, and the 3D modelling scheme is workable. For a more detailed model-based inversion, the strike direction could be more carefully taken into account.

The calculated synthetic Slingram and AEM responses demonstrated different types of coupling to tabular bodies that are anomalously electrically conductive and/or magnetically susceptible. Magnetic susceptibility causes a maximum anomaly when the primary magnetic field is parallel to the plate. The conductivity causes a maximum anomaly when the time-varying primary magnetic field (flux) passes through the plate. Simulated results demonstrated that the response caused by magnetization is more sensitive to the distance between the EM system and the target than the response caused by electromagnetic induction by eddy currents. The footprints of EM systems are different in shape and volume for conductivity and susceptibility. These theoretical EM results characterize the difference between EM induction and magnetic induction.

TMI depicts the anomalous magnetic field caused by induced and natural remanent magnetization, whereas a static remanent component has no effect on the susceptibility model inverted from AEM data. The cooperative interpretation of TMI and EM data provides a way to differentiate the contributions of induced and remanent parts in the TMI anomaly field. In magnetic measurements the inducing field is uniform, whereas in Twin Otter and Slingram measurements it is dipolar. Due to the geometrical attenuation of the EM field, the volume of influence is more local and smaller (shallower) in EM surveys than TMI surveys.

The simple 1D layered-earth susceptibility and resistivity interpretation using AEM data alone can be effectively non-unique in resistive environments, when the EM system is not sensitive enough to the conductivity structures. This ambiguity could be resolved using an EM system operating at higher frequencies, measuring densely and with various coil configurations and using 3D interpretation models. The combined inversion of magnetic TMI and EM data would also reduce the non-uniqueness.

The 3D model-based interpretation process was tested in the Kellojärvi case, where both conductivity and susceptibility have been used in the interpretation of Twin Otter AEM and ground Slingram data. The AEM interpretation process is quite straightforward, and here was carried out without

TMI information to better assess the direction of remanent magnetism. The above-mentioned ambiguity is evident in resistive locations. Additional *in situ* information could have been used in the interpretation. For example, the known lake bathymetry was important, and the outcropping magnetized rocks should have been outlined and used in the interpretation with topography. The parametric tabular 3D bodies and layers give a (rough) outline of the true conductivity and susceptibility structure, which was one aim of this work. The modelled susceptibility and conductivity values are in agreement with the measurements from the drill core samples. In the ultramafic formation, the ratio of the remanent to the induced magnetization has been estimated to be 2 or more, which agrees with petrophysics from drilled serpentinite in the study area. The direction of remanence appears to be aligned parallel to the geomagnetic field, at least in some profiles.

The ground Slingram data were found more sensitive to a thin vertical conductivity structure than AEM data. With two-frequency Slingram data, the need for TMI data is more obvious. The future goal is the joint inversion of EM and TMI data using available *a priori* information and constraints.

ACKNOWLEDGEMENTS

I would like to thank Harri Kutvonen, Heli Ojamo and Matti Niskanen for their help and Meri-Liisa Airo for her helpful comments. I also want to thank the reviewers, Markku Pirttijärvi and Ilkka Lahti, for their very constructive reviews.

REFERENCES

Abubakar, A., Habashy, T. M., Li, M. & Liu, J. 2009. Inversion algorithms for large-scale geophysical electromagnetic measurements. Inverse Problems 25, 123012, doi:10.1088/0266-5611/25/12/123012.

Airo, M.-L. & Säävuori, H. 2013. Petrophysical characteristics of Finnish bedrock – Concise handbook on the physical parameters of bedrock. Geological Survey of Finland, Report of Investigation 205, 33 p.

Beamish, D. & Leväniemi, H. 2010. The canopy effect in AEM revisited: investigations using laser and radar altimetry. Near Surface Geophysics 8, 103–115.

Commer, M. & Newman, G. A. 2008. New advances in three-dimensional controlled-source electromagnetic inversion. Geophysical Journal International, 172, 513–535.

Clark, D. A. 2014. Methods for determining remanent and total magnetizations of magnetic sources – a review. Exploration Geophysics 45, 271–304, doi: 10.1071/EG14013.

Cox, L. H. & Zhdanov, M. S. 2007. Large scale 3D inversion of HEM data using a moving footprint. 77th Annual International Meeting, SEG, Expanded Abstracts, 467–470.

Grant, F. S. & West, G. F. 1965. Interpretation theory in applied geophysics. McGraw-Hill. 584 p.

Farquharson, C. G., Oldenburg, D. W. & Routh, P. S. 2003. Simultaneous 1D inversion of loop-loop electromagnetic data for magnetic susceptibility and electrical conductivity. Geophysics, 68(6), 1857–1869, doi: 10.1190/1.1635038.

Haber, E. & Ascher, U. 2001. Fast finite volume simulation of 3D electromagnetic problems with highly discontinuous coefficients: SIAM Journal of Scientific Computations 22, 1943–1961.

Halkoaho, T. & Niskanen, M. 2012. A research report of nickel studies concerning the claim area of Pärsämänsuo 1 (register number of claim: 8344/1) in Kellojärvi, Kuhmo during years 2007–2011. Geological Survey of Finland, archive report 64/2012. 18 p + 29 app. [Electronic resource]. Available at: http://tupa.gtk.fi/raportti/arkisto/64_2012.pdf. (in Finnish)

Hautaniemi, H., Kurimo, M., Multala, J., Leväniemi, H. & Vironmäki, J. 2005. The 'three in one' aerogeophysical concept of GTK in 2004. In: Airo, M.-L. (Ed.), Aerogeophysics in Finland 1972–2004: Methods, System Characteristics and Applications. Geological Survey of Finland, Special Paper 39, 21–74.

Huang, H. & Fraser, D. C. 2001. Mapping of resistivity, susceptibility, and permittivity of the earth using a helicopter-borne electromagnetic system: Geophysics 66(1), 148–157, doi: 10.1190/1.1444889.

Leväniemi, H., Beamish, D., Hautaniemi, H., Kurimo, M., Suppala, I., Vironmäki, J., Cuss, R. J., Lahti, M. & Tartaras, E. 2009. The JAC airborne EM system AEM-05. Journal of Applied Geophysics, 67, 219–233.

Pirttijärvi, M., Abdelzaher, M. & Korja, T. 2013. Fast joint inversion of AEM and static magnetic field data. Geophysical Society of Finland, XXVI Geophysics Days, 97–99.

Plessix, R. E., Darnet, M. & Mulder, W. A. 2007. An approach for 3D multisource multifrequency CSEM modeling: Geophysics 72(5), SM177–SM184, doi: 10.1190/1.2744234.

Rahmani, A. R., Atley, A. E., Chen, J. & Wilt, M. J. 2014. Sensitivity of dipole magnetic tomography to magnetic nanoparticle injectates. Journal of Applied Geophysics 103, 199–214. [Electronic resource]. Available at: http://dx.doi.org/10.1016/j.jappgeo.2014.01.019. Last accessed 17 June 2015.

Sasaki, Y., Kim, J.-H. & Cho, S.-J. 2010. Multidimensional inversion of loop-loop frequency-domain EM data for resistivity and magnetic susceptibility: Geophysics 75(6), F213–F223, doi: 10.1190/1.3503652 .

Suppala, I., Oksama, M. & Hongisto, H. 2005. GTK airborne EM system: characteristics and interpretation guide-

lines. In: Airo, M.-L. (Ed.), Aerogeophysics in Finland 1972–2004: Methods, System Characteristics and Applications. Geological Survey of Finland, Special Paper 39, 103–118.

Tschirhart, P., Morris, B. & Hodges, G. 2013. A new regional/residual separation for magnetic data sets using susceptibility from frequency domain electromagnetic data. Geophysics, 78(6), B351–B359. doi: 10.1190/geo2012-0506.1 .

Um, E. S., Commer, M. & Newman, G. A. 2013. Efficient pre-conditioned iterative solution strategies for the electromagnetic diffusion in the Earth: finite-element frequency-domain approach. Geophysical Journal International 193, 1460–1473, doi: 10.1093/gji/ggt071 .

Wilt, M. J., Chen, J., Alumbaugh, D. L. & Rahmani, A. R. 2013. Dipole magnetics: using low frequency controlled-source EM to map magnetic anomalies. 83nd Annual International Meeting, SEG, Expanded Abstracts, http://dx.doi.org/10.1190/segam2013-0146.1 .

Won, I. J. & Huang, H. 2004, Magnetometers and electromagnetometers. The Leading Edge, 23, 448–451.

Yang, D., Oldenburg, D. W. & Haber, E. 2014. 3-D inversion of airborne electromagnetic data parallelized and accelerated by local mesh and adaptive soundings. Geophysical Journal International, 196, 1492–1507, doi: 10.1093/gji/ggt465 .

Geophysical signatures of mineral deposit types in Finland
Edited by Meri-Liisa Airo
Geological Survey of Finland, Special Paper 58, 89–106, 2015

PETROPHYSICAL AND ROCK MAGNETIC STUDIES TO AID AU EXPLORATION – CASE STUDIES FROM THE HÄME BELT, SOUTHERN FINLAND

by

Satu Mertanen[1] and Fredrik Karell[1]

Mertanen, S. & Karell, F. 2015. Petrophysical and rock magnetic studies to aid Au exploration – case studies from the Häme belt, southern Finland. *Geological Survey of Finland, Special Paper 58,* 89–106, 20 figures and 1 table.

Petrophysical, rock magnetic and anisotropy of magnetic susceptibility (AMS) measurements have been carried out on a porphyry type Cu-Au deposit in Kedonojankulma, on an orogenic gold deposit in Uunimäki and on the exploration target of Mäyrä in the Palaeoproterozoic Häme belt of Southern Finland. The mineralizations occur in strongly altered and sheared zones. The main aim of the laboratory studies has been to identify and characterize ore-related alteration processes that are reflected in the physical properties of rocks. The studies have focused on magnetic properties and the identification of magnetic minerals using rock magnetic tests. Magnetic mineralogy was verified by SEM studies.

In the Kedonojankulma quartz-plagioclase porphyrite occurrence, the induced and remanent magnetizations are slightly higher in the altered auriferous shear zone than in the less altered host rock. In the altered zone, the only magnetic mineral is monoclinic pyrrhotite with a high Curie temperature, while in the host rock the main magnetic mineral is ilmenite with minor magnetite.

In the Uunimäki gabbroic occurrence, the highest magnetization values correlate with strong IP anomalies, the magnetization being carried by monoclinic pyrrhotite with a high Curie temperature. In the more weakly magnetized rocks, the magnetization predominantly resides in ilmenite. In the strongest IP anomaly area, which is also regarded as the most gold bearing, the remanent magnetization also has strong intensity, and a Svecofennian age remanence could be isolated. The result thus suggests that provided that gold and pyrrhotite are contemporaneous at the site, the gold is post-tectonic.

Based on AMS data, the magnetic foliation planes follow the general foliation structures in both formations, although the degree of anisotropy varies considerably.

In the Mäyrä occurrence, the magnetization of the shear zone has decreased due to hydrothermal alteration. The surrounding gabbros, whether coarse-grained dark gabbro or fine-grained lighter coloured gabbro, contain magnetite as the main magnetic mineral, while the shear zone also contains pyrrhotite in addition to magnetite.

Keywords (GeoRef Thesaurus, AGI): paleomagnetism, magnetic properties, magnetic susceptibility, magnetization, petrophysics, magnetic minerals, gold ores, mineral exploration, Häme Belt, Proterozoic, Paleoproterozoic, Finland

[1]Geological Survey of Finland, P.O. Box 96, FI-02151 Espoo, Finland

E-mail: satu.mertanen@gtk.fi, fredrik.karell@gtk.fi

INTRODUCTION

Petrophysical laboratory measurements of mineralized and barren rock samples have been carried out at several locations in the Palaeoproterozoic Häme belt of southern Finland (Fig. 1). The study areas were selected utilizing airborne geophysical data. Most systematic and detailed sampling was carried out across hydrothermal alteration zones in the porphyry type Cu-Au deposit in Kedonojankulma, in the orogenic Au deposit of Uunimäki and the exploration target of Mäyrä, the results of which are described in this paper.

The main aim of the study was to identify and characterize alteration processes that are reflected in the physical properties and especially in the magnetic properties of the rocks during the mineralization processes. Circulation of hydrothermal fluids and consequent fluid–rock interaction can significantly modify the physical properties of ore-bearing deposits. These processes typically also produce compositional and textural changes in ferromagnetic minerals, which can be studied and quantified by using magnetic methods. Therefore, in addition to basic petrophysical properties (density, magnetic susceptibility and remanence), rock magnetic tests were carried out to identify the magnetic minerals and their grain sizes, which also have relevance to the stability of remanence.

Palaeomagnetic studies were conducted for some of the study objects to delineate the timing for the alteration process. AMS (anisotropy of magnetic susceptibility) studies were carried out to characterize the fabrics of the occurrences. As the known ore bodies are related to alteration zones and because detailed petrophysical investigations at the outcrop scale can delineate differences between ore and host rocks, the studied petrophysical properties have relevance to exploration.

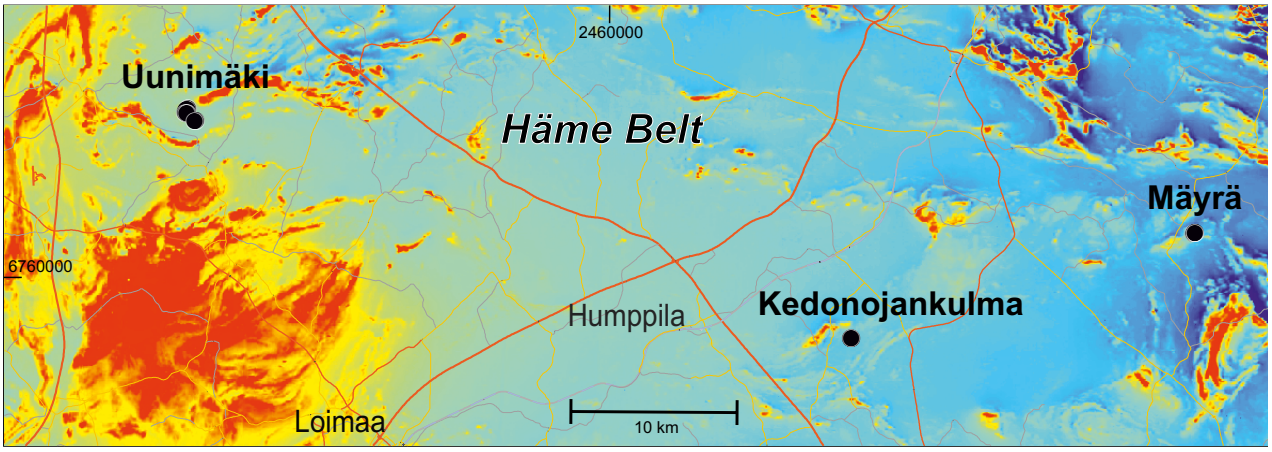

Fig. 1. Aeromagnetic map of the Häme belt showing the study areas. The studied sites are indicated by black circles and comprise Mäyrä (sites 1–3), Kedonojankulma (sites 4–10) and Uunimäki (sites 16–25).

GEOLOGICAL BACKGROUND

The bedrock of southern Finland was formed during the Svecofennian orogeny at 1.9–1.8 Ga, involving several collisional and metamorphic stages that produced different types of ore formations. The studied formations occur in the Häme belt, where the age of magmatic activity is in general 1.88 Ga (Saalmann et al. 2009), and the last active orogenic evolution took place at ca. 1.79 Ga (Lahtinen et al. 2005). The ore formations can be either syngenetic or later than the earliest deformation, but in any case their formation precedes the youngest brittle deformation at 1.79 Ga (see Eilu et al. 2012 for references).

The main study objects comprised the Kedonojankulma porphyry type Cu-Au deposit hosted by the subvolcanic quartz-plagioclase porphyritic phase of a tonalitic intrusion (Tiainen et al. 2012) and the Uunimäki orogenic gold deposit hosted by shear zones in a metamorphosed gabbro (Grönholm and Kärkkäinen 2013). In addition, a

potentially Au mineralized and strongly altered shear zone and host gabbroic rocks in the Mäyrä target were investigated.

The Kedonojankulma study area (Fig. 2) is located in the western part of the Svecofennian volcanic-intrusive Häme belt (Fig. 1). The Cu-Au occurrence is mainly located in a porphyritic tonalitic intrusion and partly in the surrounding volcanic host rocks (Tiainen et al. 2012, 2013). The granitoids surrounding the Kedonojakulma occurrence represent volcanic arc type granitoids. The size of the occurrence is about 1.5 x 0.5 km. The highest Cu-Au contents occur in a strongly altered and sheared quartz-plagioclase porphyritic phase of the tonalitic intrusion, in the Rusakkokallio outcrop (Fig. 2), where the quartz-plagioclase porphyry is cut by a network of thin quartz veins. The main ore mineral is chalcopyrite and the main magnetic mineral is pyrrhotite (Tiainen et al. 2012).

The Uunimäki gold prospect of the age of ca. 1.88 Ga in the Häme belt (Fig. 1) is hosted by shear and fault zones within a heterogeneous gabbro intrusion that is metamorphosed but only weakly deformed outside the shear zones (Grönholm and Kärkkäinen 2013). The gabbro is typically fine or medium grained. One gabbro type contains uralite phenocrysts (as remnants of igneous clinopyroxene) within fine-grained groundmass and one type is equigranular. A network of thin cross-cutting quartz veins occurs at some outcrops. Typical ore minerals include locally abundant pyrrhotite, and minor chalcopyrite, arsenopyrite and ilmenite. The Au-critical area correlates with a distinct IP anomaly that was used as the basis of petrophysical sampling. In the gravimetric maps, the geochemically gold potential NW–SE-trending zones appear to be related to gravity minima (Vuori et al. 2007). Gold-critical major shear and fault zones are also recognized in aeromagnetic maps as diffuse non-magnetic and locally gently curving lineaments.

The Mäyrä target in Hämeenlinna has not been extensively studied, but it is important as it is located in a notable till geochemical anomaly area observed in recent mapping by GTK in the Häme belt (Fig. 1) (Huhta 2013, 2014). The main rock types are a coarse-grained gabbro and a more fine-grained gabbro, the latter possibly being an inclusion in the coarse-grained rock. Both gabbro types are cut by a shear zone that might be related to hydrothermal alteration associated with the geochemical Au anomaly in the region. The main sulphide minerals are pyrrhotite and arsenopyrite.

SAMPLING, INSTRUMENTS AND METHODS

Samples were taken with a portable Pomeroy minidrill and oriented with the sun and a magnetic compass. The diameter of samples was 2.5 cm and the length ca. 6 cm. In addition to oriented core samples, oriented and un-oriented hand samples were taken from some sites for petrophysical measurements.

At Kedonojankulma (Fig. 2), samples were taken from five sites (sites 4–8). Sites 4–6 in Rusakkokallio are located close to each other in an outcrop area of about 50 x 10 m. They comprised the subvolcanic quartz-plagioclase porphyritic phase of the tonalitic intrusion that hosts the Cu-Au occurrence (Tiainen et al. 2012). At site 4, five samples were taken from the least altered quartz-plagioclase-porphyry. At site 5, five samples were taken from the more altered quartz-plagioclase-porphyry and at site 6 (close to site 5), seven samples were taken across a profile of an altered rusty shear zone. Sites 7 and 8 are located about 200 m apart from each other in Passi (Fig. 2). At site 7, the rock type is tonalite with sporadic epidote inclusions. Four core samples were taken from unaltered tonalite (samples 7a, Fig. 3) and three from epidotized and sheared inclusions in the tonalite (samples 7b, Fig. 3). At site 8, a contact between tonalite and quartz-plagioclase-porphyry is clearly visible. Three oriented hand samples were taken from the tonalite (samples 8a, Fig. 3) and three samples from the quartz-plagioclase-porphyry (samples 8b, Fig. 3).

Sampling of gabbro at Uunimäki (Fig. 14) was planned by utilizing the IP anomaly map in order to constrain the physical properties of rocks of the lowest and highest anomaly, the latter one suggested to be related to the Au occurrence. A profile across the IP anomaly, comprising 8 sites, was sampled. In addition, two sites with a weaker IP anomaly outside the profile were sampled. Approximately 5 oriented core samples were taken at each site. In addition, petrophysical measurements were carried out on three borehole cores (M211109R314,

M211109R315 and M211109R316) that were also geochemically analysed (Labtium Oy) in the course of ore potential investigations.

The exploration target Mäyrä comprises gabbroic rocks and was sampled at three sites (sites 1–3). At site one, nine oriented samples were taken across a profile over a shear zone. The width of the profile was 10 m and the most altered central part of the shear zone is about 10 cm broad (samples 1.3.–1.4). The main rock type is black coarse-grained gabbro (samples 1.1, 1.2, 1.7, 1.8 and 1.9), but the other side of the most altered zone is bordered by a band where the gabbro has a lighter colour and is more fine grained (samples 1.5 and 1.6). Corresponding to site one, coarse-grained gabbro and lighter fine-grained gabbro were sampled at two other sites (sites 2 and 3, respectively) outside the profile.

In the laboratory, samples were processed into standard cylinders (height 2.5 cm, diameter 2.1 cm). The principal petrophysical parameters measured before the palaeomagnetic and AMS measurements were magnetic susceptibility (applied field intensity of 130 A/m), electrical conductivity and density. Remanent magnetization was measured with a 2G-RF SQUID magnetometer. Alternating field and thermal demagnetizations, coupled with SQUID measurements, were applied to some of the samples. Anisotropy of magnetic susceptibility (AMS) was measured with an Agico KLY-3 kappabridge (applied field intensity of 300 A/m). Determinations of magnetic mineralogy comprised thermomagnetic analyses in an Ar atmosphere with a KLY-3/CS-3 device. Three component IRM measurements, so-called Lowrie tests (Lowrie 1990), were carried out with a Molspin pulse magnetizer, coupled with thermal demagnetizations and measurements with SQUID or GTK-built spinner magnetometers. In the Lowrie test, the sample is subjected to three different high magnetic fields (1.5 T, 0.4 T and 0.12 T) along the z-, y- and x-axes of the sample, respectively. The sample is subsequently heated to increasing temperatures (typically up to 680°C). The measurements give information on the magnetic minerals, their grain sizes and magnetic domain states (see Mertanen and Karell, 2009, 2011 for a detailed description of the method). Three Lowrie test measurements were carried out at the Solid Earth Geophysics Laboratory of the University of Helsinki (by Dr Johanna Salminen), where the thermal demagnetizations could be performed in an Ar atmosphere and the remanence measurements were carried out with a 2G-DC SQUID magnetometer.

RESULTS AND DISCUSSION

Mean petrophysical properties of all three study areas are presented in Table 1.

Kedonojankulma

Sites 4–6, Rusakkokallio

Figure 2 illustrates the locations of the sampling sites on an aeromagnetic map, which evidences the very low magnetization of the Kedonojankulma deposit. Sites 4–6 are from the Rusakkokallio quartz-plagioclase porphyry, with the highest Cu and Au contents, and sites 7–8 from the Passi area, where the outcrops are tonalite and plagioclase-quartz porphyry with low Cu and Fe. Figure 3a presents the susceptibility – density plot, and Figure 3b the susceptibility – Q-value plot of the Kedonojankulma samples. The Q-value is the relationship between the remanent magnetization and the induced magnetization, and reflects the dominance of remanence if the value is over 1.

The quartz-plagioclase porphyries at the Rusakkokallio site are typically weakly magnetized (Figs 3a and 3b). At the Rusakkokallio site 4, with the least altered quartz-plagioclase-porphyry, the magnetic susceptibilities and remanence intensities are generally lower compared to the more altered rocks of the auriferous shear zone of sites 5 and 6. In the shear zone, the overall susceptibilities and remanence intensities and, consequently, the Q-values are slightly increased due to increased amounts of pyrrhotite. The Q-values are highest within the shear zone, indicating the dominance of remanent magnetization over induced magnetization. The altered rocks (sites 5 and 6) show

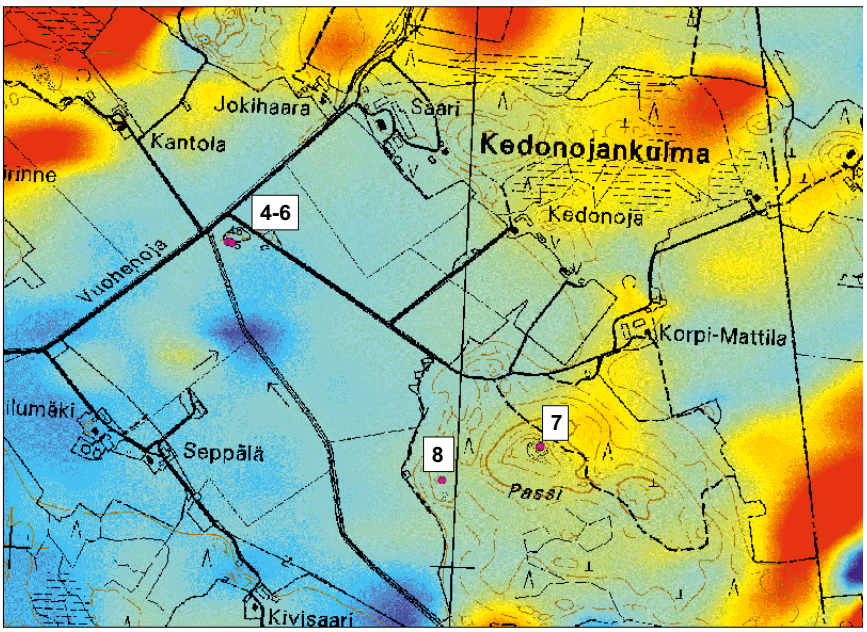

Fig. 2. Sampling sites in Kedonojankulma shown on an aeromagnetic map. Sites 4–6 are in Rusakkokallio and sites 7 and 8 in Passi. Contains data from the National Land Survey of Finland Topographic Database 03/2013.

Table 1. Mean petrophysical properties of the studied rocks

Site	Rock type	Comment	x	y	n	Density	Suscept.	Reman.	Q
						kg/m^3	x 10^{-6}	mA/m	
Kedonojankulma									
4	Q-plg-porph.	Least alt.	6761604	3311775	6	2655	154.0	1.0	0.17
5	Q-plg-porph.		6761606	3311781	6	2679	321.5	63.9	3.23
6	Q-plg-porph.	Shear zone	6761602	3311785	9	2676	214.0	41.8	3.93
7A	Tonalite		6761142	3312482	5	2735	571.0	3.7	0.13
7B	Tonalite	Epidote	6761142	3312482	3	2801	5526.7	46.3	0.22
8A	Q-plg-porph.		6761066	3312260	16	2660	695.1	19.5	1.85
8B	Tonalite		6761066	3312260	8	2742	1910.1	45.6	0.35
Uunimäki									
16	Granodiorite		6774778	3273855	14	2775	395.1	3.6	0.23
17	Gabbro		6774732	3273788	13	2904	775.5	105.6	2.92
18	Gabbro		6774680	3273773	11	3006	845.6	5.1	0.15
19	Gabbro		6774650	3273758	12	3082	1050.8	3.9	0.03
20	Gabbro		6774603	3273758	14	3007	887.6	21.2	0.03
21	Gabbro		6774532	3273696	11	2899	632.5	0.5	0.03
22	Uralite porph.		6774510	3273832	12	3022	975.6	689.4	14.73
23	Gabbro		6774489	3273772	14	2955	740.9	0.9	0.03
24	Gabbro		6774074	3274308	13	3012	759.3	2.8	0.09
25	Gabbro		6774080	3274233	12	3002	823.5	0.9	0.03
Mäyrä									
1	Gabbro	Coarse gr.	6767616	3331387	10	3002	4056.8	260.4	1.39
1	Gabbro	Shear zone	6767616	3331387	3	2963	769.3	0.9	0.03
1	Gabbro	Fine gr.	6767616	3331387	4	2938	1278.0	26.0	0.48
2	Gabbro	Coarse gr.	6767640	3331467	10	2999	7567.2	1496.3	5.84
3	Gabbro	Fine gr.	6767638	3331456	11	2902	1035.2	19.3	0.45

Note. *Site gives the site number, Q-plg-porph. is quartz-plagioclase porphyry, x,y are the coordinates of the site, n is the number of specimens. Suscept. is the magnetic susceptibility, Reman. is the remanence, Q is the Königsberger ratio (the ratio of the remanent magnetization to the induced magnetization). In Kedonojankulma, the sites in Passi are divided according to the visible occurrence of epidotic inclusions at site 7B and according to rock type at site 8.*

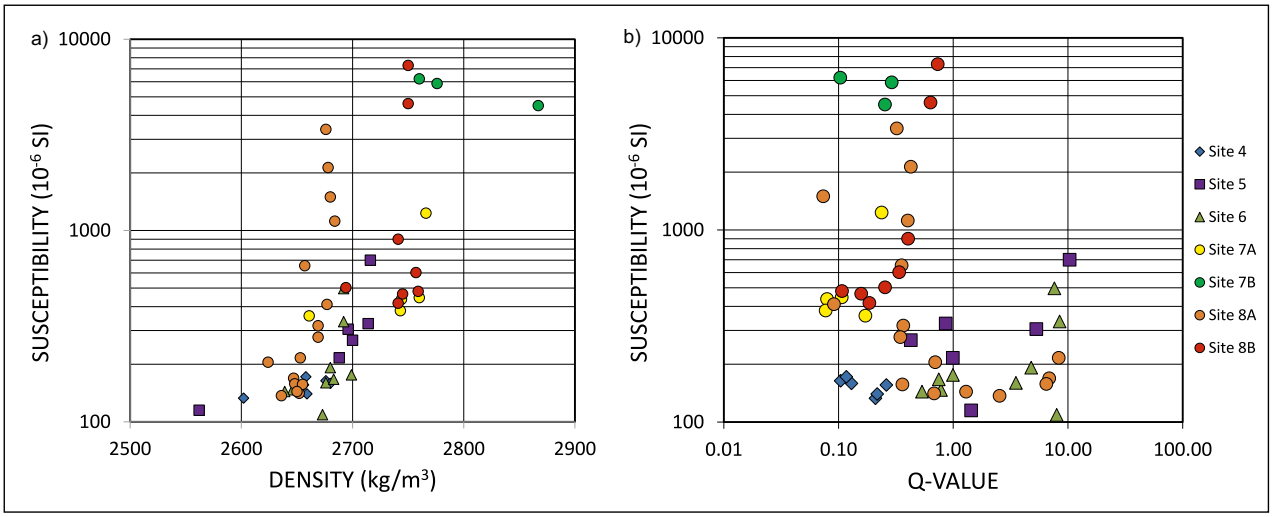

Fig. 3.a) Susceptibility – Density plot, b) Susceptibility – Q-value plot of the Kedonojankulma samples.

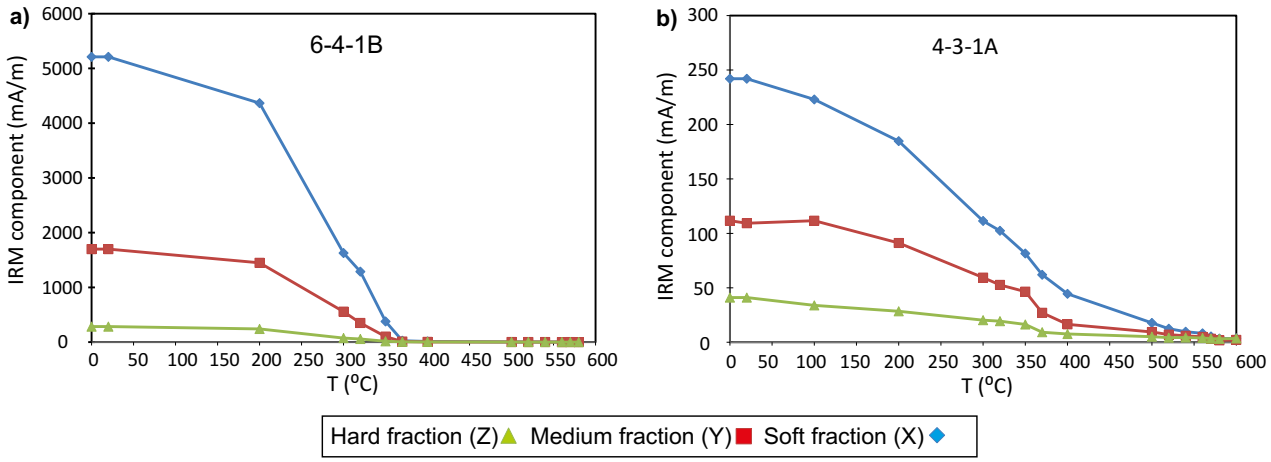

Fig. 4. Three-axis isothermal magnetization (Lowrie test) of sample 6-4-1B from the Rusakkokallio shear zone. Magnetizations were produced along three orthogonal directions: the Z component in magnetizing field 1.5 T, the Y component in field 0.4 T and the X component in field 0.12 T. a) Only pyrrhotite, with an exceptionally high Curie temperature of 350 °C, occurs, b) Lowrie test of sample 4-3-1A from the least altered plagioclase-quartz porphyry at the Rusakkokallio site. Both pyrrhotite and magnetite with unblocking temperatures of about 560 °C occur.

considerable internal variation in magnetic properties, which reflects the varying content of magnetic material in the rock. On the whole, the magnetic properties at Rusakkokallio have somewhat increased due to alteration. Densities are not markedly affected by the alteration, as both the unaltered and most altered rocks have the same approximate densities of ca. 2670 kg/m^3.

At the Rusakkokallio sites, the typical magnetic mineral is monoclinic pyrrhotite with an exceptionally high Curie temperature of ca. 370 °C (Fig. 4a, specimen 6-4-1B). The typical Curie temperature of ferrimagnetic monoclinic pyrrhotite is 320 °C, and a disordered lattice structure or impurities in the lattice were therefore considered as the source of high temperatures. According to SEM studies, however, the pyrrhotite does not contain impurities, but the composition at Rusakkokallio is typical for monoclinic pyrrhotite.

The explanation for the observed Curie temperature remains unresolved. Lowrie test measurements, including thermal demagnetizations in an argon atmosphere at the University of Helsinki, also give high Curie temperatures. As shown below (see the results for the Uunimäki deposit), the high Curie temperature of pyrrhotite seems to be a common phenomenon in the studied formations. The sheared rocks of site 6 do not contain other magnetic minerals than pyrrhotite. In addition, chalcopyrite and ilmenite are observed optically

in SEM images (Fig. 5), but they do not contribute to the magnetization properties of the rock. In the unsheared rock of site 4, pyrrhotite also has a high Curie temperature of 370 °C. In these rocks, pyrrhotite occurs together with small amounts of magnetite (Fig. 4b, specimen 4-3-1A) or more probably ilmenite (see discussion on Uunimäki). The results thus suggest that shearing was accompanied by reducing fluid flow that produced pyrrhotite at the expense of magnetite/ilmenite. The gold and/or copper were probably formed in the same process.

At sites 4–6, electrical conductivities were in general very low, except for few samples from sites 5 and 6, where the conductivity was increased due to an excess of pyrrhotite. This result is in agreement with ground IP surveys, which have revealed an increased IP anomaly in the sheared area in Rusakkokallio (Tiainen et al. 2012).

For palaeomagnetic studies, some of the samples were demagnetized in order to obtain the characteristic remanent magnetization component that could give information on the relative age of the shearing and mineralizing fluid event. However, the directions of remanence were found to be scattered at each site, and palaeomagnetic data could not therefore give further information on the timing of mineralization. The scatter of directions may indicate that the fluid flow was followed by or was contemporaneous with shearing, which randomized and destroyed the original remanence directions.

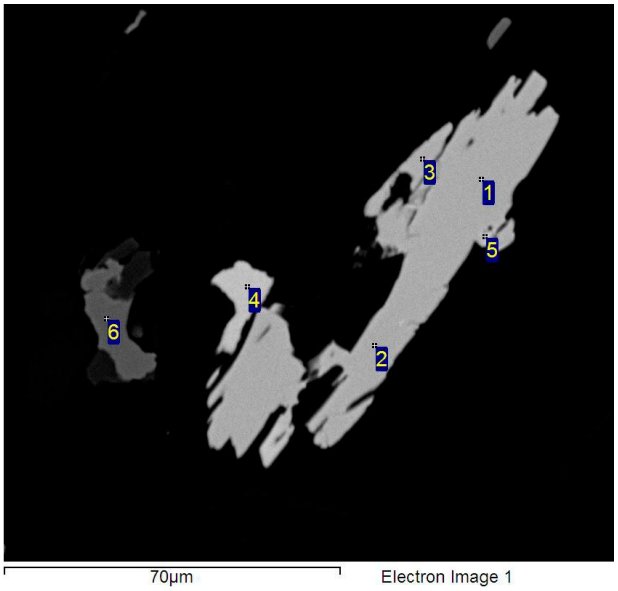

Fig. 5. SEM image of sample 6-1-1A from the shear zone in Kedonojankulma. 1-3 = pyrrhotite, 4 = chalcopyrite, 6 = ilmenite.

Sites 7–8, Passi

At Passi (Fig. 2), some of the plagioclase-quartz porphyries have similar magnetic properties to those at sites 5 and 6 of the sheared Rusakkokallio plagioclase-quartz porphyries; the low susceptibility and higher Q-value (over 1, Site 8A, Table 1) also indicate the dominance of pyrrhotite in these rocks. In some of the samples, the susceptibilities are significantly higher due to magnetite, which occurs together with only small amounts of pyrrhotite (Table 1). For example, sample 8-1-2A (Fig. 6a) has a high susceptibility value of 1500 x 10^{-6} SI compared with the mean value (695 x 10^{-6} SI) of the site (site 8A, Table 1). The magnetic mineralogy of these samples from Passi (Fig. 6a) resembles the unsheared plagioclase-quartz porphyry samples of the Rusakkokallio site 4 (Fig. 4b, site 4, Table 1), although the susceptibility values (site 8A, Table 1) are higher due to a higher amount of magnetite. The pyrrhotite has a similarly high Curie temperature of ca. 370 °C as at the Rusakkokallio sites. The magnetite-bearing tonalite (Fig. 6b) carries the highest susceptibility values (sites 7A, 7B and 8B, Table 1), consistent with aeromagnetic data. In the epidotized inclusions, the magnetization values and densities are the highest, which can also affect the aeromagnetic anomaly pattern. In two specimens of one tonalite hand sample, the magnetization values are significantly high, which reflects the unhomogeneity of the rock.

According to AMS data (Fig. 7) the magnetic foliations at Rusakkokallio strike almost vertically along the general NE–SW trend of shearing, and magnetic lineations plunge moderately to the SW. The Rusakkokallio samples have slightly lower anisotropy degrees (6–10%) than the samples from Passi (11–13%). In particular, the least altered samples from Rusakkokallio (sites 4–5) are characterized by low anisotropy degrees accompanied by low magnetic susceptibilities. At Passi, the magnetic foliations dip steeply to the SE and the magnetic lineations plunge moderately to the S-SE. The shapes of AMS ellipsoids are predominantly oblate.

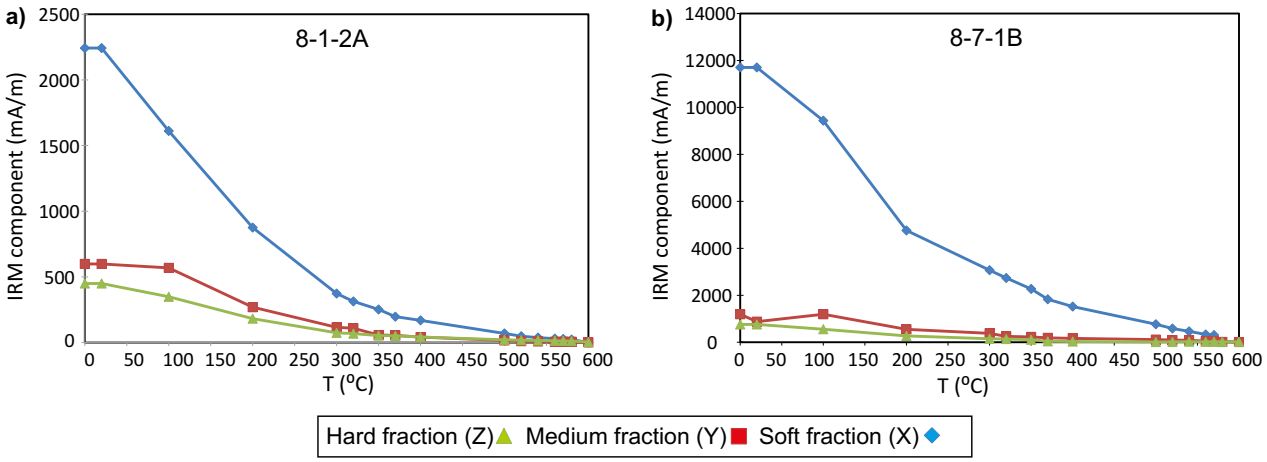

Fig. 6.a) Lowrie test of sample 8-1-2A from the plagioclase-quartz porphyry at the Passi site. Both pyrrhotite and magnetite occur. For explanations, see Fig. 4a, b) Lowrie test of sample 8-7-1B of tonalite at the Rusakkokallio site. The main ferromagnetic mineral is coarse-grained magnetite, shown as a dominance of the low coercivity x-phase.

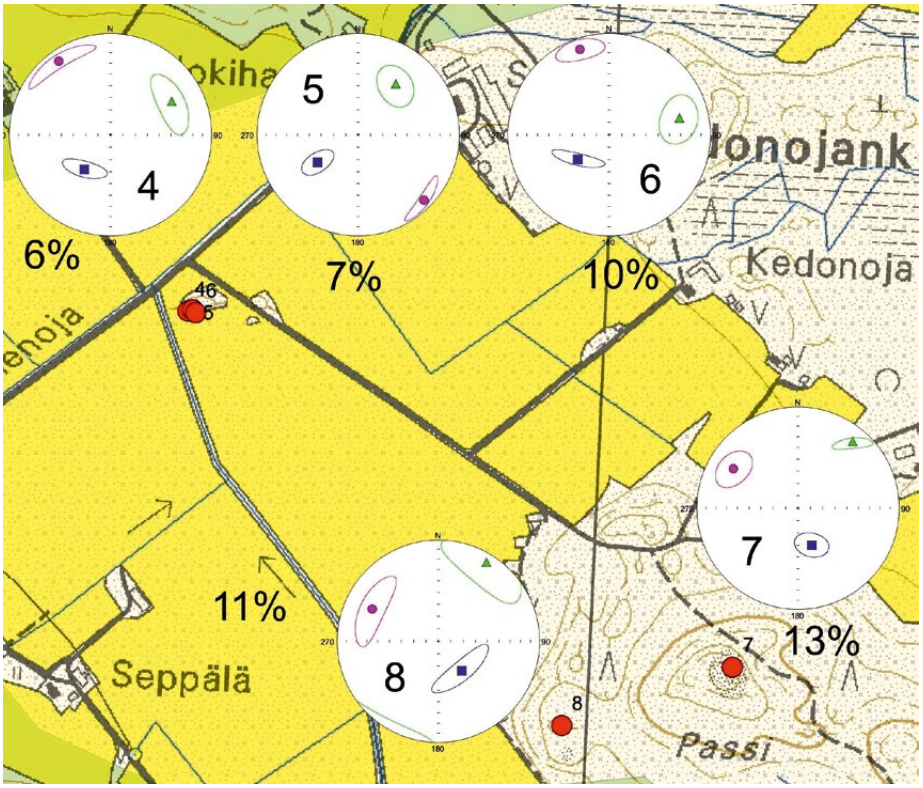

Fig. 7. AMS data from Kedonojankulma. The anisotropy degree (P') is shown as percentages for each site (numbers 4–8). The mean AMS directions of the principal axes k1 (blue square), k2 (green triangle) and k3 (red circle) are shown with their α95 confidence ellipses. Contains data from the National Land Survey of Finland Topographic Database 03/2013.

Uunimäki

The Uunimäki gabbro is characteristically weakly magnetized (Fig. 8). On the aeromagnetic map the deposit is within a NW–SE trending structure, where the total magnetization is only slightly higher compared with the surrounding granodiorite. The highest magnetization values and conductivities correlate with a strong IP anomaly (Fig. 14).

Sampling was carried out by utilizing the IP anomaly so that samples were taken outside the highest IP anomaly (sites 16, 21 and 23–25, Fig. 14) and within the highest anomaly area (sites 17–20 and 22). The susceptibility – density plot is presented in Figure 9a and the susceptibility – Q-value plot in Figure 9b.

Figure 9a presents a linear correlation between susceptibility and density, which mostly reflects the amount of magnetic minerals in the rocks. The susceptibilities are in general very low, below 1000 x 10^{-6} (SI), and for most samples the densities vary between ca. 2850 and 3050 kg/m^3. In general, susceptibilities below 1000 x 10^{-6} (SI) suggest that the samples do not contain significant amounts of ferromagnetic minerals. Exceptionally low values are seen in samples from site 16 of the surrounding granodiorite. Higher density and susceptibility values come from inside the high IP anomaly area due to increased amounts of pyrrhotite, as discussed below. Sites 17, 19 and 22 show the widest variation in magnetic properties and density, which probably reflects both the original compositional differences and the variation in the degree of alteration.

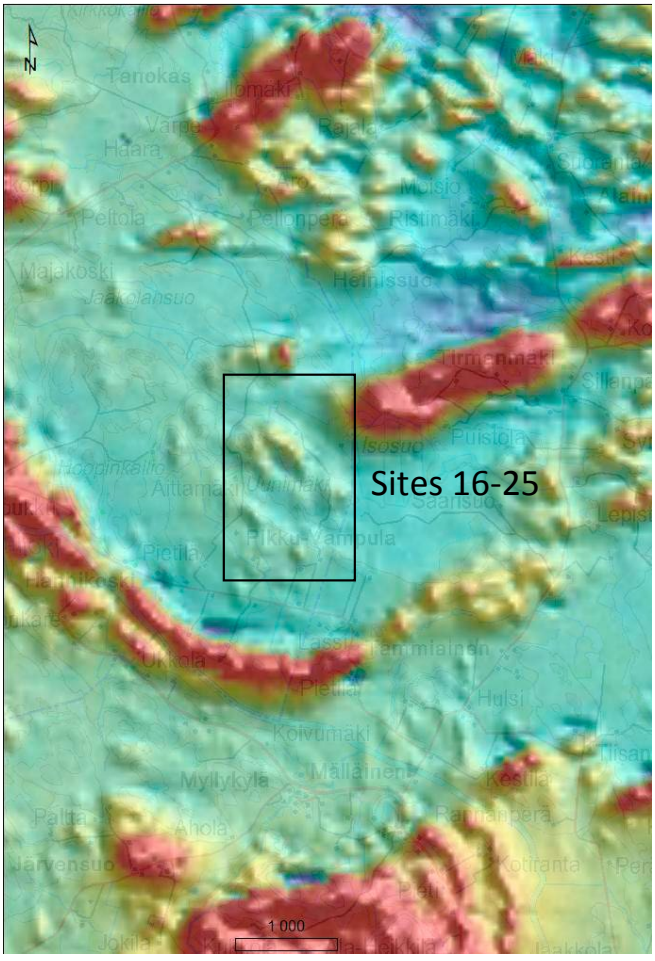

Fig. 8. An aeromagnetic map with the square showing the sampling area in Uunimäki. Detailed sampling sites are indicated in Fig. 14. Contains data from the National Land Survey of Finland Topographic Database 03/2013.

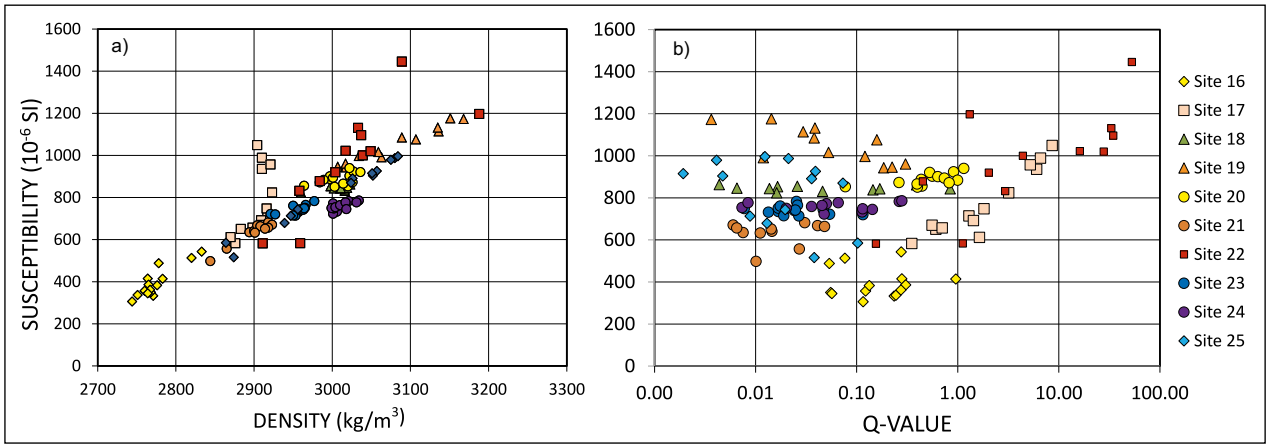

Fig. 9. Petrophysical properties of the Uunimäki deposit. a) Susceptibility – Density plot, b) Susceptibility – Q-value plot.

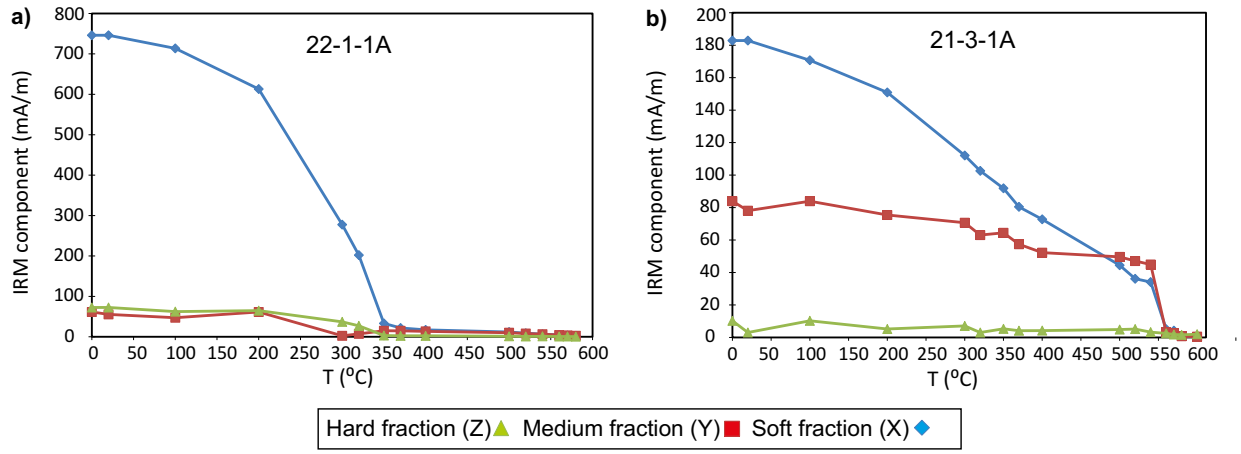

Fig. 10. Lowrie test of samples from the Uunimäki deposit. a) Sample 22-1-1 is from the highest IP anomaly and shows only coarse-grained pyrrhotite as the ferromagnetic mineral. b) Sample 21-3-1 is outside the highest IP anomaly and shows magnetite as the main ferromagnetic mineral. As discussed in the text, the magnetite may have been formed during laboratory heating.

The susceptibility – Q-value plot (Fig. 9b) illustrates that the intensities of remanent magnetization are typically below 1, indicating the dominance of induced magnetization over remanence. Only at sites 17 and 22 do the remanences dominate and show Q-values higher than 1. Site 22 is a fine-grained uralite porphyrite and has the highest magnetization values, in accordance with the highest magnetic (Fig. 8) and IP anomalies (Fig. 14).

According to Lowrie tests, the rocks with the highest IP anomaly carry monoclinic subordinate pyrrhotite with exceptionally high Curie temperatures of ca. 350–370 °C (Fig. 10a). The same high Curie temperatures were obtained from sites 17–18, 20 and 22. However, two samples from site 22 were studied with thermomagnetic curves (susceptibility versus temperature), and they show pure monoclinic pyrrhotite with a typical Curie temperature of 320 °C (Fig. 11). Likewise, according to SEM analyses of samples from sites 17 and 22 (Fig. 12), the observed pyrrhotite has a typical composition without impurities. These samples have corresponding high Q-values and susceptibilities (Fig. 9b), and both show high Curie temperatures for pyrrhotite.

Rochette et al. (1990) described an almost similar situation with an unexceptionally high unblocking temperature of 350 °C for monoclinic pyrrhotite in the Lower Jurassic schists. The origin of the high temperature was not resolved, but one explanation could be in the ordering of iron vacancies in the lattice of pyrrhotite. Zegers et al. (2003) also found high unblocking temperatures of up to 380 °C, and they suggested, based on studies by Graham et al. (1987), that small amounts of oxygen occur in the crystal lattice of pyrrhotite. As the origin of the high Curie temperature of pyrrhotite

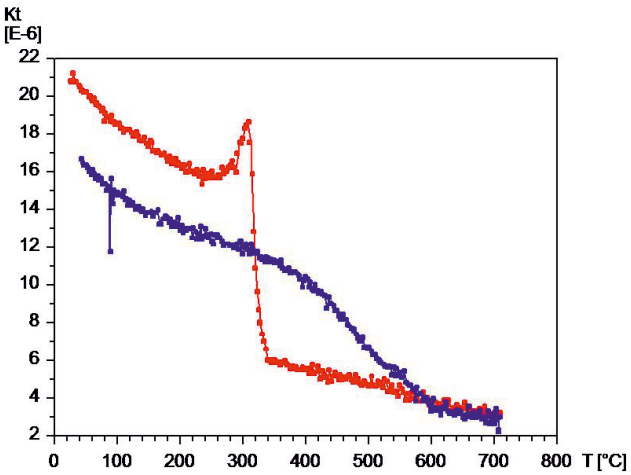

Fig. 11. Thermomagnetic curves showing magnetic susceptibility (μSI) vs. temperature (°C) for sample 22-4-1B from site 22. The red line denotes heating and the blue line is a cooling curve. The vertical axis is in arbitrary units, as the susceptibility is not corrected for actual sample volume. The heating curve shows a typical Curie temperature of 320 °C for pyrrhotite.

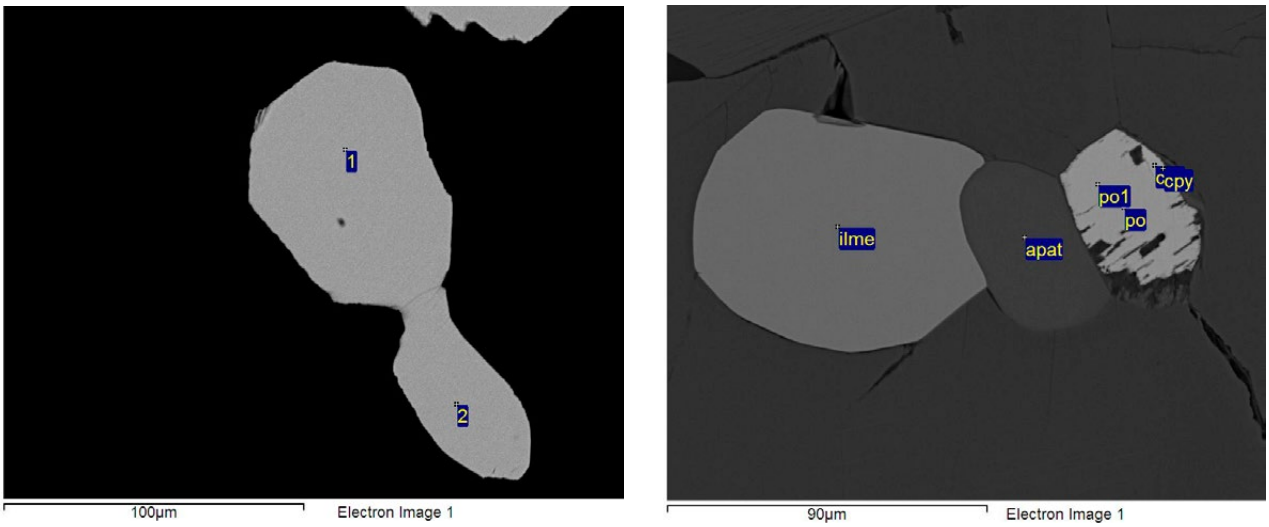

Fig. 12. SEM images from the Uunimäki deposit. a) uralite porphyritic gabbro from site 22 (sample 22-4-1B) showing solid grains of pyrrhotite (numbers 1 and 2), b) SEM image of gabbro from site 17 showing a large ilmenite grain in addition to apatite (apat) and intergrown pyrrhotite (po) and chalcopyrite (cpy).

in Uunimäki, and as shown before also in Kedonojankulma, was not resolved along this study, it should be studied more thoroughly in the future, as it may have some relevance to the occurrence of ore mineralogy. According to SEM studies, the sites of the highest IP anomaly also contain some ilmenite and chalcopyrite (Fig. 12).

The lowest magnetization values were found among weak IP anomalies (sites 16, 21 and 23–25, Fig. 14). According to Lowrie tests, these samples carry magnetite with an unblocking temperature of 560 °C (Fig. 10b, sample 23-2-1R). However, SEM studies indicate that the Fe oxide mineral is ilmenite (Fig. 12b, sample 17-1-1A). The occurrence of ilmenite instead of magnetite is supported by low susceptibilities (Fig. 9) and thermomagnetic curves that do not show Curie temperatures of magnetite. The Curie temperatures of magnetite in the Lowrie tests may be explained by laboratory heating, when mafic Fe-bearing silicate minerals or pyrrhotite have altered to magnetite. Therefore, this test is not suitable for these samples as such. It can be observed, however, that Curie temperatures of magnetite come only from the low IP anomaly areas whereas, the high IP anomaly area shows only pyrrhotite in the Lowrie and the thermomagnetic tests. In the weakly magnetic rock around the high IP anomaly, very small amounts of pure monoclinic pyrrhotite with a typical Curie temperature of 320 °C (Fig. 10b) were also revealed, in addition to ilmenite. Some of the samples also showed a very weak drop in intensity at 350–370 °C.

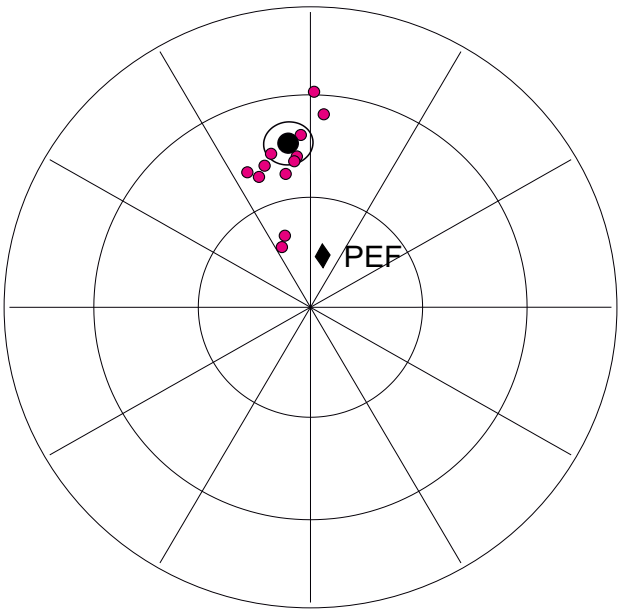

Fig. 13. Natural Remanent Magnetization (NRM) directions of samples from site 22, before AF demagnetization. The black circle with its α95 confidence circle shows the mean remanence direction after AF demagnetization of the samples. PEF shows the Present Earth's Field direction of the site.

The overall rock magnetic results from the Uunimäki gabbro thus indicate that the main ferromagnetic mineral in the unaltered rock outside the IP anomaly is ilmenite, with only a minor occurrence of pyrrhotite with the typical Curie temperature of 320 °C. In the highly altered rock with a high IP anomaly, pyrrhotite with a high Curie temperature of 350–370 °C is the dominant magnetic mineral. Whatever the reason for the high Curie temperatures, it is evident that the magnetic minerals within the high and low IP anomaly areas show clearly different behaviour. Provided that in the high IP area the gold mineralization and the dominating pyrrhotite are related and formed in the same process (Grönholm and Kärkkäinen 2013), it is possible that the high Curie temperature can be used to delineate the occurrence of gold.

Remanent magnetization directions were measured from each sample of the Uunimäki deposit. Due to deformation, the directions are typically highly scattered and no constant characteristic directions were obtained from the different sites. However, site 22 forms an exception. At this site, a consistent remanence direction was isolated, and it clearly deviates from the present direction of the Earth's magnetic field (PEF, Fig. 13). Figure 13 illustrates the remanence directions of all samples from the site before demagnetization. After alternating field demagnetization, a characteristic remanence direction was obtained from six specimens. The mean direction (declination = 352.1°, inclination = 43.9°, α95 = 6.3°, k = 115.6, n = 6 specimens) with its α95 confidence circle is presented in Figure 13. It was used to calculate a virtual geomagnetic pole (VGP) (Plat = 54.3 N, Plong = 215.1 E, dp = 4.9°, dm = 7.8°) for the site. The pole corresponds well to the poles obtained previously from late Svecofennian formations in the Fennoscandian shield (e.g. Mertanen and Pesonen 2012). The age of the magnetization is about 1800 Ma. The result is in accordance with proper isotope age datings that suggest a late Svecofennian age of 1.82–1.79 Ga for the gold mineralizing event in the Häme belt (Saalmann et al. 2009).

Provided that the remanent magnetization of site 22 is primary, formed during original cooling of the magma, the preservation of an original Svecofennian remanence direction indicates that either the site has been preserved from later tectonic processes, or that at this site a younger Svecofennian age magmatic pulse, post-dating deformation, has taken place. The rock type at site 22 is uralite porphyritic gabbro, and the site also shows the highest magnetization and conductivity values (Figs 9 and 14), and as described above, the ferromagnetic mineral at this site is pyrrhotite (Fig. 11). According to SEM studies, the pyrrhotite at this site (Fig. 12a) seems to be more solid compared to the sample from site 17, where pyrrhotite mostly occurs with chalcopyrite and is more broken (Fig. 12b). Therefore, the reason for the observation that only site 22 shows stable remanence directions while the other sites show scattered directions is the different magnetic mineralogy and texture.

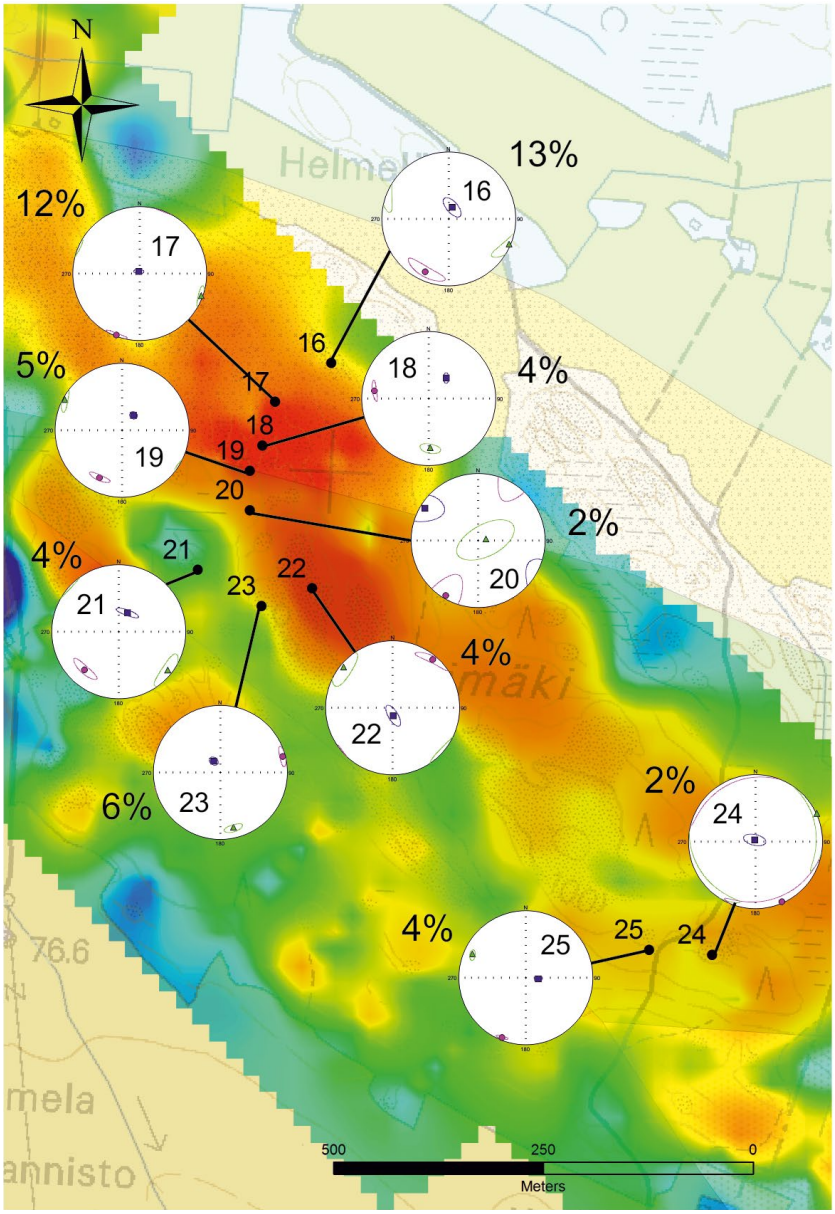

Fig. 14. IP anomaly map of the Uunimäki deposit. Sampling sites (16–25) are indicated as small black dots. The anisotropy degree (P') of magnetic susceptibility is shown as percentages for each site, and the principal axes k1 (blue square), k2 (green triangle) and k3 (red circle) are presented with their α95 confidence ellipses. Contains data from the National Land Survey of Finland Topographic Database 03/2013.

Table 1 presents the exceptionally high remanence and Q-values for site 22, which also explains the occurrence of stable remanence directions. The overall result may thus indicate that the rock with dominant pyrrhotite was formed from a separate mineralizing fluid flow event that, based on the preservation of a typical Svecofennian age remanence direction, must post-date the tectonic events of the region. Consequently, provided that pyrrhotite and the gold mineralization were formed in a simultaneous process (Grönholm and Kärkkäinen 2013), the palaeomagnetic age for pyrrhotite and gold is at maximum 1.8 Ga.

AMS directional data within Uunimäki are characterized by NW–SE striking, almost vertically dipping magnetic foliations and predominantly vertically plunging magnetic lineations (Fig. 14). The anisotropy degree is generally low, from 2–5%, but in the northern part the anisotropy degree increases up to 13%. The shapes of the AMS ellipsoids are both oblate and prolate.

In order to correlate the geochemical and petrophysical properties of the Uunimäki gabbro, three drill cores were studied (M211109R314, M211109R315 and M211109R316). Some of the rocks were defined as gabbro and others as uralite

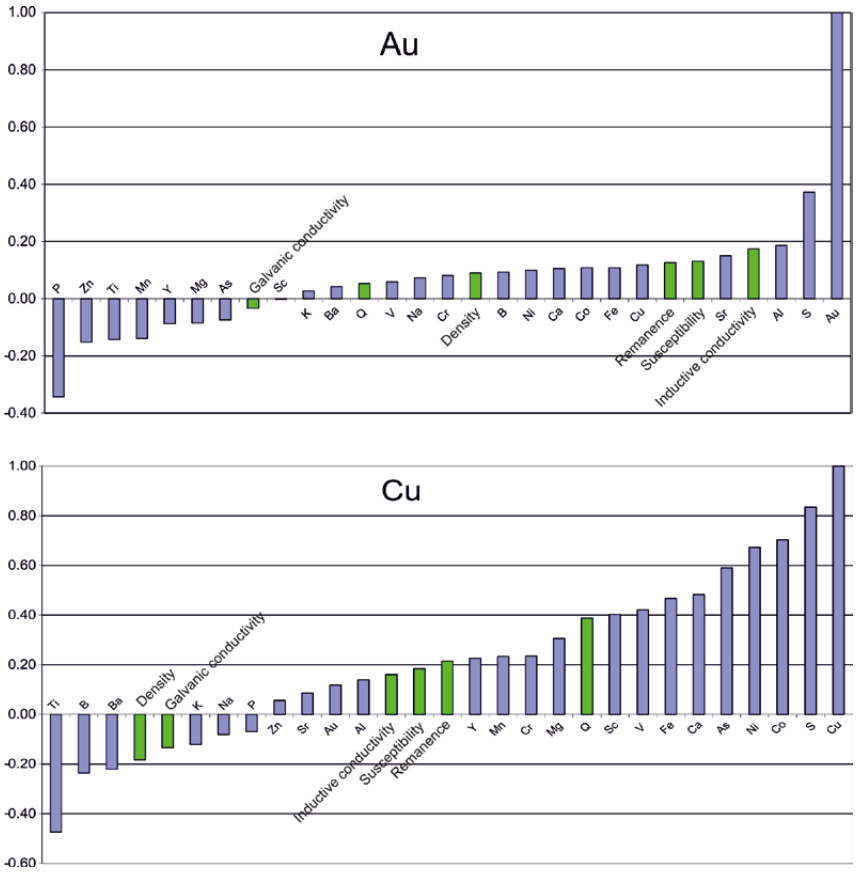

Fig. 15. Correlation of geochemical and petrophysical properties of the Uunimäki deposit. The data were obtained from three drill cores, M211109R314, M211109R315 and M211109R316.

porphyritic gabbro. The lengths of the drill cores were 65.05, 81.05 and 90.40 m. In total, 75 samples were analysed for petrophysical studies and 55 samples for geochemical studies. Petrophysical and geochemical samples were not exactly the same, but the samples were taken as close to each other as possible.

Geochemical correlations indicate that the occurrence of gold is only weakly correlated with other heavy metals (Fig. 15). From the petrophysical parameters, gold is best correlated with inductive conductivity, consistent with the occurrence of pyrrhotite. Because pyrrhotite mostly occurs as disseminated grains, it is not shown in galvanic conductivity. In the Au-bearing zones, pyrrhotite also occurs as thin veins, but because they are mostly perpendicular to the core, they are not invariably caught in the petrophysical samples.

Copper correlates with heavy metals. From the petrophysical properties it is best correlated with Q-value, as it is connected to pyrrhotite (and nickel). Copper has a negative correlation with Ti and density. Titanium is connected to magnetite, which is not related to pyrrhotite.

One reason for the weak correlation between the petrophysical parameters and geochemistry is partly because the petrophysical and chemical analyses were not conducted on the same samples.

Mäyrä

The Mäyrä target (Fig. 16) is within a prominent regional geochemical Au anomaly, but the source of gold in this area has not yet been studied. Petrophysical sampling was carried out across a shear zone that might be part of a mineralized zone (site 1, Fig. 17). The main aim was to examine how the alteration in the zone has affected the petrophysical properties. The other aim was to compare the petrophysical properties of two mafic intrusive rock types in the outcrops: one a dark coarse-grained gabbro (site 2) and the other a lighter coloured fine-grained gabbro (site 3). The sampling scheme is described under the section Methods and sampling.

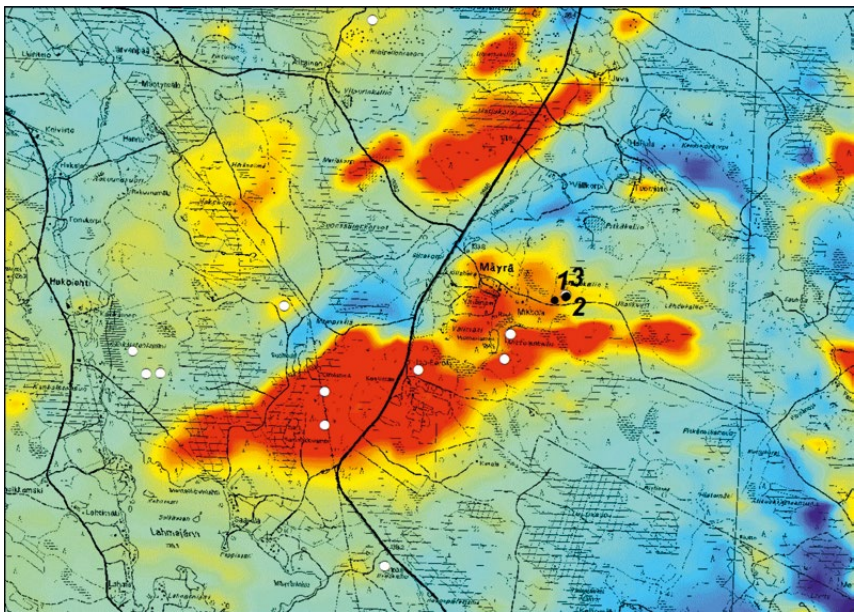

Fig. 16. Aeromagnetic anomaly map of the Mäyrä occurrence. Numbers 1–3 show the sampling sites of this study, while white dots are study locations not reported here. Contains data from the National Land Survey of Finland Topographic Database 03/2013.

Table 1 presents the mean petrophysical values for each site at the Mayrä target. The highest susceptibilities and remanences occur in the coarse grained gabbro not affected by shearing (site 1 and site 2, Fig. 18a, Table 1). In these samples, the susceptibilities have large variation ranging between 2 000–14 000 (x10^{-6} SI) and the remanences generally range between 100 and 800 mA/m. One sample has an exceptionally high remanence of about 5300 mA/m, which raises the mean value (Mäyrä, site 2, Table 1). All Q-values of the coarse grained dark gabbro of site 2 and of samples from unsheared coarse gabbro of site 1 are above 1 (Fig. 18b, Table 1). In the fine-grained gabbro of sites 1 and 3 (Table 1), the susceptibilities are lower and Q-values are below 1. In the centre of the shear zone of site 1, both the susceptibility and Q-values are the lowest (Table 1). The result indicates that due to hydrothermal alteration in the shear zone, most magnetic minerals have vanished. Densities are clearly lowered at the shear zone corresponding to densities of the fine-grained light-coloured gabbro (Fig. 18b).

According to Lowrie tests, the main magnetic mineral in the coarse-grained dark gabbro (Fig. 19a) and in the fine-grained lighter coloured gabbro is magnetite, with some amounts of pyrrhotite, while in the shear zone it is only pyrrhotite (Fig. 19b). High Q-values above 1 in the coarse-grained gabbro indicate magnetite of a small grain size accompanied by pyrrhotite. The coarse-grained black

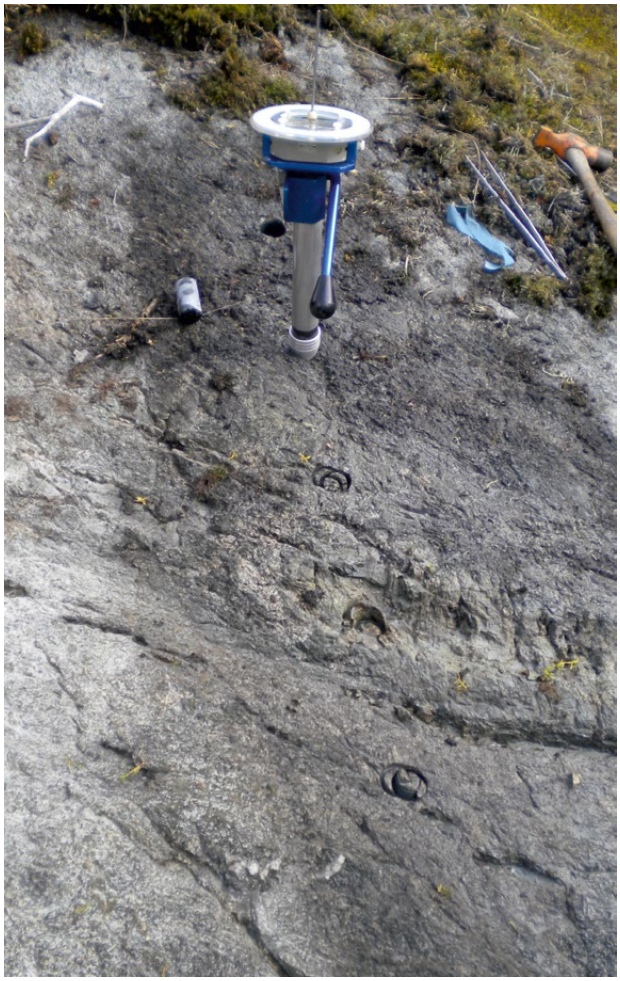

Fig. 17. Site 1 of the Mäyrä deposit showing the samples taken across a hydrothermally altered shear zone. Orientation device is placed on one of the cores.

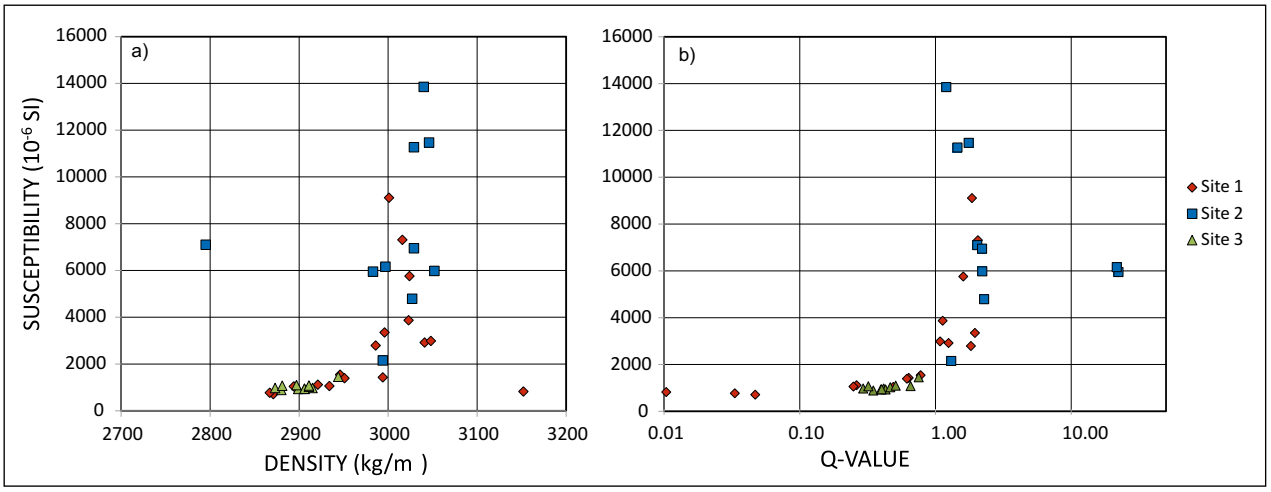

Fig. 18. Petrophysical properties of the Mäyrä gabbro a) Susceptibility – Density, b) Susceptibility – Q-value. Samples of site 1 were taken from the hydrothermally altered shear zone where the lowest values come from the shear zone and the highest values from the coarse-grained gabbro. Site 2 represents the coarse-grained gabbro and site 3 the fine-grained gabbro.

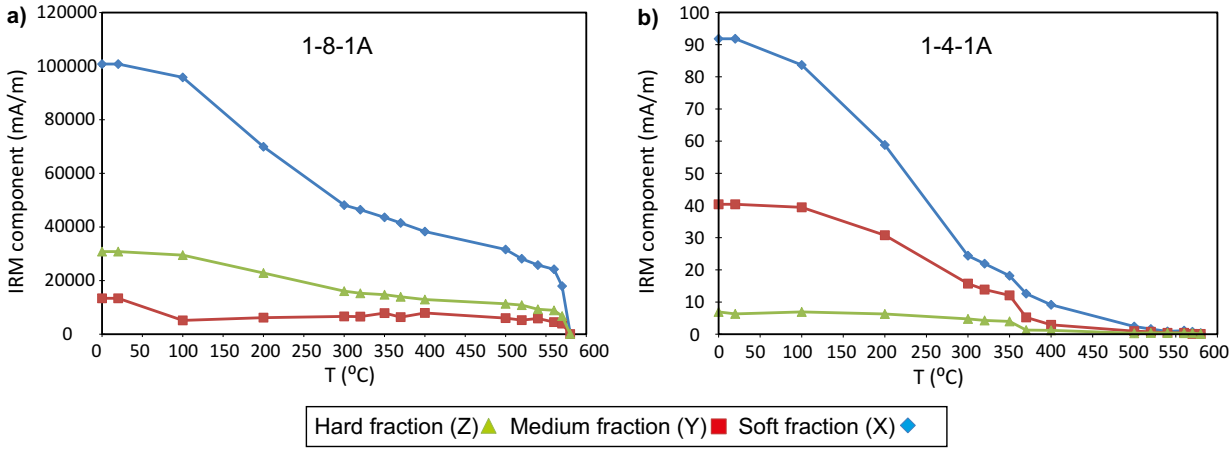

Fig. 19. a) Lowrie test of sample 1-8-1A from the coarse-grained dark gabbro shows magnetite as the main magnetic mineral, b) sample 1-4-1A from the shear zone shows pyrrhotite with a Curie temperature of ca. 370 °C in addition to magnetite (550 °C).

gabbro shows electrical conductivity, but the lighter coloured gabbro does not. Likewise, the shear zone is not clearly conductive, probably due to only small amounts of pyrrhotite.

Comparison of magnetic minerals of the coarse-grained and fine-grained gabbros shows that both contain magnetite (Fig. 20), although their magnetization behaviours and magnetization intensities are clearly different. The Curie temperature of magnetite in both samples is about 580 °C. The long tail above 600 °C in sample 1-8-1B is probably due to hematite.

Directions of remanent magnetization are generally scattered without a consistent direction in the samples. However, a certain trend can be observed in the remanence directions of the shear zone. In the middle of the shear zone (sample 1-4), a NW-pointing direction with intermediate inclination is isolated. Such a direction is typically seen in formations of Svecofennian age (see Fig. 13 from the Uunimäki site 22). The samples further away from the central shear zone carry either a NE- or SW-pointing low inclination remanence direction. It is interpreted that in the centre of the shear zone, the remanence has been locked after deformation and later than the remanence in the surrounding gabbros, which have been involved within the deformation and lost their original Svecofennian remanence direction. Therefore, it seems that as in Uunimäki, the hydrothermal event in Mäyrä is also post-tectonic. However, because these results are only based on a few samples, the interpretation is so far only speculative.

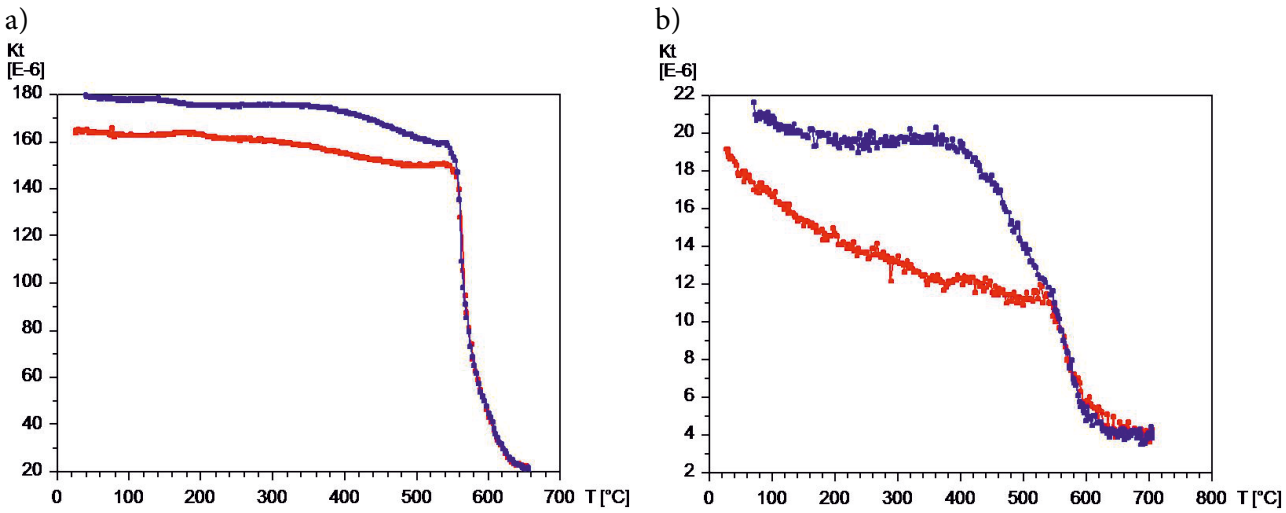

Fig. 20. Thermomagnetic curves showing the variation in susceptibility with heating (red curve) and subsequent cooling (blue curve). a) Sample 1-8-1B is from the coarse grained gabbro and b) sample 3-4-1A is from the fine-grained gabbro and shows some alteration during laboratory heating.

CONCLUSIONS

The study areas were selected by utilizing airborne geophysical data in order to delineate the source of anomalies. Detailed investigations on petrophysical and rock magnetic properties of the prospect occurrences can be used to aid in exploration by verifying the differences in the physical properties of the ore and host rock. Investigations at the outcrop scale have shown that in the porphyry type Cu-Au deposit of Kedonojankulma and in the orogenic Au deposit of Uunimäki, the magnetic properties have increased in the auriferous shear zones due to alteration of Fe-oxide to pyrrhotite. On the other hand, in the gabbroic Au-target of Mäyrä, the magnetizations have decreased due to hydrothermal alteration.

In the quartz-plagioclase porphyry of the Rusakkokallio site of the Kedonojankulma occurrence, the induced and remanent magnetizations are slightly higher in the altered auriferous shear zone than in the less altered host rock. In the altered zone, the only magnetic mineral is monoclinic pyrrhotite with an exceptionally high Curie temperature of ca. 370 °C, while in the host rocks the main magnetic mineral is ilmenite. In the Passi outcrops, some of the plagioclase-quartz porphyries have similar magnetic properties, namely low susceptibility and a higher Q-value (over 1) than in the sheared Rusakkokallio plagioclase-quartz porphyries, indicating the dominance of pyrrhotite. In some of the samples, the susceptibilities are significantly higher due to magnetite, which occurs together with only small amounts of pyrrhotite. Based on AMS data, the least altered quartz-plagioclase porphyrite in Rusakkokallio has the smallest degree of anisotropy, while the highest AMS degrees are found in the Passi outcrops. The higher values are probably due to the occurrence of magnetite, which increases the total magnetization and enhances the possibility to observe the AMS.

In the Uunimäki gabbroic occurrence, the highest magnetization values and conductivities correlate with strong IP anomalies, although the formation is weakly magnetized in general. Rock magnetic analyses show that in the samples of highest magnetization, which are believed to represent the most altered, Au-bearing part of the deposit, the only magnetic mineral is monoclinic pyrrhotite. The less altered areas show the dominance of ilmenite with minor amounts of pyrrhotite. At one site with the highest magnetization and IP values, the remanent magnetization has retained its original Svecofennian age direction, while at other sites the remanences are scattered due to the low intensity of remanence and due to deformation. Preservation of the original remanence may indicate a post-tectonic origin for the fluid that is responsible for the formation of pyrrhotite and, possibly, enrichment of gold. AMS directions are characterized by NW–SE-striking,

approximately vertically dipping magnetic foliations and vertically plunging magnetic lineations.

In the Mäyrä occurrence, the magnetization of the shear zone has decreased due to hydrothermal alteration. The surrounding gabbros, whether coarse-grained dark gabbro or fine-grained lighter coloured gabbro, contain magnetite as the main magnetic mineral, while the shear zone also contains pyrrhotite in addition to magnetite.

ACKNOWLEDGEMENTS

Meri-Liisa Airo is thanked for providing the airborne geophysical maps and for aiding in the selection of the study areas. Niilo Kärkkäinen, Jarkko Klami and Juha Haverinen are acknowledged for guidance in the field. Heikki Säävuori is thanked for making the correlation of geochemical and petrophysical data. Satu Vuoriainen, Matti Kauranne and Matti Leino are thanked for petrophysical laboratory measurements and Sari Lukkari for guidance in the SEM studies. Niilo Kärkkäinen and Tomas Kohout reviewed the manuscript and their comments are highly appreciated.

REFERENCES

Eilu, P., Grönholm, S. & Kärkkäinen, N. 2012. Lounais-Suomen kultaesiintymät. Geologi 64, 164–171 (in Finnish).

Graham, J., Bennett, C. E. G. & Riessen, A. 1987. Oxygen in pyrrhotite: 1. Thermomognetic behavior and annealing of pyrrhotites containing small quantities of oxygen, American Mineralogist 72, 599–604.

Grönholm, S. & Kärkkäinen, N. 2013. Gold in Huittinen, Southern Finland. In: Hölttä, P. (ed.) GTK Mineral Potential Workshop, Kuopio, May 2012. Geologian tutkimuskeskus, Tutkimusraportti 198 – Geological Survey of Finland, Report of Investigation 198, 26–28.

Huhta, P. 2013. Till geochemical and heavy mineral studies in Häme belt, Southern Finland. In: Hölttä, P. (ed.) GTK Mineral Potential Workshop, Kuopio, May 2012. Geologian tutkimuskeskus, Tutkimusraportti 198 – Geological Survey of Finland, Report of Investigation 198, 52–55.

Huhta, P., Kärkkäinen, N., Tiainen, M. & Herola, E. 2014. Geochemical anomalies reflecting ore-forming processes in the Svecofennian Häme Belt, southern Finland. Geologian tutkimuskeskus, Report of Investigation 207, Current research 45–47.

Lahtinen, R., Korja, A. & Nironen, M. 2005. Paleoproterozoic tectonic evolution. In: Precambrian geology of Finland: key to the evolution of the Fennoscandian Shield. Developments in Precambrian geology 14. Amsterdam, Elsevier, 481–531.

Lowrie, W. 1990. Identification of ferromagnetic minerals in a rock by coercivity and unblocking temperature properties. Geophysical Research Letter 17, 159–162.

Mertanen, S. & Karell, F. 2009. Paleomagnetic and magnetic fabric investigations on the Jokisivu gold deposit in southern Finland. Geological Survey of Finland, Research report Q 29.1/2009/37, 32 p.

Mertanen, S. & Karell, F. 2011. Rock magnetic investigations constraining relative timing for gold deposits in Finland. Bulletin of the Geological Society of Finland 83,75–84.

Mertanen, S. & Pesonen, L. J. 2012. Paleo-Mesoproterozoic Assemblages of Continents: Paleomagnetic Evidence for Near Equatorial Supercontinents. In: Haapala, I. (ed.) From the Earth's Core to Outer Space. Lecture Notes in Earth System Sciences 137, Springer-Verlag Berlin Heidelberg, 11–35.

Rochette, P., Fillion, G., Mattéi, J.-L. & Dekkers, M. J. 1990. Magnetic transition at 30-34 Kelvin in pyrrhotite: insight into a widespread occurrence of this mineral in rocks. Earth and Planetary Science Letters 98, 319–328.

Saalmann, K., Mänttäri, I., Ruffet, G. & Whitehouse, M. J. 2009. Age and tectonic framework of structurally controlled Palaeoproterozoic gold mineralization in the Häme belt of southern Finland. Precambrian Research 174, 53–77.

Tiainen, M., Kärkkäinen, N., Koistinen, E., Lohva, J., Sipilä, P. & Huhta, P. 2012. Discovery of the Kedonojankulma Cu-Au occurrence, hosted by a Svecofennian porphyritic granitoid in Southern Finland. In: Gold in Southern Finland: results of GTK studies 1998-2011. Geological Survey of Finland, Special Paper 52,73–90.

Tiainen, M., Molnár, F., Kärkkäinen N. & Koistinen, E. 2013. The Forssa–Jokioinen Cu-Au-Zn province, with special emphasis on the Kedonojankulma Cu deposit. Geologian tutkimuskeskus, Tutkimusraportti 198 – Geological Survey of Finland, Report of Investigation 198, 173–178.

Vuori, S., Kärkkäinen, N., Huhta, P. & Hölttä, P. 2007. Moreenigeokemia ja ultrapotentiaaliset rakenteet. In: Salminen, R. (ed.) Kahdeksannet geokemian päivät, 13–14.2.2007. Tiivistelmät. Vuorimiesyhdistys, Sarja B 86, 101–103 (in Finnish).

Zegers, T. E., Dekkers, M. J. & Bailly, S. 2003. Late Carboniferous to Permian remagnetization of Devonian limestones in the Ardennes: Role of temperature, fluids, and deformation, Journal of Geophysical Research 108 (B7), 2357.

Geophysical signatures of mineral deposit types in Finland
Edited by Meri-Liisa Airo
Geological Survey of Finland, Special Paper 58, 107–116, 2015

AIRBORNE RADIOMETRIC DATA AS A URANIUM EXPLORATION TOOL – CASE STUDIES FROM SOUTHERN LAPLAND

by

Laura S. Lauri[1] and Pertti Turunen[1]

Lauri, L. S. & Turunen, P. 2015. Airborne radiometric data as a uranium exploration tool – case studies from southern Lapland. G*eological Survey of Finland, Special Paper 58,* 107–116, 5 figures.

Airborne radiometric data registered at low altitudes are used for detecting the presence of potassium, uranium and thorium in the field. Ternary K-Th-U maps combined with either total radioactivity maps or separate U, Th and K-channel maps are especially important in uranium exploration, as they reveal the cause of radioactivity. During the most recent global uranium exploration boom in the 2000s, three new targets (Asentolamminoja, Rumavuoma and Rompas–Rajapalot) were located in southern Lapland. The Asentolamminoja and Rumavuoma targets are discernible as strong aeroradiometric anomalies, whereas the Rompas–Rajapalot target is only weakly delineated by airborne data. The advantage of airborne and ground radiometric measurements is that they are fast and low-cost compared to more time- and money-consuming laboratory analyses.

Keywords (GeoRef Thesaurus, AGI): mineral exploration, uranium ores, radioactivity methods, airborne methods, radioactivity survey maps, Lapland, Finland

[1]*Geological Survey of Finland, P.O. Box 77, FI-96101 Rovaniemi, Finland*

E-mail: laura.lauri@gtk.fi, pertti.turunen@gtk.fi

INTRODUCTION

Airborne radiometric data registered at low altitudes are extensively used worldwide in greenfield uranium exploration. Although the radiometric signal only reflects the top 50 cm of ground and does not work in wetland areas, it still offers an effective means to delineate radiometric anomalies that may be verified by ground checking. In addition to total count and U-channel data, ternary K-U-Th maps and U^2/Th ratios are also used in uranium exploration. In the ternary map, three colours, traditionally red for K, blue for U and green for Th, are used to highlight the relative concentration of the three radionuclides. If one of the three elements has an unusually high concentration, the map may be useful in visual inspection. The U^2/Th presentation is based on the tendency of U and Th to co-occur and to have a rather constant relative relationship.

During the most recent global uranium exploration boom in the 2000s, three new targets were located in southern Lapland (Fig. 1), representing the first new uranium prospects found in Finland since the 1980s. The Asentolamminoja target on the SE side of the town of Rovaniemi is a pure uranium target, whereas the Rumavuoma and Rompas–Rajapalot areas in the municipality of Ylitornio are gold-uranium prospects currently under an exploration license by Mawson Oy.

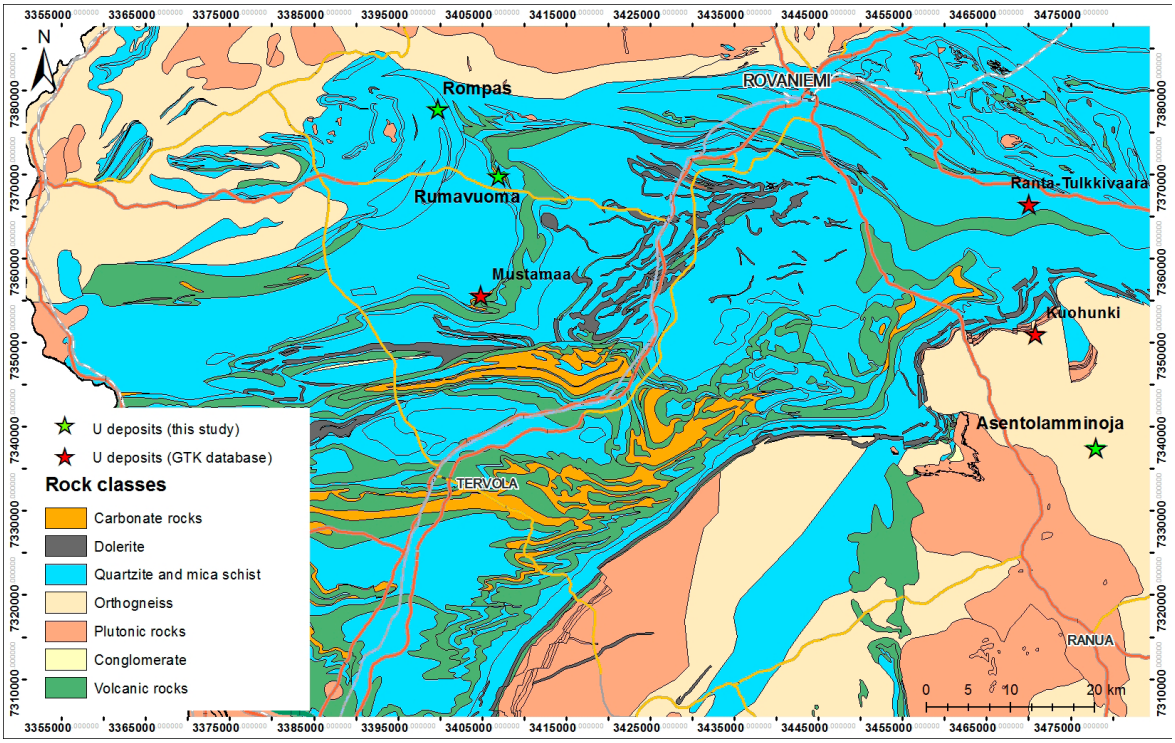

Fig. 1. Simplified bedrock map (extracted from the DigiKP database, GTK) of the study area with the locations of the U deposits marked with stars. Coordinates according to the Finnish National Grid (KKJ). Contains data from the National Land Survey of Finland Topographic Database 03/2013.

ON THE USE OF AERORADIOMETRIC MAPS IN URANIUM EXPLORATION

Gamma spectrometry is used for detecting the presence of potassium, uranium and thorium in the field. These three radionuclides are commonly present in all natural materials, whereas other radioactive elements are more rare compared to them. The ratio of radioactive ^{40}K to total K is constant, and its absolute concentration is straightforwardly measured by means of gamma spectrometry, with ^{40}K being a gamma emitter. On the other hand, because both uranium and thorium are alpha emitters, they must be indirectly detected via the radioactivity of gamma active daughter elements in their decay series. Reliable detection of uranium and thorium contents requires their decay series

to be in secular equilibrium. Some geological and anthropogenic processes may alter the secular equilibrium; however, this is rarely a problem in routine exploration. Due to the indirect detection of U and Th, the resulting U and Th contents are commonly referred to as equivalent concentrations, marked as eU and eTh.

The registration frequency in the aeroradiometric gamma detection of the flights of the Geological Survey of Finland (GTK) is 1/s (Hyvönen et al. 2005). The plane moves ca. 60 m during the measurement time period. Most of the gamma pulses measured originate from below the flight line, but also outside of it from a wider zone, and thus the radioactive zone may not be reliably delimited from the flight anomaly. Gamma ray intensity attenuates exponentially as a function of distance, and the measured radioactivity may be estimated to originate from an ellipse elongated in the flight direction. The radioactivity originating below the flight line dominates, but even the pulses beyond the rims of the ellipse, roughly measuring 260 m * 200 m, contribute around 30 % to the total count (Grasty et al. 1979). The aeroradiometric anomaly of a point source is spread to a wide area, resulting in a dim signature, and so the aeroradiometric map is not necessarily the best means of delimiting the area selected for detailed ground follow-up. The intensity of radioactivity and the calculated K, eU and eTh concentrations are projected in the centre of the ellipse.

Flight line separation and flying altitude are equally important parameters in airborne mapping. Target detectability (or ground resolution) decreases as the altitude increases, and ground coverage decreases with decreasing altitude. Also, the observed count rate decreases as flight altitude increases, because gamma rays are absorbed in air exponentially as the air column increases in thickness (Pitkin & Duval 1980). The low information density between the lines could be improved by reducing the line separation. Another method would be to increase the flying clearance from the used 35 m, but this would weaken data quality and resolution. The 200 m flight line separation in GTK's system is the result of several conflicting factors, including the available budget, size of the survey area and size of the target. A speckled map may be a hint of too sparse line spacing, as the lack of line-to-line coherency may yield a non-contourable result.

A portable scintillometer or gamma spectrometer is needed for ground follow-up of airborne radiometric anomalies. If the aeroradiometric map hints a uranium source for the radioactivity, it may be located with a scintillometer that records the total gamma radiation. The target area is scanned with the scintillometer, and the radioactive locations are marked either on a map or with a GPS. The surveys may be combined with the GPS data to produce a large-scale radioactivity map. Ground maps are rarely needed if the target area has a good radiometric coverage from the air, as both air and ground surveys produce largely similar anomaly maps.

Ground gamma spectrometry is comparable to an airborne survey in accuracy and reliability, although it gives more details on a small scale. One cause for this is the statistical property of radioactivity to fluctuate in intensity, even in undisturbed conditions. A single observation has little statistical weight. The accuracy may be improved with longer observation series, and summing time extension is more easily arranged on the ground than in the air.

The radionuclide concentrations measured with the gamma spectrometer must be carefully considered before reaching a conclusion. The higher from the ground the spectrometer is, the larger is the area from which the gamma pulses originate. The spectrometer is calibrated in such a way that the radioactivity is estimated to originate from a half-space. During a survey, the system assumes that even a small sample fills the half space, which results in a too low radionuclide content. A calibration plate measuring an area of 1 m^2 and weighing 1 ton corresponds to ~90% of the total radioactivity of a half-space measured from the plate top (Grasty et al. 1991). In effect, the measured radionuclide concentration is always lower than the total concentration, i.e. eU < U.

The visually most attractive radiation anomalies are often situated on cliffs or on exposed hill tops. If the radiation fades beyond the exposed area, the reason is not necessarily in the rock but in the damping effect of the overburden. The higher the medium density and the larger its thickness, the stronger is the attenuation. Water is in practice the most important radiation attenuator, irrespective of its state. Twelve centimetres of effective water, be it liquid, ice, gas or any combination of these, attenuates the radiation intensity to half, causing wetlands and lakes to appear as blank areas. The

fine component in till detains water and attenuates radiation, whereas high porosity sand and gravel eskers allow radon to move up and cause eU anomalies.

Uranium is a complex element in nature. It is soluble in acid water, and as rainwater is always acid, exposed U-bearing cliffs release uranium atoms, which are transported with the water flow. U is easily deposited in alkaline and reducing conditions or in organic substances or clays. Young, redeposited uranium is not, however, gamma active and is not detectable through radiation. The daughters in the U decay series, as separate elements with their own chemical properties, do not leave the original site but continue to be radioactive. It may happen that the original location is devoid of U, but radioactive due to the presence of the daughter elements, and the new site may be rich in U but not radioactive. Geochemical processes have caused a secular disequilibrium within the first depth centimetres, even though at deeper levels the normal state of affairs may be in force.

A detailed account of gamma measurements is found in an IAEA publication (IAEA 2013). The aerogeophysical routine of GTK is thoroughly described by Hautaniemi et al. (2005).

ASENTOLAMMINOJA TARGET

The Asentolamminoja area is situated 55 km SE of the town centre of Rovaniemi (Fig. 1). The bedrock of the area consists of Archaean rocks of the Pudasjärvi complex and 2.44 Ga layered intrusions of the Portimo complex. The distance from the Asentolamminoja area to the unconformity between the Archaean basement complex and the overlying Palaeoproterozoic Peräpohja belt is ca. 15 km.

The Kuohunki uranium target close to the Archaean–Proterozoic unconformity was found and to some extent drilled in the 1980s by GTK (Pyy 1981, Pääkkönen 1983, 1989). The Kuohunki area shows up as a relatively strong anomaly on both U and Th channels on the airborne radiometric maps (Figs 2a, b). On the ternary K-Th-U map, the Kuohunki area is shown to have slightly separate U and Th maxima, with the U-channel anomalies corresponding to glacial boulder trails in the field (Fig. 2c). On the SSE side of Kuohunki, an even stronger U-channel anomaly may be seen 15 km away (Fig. 2c). This anomaly, referred to as the Asentolamminoja prospect, was taken under exploration in 2007 by Areva Resources Finland Oy, the Finnish subsidiary of the French nuclear corporation Areva. When the target area was inspected with field scintillometer and spectrometer measurements, it was revealed to contain numerous radioactive glacial erratic boulders with evidence of hydrothermal alteration (see Mänttäri and Lauri 2008), thus giving the area the nickname of "10 000 boulders". Although no outcrops were found from the main boulder field area, which measures 3 km by 3 km, the boulders are of local origin based on Quaternary geological studies (Sarala 2007, 2008).

Figure 3 shows the results of the aeroradiometric measurements in the Asentolamminoja area. The total intensity in the uppermost figure is the sum of pulses in K, U and Th channels and of secondary pulses the intensity of which exceeds 0.41 MeV. The secondary pulses are generated in the reactions between the primary gamma quanta and atoms in the media – rocks, air, measuring devices – and cosmic radiation. Potassium is ubiquitous and it is responsible for the total field intensity to which the U and Th pulses are summed. The background level is so high that the less intensive U radiation generated by the uranium occurrence in the upper part of the map is seen as a very weak anomaly. The areas with weak anomalies may in general be interpreted to contain small amounts of radioactive nuclides, or be areas where radiation is attenuated by water.

The graph in the middle in Figure 3 is the eU map. The uranium occurrences are much more discernible than in the total gamma map, and they are limited to a smaller area that may be used for targeting the ground follow-up studies.

In the lowermost panel of Figure 3, the eU concentration is normalized with the eTh concentration and the ratio is multiplied by the eU concentration. This process decreases the damping effect of media (e.g., water) and transforms the eU measurement towards the ideal case, in which the bedrock is not covered by soil or water. This is justified by the tendency of U and Th to co-occur. The anomaly marked with a circle in Figure 3 illustrates a danger of this operation. Here, the low eTh content in the denominator has produced a

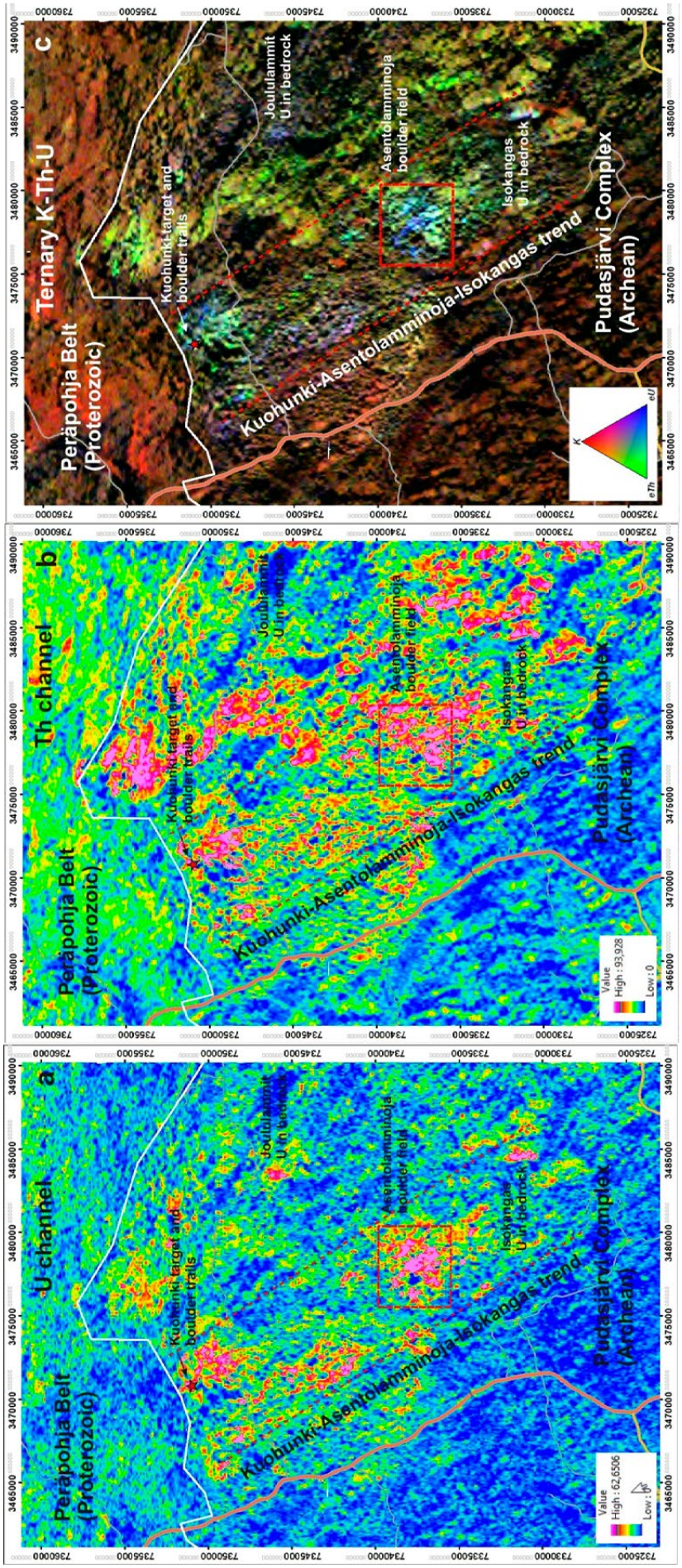

Fig. 2. a) Airborne U-channel map, b) airborne Th-channel map and c) ternary K-Th-U map of the Asentolamminoja area. The Kuohunki-Asentolamminoja-Isokangas trend is marked with red dashed lines and the Asentolamminoja boulder field is delineated with a red dashed square. The Kuohunki U-prospect is marked with a red star. The unconformity between the Archaean Pudasjärvi complex and the Proterozoic Peräpohja belt is marked with a white line. Contains data from the National Land Survey of Finland Topographic Database 03/2013.

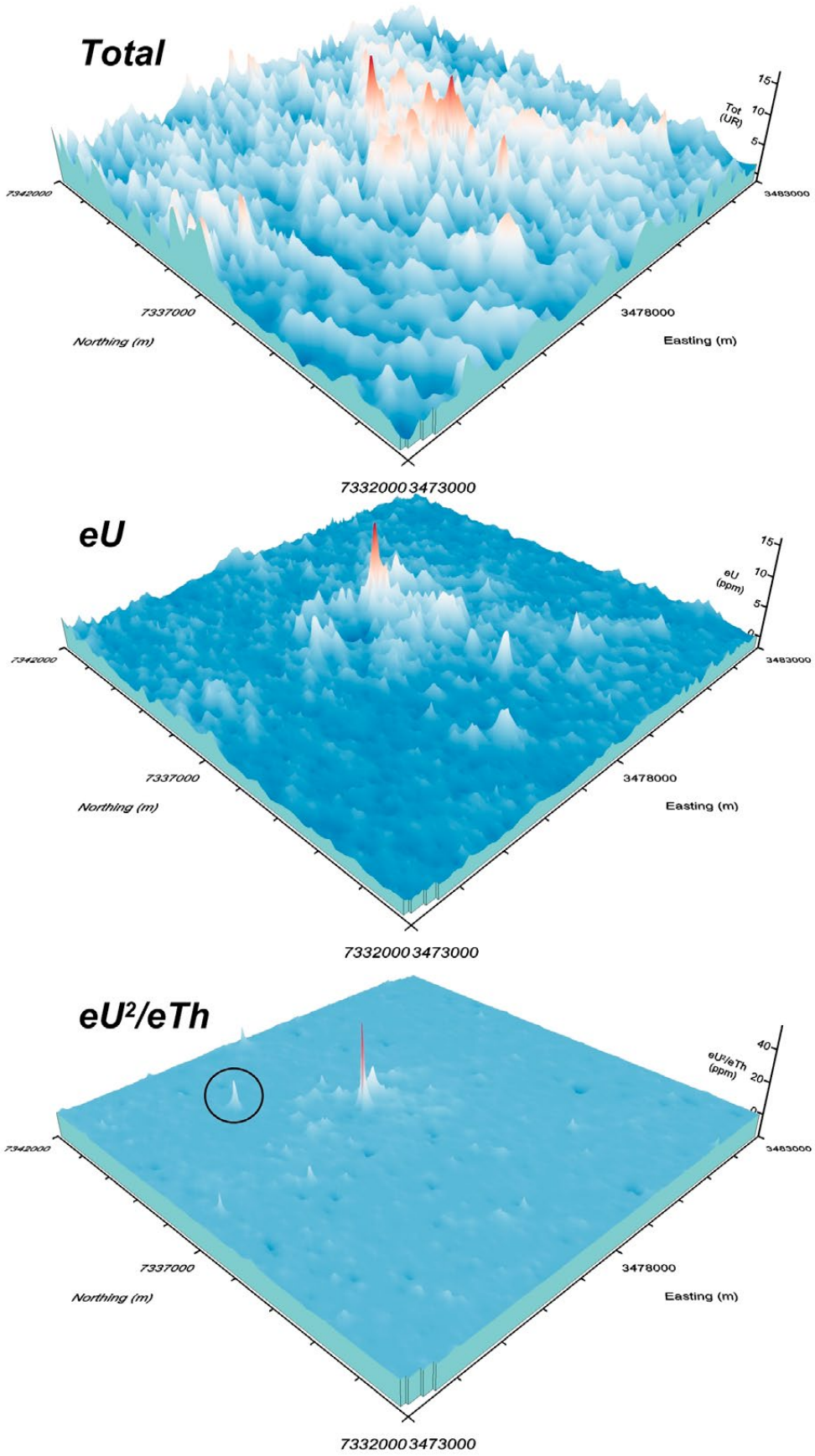

Fig 3. Airborne radiometric maps at Asentolamminoja. Top: Total intensity map. Middle: eU map. Bottom: eU^2/eTh map. The encircled peak is suspected to be a false anomaly.

false anomaly, regardless of eU content. An automatic cut-off technique can be utilized to avoid false anomalies, but a field check may be needed to verify whether the anomaly is real.

The other airborne geophysical (magnetic and electromagnetic) maps of the Asentolamminoja area do not reveal any indications of ore deposits. The weak anomalies on a flat background on aeromagnetic maps were revealed to be caused by peat bogs in ground surveys (Turunen 2008). Radon, a noble gas generated in the radioactive decay series of uranium, is soluble in water and raises the eU concentration in the wetland areas, even though the radioactivity from bedrock is attenuated. Peat is locally formed and to some degree reflects the radioactive nuclide content of the underlying bedrock. Areas covered by peat may be noisy.

Some small but strong U-channel anomalies may be observed on the NE and SE sides of the Asentolamminoja target (Figs 2a, c); these were examined in the field and found to represent small-scale radioactive alteration zones within the bedrock. The alteration type (biotitization, silicification) corresponds to the boulders within the Asentolamminoja boulder field and the Kuohunki drill cores, and most probably represents the same ore-forming system that extends all the way from the Kuohunki area through Asentolamminoja to the Isokangas area 25 km SE of Kuohunki. Although the uranium mineralization is situated within Archaean rocks, the age of the ore-forming process is most probably Proterozoic (Mänttäri & Lauri 2008).

RUMAVUOMA AND ROMPAS

The Rumavuoma and Rompas targets are situated in western Lapland, ca 40 km W of the town centre of Rovaniemi (Fig. 1). The Rumavuoma area appears on the ternary K-Th-U map as a clear uranium-channel anomaly (Fig. 4). The target was originally located in 2007 by ground follow-up of an airborne radiometric anomaly by Antti Pakonen, a former field assistant of GTK. The area was investigated in 2007–2008 by Areva Resources Finland Oy, and after 2010 by Mawson Oy. The Rumavuoma target is an outcropping area that mainly consists of uranium-bearing dolostone. The outcrops are situated within a wetland area, and the exposed outcrops have much higher background radioactivity than the surrounding peat bogs. The radiometric response of the Rumavuoma target is similar to the Mustamaa uranium prospect in the south (Fig. 4). The Mustamaa prospect, found and drilled in the 1970s (Äikäs 1980, Korvuo 1981, 1982), also shows up as a U-channel anomaly ca. 15 km south of the Rumavuoma area in a similar stratigraphic position at the contact between the subaerial Kivalo group and the submarine mica schists of the Martimo formation of the Paakkola group (Fig. 4). However, the Mustamaa prospect belongs to the phosphorite type in the classification of uranium deposits, whereas the Rumavuoma target is more probably a metasomatic type deposit (IAEA 2009).

In field season of 2008, the contact zone of the Kivalo group and the Paakkola group between the Rumavuoma area and the Mustamaa prospect was investigated by Areva Resources Finland Oy, as the contact zone seemed to be interesting in terms of uranium. Based on aeromagnetic data, the area on the NW side of Rumavuoma was included in the prospecting area, as it appeared structurally favourable to ore-forming processes with converging fault zones, although in terms of the aeroradiometric signal, the area did not look very interesting at a first glance. In late September 2008, the field assistants located high-grade uranium boulders in an area now known as North Rompas (Fig. 4), and in the following field season mineralized veins were found in outcrops in a 6-km-long and 300-m-wide area. High-grade uraninite was also found to be associated with native gold. Looking at the ternary K-Th-U map, the Rompas trend is weakly delineated as small uranium-channel anomalies, but it is by no means as spectacularly visible as the much lower grade Rumavuoma and Mustamaa targets (Fig. 4).

At a first glance, Rompas and Rumavuoma appear to differ considerably from each other on the ternary map. At Rompas, the red colour marking potassium dominates and at Rumavuoma uranium glows blue in places. The total radiation level at Rumavuoma is 3.1 UR and at Rompas 6.0 UR, which causes the general picture at Rumavuoma to

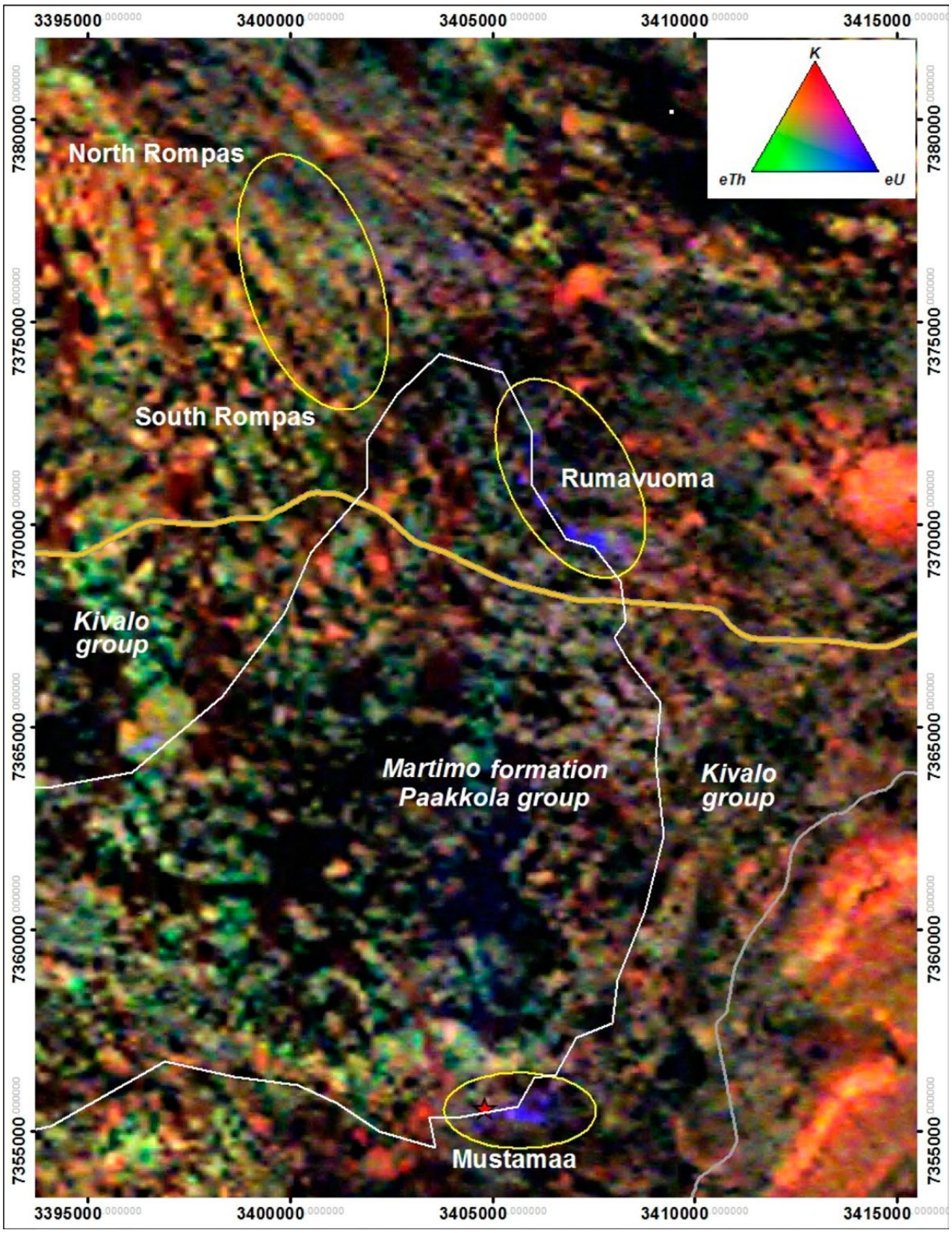

Fig. 4. Ternary K-Th-U map of the Rompas–Rumavuoma–Mustamaa area. White line separates the rocks of the Kivalo group and the Martimo formation of the Paakkola group. Contains data from the National Land Survey of Finland Topographic Database 03/2013.

be darker. The water content in the ground is the reason for the level variation, as an increased water content attenuates the radiation intensity and thus lowers the calculated radionuclide content. While water attenuates the concentrations of K, U and Th, their ratios are less affected. This is seen from the histograms in Figure 5, the data of which have been taken from inside the ellipses marked as Rumavuoma and South-North Rompas in Figure 4.

The maxima in the potassium and thorium distributions at Rumavuoma are lower than at Rompas on the concentration axis. With uranium, the differences between the targets are small, with the largest difference being the wider spread of the uranium distribution towards high concentrations in Rumavuoma, although field studies have shown that Rompas contains more high-grade uranium showings. The eU^2/eTh ratios in the two targets have much in common. It is supposed that the most important reason for the differences between the general ternary images of the two areas is the difference in the ground water content. The final solution to the problem here and elsewhere is provided by a field check.

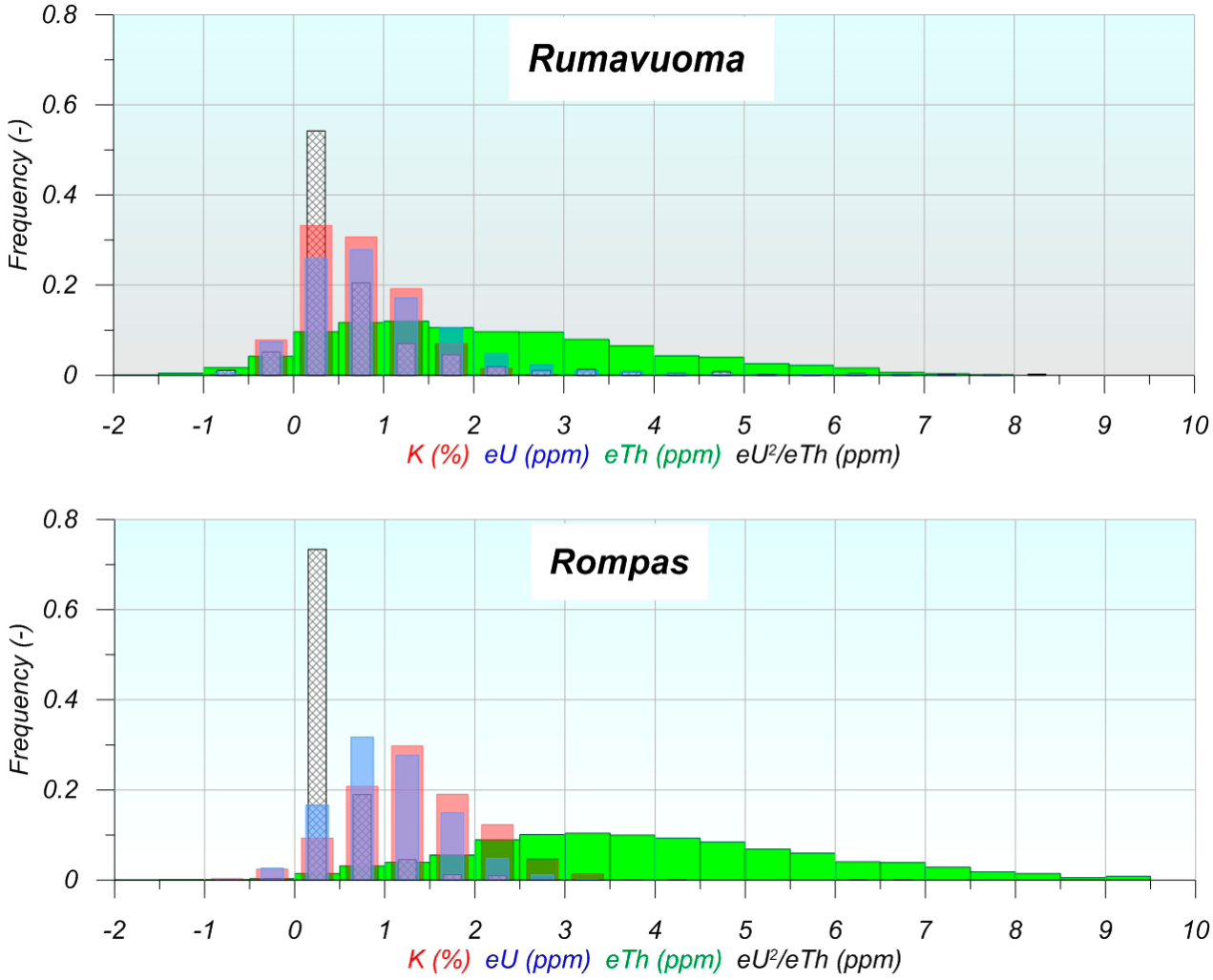

Fig. 5. Radionuclide histograms at Rumavuoma and Rompas.

CONCLUSIONS

Airborne low altitude radiometric data help to delineate areas for ground follow-up exploration with portable devices such as scintillometers and spectrometers. Ternary K-Th-U maps combined with either total radioactivity maps or separate U, Th and K-channel maps are especially important, as they reveal the cause of radioactivity. In terms of uranium exploration, the strong radiometric anomalies caused by granitoid rocks are not as interesting as pure U-channel anomalies. Interesting new targets may still be found when GTK's aeroradiometric data is carefully examined; however, the Rompas case is a good reminder that not all high-grade targets are easily located. The aeroradiometric data may also be used for gold and REE exploration, as uranium is a common element in many Au deposits, as in Rompas, and Th represents a good proxy for REE. The advantage of airborne and ground radiometric measurements is that they are fast and low-cost compared to more time- and money-consuming laboratory analyses.

REFERENCES

Äikäs, O. 1980. Uraanin jakautuminen eräissä Tervolan Mustamaan uraani-fosforiesiintymän näytteissä. Geological Survey of Finland, archive report M19/2633/80/1/60, 16 p. Available at: http://tupa.gtk.fi/raportti/arkisto/m19_2633_80_1_60.pdf. (in Finnish)

Grasty, R. L., Kosanke, K. L. & Foote, R. S. 1979. Fields of view on airborne gamma-ray detectors. Geophysics 44(8), 1447–1457.

Hautaniemi, H., Kurimo, M., Multala, J., Leväniemi. H. & Vironmäki, J. 2005. The "Three In One" aerogeophysical concept of GTK in 2004. In: Airo, M.-L. (Ed.), Aerogeophysics in Finland 1972-2004: methods, system characteristics and applications. Geological Survey of Finland, Special Paper 39, 21–74.

Hyvönen, E., Turunen, P., Vanhanen, E., Arkimaa, H. & Sutinen, R. 2005. Airborne gamma-ray surveys in Finland. In: Airo, M.-L. (Ed.), Aerogeophysics in Finland 1972-2004: methods, system characteristics and applications. Geological Survey of Finland, Special Paper 39, 119–134.

IAEA 2009. World Distribution of Uranium Deposits (UDEPO) with Uranium Deposit Classification, 2009 edition. IAEA-TECDOC-1629, 117 p.

IAEA 2013. Advances in Airborne and Ground Geophysical Methods for Uranium Exploration. IAEA Nuclear Energy Series NF-T-1.5, 72 p.

Korvuo, E. 1981. Mustamaan U-P-malmiaiheen jatkotutkimukset 1980. Outokumpu Oy, report 001/2633,2631/EK/81, 37 p.

Korvuo, E. 1982. Mustamaa 1-2 tutkimukset. Lapin Malmi, report 080/2631,2633/EK/82, 2 p.

Mänttäri, I. & Lauri, L. 2008. Alustavia U-Pb-ikämäärityksiä Ranuan Asentolamminojan radioaktiivisista lohkareista. Geological Survey of Finland, archive report K41.23/2008/01, 15 p. Available at: http://tupa.gtk.fi/raportti/arkisto/k41_23_2008_01.pdf. (in Finnish)

Pääkkönen, K. 1983. Tutkimustyöselostus Rovaniemen MLK:ssa valtausalueella Kuohunki 1, kaiv. rek. N:o 2997 suoritetuista malmitutkimuksista vuosina 1978-1980. Geological Survey of Finland, claim report M06/3613/-83/1/60, 4 p. Available at: http://tupa.gtk.fi/raportti/valtaus/m06_3613_83_1_60.pdf. (in Finnish)

Pääkkönen, K. 1989. Tutkimustyöselostus Rovaniemen MLK:ssa valtausalueella Niittuoja 1, kaiv. rek. N:o 3640/1 suoritetuista malmitutkimuksista vuosina 1982-85. Geological Survey of Finland, claim report M06/3613/-89/1/60, 7 p. Available at: http://tupa.gtk.fi/raportti/valtaus/m06_3613_89_1_60.pdf. (in Finnish)

Pitkin, J. A. & Duval, J. S. 1980. Design parameters for aerial gamma-ray surveys. Geophysics 45(9), 1427–1439.

Pyy, H. 1981. Uraanimalmitutkimukset Rovaniemen maalaiskunnan Kuohungissa vuosina 1978-1980. Geological Survey of Finland, archive report M19/3613/-81/1/60, 18 p. Available at: http://tupa.gtk.fi/raportti/arkisto/m19_3613_81_1_60.pdf. (in Finnish)

Sarala, P. 2007. Preliminary report – Surficial geology at Portimojärvi, Ranua. Geological Survey of Finland, archive report P23.4/2007/105, 8 p. Available at: http://tupa.gtk.fi/raportti/arkisto/p23_4_2007_105.pdf

Sarala, P. 2008. Ground Penetrating Radar Survey in the Asentolampi target, Portimojärvi, Ranua. Geological Survey of Finland, archive report P31.4/2008/23, 11 p. Available at: http://tupa.gtk.fi/raportti/arkisto/p31_4_2008_23.pdf

Turunen, P. 2008. VLF-R and magnetic surveys at the Asentolampi and Isokangas targets, Portimojärvi, Ranua. Geological Survey of Finland, archive report Q24.32/2008/31, 9 p. + 7 app. Available at: http://tupa.gtk.fi/raportti/arkisto/q24_32_2008_31.pdf

Geophysical signatures of mineral deposit types in Finland
Edited by Meri-Liisa Airo
Geological Survey of Finland, Special Paper 58, 117–144, 2015

HYPERSPECTRAL CLOSE-RANGE LWIR IMAGING SPECTROMETRY – 3 CASE STUDIES

by

Viljo Kuosmanen[1], Hilkka Arkimaa[1], Markku Tiainen[1] and Rainer Bärs[2]

Kuosmanen, V. , Arkimaa, H., Tiainen, M. & Bärs, R. 2015. Hyperspectral close-range LWIR Imaging spectrometry – 3 case studies. *Geological Survey of Finland, Special Paper 58*, 117–144, 14 figures and 6 tables.

Long wavelength infra-red (LWIR) imaging spectrometry data acquired with the SisuROCK instrument were tested for their ability to estimate mineral abundances in rock samples. Three diverse targets were selected to test the method. The targets were the Kemi chrome mine, the Pyhäsalmi Cu-Zn-S mine and the Kedonojankulma Cu-Au ore prospect. In Kemi, the scope was to determine whether the ore types and a few host rocks were distinguishable by LWIR. In Pyhäsalmi and Kedonojankulma, the main focus of the study was on the identification of the alteration minerals amongst other minerals. A set of exploration drilling powders from Pyhäsalmi was also included in the study. Their mineral abundances and three main chemical commodities, Cu, Zn and S, were additionally estimated.

Partial least squares regression (PLSR) and linear unmixing regression (UMXR) successfully predicted the quantities of those minerals that were 'sufficiently present'. In the Kemi case, these were: actinolite, albite, chlorite, chromite, dolomite, epidote, magnesite, quartz, serpentine, talc and tremolite. In the Pyhäsalmi and Kedonojankulma cases, they were: albite, allanite, biotite, chalcopyrite, cordierite, ilmenite, K-feldspar, laumontite, muscovite, phlogopite, plagioclase and quartz. These could be quantified with a fairly small risk, i.e. mean absolute error (MAE) ≤ 16%, Pearson correlation coefficient (CC) ≥ 0.4 and p-value ≤ 0.05. Those minerals that classify the ore types and wall rocks in the Kemi case and the main and alteration minerals in the Pyhäsalmi and Kedonojankulma cases belong to the list of the predictable minerals. In the Kemi case, the predictable minerals are: actinolite, albite, chlorite, chromite, dolomite, epidote, magnesite, quartz, serpentine, talc and tremolite. In the Pyhäsalmi and Kedonojankulma cases, they are: albite, biotite, chalcopyrite, cordierite, K-feldspar, muscovite, phlogopite, plagioclase and quartz.

PLSR and UMXR produced mutually coincident results. The accuracy for the sample composition prediction was seemingly better than that for a single mineral prediction on average. The reason for this is that the minor minerals that are present in mineral prediction are 'nearly absent' in sample composition prediction. The main minerals, including the alteration minerals, and their unknown new mixtures can be quantified using this technique with moderate accuracy, which benefits mineral exploration and mining actions.

Keywords (GeoRef Thesaurus, AGI): minerals, quantitative analysis, remote sensing, hyperspectral analysis, image analysis, spectroscopy, Kemi, Pyhäsalmi, Kedonojankulma, Finland

1 Geological Survey of Finland, P.O. Box 96, FI-02151 Espoo, Finland
2 Specim Oy, Elektroniikkatie 13, P.O. Box 110, FI-90590 Oulu, Finland

E-mail: viljo.kuosmanen@gtk.fi, hilkka.arhimaa@gtk.fi, markku.tiainen@gtk.fi

INTRODUCTION

Remote sensing and analysis involves measuring and studying samples of light and nearby electromagnetic radiation reflected or emitted from a target at varying wavelengths, preferably from 0.3 microns to 20 microns (300 to 20 000 nanometers). The variety of absorption processes and their wavelength dependence allows us to obtain information on the abundances of minerals. Due to the varying molecular structure of different minerals, their reflectance/emittance characteristics are expressed by the respective wavelengths of electromagnetic radiation. Traditionally, two parts of that wavelength area are used for mineral mapping: visible to short wavelength infrared (VSWIR, 0.3–2.5 microns) and long wavelength infrared (LWIR, 3–14 micron) areas. The VSWIR area is sensitive, for example, to clay minerals, micas, chlorites, carbonates, talc, sulphates and iron oxides, and the LWIR area is sensitive, for example, to quartz, feldspars, garnet, olivine, pyroxenes and oxides. Therefore, the VSWIR and LWIR areas highly complement each other in remote sensing.

If the remote sensor is able to scan from tens to hundreds of contiguous channels of the electromagnetic spectrum, it is defined as a hyperspectral remote sensor or an imaging spectrometer (IS). The SisuROCK (Specim Oy, Oulu, Finland) sensor is able to conduct close-range hyperspectral 'remote' sensing.

The rapid mineral mapping method using reflected and emitted hyperspectral SWIR and LWIR wavelengths of electromagnetic radiation has been introduced to mineral mining and exploration markets. At present, this hyperspectral method does not compete with the classical mineral identification methods (e.g. SEM, X-ray diffraction or MLA) as an accurate tool on a per-sample basis. However, the hyperspectral method will soon develop towards the full detection of mineral species over large sets of samples or geological surfaces. The hyperspectral method is by far the most rapid one, capable of measuring millions of spectra as pixels per minute. Furthermore, abundant minerals with developing accuracy can be quantified from the spectra. Therefore, it is important to be prepared for its utilization.

Hyperspectral close-range drill core imaging and wall rock imaging and analysis were first conducted using the PIMA spectrometer (Kruse 1996). The mining industry uses hyperspectral data for operational exploration, separation and concentration purposes. Both lateral and vertical hyperspectral close-range imaging spectrometry of rocks have been reported (Gallie et al. 2002, Bolin and Moon 2003, Ragona et al. 2006, Brown et al. 2008). These papers report that the hyperspectral imaging of rocks and rock surfaces is a very promising technique to estimate mineralogical continua, and to bridge the gap between geological point measurement and image data. It was demonstrated quite early that the number of minerals that can be detected and quantified is markedly increased by the use of thermal infrared wavelengths (Abrams et al. 1991, Hook and Kahle 1996). Thermal remote sensing of rocks was greatly developed by Salisbury et al. (1989) and Salisbury and Daria (1992).

Currently, the SisuROCK is the only commercial instrument offering a thermal (LWIR) imaging option. The commercial HyLogger (Mason & Huntington 2012) offers only a point-measurement thermal spectrometer, capturing profile-type spectral data. The Aerospace Corporation started the development of a research-type instrument named SEBASS (Spatially Enhanced Broadband Array Spectrograph System) in 1993 (Taranik et al. 2008), which has also been used in geological remote sensing and close range mineral scanning tests (Kirkland et al. 2002).

The methods used for processing imaging spectrometry data from drillcores are mostly the same as are known to the remote sensing community: spectrum matching techniques and subpixel methods (van der Meer 2006). We are especially interested in the added value of LWIR for quantitative mineral estimation, because there have been no previous publishes cases in Finland and a few in the entire world. The main interest here is, of course, to reveal the precision of the estimates of minerals.

The purpose of this study was to test and develop the interpretation of the LWIR close-range remote sensing technique for the rapid mapping of rocks and minerals in diverse mining environments. Therefore, sample sets were selected from four diverse targets: the layered intrusion-hosted Kemi Cr ore, the volcanogenic massive sulphide-type Pyhäsalmi Cu-Zn-S ore related altered country rocks, the granitoid-hosted Kedonojankulma Cu-Au ore prospect and Pyhäsalmi ore exploration

drilling powders. The samples of the current study were related to mining technology aspects rather than forming a complete set covering the whole geological regime. This study consisted of the following tasks:

- Classification of the mineral/rock samples separately using their MLA and LWIR data;
- Testing chances for quantitative mineral detection using LWIR data;
- Assessment of the accuracy of mineral quantity prediction.

This paper introduces the one way to use LWIR imaging spectrometry for mining operations and geological studies. The SisuROCK hyperspectral core logging workstation, which contains an LWIR imaging spectrometer, is described. The LWIR reflectance/emissivity spectra of the targets are described in reference to the international spectral libraries and the current measurements. A dedicated LWIR spectral library (in SisuROCK wavelength domain) has been built for the Kemi, Pyhäsalmi and Kedonojankulma cases. The geology of the ore deposits is briefly described, as well as the criteria for the selection of the samples. The main part of this report concerns the classification of rock types and the quantitative prediction minerals from the precision point of view. The prediction methods are partial linear unmixing regression (UMXR) and partial nonlinear least squares regression (PLSR). The results are validated in relation to the reference measurements, prediction of minerals and the prediction methods used.

METHODS

Imaging spectrometry using SisuROCK applied to Kemi, Pyhäsalmi and Kedonojankulma samples

SisuROCK, developed by Specim Oy (Oulu, Finland), is a fully automated hyperspectral imaging workstation for easy and high-speed scanning of drill cores. Depending on the application, SisuROCK contains a combination of the following spectral cameras: VNIR (0.4–1.0 μm), SWIR (0.97–2.5 μm), combined VNIR+SWIR (0.38–2.5 μm), LWIR (8–12 μm) and a high-resolution RGB camera. LWIR (long wave infrared) or thermal spectra usually cover the electromagnetic spectrum between 3.0–15.0 μm. For the current study, the SisuROCK OWL instrument measured the thermal spectrum between 7.065–12.35 μm. SisuROCK collects spectral and spatial information on drillcores as the core tray is automatically moved through the system. All cameras are push-broom cameras, meaning that they image a single, full image line across the target, and the target is moved under the camera to create a 2D spatial image with full spectral information for each spatial pixel. The hyperspectral imaging data of a whole core tray is acquired in less than 2 minutes. The spatial pixel size is 0.96 x 0.96 mm^2. The detailed specifications are provided on the manufacturer's website (www.Specim.fi).

The SisuROCK LWIR imaging for the current study was carried out on 16 June 2014 by the company Specim Oy in Oulu, Finland (http://specim.fi/index.php/products/geology/sisurock/). The samples were laid in two black-painted, otherwise normal drill core trays (37.0 x 103.7 cm in size), with each tray consisting of six sites for the cores/samples. The rock samples were dry and clean in the sense that they were kept in dry indoor temperatures and conditions for weeks and smoothly brushed before scanning. An automatic conveyor belt carried the trays under the field-of-view of the spectrometer. The sample set in the drill core trays contained the following (the numbers refer to Fig. 1):

- Pure mineral 'markers' (numbers 1–18, 90), powder/block (mainly ground pure mineral crystals) ;
- Ore concentrates from Kemi and Pyhäsalmi mines (20–23), powder
- Drilling powder from the Pyhäsalmi Cu-Zn-S mine (24–59, 106–107), powder
- Samples of Kemi Cr ore and host rocks (60–70, 80–89, 98–105), block and drill core
- Pyhäsalmi samples related to alteration studies (71–79, 91), drill cores
- Pyhäsalmi samples related to alteration studies (108–122), drill 'chips'
- Kedonojankulma samples related to alteration studies (92–97, 123–153), drill cores.

The marker minerals were (from 1 to 18): plagioclase (50% An), serpentine (antigorite), albite and

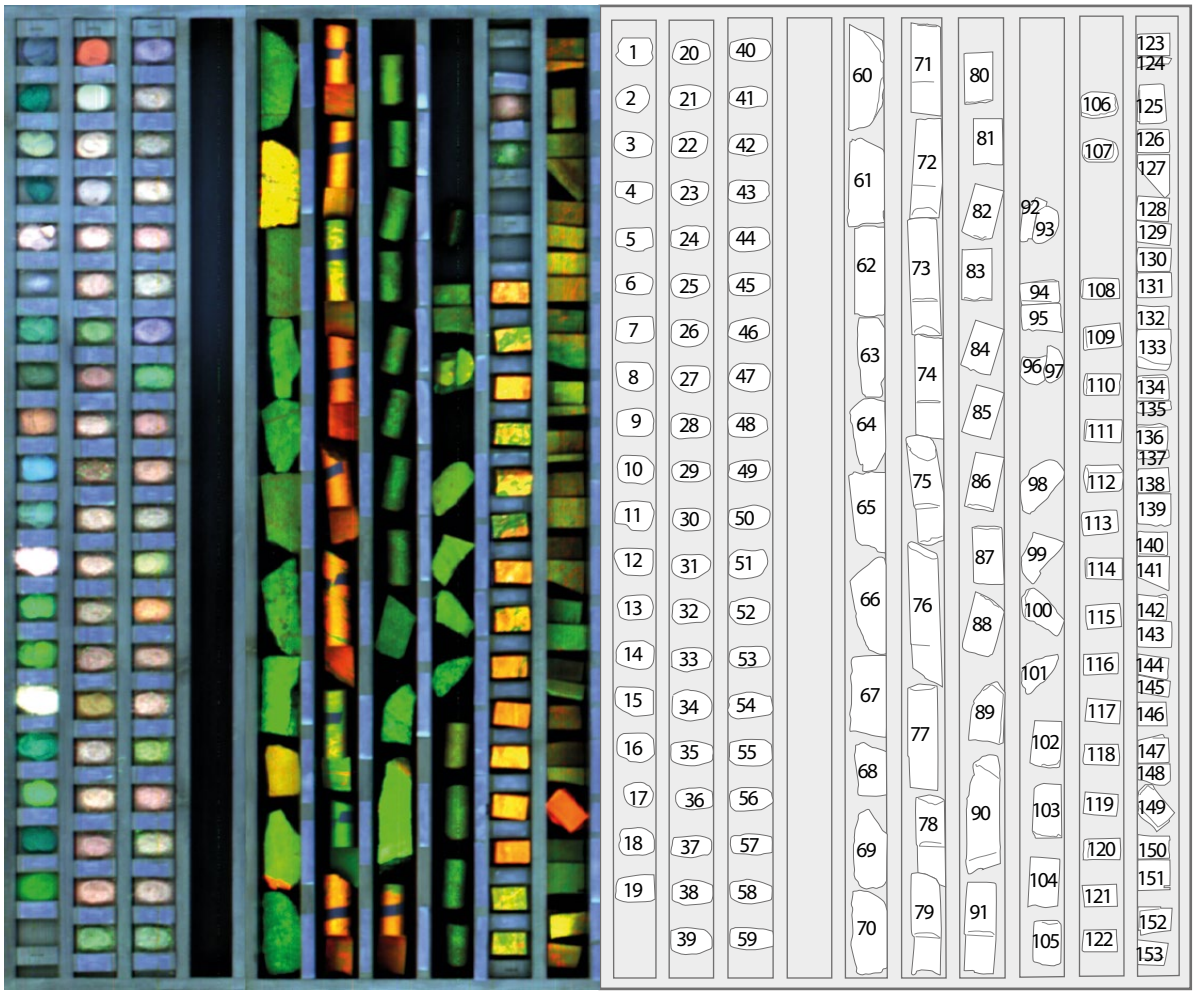

Fig. 1. A composite picture of all samples: The SisuROCK LWIR image (left) and their ID numbers (right). The mineral/chemical contents of most of the samples can be found in GTK's archives with these numbers. The colours of the LWIR image represent wavelength bands 8386 nm, 10162 nm and 11985 nm (r, g and b, respectively).

serpentine from Kemi mine, graphite, magnesite, biotite, hornblende, cordierite, apatite, phlogopite, dolomite, tremolite, chlorite (group), calcite, talc, garnet (almandine) and muscovite. Number 19 is an industrial smelted impure feldspar and not therefore used here.

The scanning produced a 117-band LWIR-image matrix for both trays. These two images were mosaicked into one combined SisuROCK LWIR image for the current studies (Fig. 1, left). This entire study was based on this image. The drawing on the right shows the sample locations and numbers that refer to the stored mineral/chemical reference data.

Preprocessing from raw data to reflectance and corrections for blinking pixels

The reflectance R is defined as the fraction of the total infrared light irradiance, incident on the surface plane of the material, that is reflected back. For the total incident light on the surface of a material:

Reflectance + Absorbance + Transmittance = 100%

The SisuROCK hyperspectral raw data (= image, dark, white [DN]) was directly transformed to reflectance, R, using the following formula:

R = (image – dark)/(white – dark) , 0≤R ≤1. We denote for clarity: R x 10000. = X0, and later in this report, X0 is also called reflectance.

The conversion of the recorded signal to reflectance removes the camera and illumination functions from the acquired data, leaving only the target material response.

The captured white reference is used as an absolute reference signal to scale the input data. The white reference target consists of a panel sheet with known, high (~100%) reflectance over the full wavelength range and reflects all wavelengths (nearly) evenly to the sensor. The dark reference level is obtained by closing the camera shutter, thereby obtaining a signal level corresponding to absolute darkness, or for thermal measurements, alternatively imaging a room-temperature dark cavity, giving the background thermal signal. This dark level was subtracted from the scanned image and from the response of the white reference. Thereafter, these magnitudes were mutually ratioed. Therefore, R is a dimensionless parameter. It describes the target's ability to reflect/emit electromagnetic radiation as a function of wavelength, in 117 wavelengths bands between 7065–12 350 nm. Reflectance was computed separately for each pixel in order to remove the variation due to individual detector pixels. Both the white and dark references were measured during each scan to remove time-dependent variation in the signal. After some noisy channels were omitted, those images that contained the planned sample set from the test areas were mosaicked into one 632 x 977 x 86 (columns x lines x bands) image. The mosaic was split into one-test-area images when necessary.

According to López-Alonso and Alda (2002), the number of bad or blinking pixels is a quality figure that defines a given detector array. However, the exact definition of a bad pixel is not standardized; it differs depending on the author of the paper. Usually, it is possible to define three types of bad pixels depending on how the output signal of the pixel depends on the number of photons (light) collected: (1) 'always on' or 'always off' pixels are those that always produce the same signal, (2) noisy pixels are those having noise greater than a fixed threshold, and (3) blinking or drifting pixels are those having temporal behaviour clearly different from those considered as good pixels. However, this classification is not universal and strongly depends on the context.

The 'blinking' or 'bad' pixel phenomenon exists in most camera detectors to a varying degree, and also in the thermal images recorded by SisuROCK. This means that the output signal intensity of a number of pixels in the 2D detector matrix does not depend on the number of photons collected. In spectral images, these can be seen as stripes in a spatial image, or peak noise in pixel spectra. These erroneous signals were filtered by calculating a moving median over three consecutive channels along the spectral dimension.

Spectral libraries

Several LWIR spectral libraries are available for the public use. A large number of emissivity spectra of minerals, rocks, vegetation and man-made objects have been collected in the ASTER library (Balridge et al. 2009). The ENVI + IDL image processing environment (Exelis/Harris Corporation, Melbourne Florida, USA) contains several spectral collections for minerals. The VSWIR area is commonly well represented, but the thermal domain is not evenly covered. The spectra may contain gaps and the data from different sources for a single mineral species are often based on different spectral sampling. The ENVI spectral library was studied in detail and the suitable material was included and scaled into the same spectral domain with the SisuROCK data. However, the analysis of the quantities is mainly based on the SisuROCK spectra.

A dedicated spectral library for the current Kemi and Pyhäsalmi-Kedonojankulma SisuROCK studies was built using the marker minerals (samples 1–18) in the combined sample image and other samples with the highest possible single mineral content (samples 80, 90 and 149). The dedicated LWIR spectral library is archived in the permanent computer storage at the Geological Survey of Finland.

Ancillary measurements

Samples as targets for various measurements

The sampling strategy was based on selecting a representative set of rocks from the diverse mining domains. All 153 samples (see Fig. 1) from the test sites were measured with the SisuROCK OWL scanner. The mineralogy of most of the samples was also assayed by other methods, which are briefly introduced in the later sections. It is important to note that the part of a sample exposed to

various assay methods was not exactly the same. The SisuROCK data are imported for computing through hand-drawn windows on the image of the samples. These windows are called regions of interest (ROIs). The ROIs were drawn in such a way that maximal reflectance information from any sample is transmitted to computing, but not the background and the shadowed parts of the rocks. The size of the ROIs varied from 500 mm^2 to 1800 mm^2. The non-coincidence of these two types of windows is naturally a source of 'small' errors.

Mineral liberation analysis, MLA

The mineral content of the chosen model targets in the combined sample set of the current study was determined by the mineral liberation analysis (MLA) method. It is a scanning electron microscope FEI Quanta 600, equipped with energy dispersive X-ray (EDX) spectrometers (Sylvester 2012). MLA is an automated mineral analysis system that can identify minerals in the polished sections of drill core, particulate or lump materials, and quantify a wide range of mineral characteristics, such as mineral species abundance, grain size and liberation. From the total of 153 samples, 108 were subjected to mineralogical assays by MLA, which scanned the sample from a window, the size of which is constantly 707 mm^2. The MLA analyses were used as ancillary response data in building the regression models for the mineral prediction. The current samples are mainly homogeneous, fine or medium grained, and the MLA measurement is consequently considered to represent the whole ROI. Therefore, the non-coincidence error between the ROI domain and the MLA domain is small.

X-ray diffraction and XRF chemical analyser

X-ray diffraction (XRD) methods were used to verify the 18 marker minerals species and in a few cases for small spots of rock samples to identify unknown minerals (http://en.gtk.fi/research/infrastructure/researchlaboratory/XRD.html).

During this study, the DELTA Handheld XRF Analyzer (OLYMPUS, Tokyo, Japan) was used for chemical element analysis of the rock drilling powder samples. The handheld XRF is a fast and cost-effective way to identify and quantify the content of models used in interpretation (http://www.olympus-ims.com/en/xrf-xrd/delta-handheld /). The measurements were repeated 4–10 times in order to minimize the error in the analysis. Most of the drilling powder samples (nos. 25–59, 106, 107) were analysed by Pyhäsalmi Mine Oy, but the concentrates (nos. 20-23) were analysed by XRF. The XRD and XRF measurement were in practice not used in the statistical prediction; they were only used to ensure the mineral species/element content in specific cases.

A quantitative interpretation method for LWIR reflectance data on rocks

Notations and preprocesses

In this report, the LWIR SisuROCK reflectance spectra of the samples are denoted as $\boldsymbol{X_0}$ ($0. \le \boldsymbol{X_0} \le 10000.$ [DN]) and the MLA mineral compositions of the same samples are denoted as $\boldsymbol{Y_0}$ ($0. \le \mathbf{Y_0} \le 100.$[area %]).

The frequency of a mineral for the variable $\boldsymbol{Y_0}$ and for the estimated results is here expressed in 'area units' [au]. The sum area for a mineral simply means the integrated mineral percentage from the MLA assays through the sample set under examination. The full content of one sample is 100% (± a small assay error) and it is equal to 100 au. We assume that the total MLA focus area on the chip of a sample is a constant 706.86 mm^2. Therefore 1 au = 7.0686 mm^2 = 7.6136 pixels in SisuROCK terms.

Because the characteristic LWIR features for minerals are mostly indicated by fluctuations in the reflectance/emittance curve, those fluctuations are optionally enhanced here to maximize the discernibility of the minerals. For this purpose, a three-term high-pass (Pratt 2001) component $\boldsymbol{r_1}$ was first computed for $\boldsymbol{X_0}$, multiplied by a constant $0 \le f \le 100$ and added to the original curve before the next steps. If the components of $\boldsymbol{X_0}$ are $a_1, a_2, \ldots, a_k$, then the high-pass component $\boldsymbol{r}$ is defined by the moving residual, where the general term of $\boldsymbol{r}$ is defined by $r_n = a_n - (a_{n-1} + a_n + a_{n+1})/3$, $(n \le k)$, except that the first and last terms are truncated. The constant f varies from 0% to 1% from the maximum reflectance 10000 , i.e. $0 \le f \le 100$. The constant f for each case was computed by minimizing the estimation errors. The enhanced spectrum is thereafter denoted as $\boldsymbol{X_1} = \boldsymbol{X_0} + f\,\boldsymbol{r}$.

Unsupervised hierarchical clustering was used here to foresee the true mineralogical clusters of the samples ($\boldsymbol{Y}_0$) and compare them with the spectral ($\boldsymbol{X}_1$) clusters of the samples. This connectivity based clustering software/procedure was here assembled from the available interactive data language (IDL) tools. The distance between elements of each cluster was used to compute the dendrogram, a 'cluster tree', which reveals the mutual hierarchy of the mineralogy and the mean spectra separately. The input for the clustering is a vector containing the pairwise distance matrix in compact form. Given a set of m items of $\boldsymbol{Y}_0$ or $\boldsymbol{X}_1$, with the distance between items i and j denoted by D(i, j), pairdistance should be an m(m-1)/2 element vector, ordered as: [D(0, 1), D(0, 2), ..., D(0, m-1), D(1, 2), ..., D(m-2, m)]. Single linkage of nearest neighbour was used here for computing the link distances between clusters for the dendrogram.

Unmixing and partial least squares regression

Mineral quantities were here estimated from the optionally filtered mean spectra of the ROIs ($\boldsymbol{X}_{1R}$) or the pixel spectra ($\boldsymbol{X}_{1P}$) and the mineral data $\boldsymbol{Y}_0$ using two methods. These were the classical unmixing (UMX) regression (UMXR) (Nielsen 1999) and partial least squares (PLS) regression (PLSR; Wold 1975, Geladi and Kowalski 1986). The role of UMX was to cross-validate the results from the PLS method. Mineralogy and analytical chemistry normally use sharp absorption peaks for the identification of species of minerals or elements and their quantities. Both PLSR and UMXR can, instead of the sharp peaks, utilize the soft variation in absorption to identify minerals or elements and their quantities.

The final estimation of quantities is based on the (optionally filtered) LWIR ROI spectra or pixel spectra as the predictor variables $\boldsymbol{X} = \boldsymbol{X}_{1R}$ or $\boldsymbol{X} = \boldsymbol{X}_{1P}$. Mineral compositions are the response variables $\boldsymbol{Y} = \boldsymbol{Y}_0$. In the usual multiple linear regression context (UMXR), the least-squares solution (Mevik and Wehrens 2007, Wold et al. 2001) for

$$\boldsymbol{Y} = \boldsymbol{XB} + \boldsymbol{\varepsilon} \quad (2)$$

is given by the regression model $\boldsymbol{B}$

$$\boldsymbol{B} = (\boldsymbol{X}^T\boldsymbol{X})^{-1}\boldsymbol{X}^T\boldsymbol{Y} \quad (3)$$

Because the regression is mostly carried out with least squares, there will be a residual term $\varepsilon \neq 0$. The problem is often that $\boldsymbol{X}^T\boldsymbol{X}$ is singular, either because the number of variables in $\boldsymbol{X}$ exceeds the number of samples or because of collinearities (Mevik and Wehrens 2007) between the variables.

PLSR is a widely used method in chemometrics, economics, and in medical and even social sciences. This approach is suitable for interpreting spectra that are highly correlated, or nearly singular matrices may occur in the procedure for calculating the regression between the predictor $\boldsymbol{X}$ and response variables $\boldsymbol{Y}$ (Wold et al. 2001).

The PLS procedure divides both $\boldsymbol{X}$ and $\boldsymbol{Y}$ into matrix components called scores and loadings by singular value decomposition (Wold 1975, Mevik and Wehrens 2007):

$$\boldsymbol{X} = \boldsymbol{WT} + \varepsilon_x \quad (4)$$

$$\boldsymbol{Y} = \boldsymbol{PQ} + \varepsilon_y \quad (5)$$

The scores $\boldsymbol{W}$ and $\boldsymbol{P}$ and loadings $\boldsymbol{T}$ and $\boldsymbol{Q}$ are calculated iteratively to maximally describe the covariance between $\boldsymbol{X}$ and $\boldsymbol{Y}$ (Wold 1975, Mevik and Wehrens 2007). We denote

$\boldsymbol{R} = \boldsymbol{W}(\boldsymbol{P}^T\boldsymbol{W})^{-1}$ then the regression term $\boldsymbol{B}$ is:

$$\boldsymbol{B} = \boldsymbol{R}\,(\boldsymbol{T}^T\boldsymbol{T})^{-1}\boldsymbol{T}^T\boldsymbol{Y} = \boldsymbol{RQ}^T \quad (6)$$

The advantage of PLSR is that the method does not necessarily need to know the spectra of the end members, i.e. the 'outermost' features in the spectral data space, as model inputs. The disadvantage of both methods is that they may produce negative 'concentrations'. The residual error term ε is uniquely expressed by the mean absolute error (MAE) and the root mean square error (RMSE). The calibration-validation error as a function of the number of samples decreases very quickly in PLSR (Krämer and Sugiyama 2011). Success in the PLSR and UMX predictions is inversely proportional to the residual error terms ε_y (RMSE and MAE) and the p-value, but proportional to the Pearson correlation coefficient (CC). All these parameters were computed for each prediction. The p-value states the risk (from 0 to 1) taken by the parameters MAE, RMSE, and CC.

The PLSR method has successfully been used for the interpretation of mineral quantities of rocks and elemental quantities in soils (Hecker et al. 2012, Middleton et al. 2011). For the current use, the UMXR and PLSR modelling methods

were coded in IDL programming language by the first author.

In practical work, we first estimated the content of all minerals within each sample represented by the ROI. Secondly, we needed to know the precision for each single mineral estimate. The mineral content is the most important information for a mining geologist and mining processes, but the parameter 'content' can only be utilized in the framework of the precision computed. Both the content and the precision parameters are computed in the same run by the PLSR (and UMXR) regression software: The mineral estimates are obtained from the rows and ROI estimates are obtained from the columns of the resulting prediction matrix. The precision estimates are obtained as residuals from the rows or columns respectively. However, because the precision of the estimates was the main target of this study, the results are represented here mainly in the light of precision and reliability parameters.

SAMPLE MATERIALS

The crucial question of this report is whether the LWIR method together with PLSR interpretation works in totally dissimilar environments. This question dictated the selection of samples from diverse environments, the Kemi and Pyhäsalmi mines and the Kedonojankulma ore prospect. The sample types were also diverse: hand specimens, dill cores and drilling powders.

Brief geological description of the Kemi chrome deposit and the selection of characteristic samples from the mine for the current study

The Kemi chrome mine is located near the town of Kemi in NW Finland, in the western part of the Tornio-Näränkävaara belt (Alapieti 2005). The substantial chromitite deposit is hosted by a layered intrusion, a chromitite layer in the lower ultramafic part of the intrusion (Alapieti and Huhtelin 2005, Iljina and Hanski 2005). U-Pb zircon data yield an Archaean age of 2.44 Ga for the Kemi intrusion (Kouvo 1977).

The 29 samples from the Kemi mine were selected by the mining experts Timo Huhtelin (pers. comm. 2014) and Ossi Leinonen (pers. comm. 2001). This sample set was not aimed to represent the whole geological regime, but instead to represent a variety of ores, soft, medium and hard ore types, and examples of wall rocks. The set of samples consisted of chromite-talc-carbonate-type soft ore, chromite-chlorite soft ore, chromite-serpentine hard ore, tremolite-chlorite-carbonate wall rocks and mafic/felsic wall rocks.

Geological description and the background for the sample selection from Pyhäsalmi and Kedonojankulma

The Pyhäsalmi Cu-Zn-S mine is located in the Pyhäjärvi commune, in the Svecofennian Proterozoic schist belt. The rocks in the area are granitoidic, dioritic and gabbroic magmatic plutonic rocks, volcanogenic felsic and mafic rocks and sedimentogenic migmatized gneisses (Korsman et al. 1997). The ore deposit is related to strong hydrothermal activity induced by bimodal volcanism, which started from the felsic type and changed into the mafic type as it continued (Mäki 1986, Kousa et al. 1997). The alteration mineralogy of the volcanites shows that the K- and Mg-enrichment in felsic volcanites correlates with quantities of sericite, cordierite, phlogopite and chlorite. Correspondingly, in mafic volcanites, the amount of cordierite, followed by chlorite, amphibole and phlogopite, is the best indicator for the alteration intensity (Puustjärvi 1999). The Pyhäsalmi samples for the current study were selected from the alteration zones around the ore deposit, bearing in mind the need to test the possibilities for mapping the alteration minerals by LWIR modelling. Altogether, 15 drill core samples from Pyhäsalmi were examined (received from J. Kousa pers comm. 2013 and Timo Mäki pers comm. 2013).

The Kedonojankulma Cu-Au ore prospect is located in the Forssa region in the municipality of Jokioinen, southern Finland. The discovered Cu-Au(-Ag-Mo) occurrence is hosted by a porphyric granitoid intrusion in the Palaeoproterozoic volcanic-intrusive Häme belt, part of the Southern Svecofennian Arc Complex in southern Finland. The fine-grained mineralization is controlled by a veined fractured and sheared, strongly altered zone in the quartz-plagioclase porphyry. The Kedonojankulma occurrence has several features that are typical of porphyry style Cu deposits. The most prominent are the metal contents and zoning, with Cu-Au-Ag-As-Mo in the core, Mo and Cu in quartz veins outside of the core and Zn-Cu-Ag in the outer zone of the intrusion. Various alteration assemblages in the mineralized zone have been identified, with silicification, chloritization, sericitization and epidotization being common (Tiainen et al. 2012, Tiainen et al. 2013).

The assumed genetic ore type of the Kedonojankulma prospect differs from the Pyhäsalmi case, but, the alteration mineralogy is partly the same and these Pyhäsalmi and Kedonojankulma alteration-related samples were therefore decided to examine jointly in the current study.

RESULTS AND DISCUSSION

Mineralogical clusters of the Kemi samples inferred from MLA

The frequent minerals encountered in the MLA studies of the Kemi samples were actinolite, albite, chlorite, chromite, biotite, calcite, dolomite, diopside, epidote, hornblende, K-feldspar, magnesite, muscovite, phlogopite, plagioclase, quartz, serpentine, talc and tremolite. Their area exceeded 1% at least in some of the samples. Chromite was mainly composed of the chromite-Mg type. Small quantities of chromite-Fe and chromite-Ti were also found, and included in the entity of 'chromite'. In

Kemi mineral prediction

Mineral index	Mineral	PLS MAE%	PLS RMSE%	PLS CC	Predictv ROIs	S-area [au]	p-value
1	**Actinolite**	**3.05**	**4.49**	**0.65**	**28**	**47.87**	**0.0001**
2	**Albite**	**4.87**	**8.84**	**0.85**	**28**	**142.39**	**0.0000**
3	**Chlorite**	**10.46**	**12.98**	**0.37**	**28**	**420.76**	**0.0499**
4	**Chromite**	**15.02**	**20.46**	**0.76**	**28**	**1019.60**	**0.0000**
5	Biotite	2.28	5.01	0.12	28	24.94	0.5450
6	Calcite	2.04	4.73	0.10	28	15.69	0.5902
7	**Dolomite**	**1.28**	**1.57**	**0.84**	**28**	**66.48**	**0.0000**
8	Diopside	2.02	3.42	-0.03	28	15.78	0.8735
9	**Epidote**	**2.05**	**3.07**	**0.52**	**28**	**24.61**	**0.0040**
10	Hornblende	1.34	2.23	0.04	28	7.70	0.8451
11	K_feldspar	1.10	2.73	-0.05	28	12.90	0.8133
12	**Magnesite**	**2.90**	**3.46**	**0.90**	**28**	**118.28**	**0.0000**
13	Muscovite	0.88	2.19	-0.03	28	10.41	0.8720
14	Phlogopite	5.54	7.91	0.06	28	50.01	0.7526
15	Plagioclase	1.35	2.00	-0.02	28	6.74	0.9199
16	**Quartz**	**2.36**	**5.18**	**0.85**	**28**	**71.49**	**0.0000**
17	**Serpentine**	**4.13**	**5.04**	**0.96**	**28**	**363.70**	**0.0000**
18	**Talc**	**3.23**	**4.47**	**0.94**	**28**	**298.17**	**0.0000**
19	**Tremolite**	**8.48**	**11.51**	**0.64**	**28**	**170.18**	**0.0002**
	Total area [au]					**2887.69**	

Table 1. The statistical descriptors for the mineral prediction by partial least squares regression (PLSR) in the Kemi case. Mineral indices are in the left column (for Figure 6). The mean absolute errors (MAEs) and root mean squared errors (RMSEs) are only acceptable for the bolded minerals. The low correlation coefficient (CC) and high p-value value exclude those minerals for which the prediction is not reliable.

addition, very small quantities of other minerals were found, such as ankerite, apatite, chalcopyrite, chamosite, iddingsite, ilmenite, magnetite, magnetite-Cr, millerite, monazite, pyrite, pyrrhotite, rutile, sphalerite, titanite, zircon and pentlandine.

In Table 1, the column 'S-area' presents the frequency [au] of the named, most important minerals in this set of the Kemi samples determined by the MLA assays. Albite, chlorite, chromite, dolomite, magnesite, phlogopite, serpentine, talc and tremolite appear in the set of samples several times.

Figure 2 presents a dendrogram, i.e. an illustration of the results from the Kemi MLA mineral

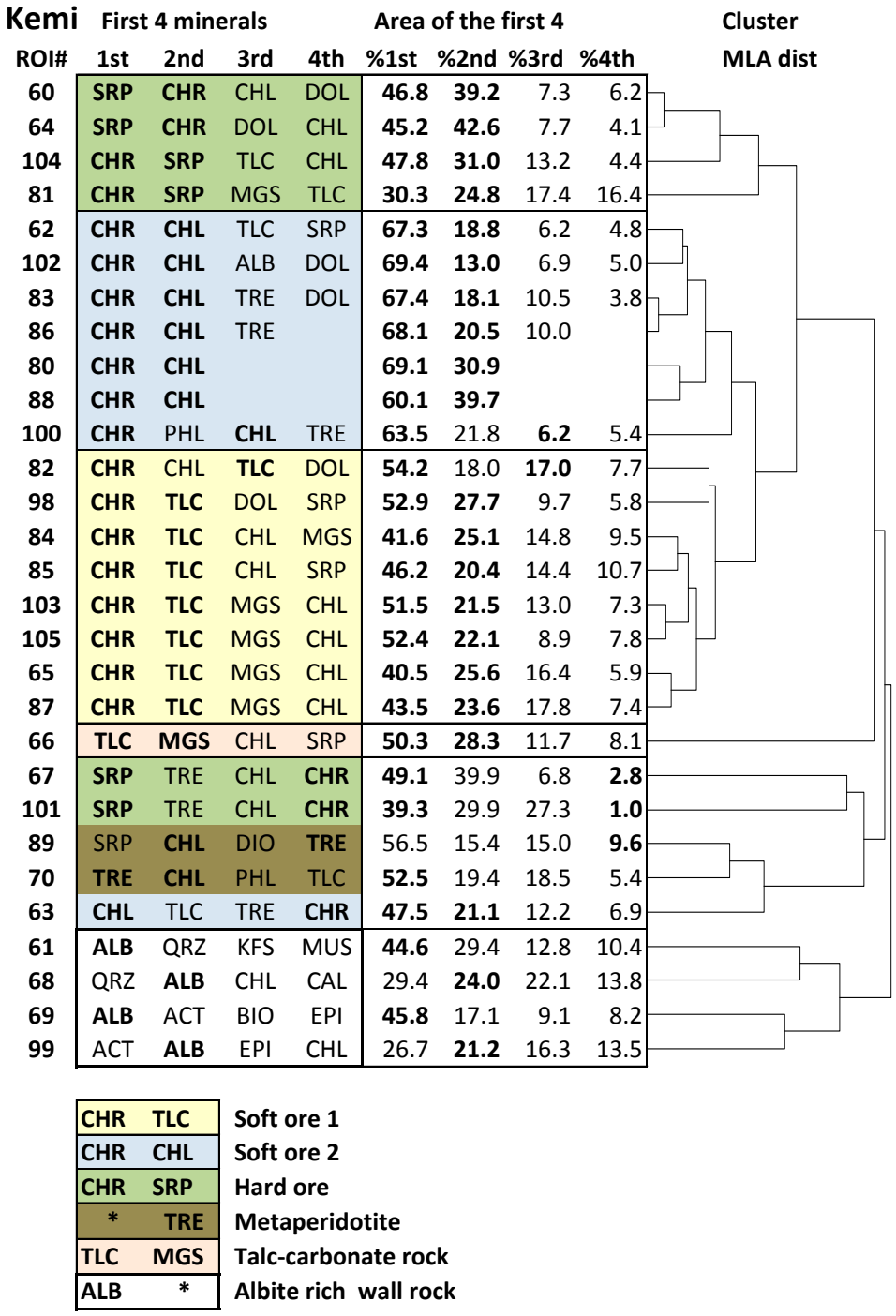

Kemi	First 4 minerals				Area of the first 4				Cluster
ROI#	1st	2nd	3rd	4th	%1st	%2nd	%3rd	%4th	MLA dist
60	**SRP**	**CHR**	CHL	DOL	**46.8**	**39.2**	7.3	6.2	
64	**SRP**	**CHR**	DOL	CHL	**45.2**	**42.6**	7.7	4.1	
104	**CHR**	**SRP**	TLC	CHL	**47.8**	**31.0**	13.2	4.4	
81	**CHR**	**SRP**	MGS	TLC	**30.3**	**24.8**	17.4	16.4	
62	**CHR**	**CHL**	TLC	SRP	**67.3**	**18.8**	6.2	4.8	
102	**CHR**	**CHL**	ALB	DOL	**69.4**	**13.0**	6.9	5.0	
83	**CHR**	**CHL**	TRE	DOL	**67.4**	**18.1**	10.5	3.8	
86	**CHR**	**CHL**	TRE		**68.1**	**20.5**	10.0		
80	**CHR**	**CHL**			**69.1**	**30.9**			
88	**CHR**	**CHL**			**60.1**	**39.7**			
100	**CHR**	PHL	**CHL**	TRE	**63.5**	21.8	**6.2**	5.4	
82	**CHR**	CHL	**TLC**	DOL	**54.2**	18.0	**17.0**	7.7	
98	**CHR**	**TLC**	DOL	SRP	**52.9**	**27.7**	9.7	5.8	
84	**CHR**	**TLC**	CHL	MGS	**41.6**	**25.1**	14.8	9.5	
85	**CHR**	**TLC**	CHL	SRP	**46.2**	**20.4**	14.4	10.7	
103	**CHR**	**TLC**	MGS	CHL	**51.5**	**21.5**	13.0	7.3	
105	**CHR**	**TLC**	MGS	CHL	**52.4**	**22.1**	8.9	7.8	
65	**CHR**	**TLC**	MGS	CHL	**40.5**	**25.6**	16.4	5.9	
87	**CHR**	**TLC**	MGS	CHL	**43.5**	**23.6**	17.8	7.4	
66	**TLC**	**MGS**	CHL	SRP	**50.3**	**28.3**	11.7	8.1	
67	**SRP**	TRE	CHL	**CHR**	**49.1**	39.9	6.8	**2.8**	
101	**SRP**	TRE	CHL	**CHR**	**39.3**	29.9	27.3	**1.0**	
89	SRP	**CHL**	DIO	**TRE**	56.5	15.4	15.0	**9.6**	
70	**TRE**	**CHL**	PHL	TLC	**52.5**	19.4	18.5	5.4	
63	**CHL**	TLC	TRE	**CHR**	**47.5**	**21.1**	12.2	6.9	
61	**ALB**	QRZ	KFS	MUS	**44.6**	29.4	12.8	10.4	
68	QRZ	**ALB**	CHL	CAL	29.4	**24.0**	22.1	13.8	
69	**ALB**	ACT	BIO	EPI	**45.8**	17.1	9.1	8.2	
99	ACT	**ALB**	EPI	CHL	26.7	**21.2**	16.3	13.5	

CHR	**TLC**	**Soft ore 1**
CHR	**CHL**	**Soft ore 2**
CHR	**SRP**	**Hard ore**
*	**TRE**	**Metaperidotite**
TLC	**MGS**	**Talc-carbonate rock**
ALB	*	**Albite rich wall rock**

Fig. 2. A dendrogram illustration for a classification of the MLA measurements of the samples from the Kemi mine. Different types of wall rocks and ores are separated, with a few exceptions. The marker mineral combination is bolded for each type. Abbreviations are: ALB = albite, ACT = actionlite, BIO = biotite, CAL = calcite, CHL = chlorite, CHR = chromite, DIO = diopside, DOL = dolomite, EPI = epidote, KFS = K-feldspar, MGS = magnesite, PHL = phlogopite, QRZ = quartz, SRP = serpentine, TLC = talc, TRE = tremolite.

data clustering. Different types of wall rocks and ore are separated in this sample set. Soft ore is divided into chromite-talc-carbonate type and chromite-chlorite type. Hard ore is seen as chromite-serpentine composite. The wall rock types are albite-dominant rock, talc-carbonate rock and metaperidotite in this sample set.

Contribution of the SisuROCK LWIR assays to the estimation of mineral quantities from the Kemi samples

Apparent mineralogical clusters inferred from the Kemi LWIR mean spectra

The filtered (constant f = 100.) LWIR mean spectra (Fig. 3) from the Kemi sample set were hierarchically clustered. The dendrogram in Figure 4 illustrates the clusters and the internal hierarchy of the LWIR spectra and possibly apparent rock types (cf. Fig. 2). The main classes are separated by the spectra, but a few exceptions occur. The internal hierarchies are about similar.

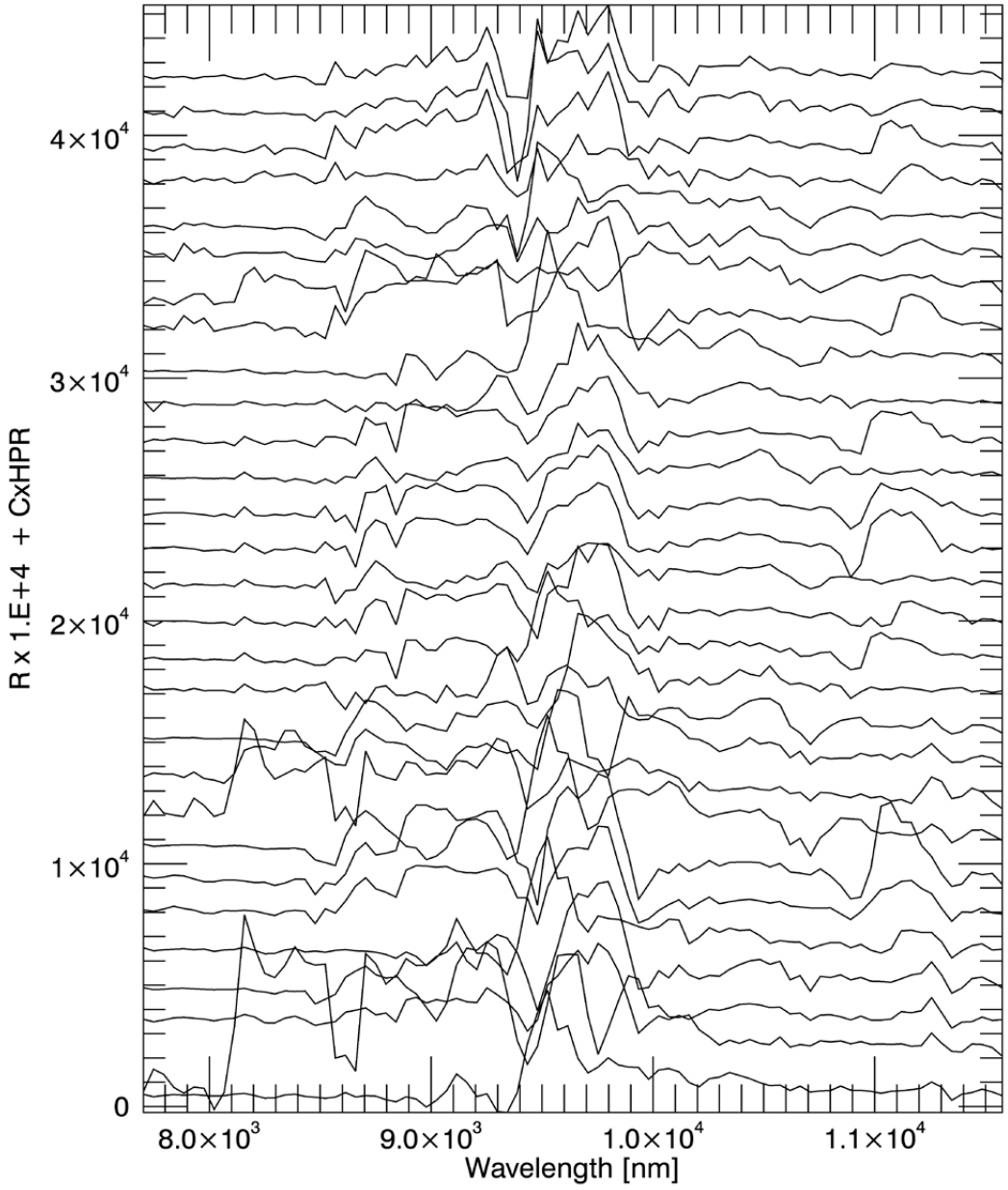

Fig. 3. The LWIR reflectance mean spectra of all 29 ROIs of the Kemi samples after the high-pass component (f = 100.) has been added to the spectra. The curves are vertically shifted for clarity.

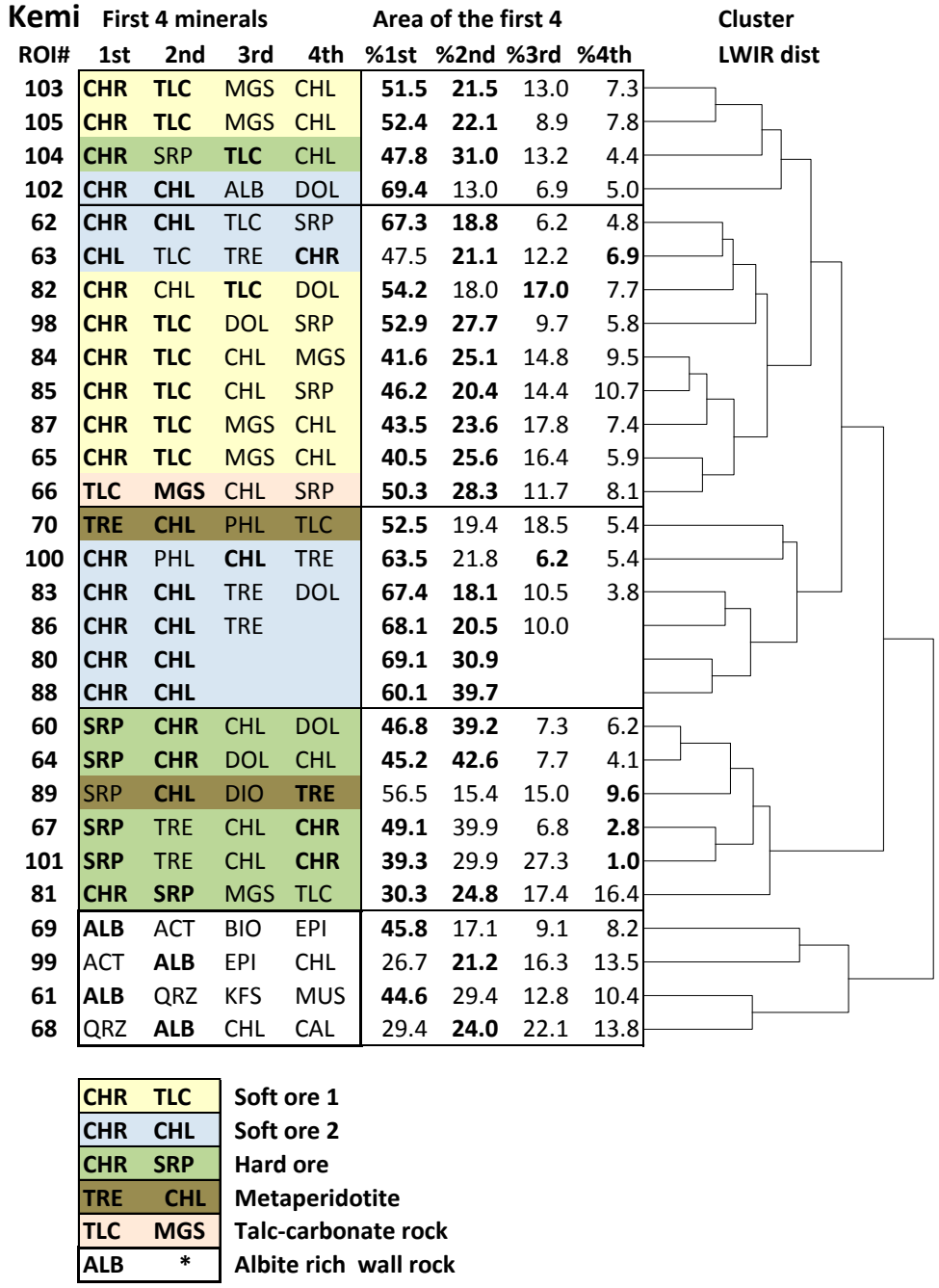

Kemi	First 4 minerals				Area of the first 4				Cluster
ROI#	1st	2nd	3rd	4th	%1st	%2nd	%3rd	%4th	LWIR dist
103	CHR	TLC	MGS	CHL	51.5	21.5	13.0	7.3	
105	CHR	TLC	MGS	CHL	52.4	22.1	8.9	7.8	
104	CHR	SRP	TLC	CHL	47.8	31.0	13.2	4.4	
102	CHR	CHL	ALB	DOL	69.4	13.0	6.9	5.0	
62	CHR	CHL	TLC	SRP	67.3	18.8	6.2	4.8	
63	CHL	TLC	TRE	CHR	47.5	21.1	12.2	6.9	
82	CHR	CHL	TLC	DOL	54.2	18.0	17.0	7.7	
98	CHR	TLC	DOL	SRP	52.9	27.7	9.7	5.8	
84	CHR	TLC	CHL	MGS	41.6	25.1	14.8	9.5	
85	CHR	TLC	CHL	SRP	46.2	20.4	14.4	10.7	
87	CHR	TLC	MGS	CHL	43.5	23.6	17.8	7.4	
65	CHR	TLC	MGS	CHL	40.5	25.6	16.4	5.9	
66	TLC	MGS	CHL	SRP	50.3	28.3	11.7	8.1	
70	TRE	CHL	PHL	TLC	52.5	19.4	18.5	5.4	
100	CHR	PHL	CHL	TRE	63.5	21.8	6.2	5.4	
83	CHR	CHL	TRE	DOL	67.4	18.1	10.5	3.8	
86	CHR	CHL	TRE		68.1	20.5	10.0		
80	CHR	CHL			69.1	30.9			
88	CHR	CHL			60.1	39.7			
60	SRP	CHR	CHL	DOL	46.8	39.2	7.3	6.2	
64	SRP	CHR	DOL	CHL	45.2	42.6	7.7	4.1	
89	SRP	CHL	DIO	TRE	56.5	15.4	15.0	9.6	
67	SRP	TRE	CHL	CHR	49.1	39.9	6.8	2.8	
101	SRP	TRE	CHL	CHR	39.3	29.9	27.3	1.0	
81	CHR	SRP	MGS	TLC	30.3	24.8	17.4	16.4	
69	ALB	ACT	BIO	EPI	45.8	17.1	9.1	8.2	
99	ACT	ALB	EPI	CHL	26.7	21.2	16.3	13.5	
61	ALB	QRZ	KFS	MUS	44.6	29.4	12.8	10.4	
68	QRZ	ALB	CHL	CAL	29.4	24.0	22.1	13.8	

CHR	TLC	Soft ore 1
CHR	CHL	Soft ore 2
CHR	SRP	Hard ore
TRE	CHL	Metaperidotite
TLC	MGS	Talc-carbonate rock
ALB	*	Albite rich wall rock

Fig. 4. A dendrogram illustration for a classification of the LWIR mean spectra of the samples from the Kemi mine. The Cr ore is separated into chromite-talc (yellow), chromite-chlorite (blue) and chromite-serpentine (green). Different types of wall rocks and ores are separated, with a few exceptions.

Quantitative mineralogical prediction from the mean spectra of the SisuROCK Kemi data

The quantitative mineral content for each sample from the Kemi mine was predicted from the filtered (f = 100.) LWIR mean spectra using the PLS regression model. The total number of samples with ROIs from Kemi was 29. The regression model for each sample in turn was built of the other 28 sample spectra.

The PLSR prediction for the main minerals produced the following accuracy parameters shown in Table 1. The classical linear unmixing (UMXR) method produced quite similar values for the error parameters as the PLSR. The simultaneous high correlation coefficient and the low p-value in Table 1 suggest that the mean absolute estimation errors (MAEs) are reliable (low p-values and moderate CCs) for actinolite, albite, chromite, dolomite, magnesite, quartz, serpentine, talc and tremolite. These well-predicted minerals cover 2744 area

units from the total 2888 au. Figure 5 shows that if the sum area [au] for a mineral is very small, it will produce a low reliability (high p-value), and vice versa. In this case, the low CC and high p-value have dropped chlorite and phlogopite from the list of the expected best success; the reason for this is discussed later in this paper. This list of well-quantified minerals essentially covers those materials that classify the ore types and the wall rocks in this sample set from the Kemi mine.

The same statistics were also computed for all Kemi ROIs (Table 2 and examples in Fig. 6, where the key to the mineral index (numbers) is in Table 1 in the two first columns). According to the correlation coefficient and the p-value, only two ROIs from 29 have unreliable estimates. They are numbers 68 and 99 (Table 2). The reason for their failure is that their mineralogy is 'strange', i.e. they do not have analogous samples among the modelling group. All other 27 ROIs obtained reliable

Kemi ROI prediction

ROI NO	PLS MAE%	PLS RMSE%	PLS CC	Predictv Minerals	S-area	p-value
60	1.58	3.05	0.99	19	100.00	0.0000
61	14.78	20.71	0.74	19	98.82	0.0003
62	2.90	3.55	0.98	19	99.98	0.0000
63	5.94	10.16	0.66	19	99.43	0.0022
64	1.16	1.82	0.99	19	99.98	0.0000
65	2.32	3.90	0.96	19	100.00	0.0000
66	3.77	7.43	0.87	19	99.93	0.0000
67	2.61	4.06	0.96	19	99.50	0.0000
68	8.76	13.15	0.18	19	99.44	0.4690
69	5.85	9.24	0.59	19	96.88	0.0078
70	5.08	9.25	0.68	19	99.79	0.0013
80	2.38	4.30	0.99	19	99.98	0.0000
81	2.46	3.80	0.95	19	99.99	0.0000
82	1.62	2.18	0.99	19	99.99	0.0000
83	1.85	2.85	0.99	19	99.78	0.0000
84	2.42	5.29	0.97	19	100.00	0.0000
85	1.23	1.73	0.99	19	100.00	0.0000
86	2.62	4.22	0.97	19	99.66	0.0000
87	2.40	4.31	0.94	19	99.99	0.0000
88	2.94	5.46	0.96	19	99.92	0.0000
89	5.66	10.58	0.73	19	98.10	0.0004
98	2.14	2.60	0.99	19	100.00	0.0000
99	6.53	8.80	0.34	19	98.31	0.1602
100	4.24	7.98	0.85	19	99.92	0.0000
101	4.28	7.47	0.79	19	98.40	0.0000
102	3.10	4.90	0.95	19	99.93	0.0000
103	2.08	2.94	0.99	19	99.99	0.0000
104	5.06	8.26	0.76	19	100.00	0.0001
105	1.86	3.20	0.97	19	100.00	0.0000
Total area [au]					**2887.71**	

Table 2. The statistical descriptors for the region of interest (ROI) prediction by partial least squares regression (PLSR) in the Kemi case. There are only two ROIs (unbolded, 68 and 99) for which the estimates and the error measures are not acceptable. The reason for this is that the quantities of the rare minerals are naturally small and they do not greatly affect the measures in the majority of the samples. The main minerals are naturally promptly represented by the area and the spectra.

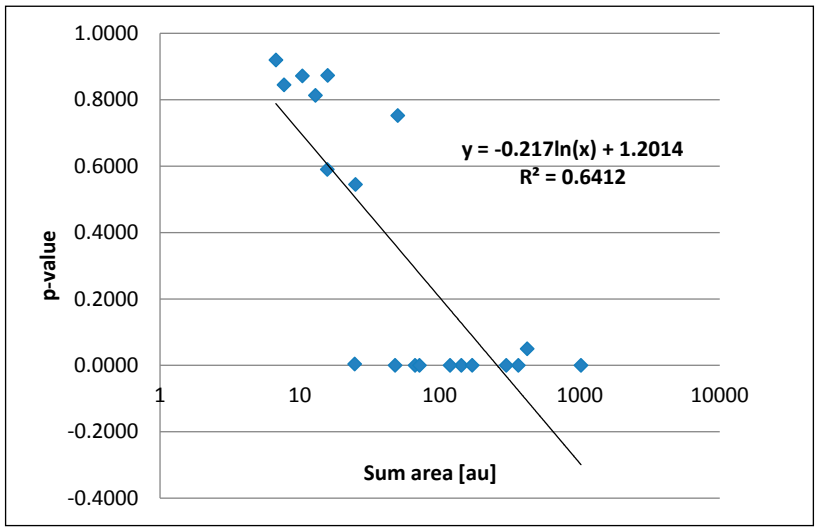

Fig. 5. The total mineral area and the risk measure p-values are logarithmically related, i.e. they are inversely proportional in the Kemi LWIR case.

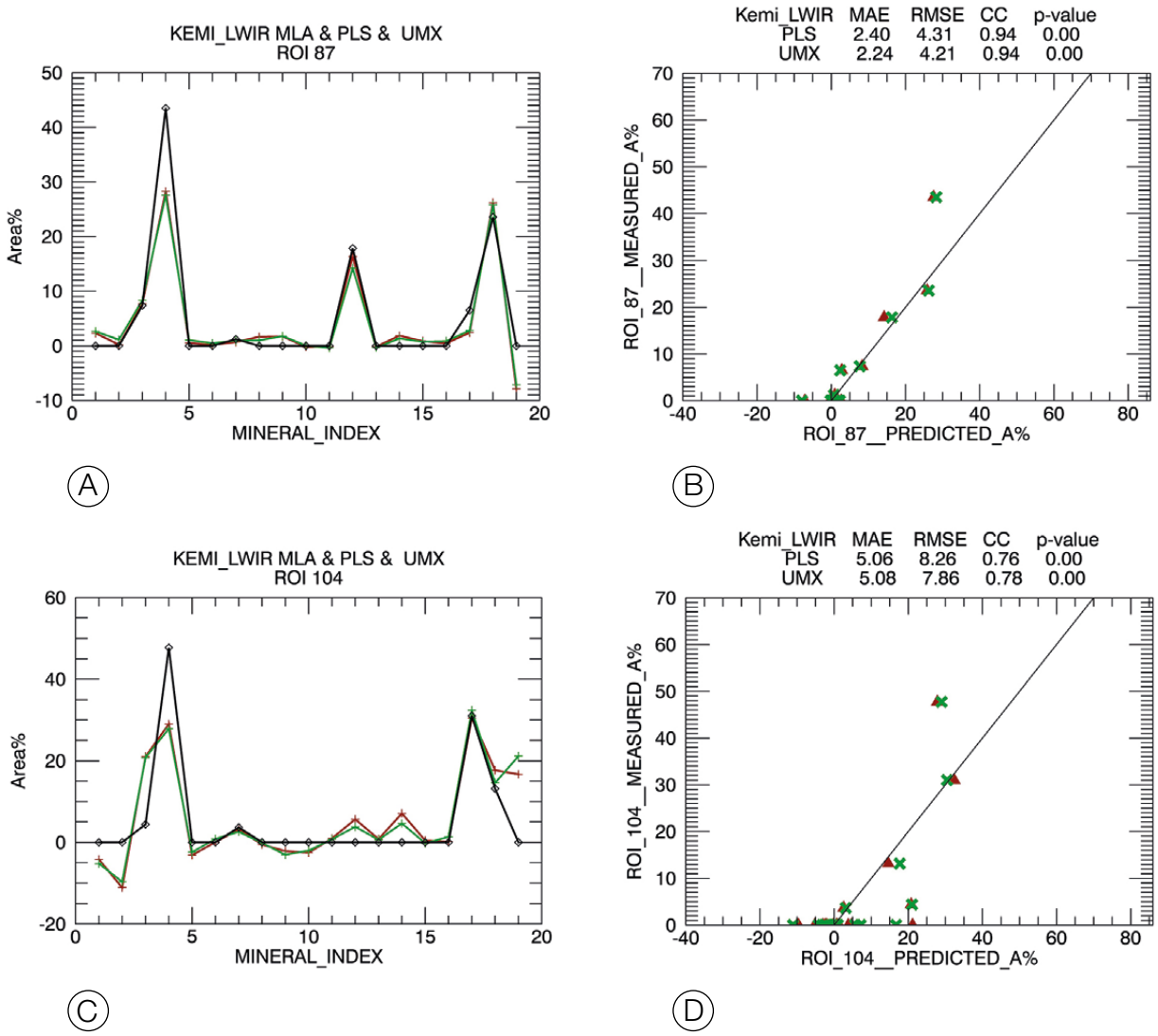

Fig. 6. Examples of the ROI prediction for the Kemi data. On the left (A and C): partial least squares estimates (PLS, red) and unmixing estimates (UMX, green) prediction from the LWIR data for the mineral contents of two Kemi ROIs, nos. 87 and 104). The measured quantities are shown by the black line. The mineral index is on the x-axis; see the respective mineral names in Table 1, the two first columns. On the right (B and D): The scatter diagrams between the predicted and the measured mineral quantities of the same ROIs. All ROI data were computed this way; the resulting statistics are presented in Table 2. In the upper figures (A and B), the dominant minerals are chlorite, chromite, magnesite and talc; and in the lower pictures (C and D) the peaks are chlorite, chromite, dolomite, serpentine and talc. Enhancement of the high-pass component (f=100.) was used for the prediction. UMX and PLS are indicated in green and red, respectively.

estimates. The quantities of the rare mineral grains are, by definition, very small and they cannot greatly affect the statistical measures, i.e. the predictions and the MLA reference quantities of the rare minerals are close to zero.

In Figure 6, the PLSR result is first printed by a red symbol and thereafter the UMX result by a green symbol. If both red and green are seen in the figures, the results are different, but if only a green colour occurs, the results coincide. In Figure 6, B and D, statistical errors and correlations and other parameters for both methods are presented on top of the diagram. Because two main minerals, namely chromite and chlorite, received only modest MAEs (Table 1), either the samples did not cover their mineralogical variation or their LWIR spectra were not unique enough to be better distinguished from the background. Concerning all mineral predictions in the Kemi case, PLSR and UMXR produced statistically very coincident results: It cannot be said which one performs better.

Quantitative mineralogical prediction from the Kemi LWIR pixel images

The LWIR SisuROCK image pixels of the Kemi samples were also interpreted for the mineral quantities using PLSR estimation. Before this, the image was still filtered by a 3-term median (Råde and Westergren 2004) along the image lines in order to avoid noise. In addition to the 29 mean spectra, the regression model was complemented with the spectra of 19 single minerals. This is necessary, because a pixel in the LWIR image may be occupied by a single mineral. All together, 48 LWIR spectra were used for the mod-

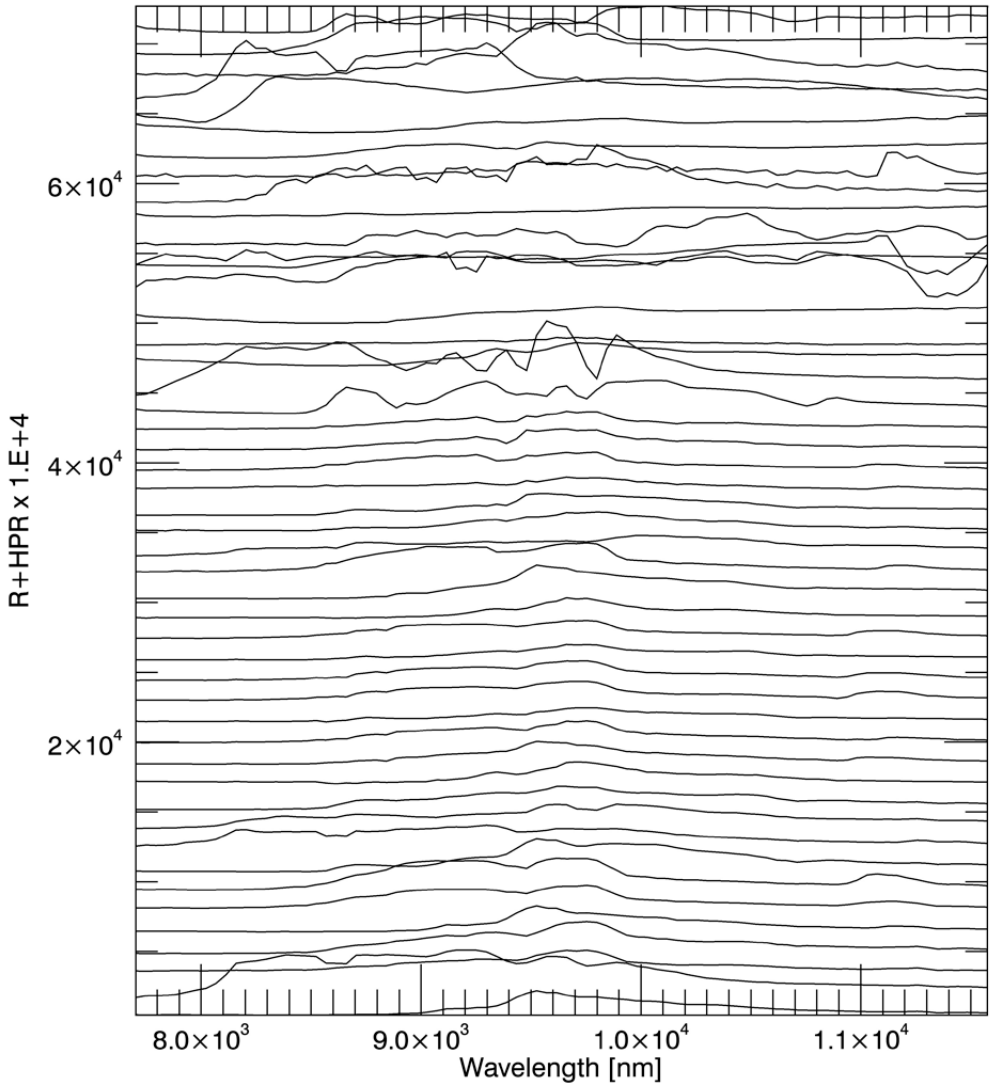

Fig. 7. The ROI and the single mineral LWIR mean spectra for the Kemi case. The ROI spectra were used for estimating quantities from the mean spectra and all were used for the estimation of mineral quantities from the Kemi pixel images. The high-pass component (f = 0.2) was not added to the original spectra. All spectra are shifted vertically for clarity.

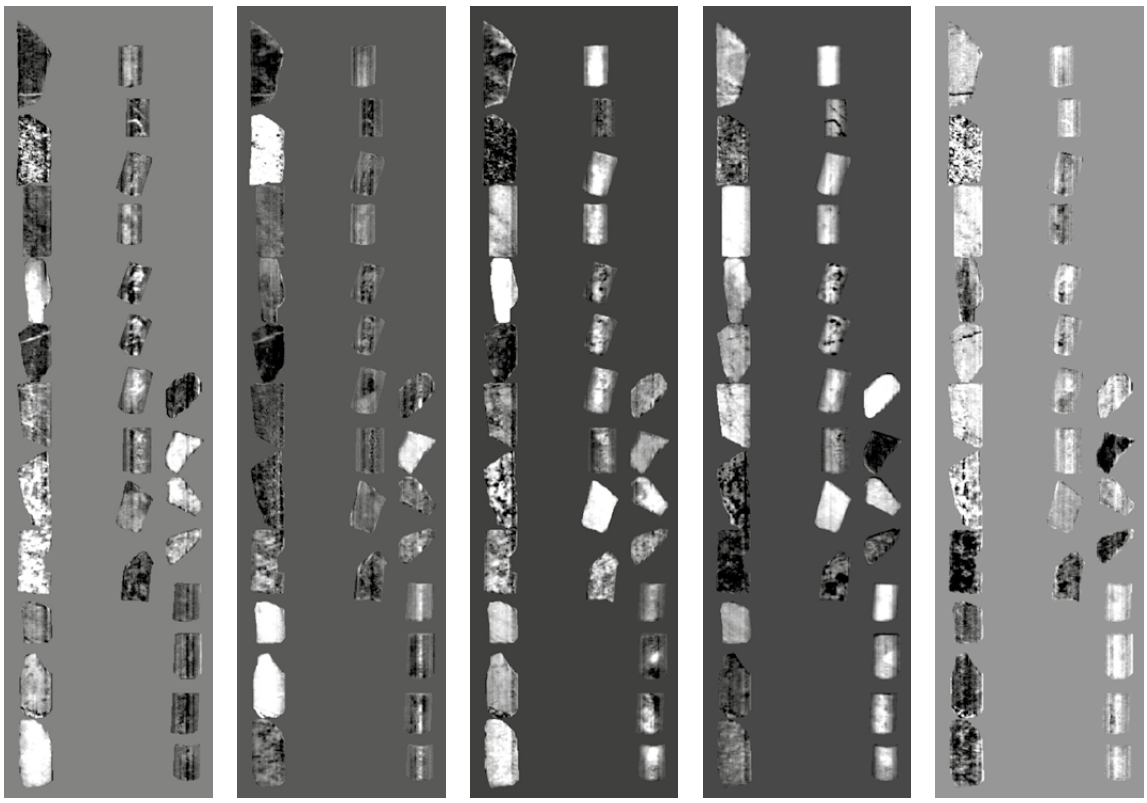

Actinolite Albite Chlorite Chromite Dolomite

Fig. 8. Illustration of the PLSR for the first five main minerals/pixel estimates about the Kemi case. The greytone variation limits from black to white for the minerals are: Actinolite 0.0-46.1%, Albite 0.0-56.8%, Chlorite, 0.0-79.5%, Chromite 0.0-100.0% and Dolomite 0.0-42.1%.

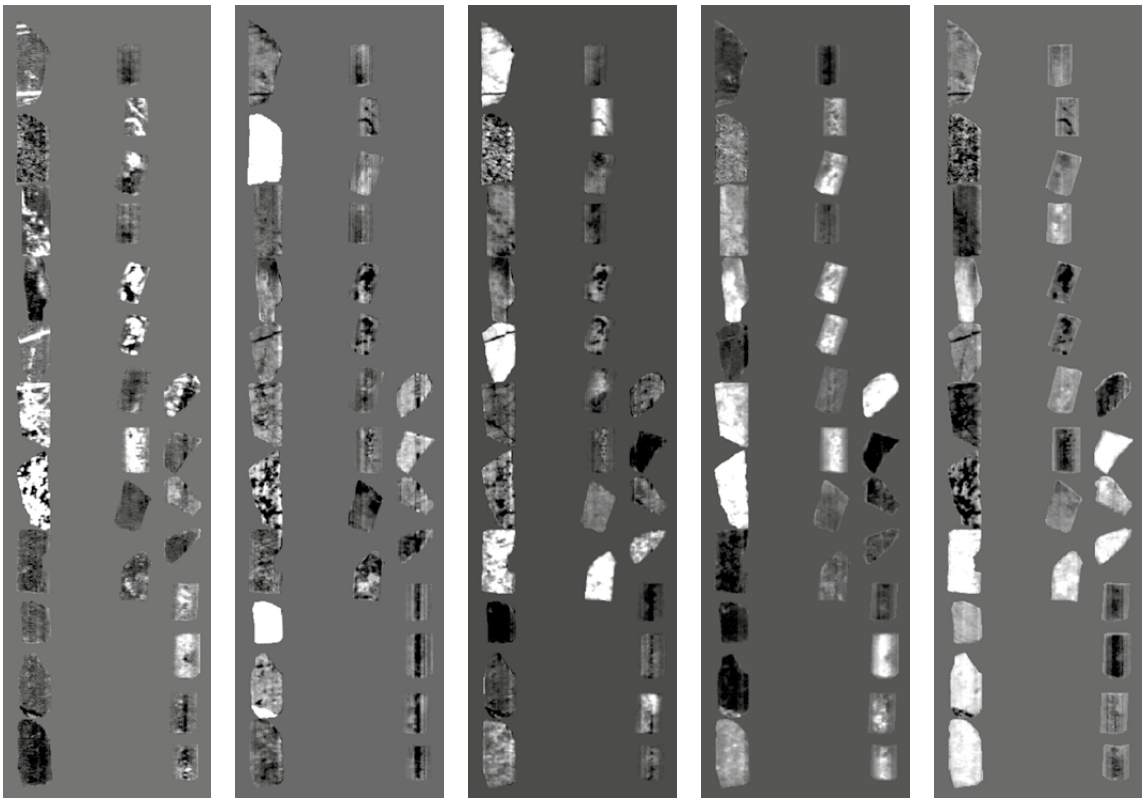

Magnesite Quartz Serpentine Talc Tremolite

Fig. 9. Illustration of the PLSR for the last five main minerals/pixel estimates about the Kemi case. The greytone variation limits from black to white for the minerals are: Magnesite 0.0-100.0%, Quartz 0.0-100.0%, Serpentine 0.0-100.0%, Talc 0.0-81.0% and Tremolite 0.0-41.2%.

elling. Their spectra are shown in their original form in Figure 7, which presents all ROI and mineral spectra that were used for this purpose. The high-pass multiplier was not used (i.e. f = 0.) for the pixel prediction, because the pixel spectra are noisier than the mean spectra. The additional spectra were those for actinolite, albite, chlorite, chromite, biotite, calcite, dolomite, diopside, epidote, hornblende, K-feldspar, magnesite, muscovite, phlogopite, plagioclase, quartz, serpentine, talc and tremolite. The result from the pixel image interpretation is expected to have a slightly lower level of accuracy than in the previous chapter for the mean spectra. The images for the predicted main minerals are presented in Figures 8 and 9.

Mineralogical clusters of the Pyhäsalmi and Kedonojankulma samples from MLA

The frequent minerals encountered in the MLA studies of the ***Pyhäsalmi*** samples related to the alteration study were (from the most common to rarest): quartz, cordierite, plagioclase, biotite, muscovite, phlogopite, pinite, pyrite, chlorite, gedrite, pyrrhotite, sillimanite, anthophyllite, talc, muscovite-chlorite mix, sphalerite and Fe oxide-mica mix. The remaining minerals covered less than 1% of the total 'surface' analysed: They were ilmenite, magnetite, apatite, kaolinite, almandine, albite, chalcopyrite, ferrogedrite, rutile, K-feldspar, calcite, an unclassified mineral, illite, gahnite, monazite-(Ce), allanite, zircon and galena.

The frequent minerals encountered in the MLA studies of the ***Kedonojankulma*** samples related to the alteration study were (from the most common to rarest): albite, quartz, K-feldspar, muscovite, chlorite, laumontite, calcite, plagioclase, allanite, chalcopyrite, epidote and illite. The remaining minerals covered less than 1% of the total 'surface' analysed: They were titanite, hornblende, biotite, pyrite, apatite, arsenopyrite, tourmaline, pyrrhotite, rutile, kaolinite, tetrahedrite, actinolite, an unclassified mineral, zircon, ilmenite, sphalerite, fluorite, britholite, scheelite, thorite, galena, claushalite(PbSe), cobaltite and silver. Table 3, column 'S-area', presents the frequency of different minerals exposed to the MLA measurements in the combined Pyhäsalmi-Kedonojankulma study.

The MLA data from the combined sample set were unsupervisedly clustered. The dendrogram (Fig. 10) shows the internal pattern of hierarchy of the mineralogical contents. The samples from the Pyhäsalmi and Kedonojankulma locate in different clusters, except for some extreme cases.

PYS-Kedo	First 4 minerals				Area of the first 4				Cluster
ROI#	1st	2nd	3rd	4th	%1st	%2nd	%3rd	%4th	MLA dist
111	PHL	QRZ	CRD	PLG	38.0	18.2	14.5	7.8	
112	CRD	MUS	QRZ	PLG	28.6	23.0	18.0	16.4	
110	QRZ	CRD	PLG	SIL	60.1	29.0	3.5	2.1	
120	QRZ	BIO	CRD	MUS	67.1	14.1	13.0	2.5	
118	QRZ	CRD	BIO	GED	46.3	23.8	21.9	2.4	
119	QRZ	CRD	BIO	CHL	56.8	21.3	17.4	2.2	
108	QRZ	CRD	BIO	MUS	41.8	24.7	14.0	10.8	
116	QRZ	PLG	MUS	BIO	51.5	21.1	12.3	9.2	
117	QRZ	MUS	PLG	BIO	59.3	15.4	9.2	6.2	
114	QRZ	PHL	CRD	PIN	51.0	15.0	13.2	9.6	
115	QRZ	PHL	BIO	CHL	55.1	34.2	8.9	1.5	
149	QRZ	ALB	CHL	KFS	99.8	0.1	0.1	0.0	
125	ALB	QRZ	KFS	CHL	30.7	21.1	14.0	10.4	
150	ALB	KFS	QRZ	CHL	33.5	19.2	11.8	11.5	
132	ALB	KFS	MUS	QRZ	31.1	24.7	17.1	10.8	
138	ALB	QRZ	KFS	CHL	39.2	28.3	18.3	5.0	
152	ALB	QRZ	KFS	CHL	39.7	30.1	16.2	7.9	
140	ALB	QRZ	KFS	CHL	35.6	30.4	17.5	6.6	
136	ALB	QRZ	KFS	CHL	38.4	27.3	16.6	4.0	
146	ALB	QRZ	KFS	CHL	39.6	34.8	15.0	5.6	
134	ALB	KFS	QRZ	CHL	43.7	24.9	23.4	3.7	
147	ALB	QRZ	KFS	CHL	39.6	25.7	23.5	5.1	
128	ALB	QRZ	KFS	PLG	34.2	30.7	12.8	8.8	
130	QRZ	KFS	ALB	CHL	31.4	30.8	28.4	4.2	
153	QRZ	ALB	KFS	CHL	35.2	30.6	26.5	4.0	
126	KFS	ALB	QRZ	CHP	40.9	30.3	14.2	4.2	
142	ALB	KFS	CHL	QRZ	71.0	13.0	6.8	3.2	
144	ALB	QRZ	KFS	CHL	51.9	16.5	13.1	9.7	
94	ALB	MUS	KFS	QRZ	53.3	21.8	11.3	9.4	
97	ALB	LAU	MUS	KFS	35.6	20.2	12.2	7.8	
121	PLG	BIO	QRZ	PRH	56.7	22.7	18.2	1.0	
122	PLG	QRZ	GED	BIO	55.7	17.3	8.1	5.3	
109	PLG	BIO	QRZ	CRD	32.9	29.3	16.5	4.9	
113	MUS	PYR	QRZ	SPH	64.1	11.6	9.9	4.1	
123	MUS	QRZ	KFS	CHP	56.0	25.3	13.2	3.8	
92	LAU	CAL	ALL	ILL	41.6	40.5	7.4	3.4	

Fig. 10. Dendrogram of the mineralogy (MLA data) for the Pyhäsalmi and Kedonojankulma samples clustered unsupervisedly using the Euclidean distance method. The four first most abundant minerals are indicated by their acronyms (after the ROI#) on the left and their respective mineral quantities [area %] by the numbers on the right. The dendrogram shows the mineralogical pattern of hierarchy for both test sites. The acronyms are: ALB = albite, ALL = allanite, BIO = biotite, CAL = calcite, CHP = chalcopyrite, CHL = chlorite, CRD = cordierite, GED = gedrite, ILL = illite, KFS = K-feldspar, LAU = laumontite, MUS = muscovite, PHL = phlogopite, PIN = pinite, PLG = plagioclase, PYR = pyrite, QRZ = quartz, SIL = sillimanite, SPH = sphalerite.

Contribution of the SisuROCK LWIR assays to the estimation of mineral quantities of the Pyhäsalmi – Kedonojankulma samples

Apparent mineralogical clusters from the Pyhäsalmi – Kedonojankulma LWIR mean spectra

The LWIR mean spectra from the combined sample set were also clustered using the high-pass enhanced (f = 100.) mean spectra. The hierarchy of the LWIR data of the Pyhäsalmi and Kedonojankulma samples is illustrated by Figure 11. When comparing this with the previous dendrogram (Fig. 10), the samples from different sites still locate in separate clusters, but there are exceptions. The internal hierarchy of the samples is approximately the same in both diagrams; only the order of the clusters may differ.

PYS-Kedo	First 4 minerals				Area of the first 4				Cluster
ROI#	1st	2nd	3rd	4th	%1st	%2nd	%3rd	%4th	LWIR dist
109	PLG	BIO	QRZ	CRD	32.9	29.3	16.5	4.9	
111	PHL	QRZ	CRD	PLG	38.0	18.2	14.5	7.8	
121	PLG	BIO	QRZ	PRH	56.7	22.7	18.2	1.0	
122	PLG	QRZ	GED	BIO	55.7	17.3	8.1	5.3	
152	ALB	QRZ	KFS	CHL	39.7	30.1	16.2	7.9	
112	CRD	MUS	QRZ	PLG	28.6	23.0	18.0	16.4	
134	ALB	KFS	QRZ	CHL	43.7	24.9	23.4	3.7	
153	QRZ	ALB	KFS	CHL	35.2	30.6	26.5	4.0	
130	QRZ	KFS	ALB	CHL	31.4	30.8	28.4	4.2	
113	MUS	PYR	QRZ	SPH	64.1	11.6	9.9	4.1	
144	ALB	QRZ	KFS	CHL	51.9	16.5	13.1	9.7	
150	ALB	KFS	QRZ	CHL	33.5	19.2	11.8	11.5	
140	ALB	QRZ	KFS	CHL	35.6	30.4	17.5	6.6	
147	ALB	QRZ	KFS	CHL	39.6	25.7	23.5	5.1	
142	ALB	KFS	CHL	QRZ	71.0	13.0	6.8	3.2	
92	LAU	CAL	ALL	ILL	41.6	40.5	7.4	3.4	
136	ALB	QRZ	KFS	CHL	38.4	27.3	16.6	4.0	
146	ALB	QRZ	KFS	CHL	39.6	34.8	15.0	5.6	
128	ALB	QRZ	KFS	PLG	34.2	30.7	12.8	8.8	
138	ALB	QRZ	KFS	CHL	39.2	28.3	18.3	5.0	
126	KFS	ALB	QRZ	CHP	40.9	30.3	14.2	4.2	
132	ALB	KFS	MUS	QRZ	31.1	24.7	17.1	10.8	
125	ALB	QRZ	KFS	CHL	30.7	21.1	14.0	10.4	
123	MUS	QRZ	KFS	CHP	56.0	25.3	13.2	3.8	
94	ALB	MUS	KFS	QRZ	53.3	21.8	11.3	9.4	
97	ALB	LAU	MUS	KFS	35.6	20.2	12.2	7.8	
118	QRZ	CRD	BIO	GED	46.3	23.8	21.9	2.4	
119	QRZ	CRD	BIO	CHL	56.8	21.3	17.4	2.2	
120	QRZ	BIO	CRD	MUS	67.1	14.1	13.0	2.5	
110	QRZ	CRD	PLG	SIL	60.1	29.0	3.5	2.1	
108	QRZ	CRD	BIO	MUS	41.8	24.7	14.0	10.8	
114	QRZ	PHL	CRD	PIN	51.0	15.0	13.2	9.6	
116	QRZ	PLG	MUS	BIO	51.5	21.1	12.3	9.2	
115	QRZ	PHL	BIO	CHL	55.1	34.2	8.9	1.5	
117	QRZ	MUS	PLG	BIO	59.3	15.4	9.2	6.2	
149	QRZ	ALB	CHL	KFS	99.8	0.1	0.1	0.0	

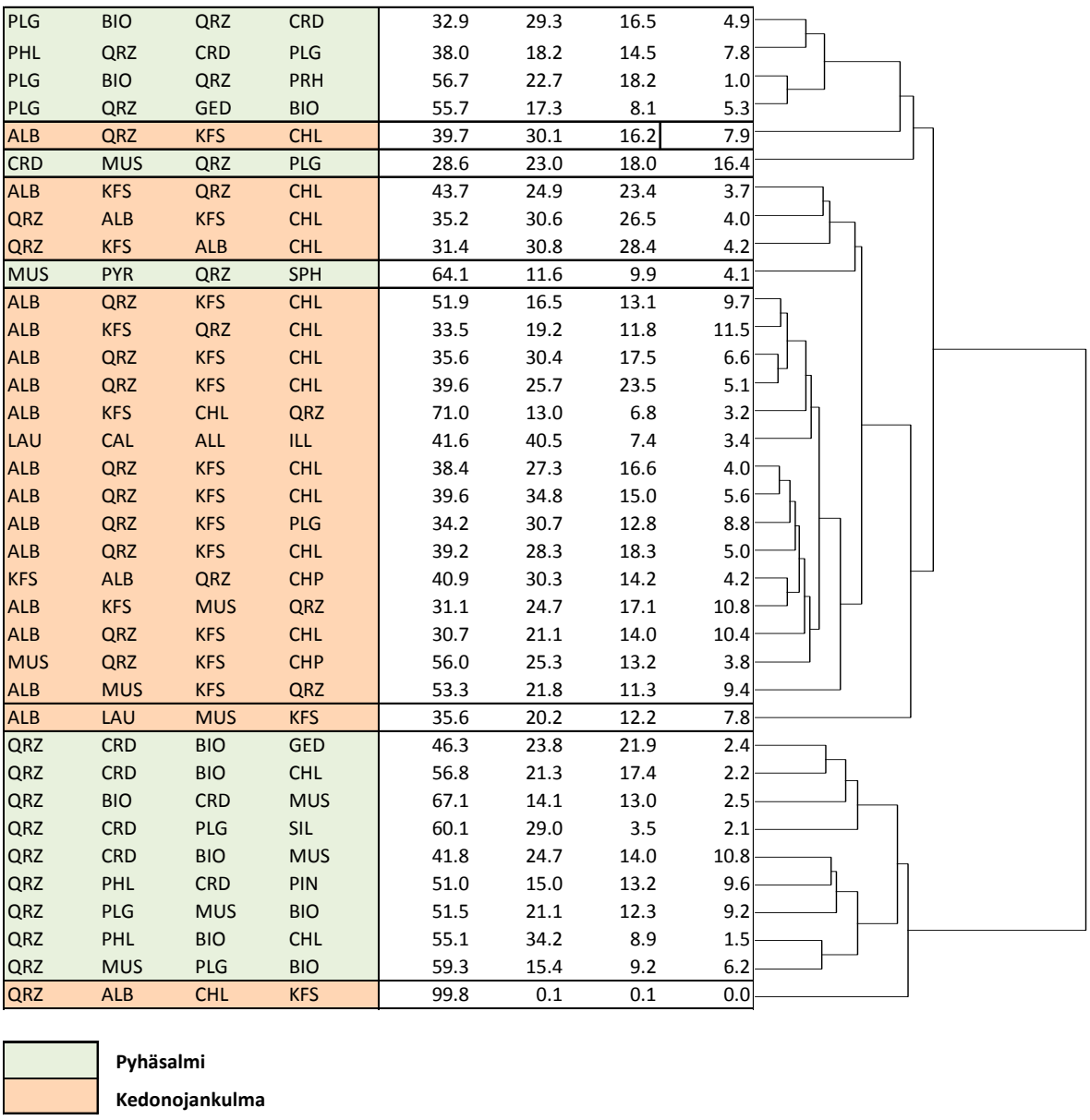

Fig. 11. Dendrogram of the LWIR spectra for the Pyhäsalmi and Kedonojankulma samples clustered unsupervisedly. The four first most abundant minerals are indicated by their acronyms (after the ROI#) on the left and their respective mineral quantities [%] by the numbers on the right. The dendrogram shows the LWIR-based pattern of hierarchy for both test sites. The mineralogical pattern and the LWIR pattern are very similar (cf. Fig. 16).

Quantitative mineralogical prediction from the mean spectra of the SisuROCK Pyhäsalmi and Kedonojankulma LWIR data

The quantitative mineral content of the Pyhäsalmi and Kedonojankulma samples was predicted using the PLS regression model on the mean spectra. The model was built for each sample from the other 35 samples out of the 36 in total. The union coverage of all the 36 samples was 3600 au (± a small area error in the MLA assays).

The predictions for the minerals produced quantity estimates, for which the respective error and reliability measures are presented in Table 3. The well-quantified minerals (bolded in Table 3) essentially cover those minerals that classify the alteration type and intensity and the wall rocks in this Pyhäsalmi and Kedonojankulma sample set. This prediction was also computed for the ROIs of the samples (Table 4). A predicted ROI (a row in Table 4) means (a predicted mineral composition and) the reliability measures for a sample.

Pyhäsalmi_Kedonojankulma mineral prediction

Mineral index	Mineral	PLS MAE%	PLS RMSE%	PLS CC	Predictv ROIs	S-area [au]	p-value
1	Actinolite	0.25	0.30	-0.02	35	0.73	0.9064
2	**Albite**	**15.75**	**21.56**	**0.56**	**35**	**711.27**	**0.0004**
3	**Allanite**	**0.94**	**1.30**	**0.63**	**35**	**28.14**	**0.0000**
4	Almandine	0.08	0.12	0.04	35	0.86	0.8011
5	Anthophyllite	0.98	1.37	0.10	35	8.44	0.5675
6	Apatite	0.10	0.12	0.19	35	3.84	0.2735
7	Arsenopyrite	0.09	0.14	-0.02	35	0.66	0.9208
8	**Biotite**	**5.57**	**8.22**	**0.45**	**35**	**166.77**	**0.0059**
9	Calcite	5.14	9.77	0.03	35	47.89	0.8465
10	**Chalcopyrite**	**0.86**	**1.21**	**0.34**	**35**	**17.15**	**0.0439**
11	Chlorite	4.27	5.85	0.21	35	119.22	0.2300
12	**Cordierite**	**1.97**	**2.80**	**0.95**	**35**	**182.27**	**0.0000**
13	Epidote	1.33	1.76	0.21	35	22.62	0.2180
14	Fe_oxide	0.04	0.06	0.05	35	0.32	0.7659
15	Feox_mica_mix	0.45	0.69	0.00	35	2.75	0.9959
16	Gedrite	1.89	2.73	0.05	35	14.53	0.7524
17	Hornblende	3.19	3.87	-0.02	35	9.54	0.9028
18	Illite	0.96	1.53	0.16	35	22.06	0.3502
19	**Ilmenite**	**0.14**	**0.18**	**0.53**	**35**	**2.23**	**0.0010**
20	**K_feldspar**	**8.02**	**10.11**	**0.67**	**35**	**362.60**	**0.0000**
21	Kaolinite	0.13	0.21	-0.12	35	2.08	0.4760
22	**Laumontite**	**4.44**	**8.04**	**0.42**	**35**	**62.92**	**0.0109**
23	Magnetite	0.36	0.52	-0.15	35	2.90	0.3928
24	**Muscovite_Chlorite_mix**	**0.34**	**0.47**	**0.41**	**35**	**7.26**	**0.0122**
25	**Muscovite**	**5.97**	**8.47**	**0.81**	**35**	**279.13**	**0.0000**
26	**Phlogopite**	**5.22**	**7.65**	**0.55**	**35**	**89.12**	**0.0005**
27	Pinite	1.89	2.66	0.22	35	31.36	0.1951
28	**Plagioclase**	**6.96**	**9.42**	**0.78**	**35**	**244.06**	**0.0000**
29	Pyrite	1.64	2.54	0.13	35	23.59	0.4432
30	Pyrrhotite	1.00	1.62	-0.07	35	13.36	0.6903
31	**Quartz**	**5.96**	**7.88**	**0.94**	**35**	**1100.71**	**0.0000**
32	Rutile	0.06	0.07	0.01	35	0.90	0.9473
33	Sillimanite	0.62	1.02	0.18	35	8.81	0.2875
34	Sphalerite	0.54	0.87	0.01	35	4.43	0.9575
35	Talc	1.15	1.93	-0.03	35	7.56	0.8608
36	Tetrahedrite	0.09	0.14	-0.01	35	0.50	0.9653
37	Titanite	0.80	1.06	0.21	35	10.44	0.2099
38	Tourmaline	0.08	0.15	-0.63	35	1.08	0.0000
39	Unclassified	0.03	0.04	-0.04	35	0.67	0.8324
40	Zircon	0.01	0.02	0.10	35	0.29	0.5654
	Total area [au]					**3615.04**	

Table 3. Statistics showing the success or failure of the mineral prediction by partial least squares regression (PLSR) concerning the LWIR spectra of the Pyhäsalmi and Kedonojankulma samples. Generally, those minerals that are abundant are more successfully estimated.

Pyhäsalmi-Kedonojankulma ROI prediction

ROI NO	PLS MAE%	PLS RMSE%	PLS CC	Predictv Minerals	S-area	p-value
92	5.61	12.83	0.00	40	100.00	0.9851
94	2.53	5.64	0.79	40	100.00	0.0000
97	5.88	13.19	-0.07	40	100.00	0.6553
108	1.74	3.16	0.92	40	100.50	0.0000
109	3.89	7.80	0.43	40	100.05	0.0060
110	3.53	7.31	0.81	40	100.08	0.0000
111	3.68	7.33	0.52	40	100.36	0.0006
112	3.41	6.42	0.63	40	100.24	0.0000
113	3.85	7.20	0.73	40	100.35	0.0000
114	2.94	5.46	0.81	40	100.77	0.0000
115	1.89	3.05	0.95	40	100.00	0.0000
116	2.32	5.10	0.82	40	101.32	0.0000
117	1.57	2.57	0.98	40	101.53	0.0000
118	1.60	2.70	0.95	40	100.14	0.0000
119	1.26	2.36	0.98	40	100.31	0.0000
120	2.03	5.43	0.90	40	101.19	0.0000
121	2.12	3.93	0.93	40	100.01	0.0000
122	1.96	3.99	0.94	40	100.34	0.0000
123	1.99	4.46	0.90	40	103.79	0.0000
125	1.03	1.87	0.96	40	100.08	0.0000
126	1.76	4.38	0.84	40	100.01	0.0000
128	1.36	2.65	0.94	40	100.57	0.0000
130	2.26	5.50	0.98	40	100.20	0.0000
132	1.14	2.17	0.97	40	101.60	0.0000
134	1.38	2.86	0.97	40	100.07	0.0000
136	1.15	2.34	0.97	40	99.90	0.0000
138	1.26	2.23	0.96	40	100.17	0.0000
140	1.25	2.68	0.98	40	100.63	0.0000
142	1.55	3.19	0.96	40	100.04	0.0000
144	1.61	4.57	0.91	40	100.01	0.0000
146	0.60	1.23	0.99	40	99.94	0.0000
147	0.84	1.43	0.99	40	100.29	0.0000
149	4.48	9.38	0.88	40	100.00	0.0000
150	1.27	2.42	0.94	40	100.03	0.0000
152	2.49	5.21	0.92	40	100.36	0.0000
153	1.17	2.16	0.97	40	100.18	0.0000
Total area [au]					**3615.06**	

Table 4. The statistical descriptors for the region of interest (ROI) prediction by partial least squares regression (PLSR) in the Pyhäsalmi-Kedonojankulma case. Here, too, there are only two ROIs (92 and 97), for which the estimates and the error measures are not acceptable. The remaining 34 ROIs are acceptable.

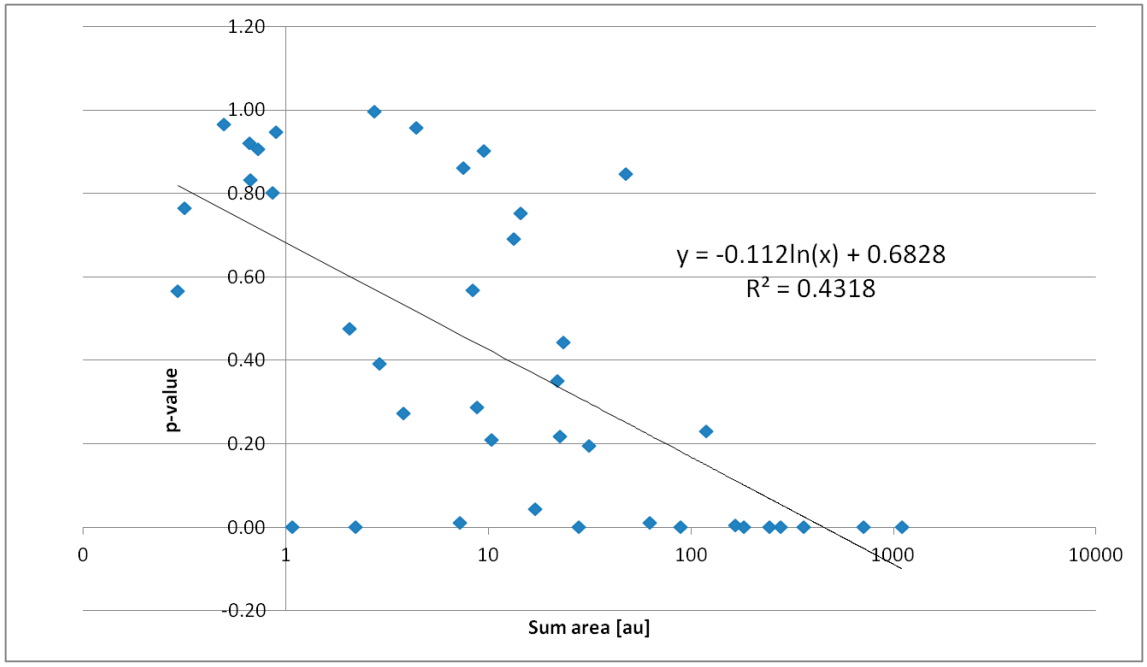

Fig. 12. In the Pyhäsalmi-Kedonojankulma case, the p-value is inversely proportional to the logarithm of the sum area exposed to the sensor.

The graph in Figure 12 shows the relationship between the sum area and the p-value: if the sum area for a mineral is small, it tends to produce a high p-value (and small CC). Albite, allanite, biotite, chalcopyrite, cordierite, K-feldspar, laumontite, muscovite, phlogopite, plagioclase and quartz are more reliably quantified than the rest of the minerals (Table 3). However, although chlorite occurs in many samples (total 421 au), it drops out from the list of well-predicted minerals. The well-predicted minerals comprise 3254 au from the total 3615 au. The 34 ROIs from total of 36 are predicted reliably, as can be seen in Table 4. It is again emphasized that this result concerns only those regression models that were constructed here based on the LWIR spectra of the 35 other samples for each one in turn out of the total of 36 samples. Concerning all mineral prediction in the Pyhäsalmi-Kedonojankulma case, the PLRS and UMXR produced statistically very similar results.

Quantitative mineralogical prediction from the SisuROCK the LWIR images of the Pyhäsalmi and Kedonojankulma samples

The estimation in this section is targeted at single pixels of the Pyhäsalmi and Kedonojankulma SisuROCK LWIR image. Before this, the image was filtered by a 3-term median (Råde and Westergren 2004) along the image lines in order to avoid noise.

This PLS Regression model was built and computed, in addition to the mean sample spectra, by also using the 18 spectra of the selected single minerals. This is natural, because a pixel in an LWIR image may be occupied by a single mineral instead of a mixture. Altogether, 55 LWIR spectra were used for the modelling. The additional single mineral spectra were actinolite, albite, biotite, calcite, chlorite, dolomite, diopside, epidote, hornblende, K-feldspar, muscovite, phlogopite, plagioclase, quartz, serpentine, talc and tremolite. The resulting accuracy of the pixel image interpretation is expected to be somewhat lower than the result in the previous section for the mean spectra, because the pixel spectra are noisier than the mean spectra. The results are illustrated in Figures 13 and 14 for those minerals that received reliable measures in the previous section.

A tentative test to predict chemistry and mineralogy from the Pyhäsalmi drilling powder samples

The hyperspectrally LWIR-imaged sample tray also contained a set of exploration drilling powders (37 samples) collected in 2001 (pers. comm. Timo Mäki 2001). All of them were chemically analysed for Cu, Zn and S, and 23 of them were also analysed for their mineralogy by MLA. The same methods were tentatively applied to these samples,

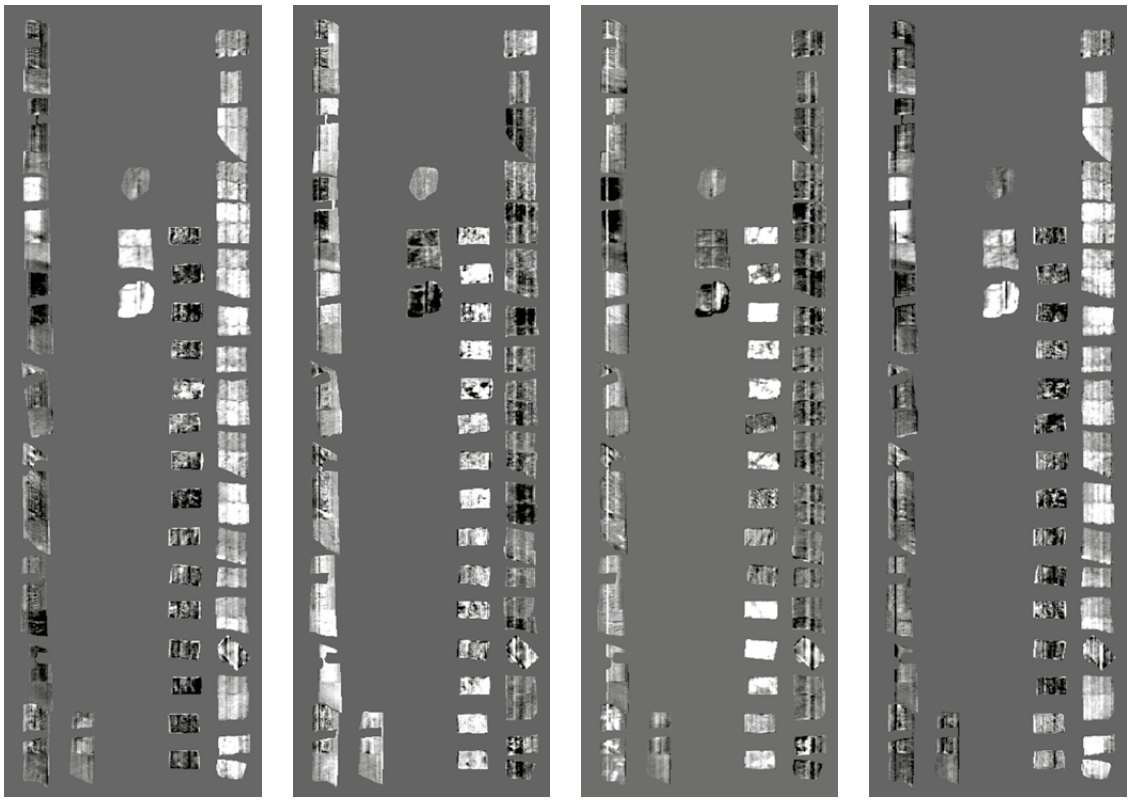

Albite Biotite Cordierite K-feldspar

Fig. 13. The first four main minerals predicted from the Pyhäsalmi-Kedonojankulma LWIR image by the PLSR model. The greytone variation limits from black to white for the minerals are: Albite 0.0-100.0%, Biotite 0.0-66.3%, Cordierite 0.0-78.6% and K_feldspar 0.0 -100.0%

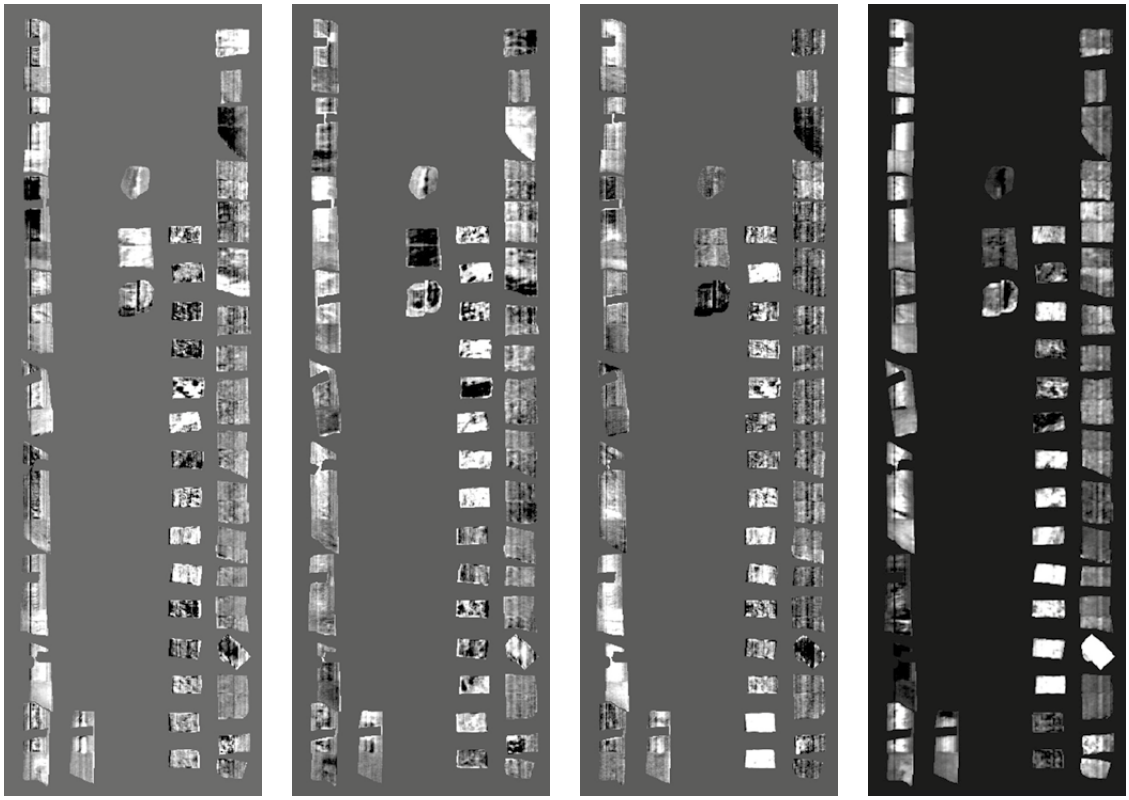

Muscovite Phlogopite Plagioclase Quartz

Fig. 14. The last four main minerals predicted from the Pyhäsalmi-Kedonojankulma LWIR image by the PLSR model. The greytone variation limits for the minerals are: Muscovite 0.0-100.0%, Phlogopite 0.0-53.6%, Plagioclase 0.0-87.7% and Quartz 0.0-100.0%

Pyhäsalmi_Powder_element prediction

Element index	Element	PLS MAE%	PLS RMSE%	PLS CC	Predictv ROIs	S-area [au]	p-value
1	**Zn**	**2.37**	**3.15**	**0.69**	**35**	**94.14**	**0.0000**
2	**S**	**11.50**	**14.94**	**0.49**	**35**	**1299.90**	**0.0023**
3	Cu	0.63	0.81	0.32	35	26.13	0.0610
Total area [au]						**1420.17**	

Table 5. Prediction parameters concerning the Pyhäsalmi drilling powder elements. The statistical error parameters suggest that the estimates are significant for Zn and S, but erroneous for Cu.

Pyhäsalmi_Powder_mineral prediction

Mineral index	Mineral	PLS MAE%	PLS RMSE%	PLS CC	Predictv ROIs	S-area [au]	p-value
1	**Actinolite**	**0.17**	**0.21**	**0.55**	**22**	**2.64**	**0.00604**
2	Albite	4.44	5.63	0.10	22	18.76	0.6587
3	Andalusite	0.31	0.60	-0.20	22	2.53	0.3663
4	Andradite	1.52	1.99	0.17	22	11.56	0.4275
5	Anthophyllite	0.26	0.43	-0.01	22	1.91	0.9702
6	**Apatite**	**0.09**	**0.12**	**0.52**	**22**	**1.27**	**0.0106**
7	Augite	0.43	0.57	0.27	22	3.70	0.2205
8	**Baryte**	**1.88**	**2.22**	**0.96**	**22**	**140.37**	**0.0000**
9	**Biotite**	**5.41**	**6.42**	**0.42**	**22**	**83.64**	**0.0455**
10	**Calcite**	**1.78**	**2.27**	**0.51**	**22**	**39.56**	**0.0138**
11	Celsian	0.73	1.12	-0.05	22	3.61	0.8208
12	Chalcopyrite	2.82	3.56	0.09	22	56.41	0.6984
13	Chlorite	5.55	7.05	-0.07	22	28.71	0.7342
14	**Clay_minerals**	**0.46**	**0.80**	**0.67**	**22**	**11.93**	**0.0004**
15	Clinozoisite	0.55	0.96	0.15	22	6.42	0.5016
16	**Cordierite**	**1.51**	**3.17**	**0.55**	**22**	**30.90**	**0.0069**
17	Diopside	1.63	2.27	0.29	22	19.32	0.1785
18	**Dolomite**	**1.60**	**3.15**	**0.68**	**22**	**30.57**	**0.0003**
19	Fe_oxide	2.15	2.69	-0.16	22	20.46	0.4670
20	**Gedrite**	**0.68**	**0.98**	**0.47**	**22**	**14.18**	**0.0246**
21	**Gypsum**	**0.60**	**0.78**	**0.55**	**22**	**10.70**	**0.0060**
22	Hornblende	2.21	3.38	0.29	22	27.85	0.1865
23	Hyalophane	0.51	1.15	-0.11	22	4.74	0.6264
24	**K_feldspar**	**0.25**	**0.35**	**0.84**	**22**	**4.91**	**0.0000**
25	Muscovite	5.85	13.79	-0.04	22	57.54	0.8601
26	Phlogopite	0.72	0.98	0.41	22	10.66	0.0533
27	**Plagioclase**	**6.63**	**9.09**	**0.76**	**22**	**149.01**	**0.0000**
28	**Pyrite**	**11.47**	**15.21**	**0.85**	**22**	**1070.53**	**0.0000**
29	Pyrrhotite	2.58	3.08	0.05	22	90.45	0.8274
30	**Quartz**	**2.32**	**2.98**	**0.93**	**22**	**127.67**	**0.0000**
31	**Serpentine**	**0.18**	**0.23**	**0.61**	**22**	**2.62**	**0.0019**
32	**Sphalerite**	**3.30**	**3.94**	**0.92**	**22**	**164.53**	**0.0000**
33	Talc	1.64	3.93	-0.09	22	18.92	0.6833
34	Tremolite	2.54	4.31	-0.03	22	26.50	0.8990
35	**Unclassified**	**0.06**	**0.08**	**0.57**	**22**	**2.49**	**0.0047**
	Total area [au]					**2297.55**	

Table 6. Prediction parameters concerning the Pyhäsalmi drilling powder minerals. The statistical error parameters suggest that the estimates for bolded minerals are acceptable.

however, bearing in mind that the samples were 'old', i.e., the surfaces of the sulphide minerals had oxidized into other chemical compounds during the 14 years of storage. The ore concentrates were not useful in this study, because the grains were covered by unknown non-mineral material. The results for the elements Cu, Zn and S are presented in Table 5. The results are, however, interesting: the elements S and Zn could be estimated with moderate accuracy (MAE ≤ 11.5%, CC ≥ 0.49, p-value ≤ 0.023), but Cu analysis was not successful. The reason is apparently that Cu has a very small variance in comparison with Zn and S, and that the surfaces of chalcopyrite may have suffered most due to oxidation.

The drilling powders were also subject to PLSR modelling with LWIR data for quantitative estimation of minerals. Those minerals that provided reliable quantity estimates are printed in bold in Table 6: actinolite, apatite, baryte, biotite, calcite, clay minerals, cordierite, dolomite, gedrite, gypsum, K-feldspar, plagioclase, pyrite, quartz, serpentine, sphalerite, and 'unclassified'. The presence of the class 'unclassified' means that there may exist a constant spectral signal from this material. Unfortunately, chalcopyrite and pyrrhotite dropped out due to high p-values or a low correlation between the predicted and measured quantities. The reason for this may be that the chalcopyrite and pyrrhotite area units [au] are small in the MLA data and that the mineral surfaces were oxidized. However, the reliably estimated minerals of the powders comprise 1888 au from the total 2298 au.

CONCLUSIONS

The SisuROCK LWIR imaging spectrometry reflectance data on rock samples was tested for ability to identify minerals and predict the mineral composition of samples. Three diverse targets were purposefully selected to test the method in versatile mineral/rock identification problems. The targets were the Kemi chromite mine, Pyhäsalmi Cu-Zn-S mine and Kedonojankulma Cu-Au ore prospect. In Kemi, the aim was to study the ore types and a few host rocks. In Pyhäsalmi and Kedonojankulma, the main focus of the study was on the identification of the alteration minerals among other minerals. A set of exploration drilling powders from Pyhäsalmi was also included in the study. They were analysed for minerals and the main chemical commodities.

The PLSR prediction result was successful for those minerals that were 'sufficiently present', i.e. comprising several percent; these could be quantitatively predicted. The reliability for their quantities and the error measures can be seen from the statistics performed. The following minerals were well quantified. They are, starting from the most reliably predicted (based on the low p-values with low or moderate MAEs), in the following list:

- Risk 0.0–1.1% (p-value x 100): albite, chromite, dolomite, magnesite, quartz, serpentine, talc, cordierite, muscovite, plagioclase, baryte, pyrite, sphalerite, K-feldspar, actinolite, tremolite, clay minerals, phlogopite, ilmenite, epidote, biotite, gypsum, apatite and laumontite.
- Risk 1.2–4.5% (p-value x 100): calcite, gedrite and chalcopyrite.
- Risk 5% (p-value x 100): chlorite

Chlorite covers a notable area in the MLA assays, but it could not be quantified with less than 5% risk. Besides chlorite, those minerals that classify the ore types and wall rocks (Kemi case) and the alteration minerals, among others (Pyhäsalmi and Kedonojankulma cases), are included in the list above.

The estimation of minerals for the drilling powders was less successful than for the solid rocks: all abundant minerals could be estimated with moderate accuracy, except pyrrhotite and chalcopyrite. The estimation of chemical elements for powders was analogous: Zn and S received moderate estimates, but not Cu. The reason for this may be that the powder samples were 14 years old and the surfaces of the mineral grains were therefore oxidized, masking the proper pyrrhotite and chalcopyrite.

As stated in the methodology section of this paper, literally negative prediction quantities occur. They illustrate the inadequacy of the sample set used for modelling in relation to the sample set to be interpreted, or the inadequacy of the spectral signature. In practical applications, the negative values are simply converted to zero, but a better option for further work is to prepare a perfect sample set and good reference data for exact regression modelling. The good reliability measures with

acceptable residuals between the predicted and measured quantities are frequently related to those minerals and/or samples that are well represented within the area exposed to the spectrometer.

The accuracy for the sample composition (ROI) prediction is seemingly better than the accuracy for single mineral prediction on average. The reason for this is that the quantities of the rare minerals are naturally small and they do not greatly affect the ROI spectra and the statistical measures. The UMXR and PLSR methods were compared for all predicted minerals in Kemi and Pyhäsalmi-Kedonojankulma cases. PLS and UMXR produced statistically very coincident results.

The main minerals, including the alteration minerals, and the unknown new mixtures of the minerals can be quantified using this LWIR & PLSR technique with accuracy, which would benefit mineral exploration and mining actions. LWIR imaging spectrometry is a rapid method for providing a quantitative estimation of the geological targets and sample compositions over large surfaces, presuming that the conditions for the prediction are carefully prepared. The key to success in quantifying a set of minerals is that the minerals have independent spectral LWIR signatures, the same minerals/rocks used in models become imaged by LWIR and MLA. It is also important that the model samples cover the variation of the mixtures of minerals.

ACKNOWLEDGEMENTS

Mr Ossi Leinonen (Avesta Polarit Oy), Mr Timo Mäki (Pyhäsalmi Mine Oy), Mr Timo Huhtelin (Outokumpu Ferrochrome Oy) and Mr Jukka Kousa (Geological Survey of Finland) are thanked for providing access to their mineral/rock sample materials. Dr Maarit Middleton (Geological Survey of Finland) and Dr Markus Törmä (Finnish Environment Institute) are gratefully acknowledged for reviewing this paper and helping to improve its structure and content. Mr Jukka Laukkanen, Ms Tuula Saastamoinen and Ms Neea Heino (all at the Geological Survey of Finland) are thanked for the MLA assays. Mr Harri Kutvonen (Geological Survey of Finland) is thanked for helping to prepare the graphics for this report.

REFERENCES

Abrams, M., Abbott, E. & Kahle, A. 1991. Combined use of visible, reflected infrared, and thermal infrared images for mapping Hawaiian lava flows. Journal of Geophysical Research—Solid Earth and Planets 96, 75–484.

Alapieti, T. T. 2005. Early Palaeoproterozoic (2.5-2.4 Ga) Tornio – Näränkävaara Layered Intrusion Belt and Related Chrome and Platinum-group Element Mineralization, Northern Finland. Chapter 1 in: Alapieti, T. T. & Kärki, A .J. (eds). Guide 51a, Geological Survey of Finland, 20 p. [Electronic resource]. Available at: http://tupa.gtk.fi/julkaisu/opas/op_051a_pages_013_032.pdf.

Alapieti, T. T. & Huhtelin, T. A. 2005. The Kemi intrusion and associated chromitite deposit. Chapter 2 in Alapieti, T. T. & Kärki, A. J. (eds). Guide 51a, Geological Survey of Finland, 20 p. [Electronic resource]. Available at: http://tupa.gtk.fi/julkaisu/opas/op_051a_pages_013_032.pdf.

Baldridge, A. M., Hook, S. J., Grove, C .I. & Rivera, G. 2009. The ASTER spectral library version 2.0. Remote Sensing of Environment 113, 711–715.

Bolin, B. J. & Moon, T. S. 2003. Sulfide detection in drill core from the Stillwater Complex using visible/near-infrared imaging spectroscopy. Geophysics 68, 1561–1568.

Brown, A. J., Sutter, B. & Dunagan, S. 2008. The MARTE VNIR Imaging Spectrometer experiment: design and analysis. Astrobiology 8, 1001–1011.

Gallie, E. A., Mcardle, S., Rivard, B. & Francis, H. 2002. Estimating sulphide ore grade in broken rock using visible/infrared hyperspectral reflectance spectra. International Journal of Remote Sensing 23, 2229–2246.

Geladi, P. &. Kowalski, B. R. 1986. "Partial least-squares regression: a tutorial," Analytica Chimica Acta, vol. 185, 1–17.

Hecker, C., Dilles, J. H., Mejde, M. van der & Meer, F. D. van der. 2012. Thermal infrared spectroscopy and partial least squares regression to determine mineral modes of granitoid rocks, Geochemistry Geophysics Geosystems, vol. 13 (3), 1–15.

Hook, S. J. & Kahle, A. B. 1996. The micro Fourier Transform Interferometer (mu FTIR)—a new field spectrometer for acquisition of infrared data of natural surfaces. Remote Sensing of Environment 56, 172–181.

Iljina, M. & Hanski, E. 2005. Layered mafic intrusions of the Torni-Näränkävaara belt. In: Lehtinen, M. Nurmi, P. A. & Rämö, O .T. (eds). 2005. Precambrian Geology of Finland – Key to the Evolution of the Fennoscandian Shield. Elsevier B.V., Amsterdam, 101–138.

Kirkland, L., Herr, K., Keim, E., Adams, P., Salisbury, J., Hackwell, J. & Treiman, A. 2002. First use of an airborne

thermal infrared hyperspectral scanner for compositional mapping. Remote Sensing of Environment 80, 447–459.

Korsman, K., Koistinen, T., Kohonen, J., Wennerström, M., Ekdahl, E., Honkamo, M. , Idman, H. & Pekkala, Y. (eds). 1997. Suomen kallioperäkartta – Berggrundskarta över Finland – Bedrock map of Finland 1 : 1 000 000, Geological Survey of Finland, Espoo, Finland.

Kousa, J., Luukas, J., Mäki, T., Ekdahl, E., Pelkonen, K., Papunen, H., Isomäki, O.-P., Penttilä, V.-J. & Nurmi, P. 1997. Geology and mineral deposits of the central Ostrobothnia. Geological Survey of Finland, Guide 41, 43–67.

Kouvo, O. 1977. The use of mafic pegmatoids in geochronometry. Abs. 5th. Europ. Coll. Geochrom, Pisa, Italy.

Krämer, N. & Sugiyama, M. 2011. The Degrees of Freedom of Partial Least Squares Regression. Journal of the American Statistical Association. vol.106, no.494, pp.697{705, 2011. [Electronic resource]. Available at: http://citeseerx.ist.psu.edu/viewdoc/download?doi=10.1.1.386.4679&rep=rep1&type=pdf . Last accessed 23 June 2015.

Kruse, F. A. 1996. Identification and mapping of minerals in drill core using hyper spectral image analysis of infrared reflectance spectra. International Journal of Remote Sensing 17, 1623–1632.

López-Alonso, J. M. & Alda, J. 2002. Bad pixel identification by means of principal component analysis. Optical Engineering 41, 2152–2157.

Mäki, T. 1986. Lithogeochemistry of the Pyhäsalmi zinc-copper-pyrite deposit, Finland. In: Prospecting in Areas of Glaciated Terrain 1986. Kuopio, Finland, 1–2 September 1986. London: The Institution of Mining and Metallurgy, 69–82.

Mason, P. & Huntington, J. F. 2012. HyLogger 3 components and pre-processing: An overview. Northern Territory Geological Survey, Technical Note 2012-002. 9 p.

Mevik, B.-H. & Wehrens, R. 2007. The pls Package: Principal component and Partial Least Squares Regression in R. Journal of Statistical Software. Vol 18, Issue 2, 1–24.

Middleton, M., Närhi, P., Kuosmanen, V., & Sutinen, R. 2011. Quantification of glacial till chemical composition by reflectance spectroscopy. Applied Geochemistry 26 (2011) 2215-2225.

Nielsen, A. A. 1999. Linear Mixture Models, Full and Partial Unmixing in Multi- and Hyperspectral Image Data.

Pratt, W. K. 2001. Digital Image Processing. Wiley & Sons, 738 p.

Puustjärvi, H. (ed.) 1999. Pyhäsalmi Modelling Project. Technical Report 13.5.1997 – 12.5.1999. 251 p., 76 app. [Electronic resource]. Available at: http://tupa.gtk.fi/raportti/arkisto/m19_3321_99_1_10.pdf.

Råde, L. & Westergren, B. 2004. Mathematics Handbook for Science and Engineering. Studentlitteratur, Lund, Sweden. 562 p.

Ragona, D., Minster, B., Rockwell, T. & Jussila, J. 2006. Field imaging spectroscopy: a new methodology to assist the description, interpretation, and archiving of paleoseismological information from faulted exposures. Journal of Geophysical Research-Solid Earth 111.

Salisbury, J. W. & Daria, D. M. 1992. Emissivity of terrestrial materials in the 8-14 MUM atmospheric window. Remote Sensing of Environment 42, 83–106.

Salisbury, J. W., Walter, L. S. & Vergo, N. 1989. Availability of a library of infrared (2.1–25.0 MU-M) mineral spectra. American Mineralogist 74, 938–939.

Sylvester, P. J. 2012. Chapter 1: use of the mineral liberation analyzer (MLA) for mineralogical studies of sediments and sedimentary rocks. Mineralogical Association of Canada Short Course 42, St. John's NL, May 2012, 1–16

Taranik, J., Riley, D., Hackwell, J., Vaughan, G. & Aslett, Z. 2008. Development of hyperspectral thermal remote sensing for geological applications. International Geological Congress, Oslo. [Electronic resource]. Available at: http://www.cprm.gov.br/33IGC/1342506.html. Last accessed 23 June 2015.

Tiainen, M., Kärkkäinen, N., Lohva, J., Sipilä, P. & Huhta, P. 2012. Discovery of the Kedonojankulma Cu-Au occurrence, hosted by a Svecofennian porphyritic granitoid in Southern Finland. Geological Survey of Finland, Special Paper 52, 73–90.

Tiainen, M., Molnar, F. & Koistinen, E. 2013. The Cu-Mo-Au mineralization of the Paleoproterozoic Kedonojankulma intrusion, Häme Belt, Southern Finland. 12th Biennial SGA Meeting, Uppsala, Sweden.

van der Meer, F. 2006. The effectiveness of spectral similarity measures for the analysis of hyperspectral imagery. International Journal of Applied Earth Observation and Geoinformation 8, 3–17.

Wold, H. 1975. Path models with latent variables: the NIPALS approach. In: Blalock, H. M. et al. (eds). Quantitative sociology: international perspectives on mathematical and statistical modeling, Academic, 307–357.

Wold, S., Sjöström, M. & Eriksson, L. 2001. PLS-regression: a basic tool of chemometrics, Chemometrics and Intelligent Laboratory Systems 58 (2), 109–130.

www.gtk.fi
info@gtk.fi

This Special Paper portrays the geophysical signatures of different mineral deposit types that are known in Finland. The first part of the publication is a review of geophysical expressions and their dependencies, and the second part contains four articles that illustrate the results of special studies in which different geophysical research methods have been used. Airborne geophysical responses – magnetic, electromagnetic and radiometric – reflect the sub-surface spatial distribution of minerals having contrasting physical properties. This publication widely introduces the petrophysical properties of ore minerals and mineral systems, because they provide mappable parameters on mineralized or barren source rocks responsible for geophysical signatures. Anomalous density, magnetic properties or electric conductivity are common to most ore minerals, in particular magnetite and sulphides. The geophysical expressions of different mineral deposit types primarily depend on the presence of these minerals and the way in which they appear.

ISBN 978-952-217-337-9 (PDF)
ISBN 978-952-217-336-2 (paperback)
ISSN 0782-8535